MULTIDIMENSIONAL HYDRODYNAMIC SIMULATIONS OF MASSIVE STARS AND
THEIR EXPLOSIONS

By

Carl Edward Fields

A DISSERTATION

Submitted to
Michigan State University
in partial fulfillment of the requirements
for the degree of

Astrophysics and Astronomy – Doctor of Philosophy

2021

ABSTRACT

MULTIDIMENSIONAL HYDRODYNAMIC SIMULATIONS OF MASSIVE STARS AND
THEIR EXPLOSIONS

By

Carl Edward Fields

Massive stars play a crucial role in galactic chemical evolution, compact object formation, and stellar feedback. Computational models of massive stars and their explosions have progressed over the decades in concert with astrophysical observations to advance our theoretical understanding of stellar evolution and transient phenomena. Stellar models have been used to constrain supernova progenitor masses of observed explosions, estimate the age of globular clusters, and determine properties of the interior of the Sun. However, despite these advances, stellar models are subject to uncertainties that can qualitatively alter the outcome and often disagree with observation. Among the sources of uncertainties in stellar models are thermonuclear reaction rates, the treatment of mixing and heat transport via convection, and pre-supernova structure in core collapse supernova simulations. The consequences of these uncertainties directly impact theoretical models of massive stars and their explosions.

In this Thesis, I explore these areas of uncertainty and consider the implications they have on our theoretical understanding of massive stars and stellar transients. I begin by considering the impact of nuclear reaction rate uncertainties on the evolution of massive stars using 1D stellar evolution models. In this work, I sample 665 nuclear reaction rates according to their temperature-dependent uncertainties in a grid of 2000 stellar models to identify key reaction rates at five evolutionary epochs. Next, I present results of a 15 $M_\odot$ stellar model evolved in 2D and 3D for the final seven minutes prior to iron core collapse. In this work, I characterize the Si- and O-shell convective properties and compare them to predictions from 1D models. Following this, I present work considering 3D simulations of stellar Si- and O-shell convection in a 14-, 20-, and 25 $M_\odot$ model. These models are simulated for the final ten minutes prior to iron core collapse and represent the largest set of 3D pre-supernova models in the literature. Following this work, I consider the

implications that models of 3D pre-supernova perturbations have on CCSN explosion properties. I present the results of 1-, 2-, and 3D neutrino-radiation-hydrodynamic CCSN simulations of a 15 $M_\odot$ using 2D/3D initial conditions. This work investigates the role that non-radial perturbations in the progenitor might have on multi-messenger signals produced in models of CCSNe. Lastly, I conclude with a brief discussion of `MESA-Web`: an online web interface to the stellar evolution toolkit, `MESA`. I discuss the current capabilities of this tool, the impact it has had over the past five years since its inception, and the future plans to continue to increase its utility as a scientific tool and resource for astronomy education. The data products as a result of this Thesis are publicly available online.

To my family, friends, and Potato for whom without their love and support none of this would be possible

ACKNOWLEDGEMENTS

of the department as well including Sevan Chanakian, Amanda Koenig, Raquel K. W. M., Scott Funkhouser, John Tran, and too many more to list. I also want to thank Steven Thomas and the AGEP community for providing a supportive community for me during my time in graduate school - and the free food!

I am thankful for those that have been role models for me over the years, making it easier for me to envision my place in academia: Dr. Lucianne W., Dr. Adam Miller, Prof. Danny Cabellero, Prof. John Johnson, Prof. Jorge Moreno, Prof. Ronald Cox, Prof. Pero Dagbovie, Prof. Jedidah Isler, Dr. Brian Nord, and Dr. Eileen Gonzales. I am thankful for Kay-Kay Realty Corp., specifically David and Michael Kotin and Lisa Giblin. I am thankful for my high school physics teacher, Mr. Chad Jacobs, who made helped shape my physics identity and inspired me to pursue physics as a career. I am grateful for my therapists: Dr. Chris Barry (undergrad), Dr. Martez Burkes (MSU), and Dr. Donnie Daggett (ASU).

TABLE OF CONTENTS

LIST OF TABLES

LIST OF FIGURES

CHAPTER 1

INTRODUCTION

1.1 Overview

The explosion of a massive star can produce ripples through spacetime and drive the creation of the elements needed for life. Their deaths can also give birth to a neutron star or black hole, providing clues into the evolution of galaxies. Simulations of massive stars and their explosions can allow us to unlock secrets about properties deep within the stellar interior, a region inaccessible to direct observation. However, simulations are subject to uncertainties that can qualitatively alter the outcome and disagree with astrophysical observations.

In this Thesis, I explore areas of uncertainty in stellar models and consider the implications they have on our theoretical understanding of massive stars and stellar transients. I will present work investigating uncertainties due to thermonuclear reaction rates, the treatment of mixing and heat transport via convection, and pre-supernova structure in core collapse supernova simulations. Decades of technological advancement and new experimental constraints provide new components in constructing next-generational stellar models. The simulations presented in this Thesis represent a step forward in our fundamental understanding of massive stars and their explosions.

1.2 Evolutionary Phases of Massive Stars

1.2.1 The Main Sequence

Stars will spend the majority of their lifetime on the Main Sequence (MS). The MS corresponds to the time in which a star is undergoing hydrostatic core H-burning. For a 15 $M_\odot$ star, this process takes on the order of $\tau_{MS} \sim 11$ Myr, compared to a star like the Sun which will have a MS lifetime much larger of $\tau_{MS} \sim 1100$ Myr (Iben, 1967; Woosley et al., 2002). In Figure 1.1 we show a Hertzsprung-Russell (HR) diagram for theoretical stellar models at 10 evolutionary points from Iben (1967). The first point (1) represents the zero-age MS (ZAMS), start of the MS, while the (2)
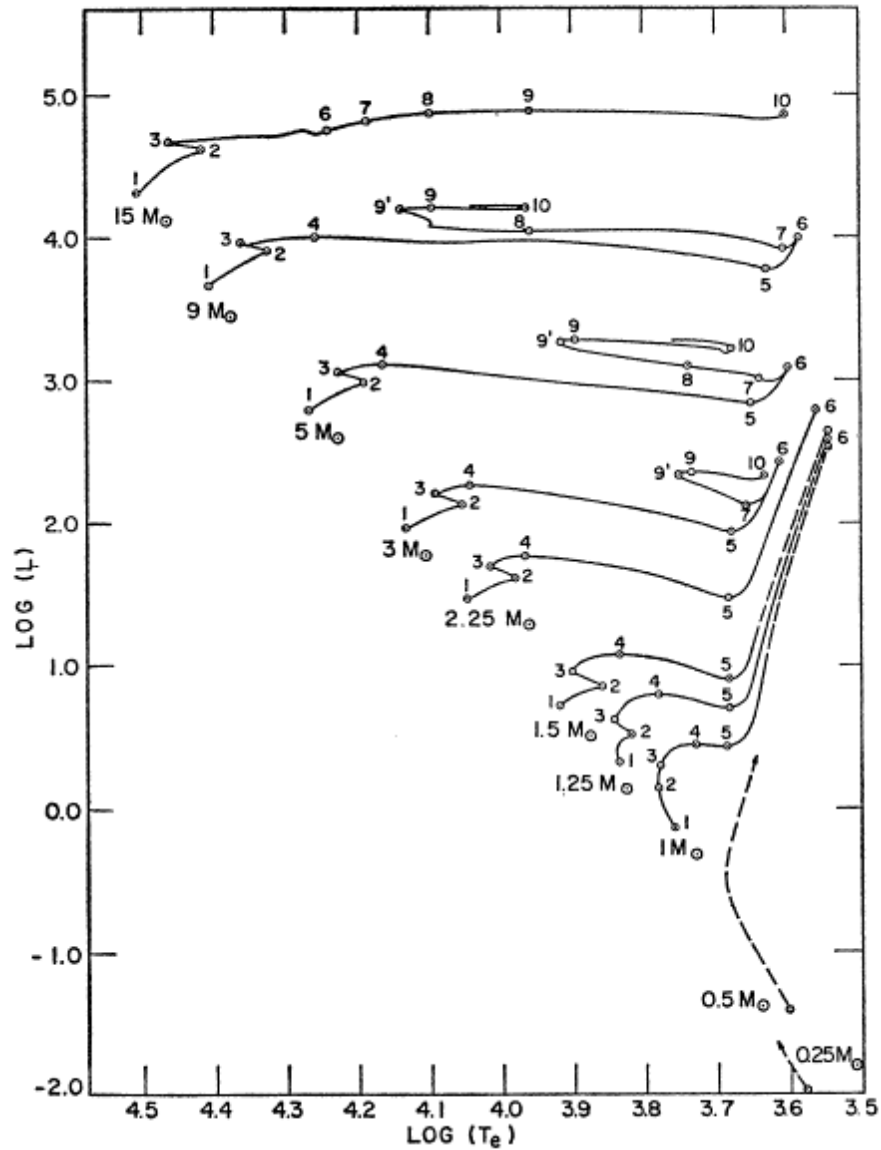
Figure 1.1: Evolutionary paths in the HR diagram of stars with initial mass M_{ZAMS}=0.25 to 15 $M_\odot$. Dashed lines denote estimated evolutionary tracks. Figure from Iben (1967).

label denotes the approximate terminal age MS (TAMS), the point at which the star has exhausted

its fuel of core hydrogen.

1.2.2 Core He-Burning

After leaving the main-sequence, the core begins to contract as their is no nuclear energy generation

via thermonuclear reactions to produce a pressure source. The overall contraction phase proceeds

from points (2) and (3) in Figure 1.1. At point (3), a new energy source is established as H-burning continues in a shell above the newly formed He-core, moving outward in mass to process the remainder of H left in the core. A portion of the energy generated in the shell is absorbed by the envelope leading to significant expansion. In the case of the 15 $M_\odot$ model, the star becomes a Supergiant. The He-core grows in mass due to the H-shell burning until reaching the approximate Schönberg-Chandrasekhar limit,

$$\left(\frac{M}{M_{\rm ic}}\right) = 0.37 \left(\frac{\mu_{\rm e}}{\mu_{\rm ic}}\right)^2 \tag{1.1}$$

the maximum mass for an inert isothermal core to support an overlying envelope (Schönberg & Chandrasekhar, 1942). Once this limit is reached, core contraction and a subsequent increase in temperature proceeds rapidly until conditions are met for core He-burning to occur. At point (6) He is ignited in the core at a temperature of $T \sim 2 \times 10^8$ K. For a 15 $M_\odot$ star, this burning phase lasts approximately 2 Myr. During this time, the star moves through the red supergiant phase of the HR diagram, points (6) - (10).

1.2.3 Carbon Burning

Once He is depleted in the core, helium continues to burn in a shell beneath the H-shell burning region and above the nascent CO core. The core contracts and again increases in density and temperature until the conditions for core C burning is met. The ashes of core He burning are primarily are ^{12}C and ^{16}O. The lowest Coulomb barrier of the possible reaction sequences is ^{12}C + ^{12}C and thus initiates the C burning phase of the stars life. The primary products of this burning phase are ^{16}O, ^{20}Ne and ^{24}Mg. For a 15 $M_\odot$ model this process takes place over a few kyr. This phase is also the first burning stage where energy losses due to thermal neutrino processes such as pair-annihilation become relevant (Fowler & Hoyle, 1964; Itoh et al., 1996a). These neutrino losses contribute significantly to increasing the core temperature and reducing the burning timescales as the star continually tries to maintain hydrostatic equilibrium (Deinzer & Salpeter, 1965).

1.2.4 Advanced Nuclear Burning

Following C-burning, massive stars will continue to burn heavier elements on shorter timescales and at higher temperatures. At this point in time, the nuclear burning timescales make the use of the HR diagram less useful as the dynamical timescale, $\tau_{\text{dyn.}} \approx (G\bar{\rho})^{-1/2}$, is much larger near the surface. Of the advanced nuclear burning stages Si burning is worthy of mention due to its complex nature.

Silicon burning in the core of a massive star proceeds differently than the other advanced burning stages. Fusion reactions of two ^{28}Si (or ^{28}Si + ^{32}S) nuclides are unlikely due to the large Coulomb barrier. Photodisintegration, a process by which a high energy gamma ray removes a neutron, proton, or alpha particle from a nucleus, in massive stars it operates to break up some of the available ^{28}Si and residual lighter nuclei to produce a surplus of free particles. These free nuclei are quickly captured by the remaining ^{28}Si to form heavier elements of ^{32}S, ^{36}Ar, and ^{40}Ca up an alpha chain until reaching ^{56}Ni. Here, the term alpha chain represents a sequence of (α, γ) reactions that build heavier nucleons through the continued capture of alpha particles onto lighter nuclei. In some reduced reaction networks used in stellar models, these channels are the only ones that are followed allowing simulations to reduce computational memory requirements of storing information about adjacent, less significant isotope in each cell (Timmes et al., 2000). Nuclei near an the iron peak, atomic mass number of $A = 56$, are the most tightly bound nuclei with the largest binding energy per nucleon. The result is that the conditions in the core of a massive star lead to the formation of a core composed of iron peak elements. As Si-burning proceeds in a shell above the iron core, the core grows in mass and approaches the effective Chandrasekhar mass limit (Baron & Cooperstein, 1990),

$$M_{\text{Ch,eff.}} \equiv 5.76 Y_e^2 \times \left[1 - 0.057 + \left(\frac{s_e}{\pi Y_e} \right)^2 + 1.21 \left(\frac{s_e}{A} \right) \right] M_\odot , \tag{1.2}$$

the fate of the star grows near.

1.3 Evolutionary Fates

1.3.1 Electron-Capture Supernova Explosions

The fate of massive stars in the range of $M_{\mathrm{ZAMS}} \approx 8 - 11\ M_\odot$ have been a topic of discussion for years due to their complex nature (Woosley & Heger, 2015). These stars are massive enough to reach the conditions necessary to ignite carbon in the core often followed by off center C-burning episodes to produce an O-Ne-Mg core (Farmer et al., 2015). However, for models within this mass range the question becomes whether or not the O-Ne-Mg core will grow sufficiently in mass to reach conditions to ignite Ne and proceed towards iron core collapse as our 15 $M_\odot$ model. Below a critical O-Ne-Mg core mass of $M \approx 1.37\ M_\odot$ (Nomoto, 1984), the star will follow an evolutionary path expected to form an O-Ne-Mg white dwarf. Alternatively, some stars that fail to eject their envelope and that are below this mass threshold are expected to collapse as electron-capture supernovae.

In degenerate O-Ne-Mg cores, electron captures onto ^{20}Ne and ^{24}Mg act to effectively decrease the specific electron fraction and thus the effective Chandrasekhar mass (Equation 1.2). In doing so, the core eventually becomes gravitationally unstable and collapse ensues. During collapse, O is ignited, but due to the rapid rate of electron captures, collapse is able to overcome the O deflagration and continue unimpeded until the central density reaches a few times nuclear density. The properties of electron-capture supernovae (ECSNe) progenitors differ from more massive stars and as such they can help explain different observational properties otherwise not possible with more massive models (e.g., in producing heavy r-process elements (Wanajo et al., 2011)). In Figure 1.2 the fates of massive star stellar models in the mass range of 7-11$M_\odot$ are summarized. For the remainder of this Thesis we will focus on the majority of massive stars above a mass of 11 $M_\odot$ which we expect to form an iron core.

1.3.2 Core-Collapse Supernova Explosions

Stars with an initial mass greater than $\approx 11\ M_\odot$ will evolve to build an inert core primarily consisting of nuclei near the iron peak. Si-shell burning occurs outside of the iron core increasing its mass
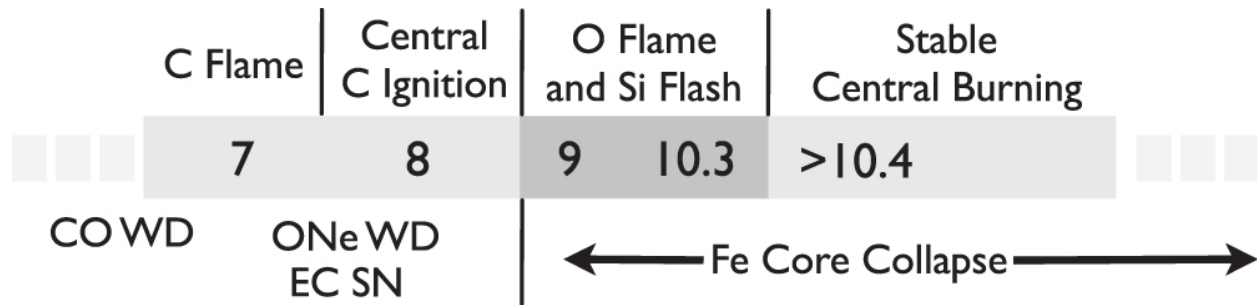
Figure 1.2: Evolutionary fates for a sample of stellar models in the mass range of 7-11 $M_\odot$. For this particular set of models, stars below 7 $M_\odot$ form CO WDs, stars from 7-8 $M_\odot$ ignite C off-center whereas from 8-9 $M_\odot$ it ignites centrally. For models in the mass range 7-9 $M_\odot$ a degenerate O-Ne-Mg core is produced that cools to a WD if the envelope is lost or results in a ECSNe if envelope remains. Stars above $9M_\odot$ ignite Si either off-center (up to $\approx$ 10.3 $M_\odot$) or centrally (above $10.3M_\odot$) to end in iron core-collapse. Figure from Woosley & Heger (2015).

towards its effective Chandrasekhar limit. Near this limit, the increasingly degenerate material experiences thermal pressure support being removed from the core via photodisintegration. Core contraction starts to occur due to the thermal support loss. This contraction leads to an increase in density and temperature within the stellar core accelerating the capture of electrons onto protons further removing pressure support provided by electron degeneracy and decreasing the adiabatic index, the core begins to contract further. The reduction of the required adiabatic index to maintain hydrostatic equilibrium causes a gravitational instability and dynamical collapse of the core ensues.

Core-collapse is halted when the inner core reaches a density of $\rho \sim 6 \times 10^{14}$ g cm^{-3} and the strong nuclear force becomes repulsive. The inner core collides with the infalling material and recoils to cause the formation of a pressure wave traversing outward that quickly steepens into a shock. The shock travels outward at speeds of $v \sim 0.25c$ continually losing energy due to the photodisassociation of the supersonic free-falling outer iron core and due to inward momentum of the material leading to ram pressure. On the timescale of a few hundred ms, the shock stalls at an approximate radius of 200 km, the location where the pressure from the shock and the infalling matter are balanced.

The *delayed* neutrino heating mechanism (Bethe & Wilson, 1985; Janka & Mueller, 1996) proposes one possible solution for revival of the stalled shock. The mechanism in its current form suggests that the neutrinos emitted by the newly formed proto-neutron star (PNS) can be reabsorbed

at a larger radius corresponding to the location where the net energy loss rate is less than the local rate of energy deposition by neutrinos. Above this radius and outward to the location of the standing shock is known as the gain region. Within this region, net heating by neutrinos can facilitate thermal pressure support to drive the shock outward and launch a successful explosion.

CCSNe play a critical role in many areas of astronomy. Galactic chemical evolution models require accurate explosion energies predicted for a given progenitor (Timmes et al., 1995; Kobayashi et al., 2020). Nucleosynthetic yields and remnant properties rely on fallback material and mixing dynamics (Chan et al., 2020). Observations of superluminous supernovae (SLSNe) such those found by the *Zwicky Transient Facility* depend on properties of the PNS for a central engine or shock interaction with the interstellar medium hypothesis to explain the unusually bright transients (Eftekhari et al., 2019; Lunnan et al., 2020).

Observations of CCSNe are categorized by the features of the optical spectra. Some of those features include peak brightness and particular atomic absorption or emission features. The most common explosion type is classified as a type-II supernova owing to strong H line features. Beyond this classification many further sub-classes are established. Two primary classes are based on a plateau (Type IIP) or linear decline of the light curve (Type IIn). These two sub-classes make up $\approx 59\%$ and 3% of all CCSN explosions, respectively (Smartt et al., 2009). Identifying CCSN progenitors has been a goal of observational efforts to help constrain theoretical models of red supergiants (RSGs) and explosion models. In Figure 1.3 we show a cumulative frequency plot of observationally derived progenitor masses for Type IIP supernova explosions (Smartt, 2009). Progenitor masses can be determined by using theoretical stellar models to determine a final luminosity to be compared to the observational value placing an upper limit of the initial mass.

1.4 Motivating New Models of Massive Stars and CCSNe

1.4.1 Nuclear Reaction Rates

At the heart of computational models of stellar structure and evolution are nuclear reaction rates. The low transmission probabilities at astrophysically relevant energy ranges have presented a challenge
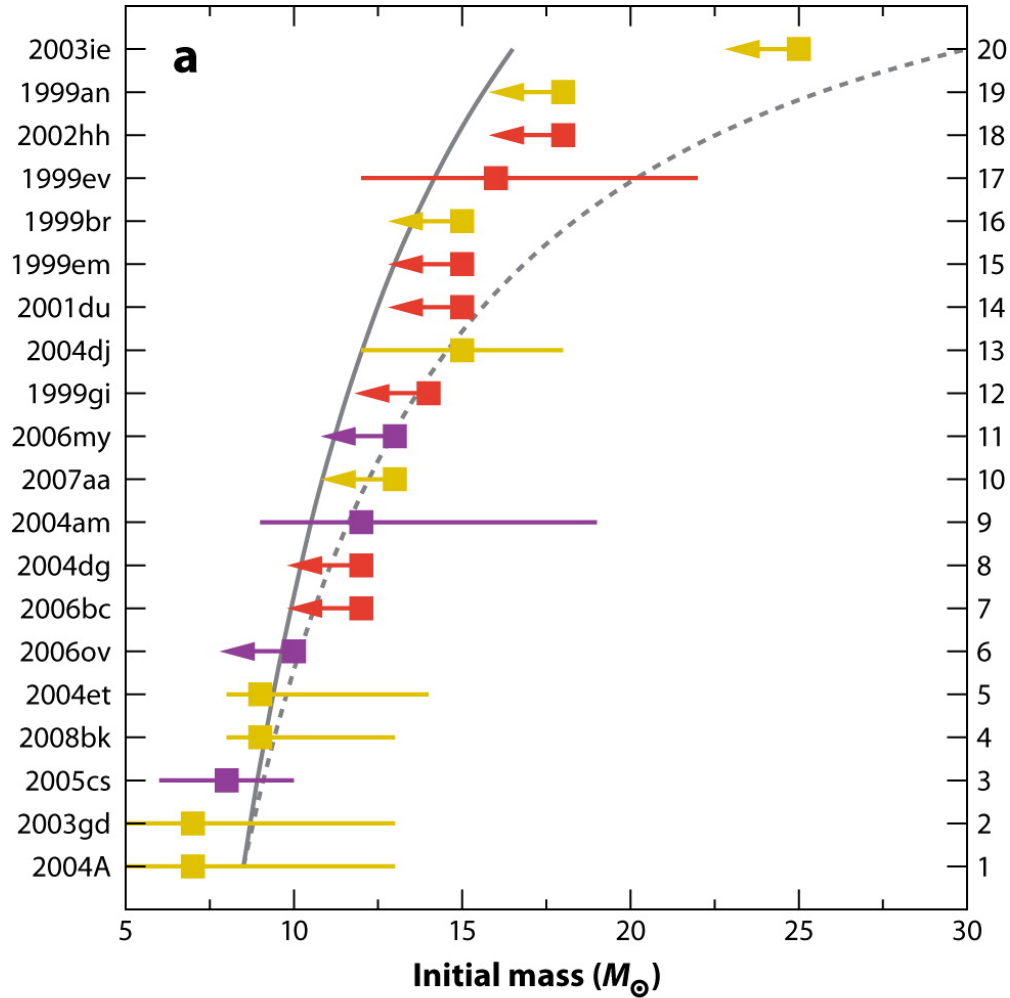
Figure 1.3: A cumulative frequency plot of the masses of II-P progenitors of observed supernovae. The solid line represents a Salpeter IMF best fit to the observed data with a minimum mass of $8.5M_\odot$ and maximum mass of $16.5M_\odot$ while the dashed line has a maximum mass of $30M_\odot$. The right axis is a cumulative count of events within these two limits. The events are colored according to the metallicity used in model ranging from the composition of the Large Magellanic Cloud to Solar. The supernovae are grouped in metallicity bins log O/H + 12 = 8.3-8.4 (gold), 8.5-8.6 (red), 8.7-8.9 (purple). Figure from Smartt (2009).

for direct measurements of nuclear cross sections - a key component in determining reaction rates. The astrophysical S factor, a rescaling of the nuclear cross section can be measured near 100 keV to 1 MeV. However, most temperatures experienced in stellar environments are at energies of 0.1 to 100 keV and thus require theoretical models or extrapolation in the absence of experimental data.

Key nuclear reaction rates can have different impacts on stellar evolution properties. For example, the $^{14}N(p,\gamma)^{15}O$ is the slowest nuclear reaction rate in the CNO cycle. As such, the
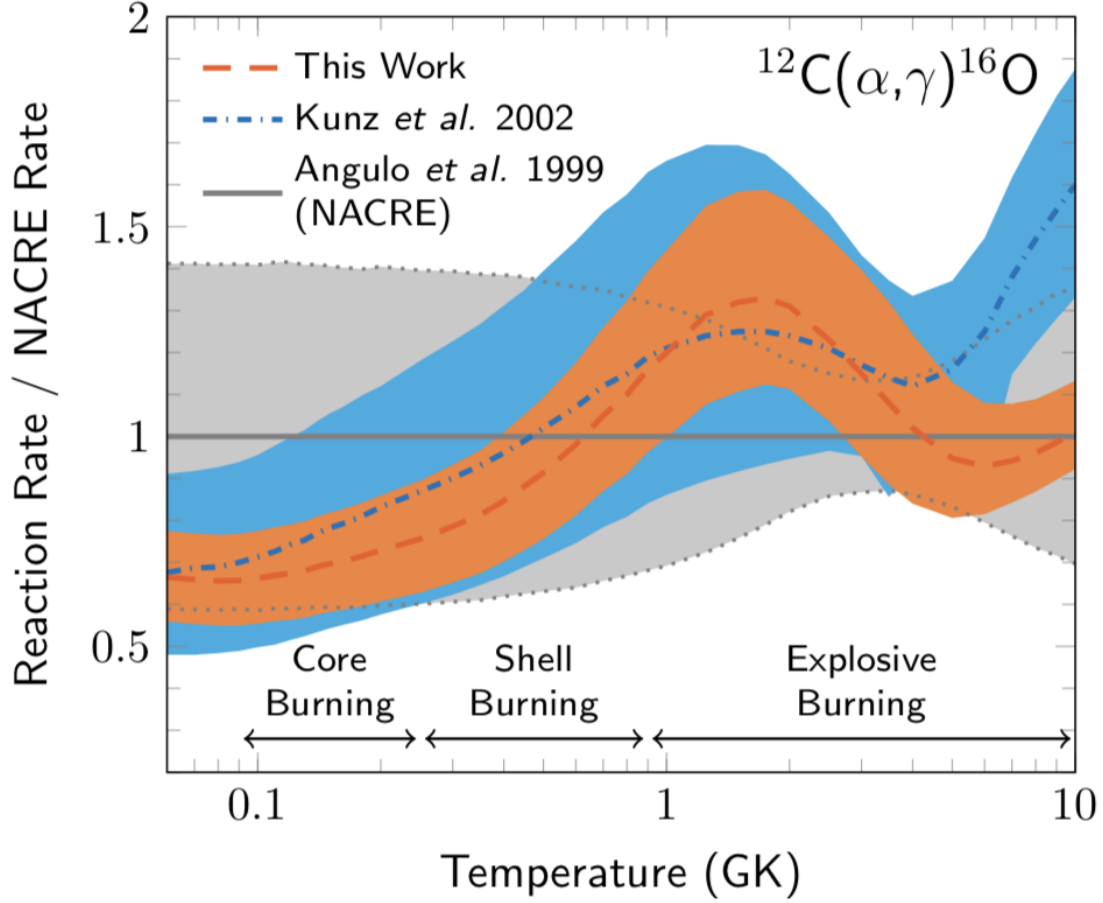
Figure 1.4: Nuclear reaction rate for $^{12}C(\alpha, \gamma)^{16}O$ normalized compared to two rates over a range of Helium burning conditions. Figure from deBoer et al. (2017).

reaction rate can alter the MS turnoff time estimated for a stellar population. Recent direct measurements of the cross section for this reaction down to energies of 70 keV were performed by LUNA Collaboration et al. (2006a). The result of the updated nuclear reaction rate led to change in turnoff age and surface properties for stellar models above 1 $M_\odot$ (Tognelli et al., 2011). Of particular interest to massive stars is the $^{12}C(\alpha, \gamma)^{16}O$ nuclear reaction. This reaction can operate at different times during the life of a massive star but of particular importance is when it competes with the triple-α reaction during core He-burning. West et al. (2013) investigated the impact of these two nuclear reactions when multiplied by their median values within their experimental uncertainties. They evolved a grid of stellar models to the end of core He-burning and found that they can produce ranges of central ^{12}C mass fractions of $X_c(^{12}C) \approx 0\text{-}0.42$.

Recent progress on determining the $^{12}\mathrm{C}(\alpha, \gamma)^{16}\mathrm{O}$ reaction rate was performed by deBoer et al. (2017) using an $R-$matrix analysis informed by past measurements and experimental uncertainties. In Figure 1.4 we show the $^{12}\mathrm{C}(\alpha, \gamma)^{16}\mathrm{O}$ compared to three other tabulated rates used in past studies. As a part of this Thesis work, I have implemented the updated tabulated reaction rate into the `starkiller-astro` microphysics routines [1] and within the `FLASH` simulation framework (the StarKiller Microphysics Development Team et al., 2019). The `starkiller-astro` project is a collection of microphysical routines commonly used together with AMReX codes which include the fully compressible hydrodynamics code, CASTRO (Almgren et al., 2010). In Chapter 2, we present work building on these efforts that utilize temperature-dependent uncertainties in evaluating the impact of nuclear reaction rates on massive star models.

1.4.2 Stellar Convection

The Schwarzschild criterion describes a region is *stable* against convection if

$$\nabla_{\mathrm{rad.}} < \nabla_{\mathrm{ad.}} \, , \tag{1.3}$$

where $\nabla_{\mathrm{ad.}}$ is the adiabatic (no heat exchange) temperature variation of a fluid element undergoing a change in pressure. This is defined as

$$\nabla_{\mathrm{ad.}} = \frac{d\log T}{d\log P} \, . \tag{1.4}$$

The quantity $\nabla_{\mathrm{rad.}}$ is the actual gradient of the temperature for a star in hydrostatic equilibrium in a region where the only means of energy transport is via radiation. An alternative criterion is the Ledoux criterion where Equation 1.3 becomes

$$\nabla_{\mathrm{rad.}} < \nabla_{\mathrm{ad.}} + \nabla_\mu \, , \tag{1.5}$$

for an ideal gas. This modified equation takes into account spatial gradients in the mean molecular weight,

$$\frac{1}{\mu} = \sum_i \frac{(Z_i + 1)X_i}{A_i} \, . \tag{1.6}$$

---

[1]https://github.com/starkiller-astro
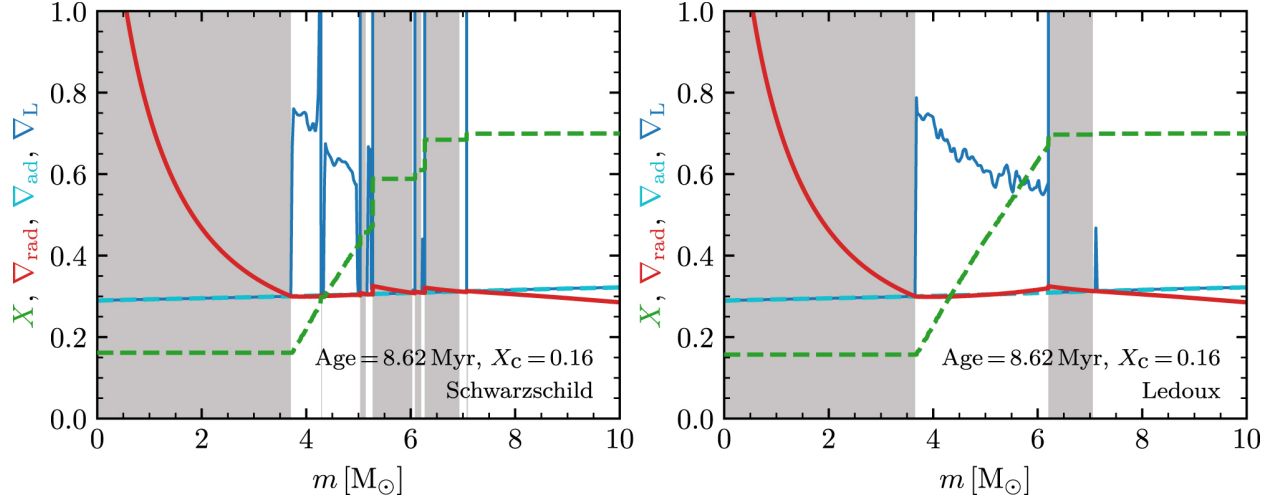
Figure 1.5: Profiles of the different gradients that determine convective stability in a 16 $M_\odot$ 1D stellar evolution model. The quantity X is the hydrogen mass fraction and ∇_L is the Ledoux gradient, the sum of the radiative and mean molecular weight gradients. The gray shading represents regions that are convective. Figure from Paxton et al. (2018).

In chemically homogenous regions, this equation reduces to the Schwarzschild criterion. Additional mixing processes can occur at the boundaries of radiative and convection mixing. Among these processes are thermohaline, semi-convection, and convective boundary mixing (Langer et al., 1983; Brown et al., 2013; Davis et al., 2018). In Figure 1.5 we show profiles of the various gradients in a stellar evolution model of a 16 $M_\odot$ star using MESA (Paxton et al., 2018). At low specific mass coordinate, corresponding to the center of the stellar model, the radiative gradient is large due to the energy generation rate exceeding the condition for convection to occur.

Spherically symmetric stellar evolution calculations use mixing length theory (MLT) to describe energy transfer via convection (Cox & Giuli, 1968). MLT has been shown to accurately represent convection in 1D models when calibrated to radiation hydrodynamic simulations of surface convection in the Sun (Trampedach et al., 2014). Despite the utility of MLT in 1D, multidimensional effects in the late stages of nuclear burning in the life of a massive star can lead to conditions that differ significantly from spherical symmetry (Arnett et al., 2009; Arnett & Meakin, 2011; Viallet et al., 2013). Moreover, additional mixing processes that are subject to free parameters in 1D might operate at the edges of stellar convective and radiative boundaries. These processes can alter internal structure of stars in advanced burning stages (Davis et al., 2018). The situation is
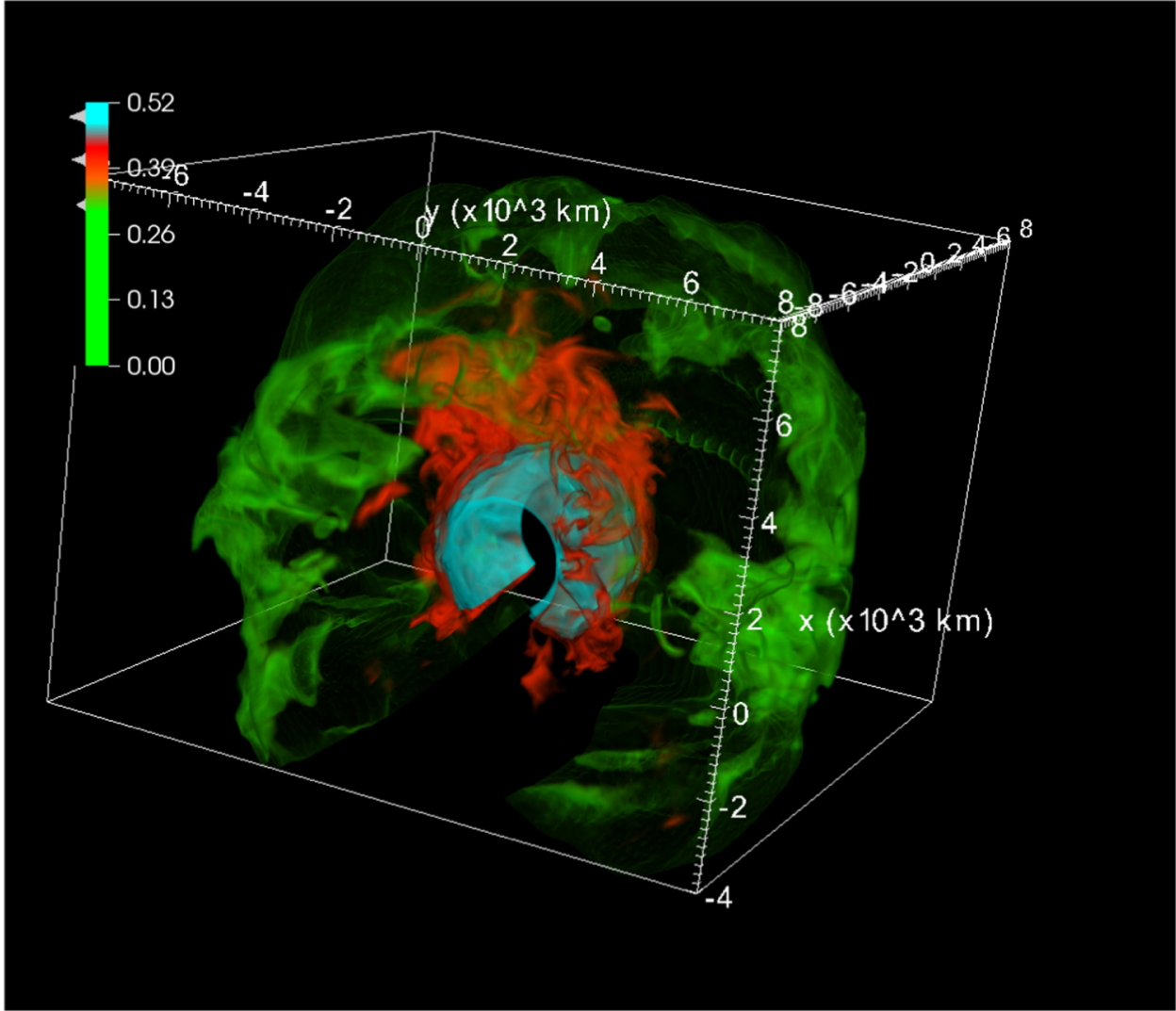
Figure 1.6: Volume rendering of the silicon mass fraction for a 3D hydrodynamic simulation of O-shell convection of a 18 $M_\odot$ star at the onset of collapse. Figure from (Müller et al., 2016b).

further complicated in models including rotation and magnetism as these models also include free parameters only operating in the presence of rotation. An accurate description of the convective properties of a massive star is crucial to our understanding of stellar structure and transient phenomena. In Figure 1.6 we show a volume rendering of the silicon mass fraction for a 3D hydrodynamic simulation of O-shell convection of a 15 $M_\odot$ star at the onset of collapse (Müller et al., 2016b). In this work they found that in the final moments prior to collapse, a large scale $\ell = 2$ mode emerged in the power spectrum for the spherical harmonic decomposition of the radial velocity. Such a large scale mode observed at the onset of collapse in a massive star could have favorable implications for

the explodability of a particular progenitor model (Hanke et al., 2012; Couch et al., 2015; Couch & Ott, 2015).

Current simulations of CCSNe can now include General Relativity (Roberts et al., 2016), neutrino transport via multidimensional two-moment schemes such (Shibata et al., 2011; O'Connor & Couch, 2018a), and grid schemes that allow for higher spatial resolutions (Nagakura et al., 2019). However, the majority of these simulations utilize progenitor models taken from 1D stellar evolution codes at the start of iron core-collapse and followed through to a time of about 5-10 ms post bounce in 1D. This process cannot adequately take into account the scale of convection or provide information about the chaotic, convective nuclear shell burning expected to take place in massive stars approaching core-collapse (Meakin & Arnett, 2007). The turbulent non-radial motions observed in multidimensional simulations of massive stars could potentially provide a means for achieving successful explosion in otherwise weak or failed CCSN explosion models.

Couch & Ott (2013) investigated the impact of progenitor perturbations in 3D CCSN models. They found that their when inducing velocity perturbations, motivated by multidimensional simulations of Si-shell burning (Arnett & Meakin, 2011), their perturbed 3D CCSN model was either able to achieve explosion or evolve closer to explosion than the unperturbed counterparts. The perturbations led to a significant increase in anisotropic kinetic energy within the gain region. Couch et al. (2015) evolved a 3D simulation for the last $\sim$ 3 minutes before iron core-collapse of a $15M_\odot$ star using a 21 isotope nuclear reaction network. This 3D model showed significant non-radial kinetic energy *prior* to collapse that was amplified during the collapse phase. In their 3D CCSN models they found that the 3D progenitor model exploded earlier and more energetically than the 1D angle-average counterpart. The implication of these results is that 3D progenitor models have a crucial and qualitative impact on CCSNe. In Chapter 3 and Chapter 4, we present work building on these efforts that develop multidimensional models of stellar convection in massive stars.
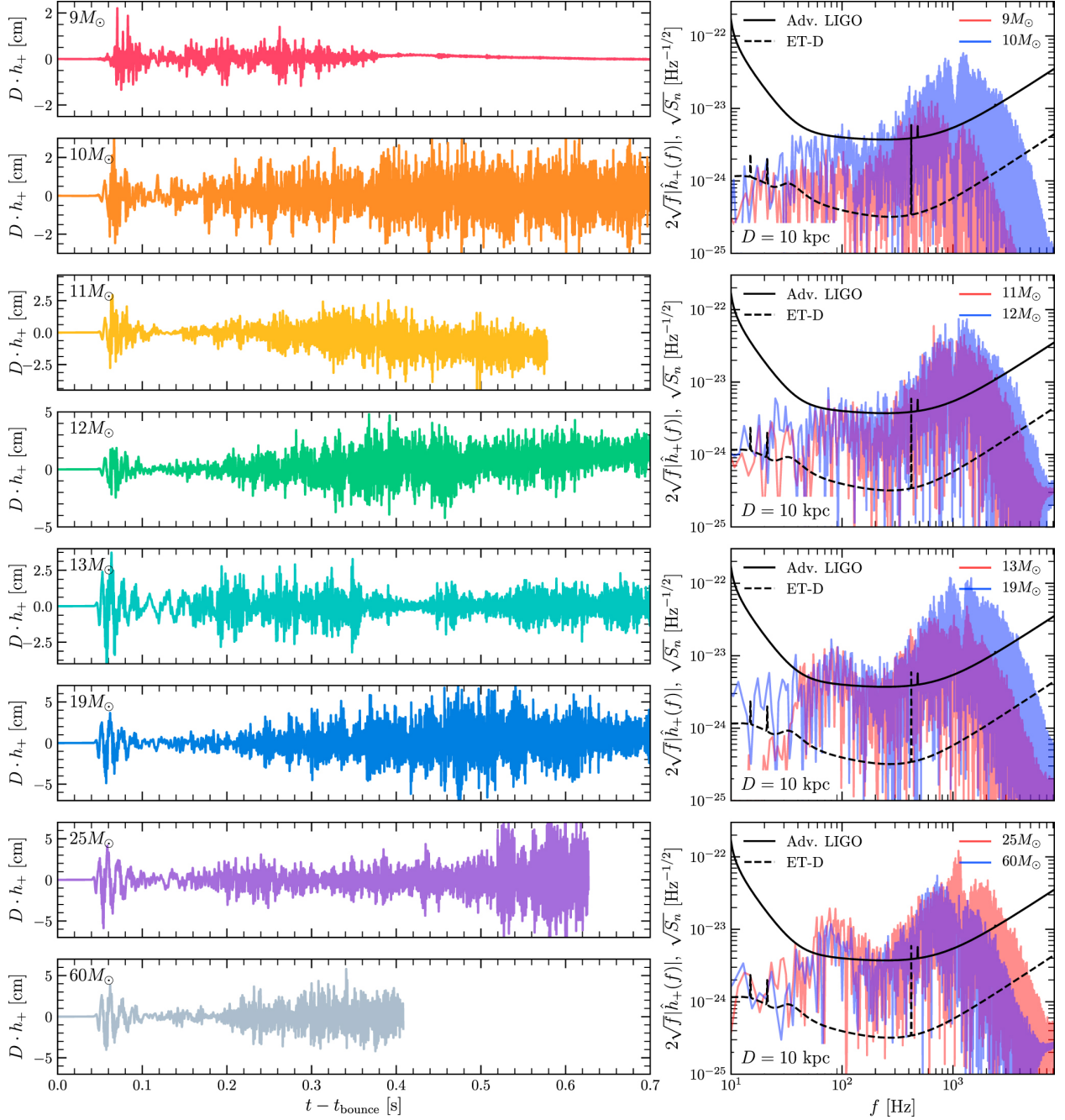
Figure 1.7: Predicted gravitational wave strain for 3D rotating CCSN explosion models (left) and power spectrum density of gravitational wave emission compared to the design sensitivity of Advanced LIGO and Einstein Telescope (and J Aasi et al., 2015). Figure from (Radice et al., 2019).

1.4.3 Multi-messenger Signals Produced by Massive Star Explosions

Multi-messenger (electromagnetic, gravitational wave, and neutrino) signals are a natural outcome of a CCSN explosion, or the failed explosion (O'Connor & Ott, 2011), of a massive star. In the case

of rotation, 2D/3D simulations of CCSNe show that their are many ways in which the explosion can produce gravitational wave (GW) emission. Rotation can produce a bounce signal due to the centrifugal readjustment of the collapsing PNS that can lead to a burst of GW emission (Richers et al., 2017). Convection in the gain region during explosion can excite oscillations in the PNS that can contribute GW emission at later times (Pajkos et al., 2019). Instabilities such as the standing shock accretion instability (SASI) can also produce signature periodic GW strain signals as well (Andresen et al., 2019).

CCSNe generate GW emission and for nearby sources are detectable by current and next generation GW detectors (e.g., aLIGO, VIRGO)(Gossan et al., 2016; Pan et al., 2020). Figure 1.7 shows the plus polarization of the gravitational wave strain for models in the mass range of 9 - 60 $M_\odot$ compared to the noise curves of detectable events for Advanced-LIGO and the Einstein Telescope at 10 kpc (Radice et al., 2019). In most cases, the CCSN explosion models show high-frequency emission within the aLIGO band for a very nearby source at $D = 10$ kpc. O'Connor & Couch (2018a) also show that the 3D progenitor structure can alter the GW spectrum to cause an increase in the GW amplitude over the non-perturbed models and thus impact our predictions for GW emission from CCSNe (Andresen et al., 2019). Gound-based neutrino detectors such Super-Kamiokande will also be able to detect a few thousand events from a Galactic CCSN explosion. Neutrino emission could be combined with GW signals to determine properties of the progenitor like never before (Warren et al., 2020). In Chapter 5, we present work performing multidimensional neutrino-radiation-hydrodynamic simulations of CCSN explosions using 2D/3D progenitor models.

1.5 Computational Tools and Methods

Our two primary software instruments used throughout the work presented here are the stellar evolution toolkit Modules for Experiments in Stellar Astrophysics (MESA) (Paxton et al., 2011, 2013, 2015, 2018, 2019) and the FLASH simulation framework (Fryxell et al., 2000; Dubey et al., 2009). In the following subsections, we discuss these software instruments in more detail.

1.5.1 Modules for Experiments in Stellar Astrophysics - `MESA`

`MESA` is an open-source stellar evolution toolkit based on the EZ stellar evolution code (Eggle-ton, 1971; Paxton, 2004). `MESA` solves the 1D stellar structure and evolution equations in their Lagrangian formulation (mass as an independent spatial variable),

$$\frac{d\log P}{dm} = -\frac{Gm}{4\pi r^4 \rho} , \tag{1.7}$$

$$\frac{d\log T}{dm} = \frac{d\log P}{dm} \nabla , \tag{1.8}$$

$$\frac{d\log r}{dm} = \frac{1}{4\pi r^3 \rho} , \tag{1.9}$$

and

$$\frac{dL}{dm} = \epsilon_{\text{nuc}} - \epsilon_\nu - \frac{Du}{Dt} + \frac{P}{\rho^2}\frac{D\rho}{Dt} , \tag{1.10}$$

where P is the pressure, G the gravitational constant, r radius, ρ mass density, T temperature, ϵ_{nuc} the nuclear energy generation rate, ϵ_ν the energy loss rate due to neutrinos, u is the velocity, and m is the Lagrangian mass coordinate. `MESA` solves these equations along with those governing nuclear reactions in a fully coupled manner. The code offers adaptive mesh refinement based on changes in the stellar structure and sophisticated timestep controls. Since its inception in 2010, `MESA` has been a valuable tool in the field of astronomy and astrophysics with an active network of contributors building on its capabilities. In the following subsections, we will briefly discuss some of the core components of `MESA` and how they affect the simulations presented in this Thesis.

1.5.1.1 Nuclear Burning

In practice, computational models utilize nuclear reaction rate libraries which are comprised of tabulated reaction rates as functions of temperature. The reaction rate tables are then interpolated to give a rate for a cell at a given temperature. These libraries are comprised of experimentally derived nuclear reaction rates when possible and theoretical rates if necessary. Some libraries

instead provide polynomial coefficients for codes to utilize in a fit to a given nuclear reaction. `MESA` allows for users to choose a specific nuclear reaction rate library from its available options. The default rate library is the Nuclear Astrophysics Compilation of REaction rates (NACRE) library (Angulo, 1999; Xu et al., 2013). Nuclear burning is implemented in `MESA` using a set of sparse-matrix, semi-implicit ODE solvers. `MESA` uses a variable-order Bader-Deuflhard semi-implicit time integration algorithm along with the MA28 linear algebra package. This combination was found to represent the best balance between efficiency and accuracy (Timmes et al., 2000).

In its current form, `MESA` utlizes a variety of different nuclear reaction network sizes. For the models presented in Chapters 3 and Chapters 4, we use the `aprox21.net` network. This network is a hard-wired (specific reaction channels are pre-determined) alpha-chain network that has been shown to provide an inexpensive network that gives an approximate match to the nuclear energy generation rates predicted by larger networks (Timmes et al., 2000). This choice of reaction network was used to maintain consistency between the `MESA` input models used in our `FLASH` simulations.

1.5.1.2 Equation of State

`MESA` uses ρ and T as independent variables to determine thermodynamic properties with the help of different tables across different $\rho - T$ ranges. For the most relevant $\rho - T$ conditions for the models considered in this work, `MESA` uses the Helmholtz equation of state (EoS). The Helmholtz EoS is an electron-positron EoS based on table interpolation of the Helmholtz free energy (Timmes & Swesty, 2000). The table has been used widely for many different astrophysical simulations on account of its balance of speed, thermodynamic consistency, and accuracy.

1.5.2 `FLASH` Simulation Framework

`FLASH` is an adaptive mesh refinement (AMR) hydrodynamics code to model astrophysical thermonuclear flashes (Fryxell et al., 2000). Since its inception, `FLASH` has been extended to simulate a variety of astrophysical problems including neutrino-radiation hydrodynamics of core-collapse supernova explosions and stellar convection. In this Thesis, we focus on these two capabilities of

`FLASH`. In the following subsections, we summarize some of the key methods implemented and utilzed in the `FLASH` simulation framework.

1.5.2.1 Hydrodynamics

The hydrodynamics module in `FLASH` solves the Euler equation's for compressible gas dynamics. In terms of conserved variables and negelecting nuclear reactions and source terms, the equations can be written as

$$\frac{\partial \rho}{\partial t} + \nabla \cdot (\rho \mathbf{v}) = 0 \,, \tag{1.11}$$

$$\frac{\partial \rho \mathbf{v}}{\partial t} + \nabla \cdot \rho \mathbf{v} \mathbf{v} + \nabla P = \rho \mathbf{g} \,, \tag{1.12}$$

$$\frac{\partial \rho E}{\partial t} + \nabla \cdot (\rho E + P) \mathbf{v} = \rho \mathbf{v} \cdot \mathbf{g} \,, \tag{1.13}$$

where ρ is the fluid density, $\mathbf{v}$ the velocity, P the pressure, $\mathbf{g}$ the gravitational acceleration, and E is the total (internal + kinetic) energy. Lastly, for reactive flows an additional advection equation is solved

$$\frac{\partial \rho X_l}{\partial t} + \nabla \cdot \rho X_l \mathbf{v} = 0 \,, \tag{1.14}$$

where X_l is the mass fraction of the l-th species. The current version of `FLASH` offers many methods of solving these equations. In the simulations presented in this Thesis, we utilize two different methods for two different astrophysical applications.

For modelling stellar convection, as will be discussed in Chapter 3 and Chapter 4, we utilize the directionally unsplit third order Piecewise Parabolic Method (PPM) solver (Lee, 2013). The PPM solver is an extension to the Godunov Scheme, a finite-volume scheme for solving partial differential equations. Recent efforts in modelling stellar convection have utilized methods built on PPM in simulations of O-shell convection (Jones et al., 2017; Andrassy et al., 2020). For

our CCSN explosion simulations, we utilize a weighted essentially non-oscillatory (WENO) finite volume scheme that demonstrates fifth-order spatial convergence rates.

1.5.2.2 Radiative Transfer

Some of the first three-dimensional models of core-collapse supernova explosions used simplified methods for neutrino transport such as light-bulb approximations that helped reduced the computational cost (Nordhaus et al., 2010). These models suggested that 3D simulations required less driving neutrino luminosity ($\approx 40 - 50\%$) than their 2D and 1D counterparts and would explode more promptly ($\approx$ 50 - 100 ms earlier) as a result. Other groups, failed to reproduce these trends in their 1-,2-, and 3D models using a similar approximation for neutrino transport (Couch & O'Connor, 2014). The results from their work suggested a more complicated picture where the 3D models exploded later than the 2D models owing in part to the difference in the nature of the turbulent convection. They found that in 2D, the inverse turbulent energy cascade pushes energy towards larger physical scales that are more favorable for explosion (Hanke et al., 2012).

In Chapter 6 of this Thesis, we perform neutrino-radiation hydrodynamic simulations of core-collapse supernova explosions. For these simulations we utilize the multidimensional, two-moment, energy-dependent, multispecies, neutrino radiation transport scheme, so called `M1` as implemented in `FLASH` . The details of this implementation are described in O'Connor & Couch (2018b). Here we summarize the main points.

The `M1` scheme for neutrino radiation hydrodynamics evolves the zeroth and first angular moments of the neutrino distribution function. The scheme is then closed with an analytical approximation for the higher moments of the distribution function (Shibata et al., 2011). In this scheme, three species of neutrinos are followed, ν_e, $\bar{\nu}_e$, and ν_x, electron, anti-electron, and heavy type neutrinos. The heavy type neutrinos are a combination for μ and τ type neutrinos are their anti-counterparts. Neutrinos are described by a distribution function which characterizes the number of neutrinos in a phase-space volume element and which obeys the relativistic Boltzmann equation,

$$\frac{d\,x^\mu}{d\tau}\frac{\partial f}{\partial x^\mu} + \frac{d\,p^i}{d\tau}\frac{\partial f}{\partial p^i} = (-p^\mu u_\mu)S(p^\mu, x^\mu, f)\,, \tag{1.15}$$

19

where τ is the affine parameter of the neutrino trajectory, u^μ is the four-velocity of the medium, and p^μ the four-momentum of radiation (Shibata et al., 2011). The term $S(p^\mu, x^\mu, f)$ describes the emission, scattering, and absorptions terms of the neutrinos. In natural units, $\hbar = c = 1$, the zeroth, first, and second moments of the distribution function in momentum space are, the energy density

$$E_\nu = \int \epsilon f(p^\mu, x^\mu) \delta(h\nu - \epsilon) d^3 p \,, \tag{1.16}$$

the radiation flux,

$$F_\nu^j = \int p^j f(p^\mu, x^\mu) \delta(h\nu - \epsilon) d^3 p \,, \tag{1.17}$$

and the radiation pressure,

$$P_\nu^{ij} = \int p^i p^j f(p^\mu, x^\mu) \delta(h\nu - \epsilon) d^3 p / \epsilon \,. \tag{1.18}$$

The analytic closure mentioned above is obtained under the following assumptions. In regions where the radiation is isotropic, the second moment is given as

$$P^{ij} = P^{ij}_{\text{thick}} = \delta^{ij} E / 3 \,, \tag{1.19}$$

while in regions far from the source,

$$P^{ij} = P^{ij}_{\text{thin}} = E(F^i F^j) / F^2 \,. \tag{1.20}$$

For the regions in between these limits, an interpolation is performed, giving a relation for the second moment as,

$$P^{ij} = \left[\frac{3(1 - \chi)}{2} \frac{\delta^{ij}}{3} + \frac{3\chi - 1)}{2} \frac{F^i F^j}{F^2} \right] E \,. \tag{1.21}$$

The quantity χ is taken to be,

$$\chi = \frac{1}{3} + \frac{2}{15} \left[3f^2 - f^3 + 3f^4 \right] \,, \tag{1.22}$$

where $f = \sqrt{(F^i F_i / E^2)}$ is the flux factor. For isotropic radiation, $f = 0$, where $\chi = 1/3$ and $P^{ij} = P^{ij}_{\text{thick}}$. For fully forward-peaked radiation, $f = 1$. The above equations are solved via operator splitting from the hydrodynamics and first order temporal and second order spatial accuracy. For

each hydrodynamic step, the updated variables are used to compute the matter interactions while substeps are taken to compute the radiation fluxes. Efficient and accurate coupling is maintained between the hydrodynamics and radiation due to the strict explicit timestep constraint by the radiation field.

In all of our `FLASH` simulations of stellar convection (Chapter 3 and Chapter 4) we also utlize the Helmholtz EoS. In Chapter 5 we use the SFHo EoS (Steiner et al., 2013). Unlike `MESA`, `FLASH` solves nuclear burning and hydrodynamics separately. In order to prevent decoupling between these units, we impose a limit to the timestep taken by the burner such that $\delta t = \texttt{eNucDtFactor} E_{\text{int.}}/E_{\text{nuc.}}$, that is the timestep does not exceed some fraction of the ratio of the internal and nuclear energy. Our simulations use a value of 1% of this ratio, a value also used in Couch et al. (2015). Our CCSN simulations do not include nuclear burning. The specific details of the simulations are discussed further in their respective chapters.

1.6 `MESA-Web:` An online interface to the `MESA` code

Stellar evolution codes can be complicated to use, so we offer MESA-Web, a web-based interface to the stellar evolution code, Modules for Experiments in Stellar Astrophysics. MESA-Web can be used for education purposes to calculate stellar models over a range of physical parameters, extending capabilities of similar online tools such as Rich Townsend's EZ-Web[2]. A large part of the motivation behind creating and maintaining the MESA-Web online interface is to allow educators to utilize MESA in the classroom without additional barriers that students may face in downloading / installing MESA. The use of computational resources in astronomy is important and has been a topic for advocacy in the need for more computational literacy (Zingale et al., 2016). Part of my work in graduate school has been developing `MESA-Web`, maintaining its online status, and improving ways in which it can be used in astronomy classrooms. This work will be discussed in Chapter 6.

---

[2]http://www.astro.wisc.edu/ townsend/static.php?ref=ez-web

1.7   Outline

Simulations of massive stars are subject to uncertainties that can stem from nuclear reaction rates and the treatment of convection in 1D. Moreover, these models serve as input for multidimensional radiation-hydrodynamic simulations of CCSNe. The consequences of these uncertainties directly impact our predictive capability in leveraging theoretical models as a comparison to a comparison to observational and experimental data. This Thesis will focus on nuclear reaction rate uncertainties (Chapter 2) and stellar convection in multidimensional massive star models (Chapter 3 and Chapter 4), and the impact that progenitor models have on multi-messenger signals of CCSNe (Chapter 5). Chapter 6 will cover `MESA-Web` an online web interface to `MESA` for use in astronomy education and in the last Chapter we summarize the key findings of this Thesis.

THE IMPACT OF NUCLEAR REACTION RATE UNCERTAINTIES ON THE
EVOLUTION OF CORE-COLLAPSE SUPERNOVA PROGENITORS

From a little spark may burst a flame. - Dante Alighieri, (Paradiso)

2.1   Abstract

We explore properties of core-collapse supernova progenitors with respect to the composite uncertainties in the thermonuclear reaction rates by coupling the reaction rate probability density functions provided by the STARLIB reaction rate library with `MESA` stellar models. We evolve 1000 15 $M_\odot$ models from the pre main-sequence to core O-depletion at solar and subsolar metallicities for a total of 2000 Monte Carlo stellar models. For each stellar model, we independently and simultaneously sample 665 thermonuclear reaction rates and use them in a `MESA` in situ reaction network that follows 127 isotopes from ^{1}H to ^{64}Zn. With this framework we survey the core mass, burning lifetime, composition, and structural properties at five different evolutionary epochs. At each epoch we measure the probability distribution function of the variations of each property and calculate Spearman Rank-Order Correlation coefficients for each sampled reaction rate to identify which reaction rate has the largest impact on the variations on each property. We find that uncertainties in ^{14}N$(p, \gamma)^{15}$O, triple-α, ^{12}C$(\alpha, \gamma)^{16}$O, ^{12}C$(^{12}$C,$p)^{23}$Na, ^{12}C$(^{16}$O,$p)^{27}$Al, ^{16}O$(^{16}$O,$n)^{31}$S, ^{16}O$(^{16}$O,$p)^{31}$P, and ^{16}O$(^{16}$O,$\alpha)^{28}$Si reaction rates dominate the variations of the properties surveyed. We find that variations induced by uncertainties in nuclear reaction rates grow with each passing phase of evolution, and at core H-, He-depletion are of comparable magnitude to the variations induced by choices of mass resolution and network resolution. However, at core C-, Ne-, and O-depletion, the reaction rate uncertainties can dominate the variation causing uncertainty

in various properties of the stellar model in the evolution towards iron core-collapse.

2.2 Introduction

Core-collapse supernova (SN) explosions are one possible fate of a star with a zero age main-sequence mass of M $\gtrsim$ 9 $M_\odot$ (e.g., Woosley et al., 2002; Woosley & Heger, 2007; Farmer et al., 2015). The structure of the progenitor at the time of explosion can lead to a large variety of observed transient phenomena (e.g., Van Dyk et al., 2000; Ofek et al., 2014; Smith et al., 2016).

For progenitors experiencing mass loss, stellar winds may strip the H-rich envelope, and possibly some of the He-rich envelope, prior to core-collapse (e.g., Smith, 2014; Renzo et al., 2017). Explosions of these stars are characterized by an absence of hydrogen absorption features and weak or non-existent absorption lines of silicon in their spectra (Smartt, 2009; Dessart et al., 2011; Smartt, 2015; Reilly et al., 2016; Sukhbold et al., 2016). Progenitors with most of the H-rich envelope present at the end of their life are characterized as Type II supernovae that can be sub-divided into multiple classes based on lightcurve and spectral properties (Filippenko, 1997; Wang & Wheeler, 2008; Jerkstrand et al., 2015).

In some cases, a massive star with sufficient rotational energy at core collapse can produce a rapidly rotating, highly magnetic proto-neutron star capable of leading to a significantly enhanced energetic transient. Such a scenario has been postulated to explain the most energetic supernova observed to date, ASASSN-15lh (Sukhbold & Woosley, 2016; Chatzopoulos et al., 2016b; Chen et al., 2016), although Leloudas et al. (2016) offers on an alternative hypothesis on the nature of ASASSN-15lh.

Alternatively, a massive star may undergo iron core-collapse but the resulting shocks are insufficient to unbind the star, leading to accretion onto the nascent proto-neutron star and pushing it past its maximum mass. These "failed supernovae" (e.g., O'Connor & Ott, 2011) can produce stellar mass black holes at the rate suggested by the detection of GW150914, GW151226, and GW170104 (Abbott et al., 2016b,a, 2017), although a broad consensus on which massive stars produce black holes has not yet been reached (Timmes et al., 1996; Fryer & Kalogera, 2001; Heger

et al., 2003; Eldridge & Tout, 2005; Zhang et al., 2008; Ugliano et al., 2012; Clausen et al., 2015; Sukhbold et al., 2016; Müller et al., 2016a; Woosley, 2016; Kruckow et al., 2016; Sukhbold et al., 2017; Limongi, 2017).

For more massive progenitors, pair-instability leads to a partial collapse, which in turn causes runaway burning in the carbon-oxygen core (Fowler & Hoyle, 1964; Rakavy & Shaviv, 1967; Barkat et al., 1967; Rakavy et al., 1967; Fraley, 1968). A single energetic burst from nuclear burning can disrupt the entire star without leaving a black hole remnant behind to produce a pair-instability supernova (Ober et al., 1983; Fryer et al., 2001; Kasen et al., 2011; Chatzopoulos et al., 2013). Alternatively, a series of bursts can trigger a cyclic pattern of nuclear burning, expansion and contraction, leading to a pulsational pair-instability supernova that leaves a black hole remnant (Barkat et al., 1967; Woosley & Heger, 2007; Chatzopoulos & Wheeler, 2012; Woosley, 2017; Limongi, 2017). A variety of outcomes is possible depending on the star's mass and rotation.

At the heart of these evolutionary pathways are nuclear reaction rates. These rates regulate the evolution of the star and can significantly modify the stellar structure of the progenitor star at the end of its life. A direct consequence of uncertainties in the reaction rates can result in differences in the nucleosynthesis and explosion properties (Rauscher et al., 2002; Woosley & Heger, 2007; Sukhbold et al., 2016; Rauscher et al., 2016).

Most reaction rate libraries provide recommended nuclear reaction rates based on experiment (when possible) or theory. Examples include CF88 Caughlan & Fowler (1988), NACRE (Angulo, 1999; Xu et al., 2013), JINA REACLIB (Cyburt et al., 2010), and STARLIB (Sallaska et al., 2013). STARLIB takes the additional step of providing the median or recommended thermonuclear reaction rate *and* the factor uncertainty ($f.u.$) as a function of temperature. The factor uncertainty is an estimate of the uncertainty associated with a reaction rate at a given temperature given the available nuclear physics data. Monte Carlo (Longland et al., 2010; Longland, 2012; Iliadis et al., 2015, 2016) or Bayesian (Iliadis et al., 2016; Gómez Iñesta et al., 2017) based reaction rates generate probability density functions (PDFs) to provide a final *median* rate and a temperature-*dependent* uncertainty. The availability of formally derived temperature-dependent uncertainties

allows statistically rigorous studies on the impact of the composite uncertainty on stellar models.

Reaction rate sensitivity studies have been considered for X-ray burst models (Cyburt et al., 2016) and massive star models through core He-burning (West et al., 2013) and for *s*-process nucleosynthesis (Nishimura et al., 2017). In some of these and similar studies, temperature-*independent* estimates of the reaction rate uncertainties are applied as constant multiplicative factors on the recommended rate at all temperatures. This method can lead to an under- or over-estimate of the reaction rate for different stellar temperatures. Another common approximation is "post-processing" of thermodynamic trajectories from stellar models (e.g., Magkotsios et al., 2010; Rauscher et al., 2016; Harris et al., 2017), which also usually use a constant multiplicative factor at all temperature points. Post-processing thermodynamic trajectories neglect the feedback of the changes in the reaction rates on the underlying stellar model.

Fields et al. 2016 (Paper F16) addresses some of the shortcomings of these approximations by using a Monte Carlo stellar model framework with temperature-dependent uncertainties on the reaction rates from STARLIB. Specifically, used on $3\,M_\odot$ stellar models evolved from the pre main-sequence to the first thermal pulse. Each of the 1000 models uses one set of reaction rates generated from the reaction rate PDFs. These Monte Carlo stellar models probed the effect of reaction rate uncertainties on the structure and evolution of stars that form carbon-oxygen (CO) white dwarfs. Paper F16 sample 26 reaction rates of the 405 total rates in the chosen reaction network, which can bias identifying the reactions that play role in altering the stellar structure.

In this paper, we apply the same Monte Carlo framework to massive star models. We consider all forward reactions in a suitable reaction network (reverse rates are calculated by detailed balance) to eliminate potential biases from selecting a limited set of reactions. Our workflow couples temperature-dependent reaction rate uncertainties from STARLIB (Sallaska et al., 2013) with Modules for Experiments in Stellar Astrophysics (`MESA`) stellar models (Paxton et al., 2011, 2013, 2015). We sample the reaction rates independently and simultaneously according to their respective PDFs. These sampled rates form input for $15\,M_\odot$ models evolved from the pre main-sequence to core O-depletion. We focus on $15\,M_\odot$ models as they approximately represent the most numerous

SNe by number for a Salpeter initial mass function with slope $\Gamma = -1.35$, and a lower limit of $9\,M_\odot$ for stars that become SNe (Salpeter, 1955; Scalo, 1986; Sukhbold & Woosley, 2014; Farmer et al., 2015). We consider solar and subsolar metallicities to explore the effect of reaction rate uncertainties on stars in different galactic environments.

This paper is novel in two ways. First, we sample a large number of reaction rates (665 forward reactions) in a Monte Carlo stellar model framework where the rates are sampled *before* the stellar model is evolved. This accounts for changes in the stellar structure due to reaction rate uncertainties, and is fundamentally different than post-processing schemes. Second, we quantify the variation of key quantities of the stellar models at five key evolutionary epochs. This allows determination of (1) the most important reactions overall, and (2) when these key reactions play a crucial role in the life of a massive star. In short, this paper presents the first Monte Carlo stellar evolution studies of massive stars that use PDFs for the nuclear reaction rate uncertainties and complete stellar models.

In Section 2.3 we describe the input physics of our models. In Section 2.4 we discuss our Monte Carlo stellar model framework and quantify the uncertainty of a few key nuclear reactions. Before presenting the results of our survey, we describe the characteristics of baseline $15\,M_\odot$ models evolved using *median* reaction rates from STARLIB in Section 2.5. In Section 2.6 we present our main results. In Section 5.5 we compare our results to previous efforts and make an assessment of the overall impact of the uncertainties due to nuclear reactions relative to other quantified sources of uncertainty (e.g., Farmer et al., 2016). In Section 6.5 we summarize our results.

2.3 Input Physics

We evolve $15\,M_\odot$ models using `MESA` (version 7624, Paxton et al., 2011, 2013, 2015). All models begin with an initial metallicity of $Z = Z_\odot = 0.0153$ ("solar", Caffau et al., 2010; Grevesse & Sauval, 1998; Asplund et al., 2009; Vagnozzi et al., 2017) or $Z = 2 \times 10^{-3} Z_\odot = 0.0003$ ("subsolar"). Solar metallicity models use isotopic distributions from Lodders et al. (2009), while subsolar models use the methods of West & Heger (2013)[1]. The metallicity-dependent isotopic distributions

---

[1] Available from `http://mesa-web.asu.edu/gce.html`

27

from West & Heger (2013) reproduce α enhancement trends for a large sample of low Z stars in the Milky Way halo (Frebel et al., 2010) thus motivating our choice for these distributions over solar-scaled compositions.

Farmer et al. (2016) show convergence of key quantities in 15 $M_\odot$ `MESA` models at the $\simeq 10\%$ level when the reaction network contains $\gtrsim 127$ isotopes. Following their results, each stellar model utilizes the in-situ nuclear reaction network `mesa_127.net`, which follows 127 isotopes from ^{1}H to ^{64}Zn coupled by 1201 reactions. Figure 2.1 shows the 127 isotopes and their linking nuclear reactions. The isotopic abundance distributions we use contains 288 isotopes from ^{1}H to ^{238}U. We add the residual mass fraction ($\lesssim 10^{-5}$) of the 161 isotopes not in the reaction network to the initial ^{1}H mass fraction to maintain baryon number conservation $\sum_{i=1}^{127} X_i = 1$, where X_i is the mass fraction of isotope i.

We include mass loss using the `Dutch` wind loss scheme (Nieuwenhuijzen & de Jager, 1990; Nugis & Lamers, 2000; Vink et al., 2001; Glebbeek et al., 2009) with an efficiency of η=0.8. We neglect the effects of rotation, magnetic fields, and rotation induced mass loss in this study.

We use the Ledoux criterion for convection with an efficiency parameter of $\alpha_{\mathrm{MLT}} = 2.0$, and the `mlt++` approximation for convection (Paxton et al., 2013). We include convective boundary mixing (overshoot, thermohaline, and semi-convection) with baseline values following Farmer et al. (2016). For convective overshoot we use $f = 0.004$ and $f_0 = 0.001$, which can reproduce mass entrainment rates found in idealized 3D simulations of explosive O-shell burning in massive stars (Jones et al., 2017). For simplicity, we apply the same overshoot efficiency to all boundaries. For thermohaline mixing, we use $\alpha_{\mathrm{th}} = 2.0$ (Traxler et al., 2011; Brown et al., 2013; Garaud et al., 2015). Semi-convection uses an efficiency of $\alpha_{\mathrm{sc}} = 0.01$ (Zaussinger & Spruit, 2013; Spruit, 2013).

We use the `MESA` control `mesh_delta_coeff`, δ_{mesh}, to monitor mass resolution, which accounts for the gradients in the structure quantities to decide whether a cell should be split or merged. The default `MESA` value is unity. In this work, we use δ_{mesh}=0.5. This results in $\simeq 2300$ cells at the terminal age main-sequence (TAMS), $\simeq 4700$ at core He-depletion, and $\simeq 2100$ cells during core O-burning. Section 2.5 discusses the sensitivity of our results to mass resolution.

28

We use several of `MESA`'s timestep controls. The parameter `varcontrol_target`, w_t, broadly controls the temporal resolution by restricting the allowed relative variation in the structure between timesteps. The default value is $w_t=1 \times 10^{-4}$. In this work, we use $w_t=5 \times 10^{-5}$, except during off-center C-burning where we use $w_t=1 \times 10^{-5}$ to further improve time resolution. We also control the rate of fuel depletion with the `delta_lg_X*` timestep controls, where the asterisk denotes a major fuel (i.e. H, He, C, Ne, or O). In total, we observe timesteps of $\Delta t \simeq 2 \times 10^4$ yr on the main sequence, $\Delta t \simeq 4 \times 10^3$ yr during core He-burning, and $\Delta t \simeq 12$ hr during core O-burning. Section 2.5 discusses the sensitivity of our results to temporal resolution.

For each stellar model, we sample 665 forward reaction rates from STARLIB Archived Version 5 (Sallaska et al., 2013) simultaneously and independently within their temperature-dependent uncertainties. We calculate reverse rates directly from the forward rates using detailed balance. We utilize the work of Alastuey & Jancovici (1978) and Itoh et al. (1979) for reaction rate screening factors. The fitting formula of Itoh et al. (1996b) provide the thermal neutrino energy losses. Weak reactions rates, in order of precedence, are from Langanke & Martínez-Pinedo (2000), Oda et al. (1994), and Fuller et al. (1985).

Each stellar model evolves from the pre main-sequence until the central $X(^{16}O) \simeq 1 \times 10^{-3}$. We use 1000 solar and subsolar stellar models, for a total of 2000 Monte Carlo stellar models. All `MESA` inlists and many of the stellar models are available at `http://mesastar.org`.

2.4   Reaction Rate Sampling

We construct a sampled nuclear reaction rate following Iliadis et al. (2015). We summarize the key characteristics here. The STARLIB rate library provides the *median* reaction rate, $\langle \sigma v \rangle_{\mathrm{med}}$, and the associated $f.u.$, over the temperature range 10^{6-10} K. A log-normal PDF is assumed for all reaction and decay rates, and these PDFs are described by the location and spread parameters, μ and σ, respectively. These parameters are obtained using the median rate and $f.u.$ tabulated in
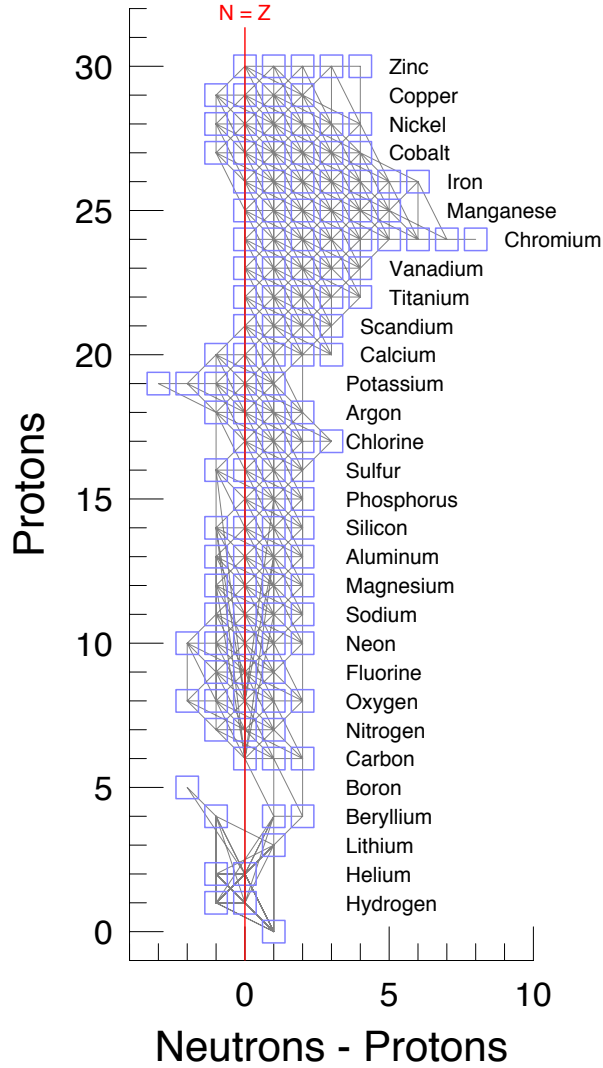
Figure 2.1: Proton number versus neutron excess for the adopted 127 isotope reaction network. Thermonuclear and weak reaction rates coupling the isotopes are marked by gray lines, and symmetric matter ($N=Z$) is marked by a red line.

STARLIB as $\sigma = \ln f.u.$ and $\mu = \ln \langle \sigma v \rangle_{\text{med}}$. These two parameters give a complete description of the reaction rate probability density at any temperature point and form the basis of our sampling scheme.

A sampled reaction rate is drawn from a log-normal distribution (e.g., Evans et al., 2000) for an arbitrary quantity, x, as

$$x_i = e^{\mu + \sigma p_i} \equiv e^{\mu}(e^{\sigma})^{p_i} \, . \tag{2.1}$$

Using the relations for μ and σ, we obtain a sampled rate distribution as a function of temperature

from

$$\langle \sigma v \rangle_{\text{samp}} = e^{\mu} (e^{\sigma})^{p_{i,j}} = \langle \sigma v \rangle_{\text{med}} f.u.^{p_{i,j}} ,\qquad (2.2)$$

where $p_{i,j}$ is a standard Gaussian deviate with mean of zero and standard deviation of unity. The i index correspond to the stellar model of grid size N and the j index corresponds to the number of reactions sampled.

We refer to $p_{i,j}$ as the rate variation factor for the j-th reaction. From Equation 2.2, a rate variation factor of $p_{i,j} = 0$ corresponds to the *median* STARLIB reaction rate. For large rate variation factors, the extent of change of the reaction rate at a given temperature point is limited by the factor uncertainty.

For example, for the $^{12}\text{C}(\alpha,\gamma)^{16}\text{O}$ reaction rate (Kunz et al., 2002), STARLIB shows that the largest value of factor uncertainty is $f.u. = 1.403$ at $T = 0.4$ GK. For typical extrema of a Gaussian distribution such as those used to generate our rate variation factors, one could expect values of $p_{i,j} = +3.5, -3.5$. In such a scenario, this would represent a change in the sampled nuclear reaction rate of $\langle \sigma v \rangle_{\text{samp}} \simeq 3.27 \times \langle \sigma v \rangle_{\text{med}}$ for $p_{i,j} = +3.5$ and $\simeq 0.31 \times \langle \sigma v \rangle_{\text{med}}$ for $p_{i,j} = -3.5$ at $T = 0.4$ GK. At all other temperature points, the modification of the median rate may be less for the same value of $p_{i,j}$.

In Figure 2.2 we plot the $f.u.$ for the $^{12}\text{C}(\alpha,\gamma)^{16}\text{O}$, $^{14}\text{N}(p,\gamma)^{15}\text{O}$, $^{23}\text{Na}(p,\gamma)^{20}\text{Ne}$, and triple-$\alpha$ reaction rates over typical core He-, C-, Ne-, and O-burning temperatures. The $^{12}\text{C}(\alpha,\gamma)^{16}\text{O}$ rate has the largest factor uncertainty across the temperature ranges considered. At higher temperatures such as those expected in more advanced burning stages post core O-burning, the uncertainty in the $^{12}\text{C}(\alpha,\gamma)^{16}\text{O}$ begins to be overtaken by the uncertainty in the triple-α reaction.

We simultaneously and independently sample 665 forward thermonuclear reaction rates. For each reaction, we generate N=1000 random Gaussian deviates to modifying the reaction rates in the stellar models. Our choice for the sample size is motivated by the scaling of the sampling error for perfectly uncorrelated distributions. For such a distribution we expect a standard error of $\sigma/\sqrt{N} \simeq 3\%$. Since MESA calculates inverse rates directly from the forward rates using detailed balance, we also implicitly sample the corresponding 665 inverse rates. However, the corresponding
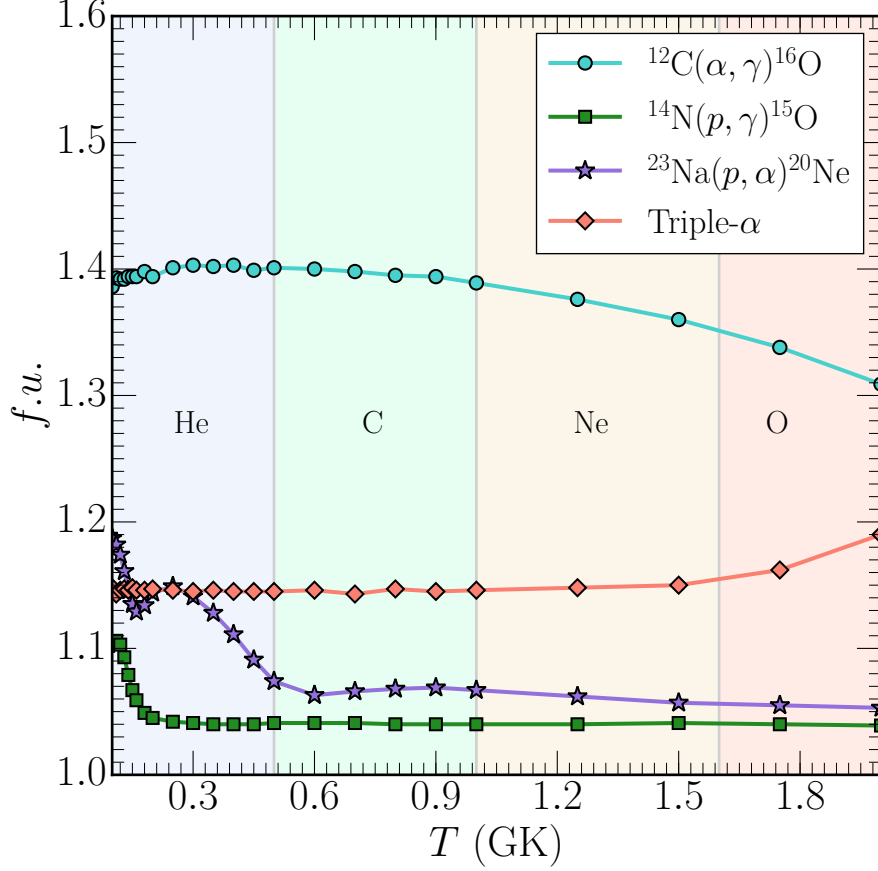
Figure 2.2: The factor uncertainty as a function of temperature provided by STARLIB for the $^{12}C(\alpha,\gamma)^{16}O$, $^{14}N(p,\gamma)^{15}O$, $^{23}Na(p,\gamma)^{20}Ne$, and triple-α reactions over different approximate core burning temperatures.

inverse sampled rates are not independent of the forward sampled reactions.

Reaction rates derived from Monte Carlo sampling of experimental nuclear data are available for 33 of the 665 reactions considered (Iliadis et al., 2010; Sallaska et al., 2013; Iliadis et al., 2015, 2016). For other reactions, Monte Carlo or Bayesian derived rate distributions are not yet available. In these such cases, *median* rate values and the corresponding temperature dependent $f.u.$ are obtained from estimates of experimental uncertainty where available. In the absence of experimental nuclear physics input, theoretical *median* reaction rates are obtained from Hauser-Feshbach model calculations with the `TALYS` software instrument (Goriely et al., 2008). Such theoretical rates are given a constant uncertainty of $f.u. = 10$ at all temperature points.

We assume the random Gaussian deviate is independent of temperature, $p_{i,j}(T) = $ constant
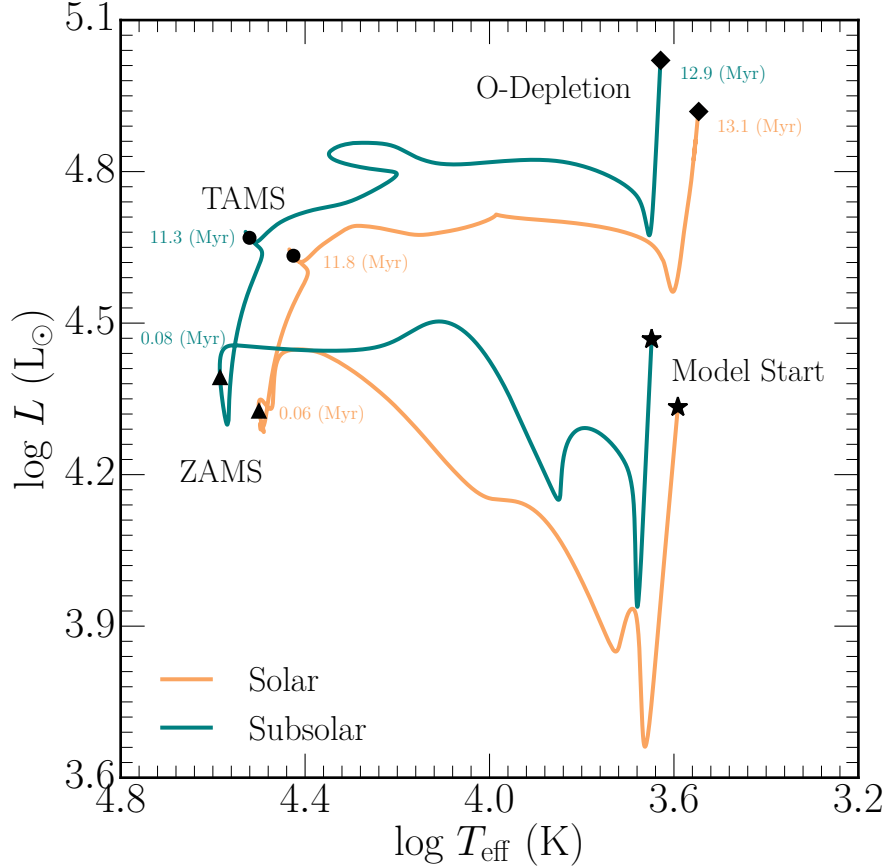
Figure 2.3: Hertzsprung-Russell diagram of the baseline 15 $M_\odot$ solar and subsolar models. Star symbols denote the beginning of each stellar model, triangles denote the ZAMS, circles denote the TAMS, and diamonds denote core O-depletion. Ages at these stages are annotated.

(Iliadis et al., 2015). This simplification obtains similar levels of uncertainties as more intricate sampling schemes (Longland, 2012). We stress that despite this simplification, the $f.u.$ provided by STARLIB is temperature-*dependent*. This allows us to follow changes in the uncertainty that may occur due to different resonance contributions.

The sampled reaction rate distributions are then constructed using Equation (2.2). Each nuclear reaction rate in STARLIB has a total of 60 T, $\langle \sigma v \rangle_{\mathrm{med}}$, and $f.u.$ data points. A sampled reaction rate also contains 60 data points and is then passed to MESA in tabular form. MESA interpolates between data points to construct a smoothed sampled nuclear reaction rate defined by 10,000 reaction rate data points as a function of T.

2.5 Properties of the baseline 15 $M_\odot$ stellar models

Before presenting the results of our Monte Carlo stellar models survey, we discuss the properties of the baseline 15 $M_\odot$ solar and subsolar models. These baseline models were evolved using the input physics described in Section 2.3 and the *median* STARLIB nuclear reaction rates. A *median* reaction rate is obtained in our sampling scheme by a Gaussian deviate of zero, $p_{i,j} = 0$.

Figure 2.3 shows a Hertzsprung-Russell diagram of the solar and subsolar baseline 15 $M_\odot$ stellar models. The start of the stellar models, the zero age main sequence (ZAMS), terminal age main sequence, and the ending point of core O-depletion are annotated. The subsolar model is brighter and hotter than the solar model primarily because a smaller metallicity decreases the opacity in the stellar atmosphere. At ZAMS, the subsolar model has a luminosity and effective temperature of $\log(L/L_\odot) \simeq 4.39$ and $\log(T_{\mathrm{eff}}/\mathrm{K}) \approx 4.58$ while the solar model has $\log(L/L_\odot) \simeq 4.33$ and $\log(T_{\mathrm{eff}}/\mathrm{K}) \simeq 4.50$. The solar model spends $\simeq 11.2$ Myr on the main sequence while the subsolar model spends $\simeq 11.7$ Myr.

The ZAMS homology relations for CNO burning, constant electron scattering opacity, and radiative transport (Hoyle & Lyttleton, 1942; Faulkner, 1967; Pagel & Portinari, 1998; Bromm et al., 2001; Portinari et al., 2010) are:

$$
\begin{aligned}
\left(\frac{T_{\mathrm{eff}}}{3 \times 10^4\ \mathrm{K}}\right) &\simeq \left(\frac{Z}{Z_\odot}\right)^{-1/20} \left(\frac{M}{15\ M_\odot}\right)^{1/40} \\
\left(\frac{R}{6\ R_\odot}\right) &\simeq \left(\frac{Z}{Z_\odot}\right)^{1/11} \left(\frac{M}{15\ M_\odot}\right)^{5/11} \\
\left(\frac{L}{2 \times 10^4 L_\odot}\right) &\simeq \left(\frac{Z}{Z_\odot}\right)^{-1/55} \left(\frac{M}{15\ M_\odot}\right).
\end{aligned}
\tag{2.3}
$$

The ZAMS positions of the solar and subsolar models in Figure 2.3 and commensurate with the trends of Eq. 2.3.

At the TAMS, the nascent He-rich core is surrounded by a thin H-burning shell. The core contracts and its temperature increases, while the outer layers of the star expand and cool. The star becomes a red giant (e.g., Iben, 1966, 1991; Stancliffe et al., 2009; Karakas & Lattanzio, 2014). The solar model spends $\simeq 1.54$ Myr undergoing convective core He-burning and the subsolar model
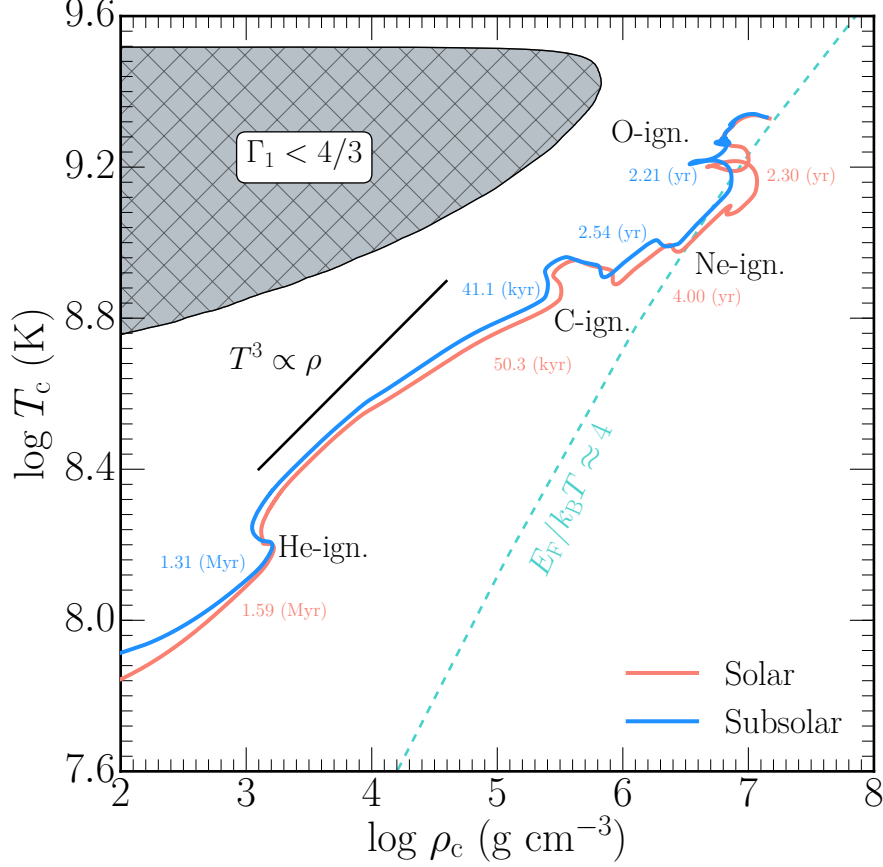
Figure 2.4: Evolution of the central density and temperature for the solar and subsolar baseline models. Approximate core burning locations, times until O-depletion, radiation entropy scaling relation - $T^3 \propto \rho$, electron degeneracy line $E_F/k_B T \simeq 4$ where E_F is the Fermi energy, and electron-positron pair dominated region are annotated.

spends $\simeq 1.27$ Myr. At He-depletion, the solar model has a He-core mass of $M_{He\text{-}Core} \simeq 4.24\,M_\odot$ and a $^{12}C/^{16}O$ ratio of 0.34. The subsolar model has a more massive, slightly more C-rich core with $M_{He\text{-}Core} \simeq 4.80\,M_\odot$ and $^{12}C/^{16}O \simeq 0.36$.

The trajectory of the baseline models in the $T - \rho$ plane are shown in Figure 2.4. In general, the tracks are qualitatively similar. The largest difference is the subsolar model undergoes hotter, less dense core burning. This is a result of the decreased stellar envelope opacity and larger luminosity shown in Figure 2.3. Figure 2.5 shows Kippenhahn diagrams for the baseline models post core He-burning. The C-burning features of both baseline models are similar; they both ignite carbon convectively at the core and undergo three convective C-burning flashes that recede outward in mass coordinate.
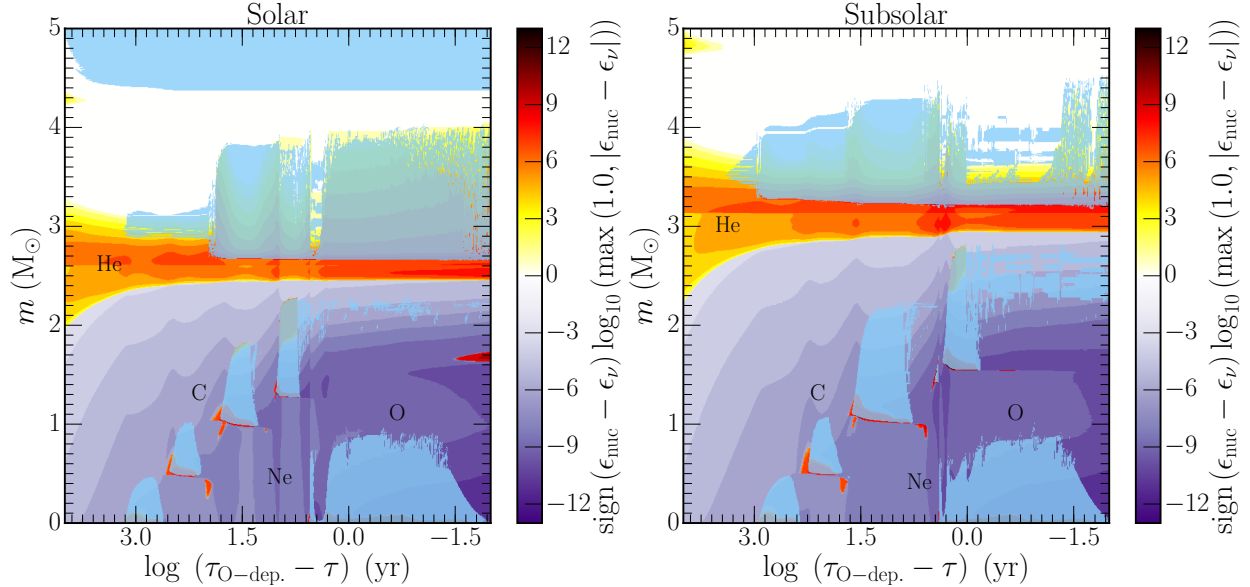
Figure 2.5: Kippenhahn diagrams for the solar (left) and subsolar (right) baseline stellar models post core He-burning. Annotated is the He-burning shell and the convective C, Ne, and O-burning episodes. The x-axis is the logarithmic difference between the age at O-depletion, $\tau_{\text{O-dep.}}$, and the current age of the model, τ. Dark orange to red correspond to regions of strong nuclear burning, light to dark purple to cooling regions, and white to regions balancing heating and cooling. Blue shows convective regions, gray marks regions of convective overshoot. Semi-convective and thermohaline regions are not shown.

Post C-depletion, the photodisintegration of ^{20}Ne drives convective core Ne-burning. This burning phase lasts $\simeq 1.7$ years for the solar model and $\simeq 0.33$ years for the subsolar model. After Ne-depletion, core O-burning begins at $T_c \simeq 1.8 \times 10^9$ K and $\rho_c \simeq 9.1 \times 10^6$ g cm^{-3}. The initial core O-burning episode is energetic enough to drive a large convection region that initially extends to $\simeq 0.9\,M_\odot$. At core O-depletion, we find a composition of $X_c(^{32}$S$) \simeq 0.524$, $X_c(^{34}$S$) \simeq 0.189$, and $X_c(^{28}$Si$) \simeq 0.244$ for the solar model. Other isotopes show central mass fractions of $X_c \lesssim 10^{-2}$. The subsolar model has an O-depletion composition of $X_c(^{32}$S$) \simeq 0.522$, $X_c(^{34}$S$) \simeq 0.175$, and $X_c(^{28}$Si$) \simeq 0.236$ with other burning products having negligible central mass fractions. The central electron fraction at this point is $Y_{e,c} \simeq 0.4936$ and $Y_{e,c} \simeq 0.4942$ for the solar and subsolar models, respectively. Our choice of stopping criterion does not signify the end of O-burning.

Lastly, we consider the impact of mass and temporal resolution on key physical parameters relevant to this paper by evolving eight additional baseline models. Figure 2.6 shows the results
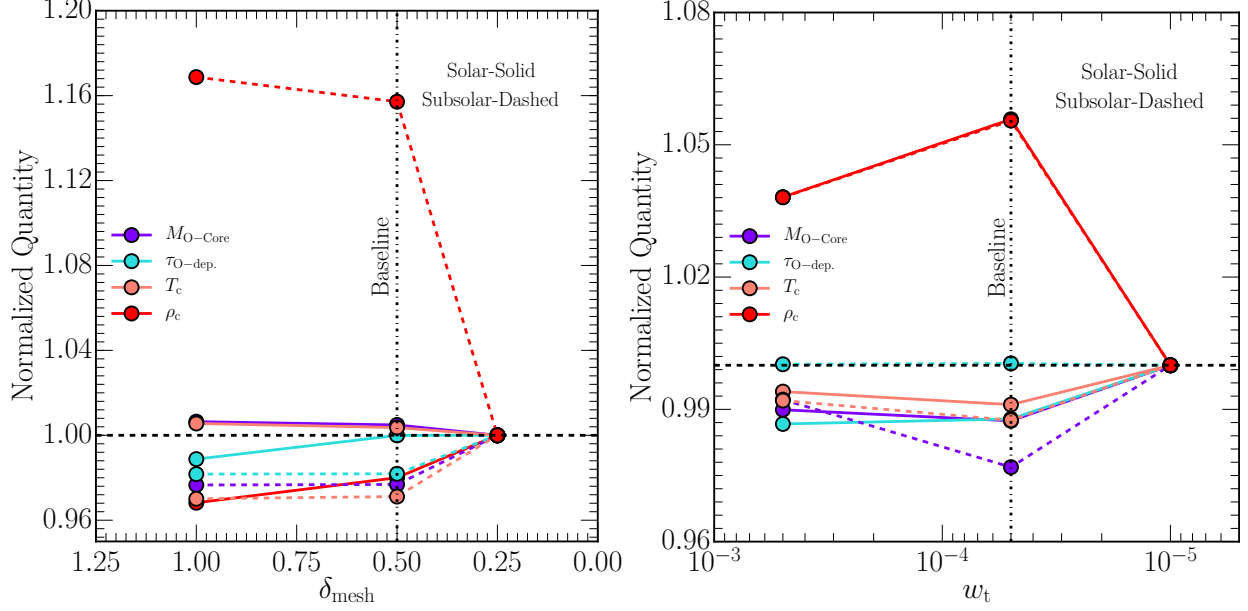
Figure 2.6: Four normalized quantities at core O-depletion as a function of the mass (left) and temporal (right) resolution controls δ_{mesh} and w_t: mass of the oxygen core - $M_{O\text{-}Core}$, age - $\tau_{O\text{-}dep.}$, central temperature - T_c, and central density - ρ_c. All quantities are normalized to their values at $\delta_{mesh} = 0.25$ and $w_t = 1 \times 10^{-5}$. A vertical black dash-dot line marks the resolution used for the Monte Carlo stellar models. A black dashed horizontal line marks a value of unity, i.e. no variance with respect to changes in mass or temporal resolution. Solid lines correspond to the solar models and dashed lines to the subsolar models.

for $\delta_{mesh} = (1.0, 0.25)$ at our fixed baseline temporal resolution of $w_t = 5 \times 10^{-5}$, and $w_t = (5 \times 10^{-4}, 1 \times 10^{-5})$ at our baseline mass resolution of $\delta_{mesh} = 0.5$. Otherwise the solar and subsolar models use the same *median* reaction rates and input physics as the baseline models. For δ_{mesh}, the largest variation is $\simeq 13\%$ in the central density for the subsolar models. All other quantities have variations $\lesssim 7\%$ at the highest mass resolution considered. For w_t, the largest variation is $\lesssim 5\%$ in the central density, and all other quantities have variations of $\lesssim 3\%$.

2.6 Monte Carlo Stellar Models

We evolve two grids of Monte Carlo stellar models. The first grid consists of 1000 Monte Carlo stellar models at solar metallicity. Each model has a different set of sampled nuclear reactions; otherwise each model has the same input physics as the baseline model. We refer to this set of models as the "solar grid". The second set consists of 1000 models at a metallicity of $Z=0.0003$,

henceforth the "subsolar grid". Each stellar model takes $\simeq 60$ hours on 4 CPUs. The total computational expense is $\simeq 0.48$ M CPU hours and generates $\simeq 1$ TB of data.

Some properties of a stellar model may be more important at different evolutionary phases. For example, the time spent on the main-sequence is a direct consequence of the $^{14}\text{N}(p,\gamma)^{15}\text{O}$ reaction which modulates the rate at which the CNO cycle may proceed (Imbriani et al., 2004). At core He-depletion, the central carbon mass fraction, temperature, or density affects whether carbon ignites radiatively or convectively (Lamb et al., 1976; Woosley & Weaver, 1986; Petermann et al., 2017). Such features are directly linked to key nuclear reaction rates. We thus consider different properties of our stellar models at five evolutionary epochs: central H-, He-, C-, Ne-, and O-depletion. The properties considered at each epoch are commonly held to be significant for connecting presupernova stellar models to observed transients, stellar yields for chemical evolution, or predicting SN properties (e.g., Nomoto et al., 2013; Couch et al., 2015; Janka et al., 2016; Côté et al., 2017).

To determine the reaction rates that have the largest impact on different properties of the stellar models at different evolutionary phases, we use a Spearman Rank-Order Correlation (SROC) analysis. A SROC is the Pearson correlation coefficient between the rank values of two variables (Myers & Well, 1995). The N raw scores A_i and B_i are converted to ranks $\text{rg}A_i$ and $\text{rg}B_i$, sorted in descending order according to magnitude, and the SROC is

$$r_{\text{S}} = \frac{\text{cov}(\text{rg}A, \text{rg}B)}{\sigma_{\text{rg}A}\sigma_{\text{rg}B}} , \qquad (2.4)$$

where $\text{cov}(\text{rg}A, \text{rg}B)$ is the covariance matrix of the two variables A_i and B_i, and $\sigma_{\text{rg}A}$ and $\sigma_{\text{rg}B}$ are the standard deviations of A and B, respectively A SROC of $r_{\text{S}} = +1$ represents a perfectly monotonically increasing relationship, $r_{\text{S}} = 0$, perfectly uncorrelated, and $r_{\text{S}} = -1$, monotonically decreasing.

2.6.1 Hydrogen Depletion

We consider six properties at core H-depletion, which we define as the time point when the central ^1H mass fraction drops below $\simeq 10^{-6}$: the mass of the He core $M_{\text{He-Core}}$, age τ_{TAMS},
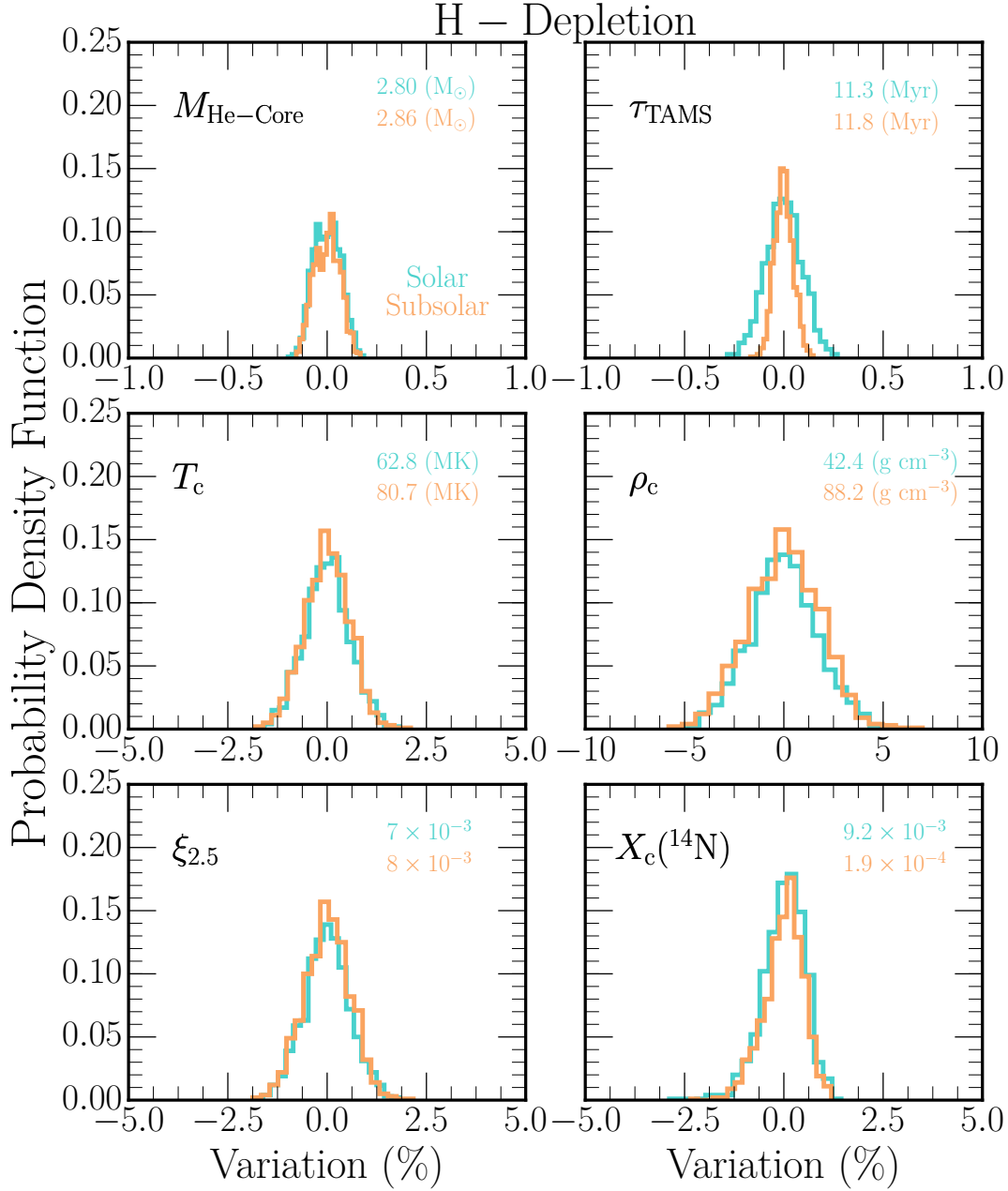
Figure 2.7: Probability density functions for six properties of the grid of Monte Carlo stellar models. The x-axis represents the difference of a model value for a given property and the arithmetic mean of all values obtained for that property. This quantity is then normalized to the mean of the distribution. This distribution is referred to as the "variation". The blue histograms correspond to the solar models while the tan histograms denote the subsolar models. The properties shown are $M_{\text{He-Core}}$ - the mass of the He core, τ_{TAMS} - the age at hydrogen depletion, T_c - central temperature, ρ_c - central density, $\xi_{2.5}$ - compactness parameter measured at $m = 2.5\ M_\odot$, and $X_c(^{14}\text{N})$ - central ^{14}N mass fraction. All properties are measured at H-depletion, when $X(^1\text{H}) \lesssim 10^{-6}$. Annotated are the arithmetic means of each property corresponding to a variation of zero.
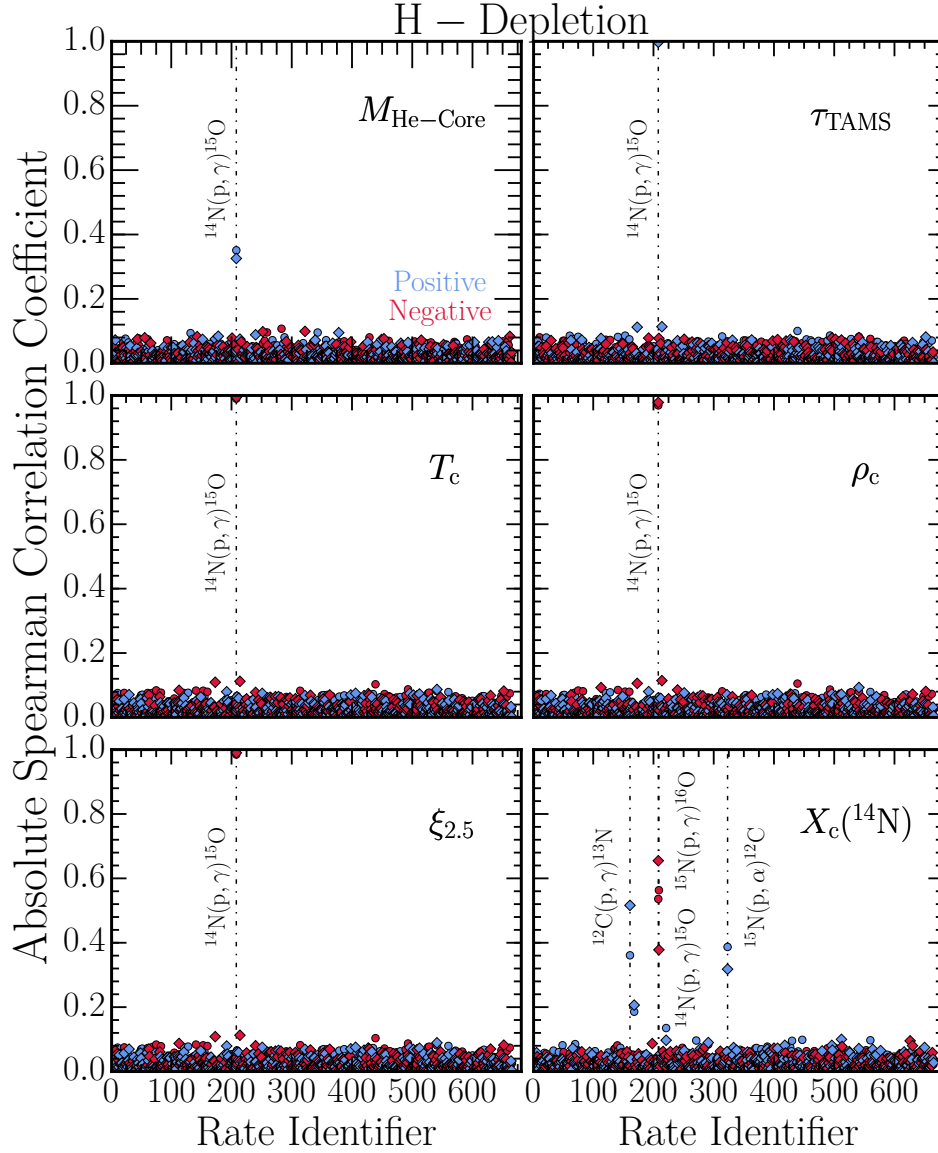
Figure 2.8: The absolute Spearman Rank-Order Correlation Coefficients for the 665 independently sampled thermonuclear reaction rates for the solar and subsolar grid of 1,000 Monte Carlo stellar models. For a single nuclear reaction, the array of 1,000 Gaussian deviates that were used to construct the sampled rate distributions is compared to six properties of the stellar models to determine the correlation coefficient. The solar metallicity coefficients are denoted by circles and subsolar metallicity by diamonds. A positive correlation is denoted by a blue marker while a negative coefficient is represented by a red marker. The x-axis corresponds to an arbitrary "rate identifier" used to track the thermonuclear reaction rates sampled in this work. The quantities considered are $M_{\text{He-Core}}$ - the mass of the He core, τ_{TAMS} - the age, T_{c} - the central temperature, ρ_{c} - the central density, $\xi_{2.5}$ - the compactness parameter, and $X_{\text{c}}(^{14}\text{N})$ - the central neon-14 mass fraction. All quantities are measured when $X_{\text{c}}(^1\text{H}) \lesssim 1 \times 10^{-6}$. Key nuclear reactions with large SROC values are annotated.
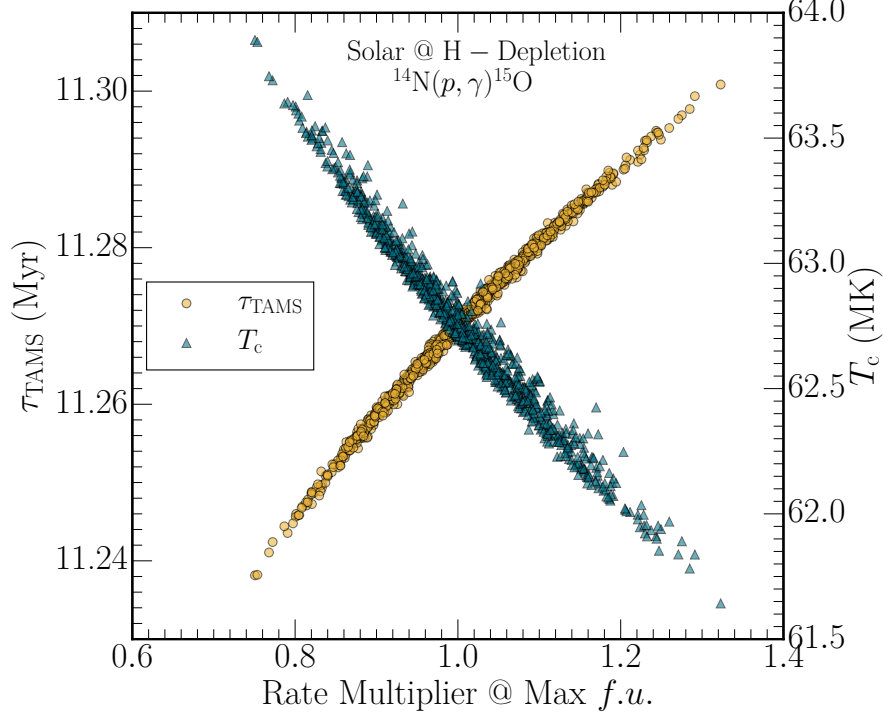
Figure 2.9: The age and central temperature at H-depletion as a function of the max rate multiplier applied to the $^{14}N(p, \gamma)^{15}O$ reaction rate for the grid of solar metallicity stellar models. The max $f.u.$ for $^{14}N(p, \gamma)^{15}O$ is $\simeq 1.1$. Best-fit lines to the two trends yield the slope of the thermostat mechanism to be $d\tau_{TAMS}/dT_c \simeq -0.03$ Myr/MK.

central temperature T_c, central density ρ_c, compactness parameter, effectively the depth of the gravitational potential well at the expected maximum mass of a neutron star, and central ^{14}N mass fraction $X_c(^{14}N)$.

2.6.1.1 Probability Distribution Functions

Figure 2.7 shows the PDFs of these six properties of the stellar models at this epoch. The x-axis is the variation, $(X_i - \bar{X})/\bar{X}$, where X_i is a value of a property for a single model and $\bar{X}$ is the arithmetic mean of the distribution. The amplitude of the histogram corresponds to the fraction of the 1000 models within a given bin. In this paper, the number of bins is chosen according to the Rice Rule, $k = 2n^{1/3}$, where k is the number of bins and n is the number of samples (Lane, 2013). While different bin widths can reveal different features of the distribution, we find this choice of bins sufficient for the discussion of the histograms presented here.

Throughout this paper we use the 95% Confidence Interval (CI) limits. These are defined, for each PDF, to be the limits corresponding to the unique cumulative distribution function containing 95% of the PDF. This allows reporting the most likely ($\sim 2\sigma$) values of a property without the effects of outliers in the data. This definition is different than a canonical CI derived from an assumed distribution function model of the data.

We define $M_{\text{He-Core}}$ as the mass coordinate where $X(^1\text{H}) < 0.01$ and $X(^4\text{He}) > 0.1$. The 95% CI widths of the $M_{\text{He-Core}}$ PDFs span a narrow $\simeq \pm 0.1\%$ across the mean of the distribution for both solar and subsolar models. Both PDFs show well-defined zero variation peaks of $2.80\,M_\odot$ for the solar models and $2.86\,M_\odot$ for the subsolar models.

The 95% CI width of the τ_{TAMS} PDF for the solar models, $\simeq \pm 0.2\%$, is larger than the width of the PDF for the subsolar models, $\simeq \pm 0.1\%$. We defer an explanation of this difference until we discuss Figure 2.8. The solar and subsolar PDFs are symmetric about their zero variation values of 11.3 Myr and 11.8 Myr, respectively.

The T_c and ρ_c PDFs show the solar models are slightly cooler and less dense than the subsolar models, with zero variation values of $T_c \simeq (62.8\text{ MK}, 80.7\text{ MK})$ and $\rho_c \simeq (42.4\text{ g cm}^{-3}, 88.2\text{ g cm}^{-3})$, respectively. After H-depletion, the solar models will proceed to burn He at a cooler core temperature but more dense core. This trend is seen in Figure 2.4. Note the subsolar models have larger T_c and yet *longer* lifetimes τ_{TAMS}. In addition, the 95% CI width of the T_c PDFs are $\simeq 1.2\%$, and the 95% CI width of the ρ_c PDFs are $\simeq 4\%$.

Traditionally $\xi_{2.5}$ is evaluated at core collapse. Our motivation for measuring $\xi_{2.5}$ starting at H-depletion is to assess the evolution of the variability in $\xi_{2.5}$; when do significant variations first seed and how do the variation grow. The 95 % width of the $\xi_{2.5}$ PDF at H-depletion, $\simeq 1.2\%$, is dependent upon the narrow $M_{\text{He-Core}}$ PDF and the wider ρ_c PDF. In addition, $\xi_{2.5}$ depends on the gradient of the density profile. The zero variation values of the solar and subsolar grids show small differences at this epoch with $\xi_{2.5} \simeq (7\times10^{-3}, 8\times10^{-3})$, respectively.

Nitrogen is the dominant metal in the ashes of H-burning in massive stars because the $^{14}\text{N}(p,\gamma)^{15}\text{O}$ rate is the smallest in the CNO cycles (e.g., Iben, 1966). This is reflected in the

$X_c(^{14}N)$ PDFs by the zero variation values, 9.2×10^{-3} for the solar models and 1.9×10^{-4} for the subsolar models, being approximately equal to the sum of the ZAMS CNO mass fractions. The 95% CI width of the $X_c(^{14}N)$ PDF, $\simeq \pm 1\%$, is consistent with the spreads in the other quantities measured.

2.6.1.2 Spearman Correlation Coefficients

Figure 2.8 shows the SROC coefficients for the solar and subsolar grids. The coefficients for the solar grid is shown by circles while the subsolar grid is shown by diamond markers. A positive correlation coefficient is represented by a blue marker, while a negative coefficient is denoted by a red marker. For each property shown, the rate identifier corresponding to the largest magnitude SROC coefficients are marked by a vertical dashed line and label.

The $^{14}N(p, \gamma)^{15}O$ rate has a large impact on all the quantities we measure. For example, the $^{14}N(p, \gamma)^{15}O$ rate has the largest SROC coefficient for τ_{TAMS}, with $r_s \simeq +0.99$ for the solar and subsolar models. Coefficients of the remaining 664 reactions are significantly smaller, $O(10^{-2})$. This suggest that τ_{TAMS} is a directly dependent on the $^{14}N(p, \gamma)^{15}O$ rate, with a larger rate *increasing* the lifetime to core H-depletion (e.g., Imbriani et al., 2004; Weiss et al., 2005; Herwig et al., 2006).

Increasing a reaction rate usually increases the nuclear energy generation rate, which deposits its energy into thermal energy. The core temperature rises. Via the equation of state, the pressure increases, which causes the stellar core to expand. This expansion decreases T_c and ρ_c, and thus causes nuclear burning to proceed at a slower rate. The net result of increasing an energetically important reaction rate is a longer burning lifetime and a decreased T_c and ρ_c. This is the well-known thermostat mechanism (e.g., Hansen et al., 2004; Iliadis, 2007).

Figure 2.9 shows the age and T_c at H-depletion for the solar models as a function of the rate multiplier applied at max $f.u.$ for the $^{14}N(p, \gamma)^{15}O$ reaction. Least-square fits to the linear trends yield the slope of the thermostat mechanism: $d\tau_{TAMS}/dT_c$, $\simeq -0.03$ Myr/MK. This correlation is confirmed by the large and negative SROC coefficients between the $^{14}N(p, \gamma)^{15}O$ rate and $\xi_{2.5}, T_c$,

and ρ_c. The thermostat mechanism also causes the slightly larger zero variation of $M_{\text{He-Core}}$ for the subsolar models relative to the solar models in Figure 2.7.

2.6.1.3 Impact of the Measurement Point

To assess the impact of the choice of the measurement point, we repeat our SROC analysis during core H-burning at the point $X_c(^1\text{H}) \simeq X_c(^4\text{He})$. We compare the magnitude of the SROC values for τ_{TAMS}, T_c, ρ_c, and $\xi_{2.5}$ for both the solar and subsolar models.

Qualitatively, $^{14}\text{N}(p, \gamma)^{15}\text{O}$ still drives the variation in the age with a positive correlation, and the variations in T_c, ρ_c, and $\xi_{2.5}$ with negative correlations. The difference of the SROC values between the two epochs agree to $\lesssim 0.01$ for T_c, ρ_c, and $\xi_{2.5}$ and $\lesssim 0.2$ for τ_{TAMS}. This re-evaluation suggests the PDFs vary slightly based on the chosen measurement point and identifying the key reactions from the SROC analysis is an invariant.

2.6.2 Helium Depletion

We measure the integrated impact of the uncertainties in the reaction rates at the point when the central helium mass fraction $X(^4\text{He}) \lesssim 10^{-6}$.

2.6.2.1 Probability Distribution Functions

Figure 2.10 shows the PDFs of eight properties from the stellar models at this epoch: mass of the CO core $M_{\text{CO-Core}}$, the elapsed time between H-depletion and He-depletion $\tau_{\text{He-burn}}$, central temperature T_c, central density ρ_c, central ^{22}Ne mass fraction $X_c(^{22}\text{Ne})$, compactness parameter $\xi_{2.5}$, central ^{12}C mass fraction $X_c(^{12}\text{C})$, and central ^{16}O mass fraction $X_c(^{16}\text{O})$.

The 95% CI width of the $M_{\text{CO-Core}}$ PDF spans $\simeq \pm 2\%$ for the solar and subsolar grids. Both PDFs show a well-defined peak of 2.41 $M_\odot$ for the solar models and 2.95 $M_\odot$ for the subsolar models and an extended tail for negative variations. That is, changes in the reaction rates are more likely to produce smaller C cores than more massive C cores. This asymmetry accounts for the PDFs not being centered at zero variation.
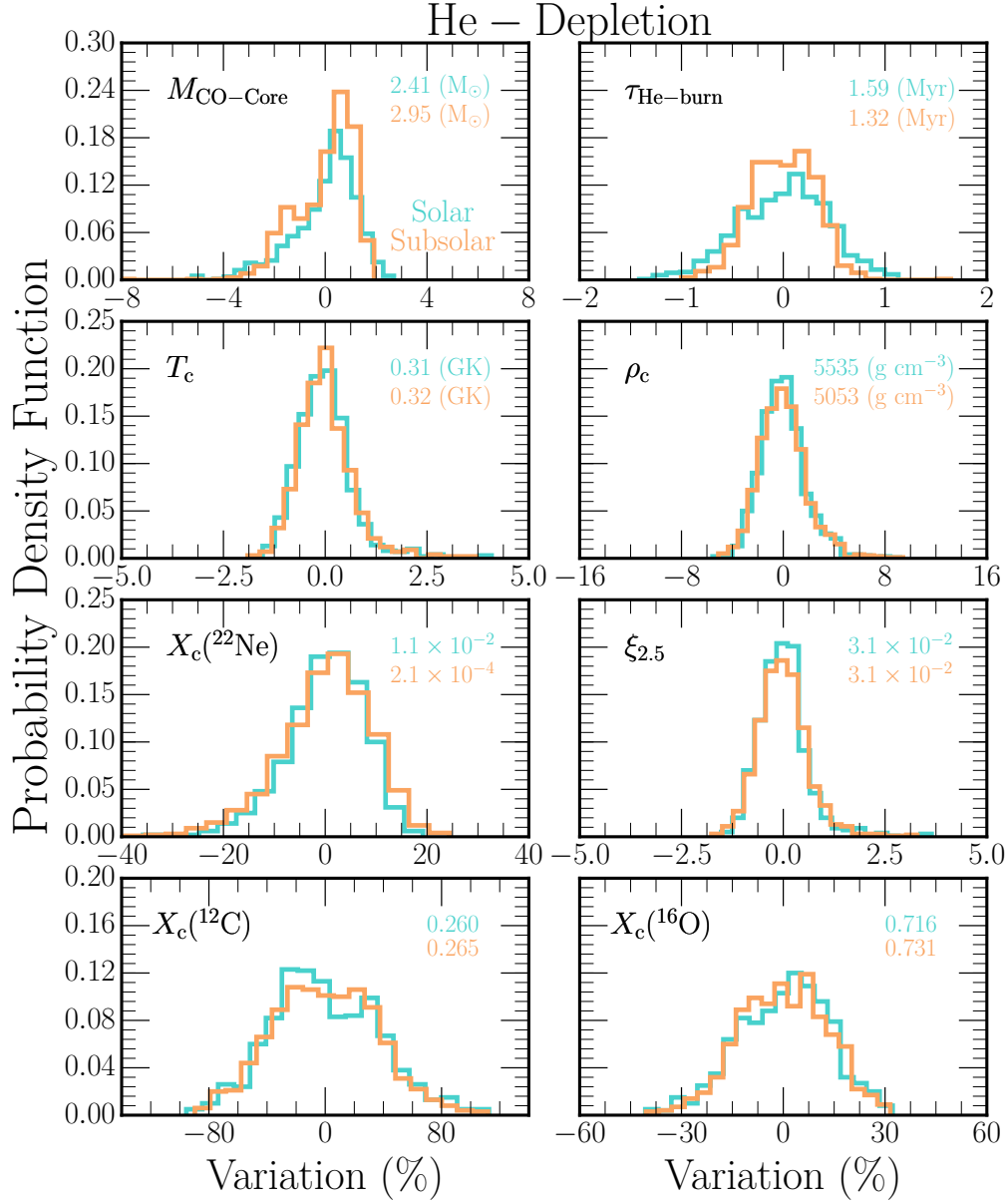
Figure 2.10: Same as in Figure 2.7 except we consider $M_{\text{CO-Core}}$ - the mass of the CO core, $\tau_{\text{He-burn}}$ - the elapsed time between H-depletion and He-depletion, T_{c} - the central temperature, ρ_{c} - the central density, $X_{\text{c}}(^{22}\text{Ne})$ - the central neon-22 mass fraction, $\xi_{2.5}$ - the compactness parameter, $X_{\text{c}}(^{12}\text{C})$ - the central carbon-12 mass fraction, and $X_{\text{c}}(^{16}\text{O})$ - the central oxygen-16 mass fraction all measured at He-depletion.

The solar and subsolar grid PDFs for $\tau_{\text{He-burn}}$ have a 95% CI spread of $\simeq \pm 1\%$, suggesting rate uncertainties have a smaller impact on $\tau_{\text{He-burn}}$. The solar PDF is slightly wider the subsolar PDF, and both PDFs are symmetric about their respective arithmetic means.

The T_{c} and ρ_{c} PDFs show 95% CI widths of $\simeq \pm 1.5\%$ and $\simeq \pm 3.5\%$, respectively, for both
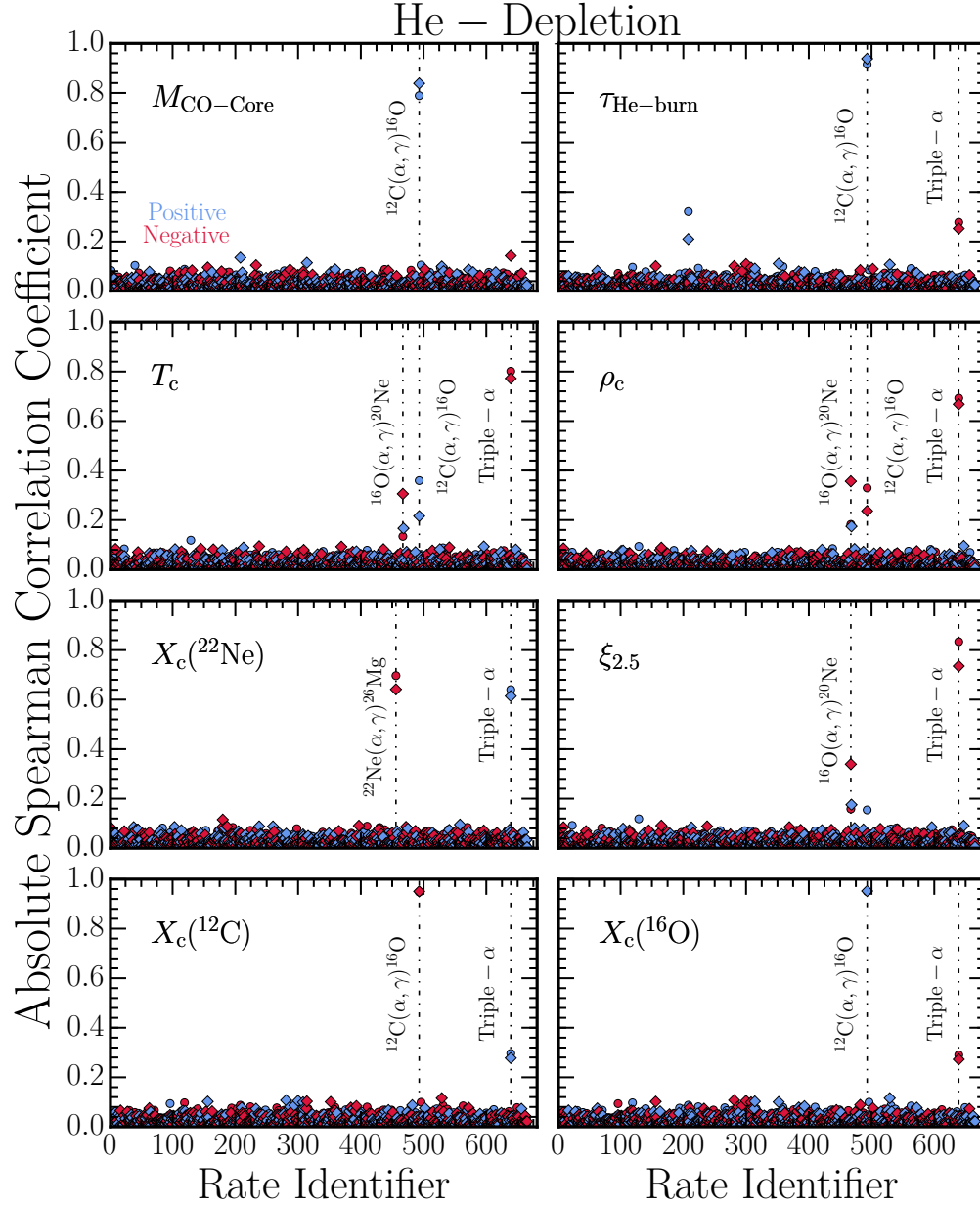
Figure 2.11: Same as in Figure 2.8. The quantities considered are $M_{\text{CO-Core}}$ - the mass of the CO core, $\tau_{\text{He-burn}}$ - the elapsed time between H-depletion and He-depletion, T_c - the central temperature, ρ_c - the central density, $X_c(^{22}\text{Ne})$ - the central neon-22 mass fraction, $\xi_{2.5}$ - the compactness parameter, $X_c(^{12}\text{C})$ - the central carbon-12 mass fraction, and $X_c(^{16}\text{O})$ - the central oxygen-16 mass fraction. All quantities used here were measured at He-depletion.

solar and subsolar models. Both PDFs are centrally peaked with $\lesssim 1\%$ differences between the arithmetic means of the solar and subsolar models. Both PDFs exhibit long tails in the positive variation direction, indicating some combinations of the reaction rates produce cores that are $\simeq 5\%$ hotter than the mean and $\simeq 10\%$ denser than the mean.
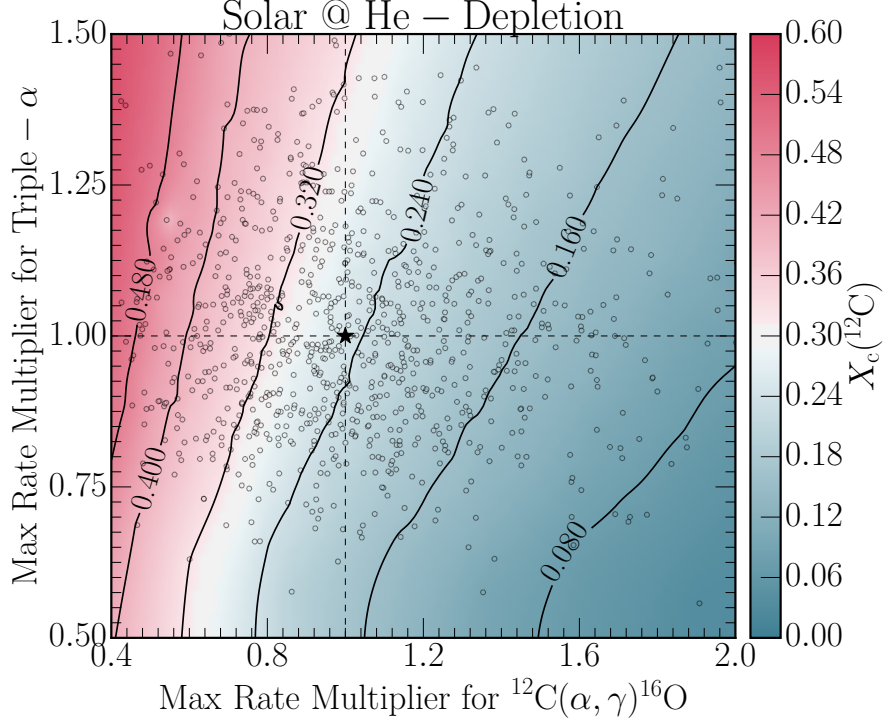
Figure 2.12: Central carbon mass fraction at helium depletion for solar models as a function of the rate multiplier at max $f.u.$ applied to the $^{12}C(\alpha, \gamma)^{16}O$ and triple-α rates. The heatmap uses bi-linear interpolation and extrapolation of the models, which are shown by gray circles. Contour lines of constant $X_c(^{12}C)$ shown by solid black lines. Also shown by a dashed line is the value of a rate multiplier of unity for both reactions. Lastly, the black star denotes the value of $X_c(^{12}C)$ found for the *median* reaction rates. Compare with Figure 20 of West et al. (2013).

The solar and subsolar grid PDFs for $X_c(^{22}Ne)$ PDF are nearly the same. However, the arithmetic mean of the two PDFs differ by a factor of $\simeq 50$. The reason for this difference is that most of a ZAMS star's initial metallicity Z comes from the CNO and ^{56}Fe nuclei inherited from its ambient interstellar medium. The slowest step in the hydrogen burning CNO cycle is $^{14}N(p, \gamma)^{15}O$, which causes all the CNO catalysts to pile up at ^{14}N at core H-depletion. During He-burning the sequence $^{14}N(\alpha,\gamma)^{18}F(\beta^+, \nu_e)^{18}O(\alpha,\gamma)^{22}Ne$ converts all of the ^{14}N into the neutron-rich isotope ^{22}Ne. Thus, $X_c(^{22}Ne)$ at core He-depletion is linearly dependent on the initial CNO abundances. The subsolar models have $\simeq 50$ times less initial CNO than the solar models, accounting for the difference in the arithmetic means.

The solar and subsolar PDFs for $\xi_{2.5}$ are similar in peak amplitude, 95% CI width ($\simeq 1.2\%$), symmetry about zero variation, and mean arithmetic value. That is, rate uncertainties have little

impact on differentiating between solar and subsolar metallicities. Similar to the T_c and ρ_c PDFs, there are outlier models whose reaction rate combinations produce larger $\xi_{2.5}$.

The largest variations occur in the $X_c(^{12}C)$ and $X_c(^{16}O)$ PDFs with 95% CI widths of $\simeq \pm 70\%$ and $\simeq \pm 25\%$, respectively. The common driver for these variations are the triple-α, $^{12}C(\alpha, \gamma)^{16}O$, and $^{16}O(\alpha, \gamma)^{20}Ne$ rates, whose roles we discuss below.

2.6.2.2 Spearman Correlation Coefficients

Figure 2.11 shows the SROCs for the 665 independently sampled thermonuclear reaction rates against the eight quantities considered in Figure 2.10. The $M_{CO\text{-}Core}$ is chiefly set by the $^{12}C(\alpha, \gamma)^{16}O$ rate with $r_s \simeq +0.8$ for both metallicity grids. Larger $^{12}C(\alpha, \gamma)^{16}O$ rates build larger CO core masses. The triple-α rate plays a smaller role with $r_s \simeq -0.17$ for both metallicity grids. Similarly, $\tau_{He\text{-}burn}$ is primarily set by the $^{12}C(\alpha, \gamma)^{16}O$ rate with coefficients of $r_s = (+0.92, +0.94)$, respectively. The triple-α rate plays a less significant role with $r_s \simeq -0.25$.

In contrast, T_c and ρ_c are chiefly affected by the uncertainties in the triple-α rate with $r_s \simeq -0.8$ and $r_s \simeq -0.7$, respectively. These large negative SROCs mean the thermostat mechanism, discussed for H-burning, namely larger energy producing reaction rates yield cooler and less dense cores, operates during He burning. The $^{12}C(\alpha, \gamma)^{16}O$ and $^{16}O(\alpha, \gamma)^{20}Ne$ rates play smaller roles with $r_s \leq +0.4$. Note that the positive correlation means larger $^{12}C(\alpha, \gamma)^{16}O$ rates produce hotter cores, in juxtaposition to the triple-α rate. This is because a larger $^{12}C(\alpha, \gamma)^{16}O$ converts more carbon into oxygen, so the core burns hotter at any given triple-α rate (which dominates the energy generation) to satisfy the luminosity demanded by the surface of the stellar model. Outliers with positive variations in the T_c and ρ_c PDFs of Figure 2.10 are caused by combinations of the $^{12}C(\alpha, \gamma)^{16}O$ and triple-α reactions. For a small triple-α rate, the model will be hotter and more dense. When this is coupled with a large $^{12}C(\alpha, \gamma)^{16}O$ rate, the stellar models at He-depletion have a hotter and denser core with T_c increased by $\simeq +5\%$ and and ρ_c increased by $\simeq +10\%$.

The mass fraction of the neutron-rich ^{22}Ne isotope, is set by the competition between the triple-α and $^{22}Ne(\alpha, \gamma)^{26}Mg$ rates. The triple-α rate sets T_c and ρ_c, with a larger rate giving cooler and

denser cores that favor the production of ^{22}Ne by the sequence ^{14}N$(\alpha,\gamma)^{18}$F$(\beta^+, \nu_e)^{18}$O$(\alpha,\gamma)^{22}$Ne. This is the origin of the positive SROC coefficient for the triple-α rate in the solar and subsolar grids. On the other hand, ^{22}Ne$(\alpha,\gamma)^{26}$Mg destroys ^{22}Ne, storing the neutron excess in ^{26}Mg. This accounts for the negative SROC coefficient of ^{22}Ne$(\alpha,\gamma)^{26}$Mg for both metallicity grids.

$\xi_{2.5}$ is chiefly set by the triple-α rate with $r_s = -0.83$ and $r_s = -0.74$ for the solar and subsolar models respectively. A larger triple-α rate produces a smaller $\xi_{2.5}$, due to the decrease in overall density of the stellar core. For the subsolar models the ^{16}O$(\alpha, \gamma)^{20}$Ne rate plays a smaller role ($r_s = -0.34$), but also decreases $\xi_{2.5}$ as the rate becomes larger. The solar and subsolar PDFs for $\xi_{2.5}$ shows outliers with variations up to $\simeq 5\%$. These outliers form from same combination of reaction rates that produce denser stellar models. Namely, models with high $\xi_{2.5}$ have either a depressed triple-α rate, an enhanced ^{12}C$(\alpha, \gamma)^{16}$O, or both.

During quiescent He-burning the 3α-process and the ^{12}C$(\alpha, \gamma)^{16}$O reaction burn with high efficiency through pronounced resonance mechanisms (e.g., deBoer et al., 2017). In contrast, the ^{16}O$(\alpha, \gamma)^{20}$Ne reaction lacks any such resonance enhancement in the stellar energy range making its rate comparatively much lower. This essentially prohibits significant He-burning beyond ^{16}O and maintains the ^{12}C/^{16}O balance we observe today.

The ^{12}C$(\alpha, \gamma)^{16}$O rate sets $X_c(^{12}$C$)$ and $X_c(^{16}$O$)$ for both solar and subsolar models with $r_s \simeq -0.95$ and $r_s \simeq +0.95$, respectively. A larger ^{12}C$(\alpha, \gamma)^{16}$O rate destroys more C and produces more O. The triple-α rate plays a smaller role in setting $X_c(^{12}$C$)$ and $X_c(^{16}$O$)$ with $r_s \simeq +0.29$ and $r_s \simeq -0.28$, respectively. A larger triple-α rate produces more C and less O. These results suggest $X_c(^{12}$C$)$ and $X_c(^{16}$O$)$ are determined primarily by the uncertainties in these two reaction rates.

2.6.2.3 Triple-α and ^{12}C$(\alpha, \gamma)^{16}$O

Figure 2.12 shows $X_c(^{12}$C$)$ at He-depletion for the solar models as a function of the rate multiplier at max $f.u.$ (over core He-burning temperatures) applied to the ^{12}C$(\alpha, \gamma)^{16}$O and triple-α rates (see Figure 2.2). A ^{12}C$(\alpha, \gamma)^{16}$O rate that is small relative to median value and a triple-α rate that is large relative to its median value produces a large $X_c(^{12}$C$)$. Conversely, a high ^{12}C$(\alpha, \gamma)^{16}$O rate

and a small triple-α rate produces a small $X_c(^{12}C)$. When both rates are at the median value of their respective PDFs, unity rate multipliers in Figure 2.12, $X_c(^{12}C) \simeq 0.26$ (see Figure 2.10). The trend is commensurate with West et al. (2013, their Figure 20).

2.6.2.4   Impact of the Measurement Point

Core He-burning is initiated by the triple-α reaction releasing ≈ 7.27 MeV of energy. At early times, nuclear energy generation in the core is governed by this reaction rate. The emergence of fresh ^{12}C as a product of the triple-α reaction allows $^{12}C(\alpha, \gamma)^{16}O$ to convert the ^{12}C ashes into ^{16}O in a race between the two reactions to consume the He fuel (e.g., deBoer et al., 2017). The $^{12}C/^{16}O$ ratio is determined by these two reaction rates.

Due to this evolution, we re-evaluate our SROC coefficients midway through the core He-burning process, when $X_c(^{4}He) \simeq 0.5$. The structural properties $- T_c$, ρ_c and $\xi_{2.5}$ $-$ agree qualitatively when comparing the midway and depletion points of the solar models. A midway measurement point yields $\simeq 15\%$ stronger correlations. The triple-α rate still drives the variations with a negative SROC. For $X_c(^{12}C)$ and $X_c(^{16}O)$ the midway and He-depletion measurement points for the solar models differ by $\Delta |r_s| \lesssim 2\%$ in the SROC values.

When measuring midway through the core He-burning process, variations in $\tau_{He\text{-burn}}$ for the solar models become mainly driven by the $^{14}N(p, \gamma)^{15}O$ rate with a positive SROC coefficient. An increase in this rate causes the stellar core to proceed through core H-burning at lower T_c. When measuring $\tau_{He\text{-burn}}$ midway through He-burning, we find the $^{14}N(p, \gamma)^{15}O$ rate also yields a negative SROC coefficient for T_c. Models with lower T_c proceed through He-burning at a slower rate, hence increasing the helium burning lifetime $\tau_{He\text{-burn}}$.

2.6.3   Carbon Depletion

Next, we measure the integrated impact of the reaction rate uncertainties at the point when the central carbon mass fraction $X_c(^{12}C) \lesssim 1 \times 10^{-6}$.
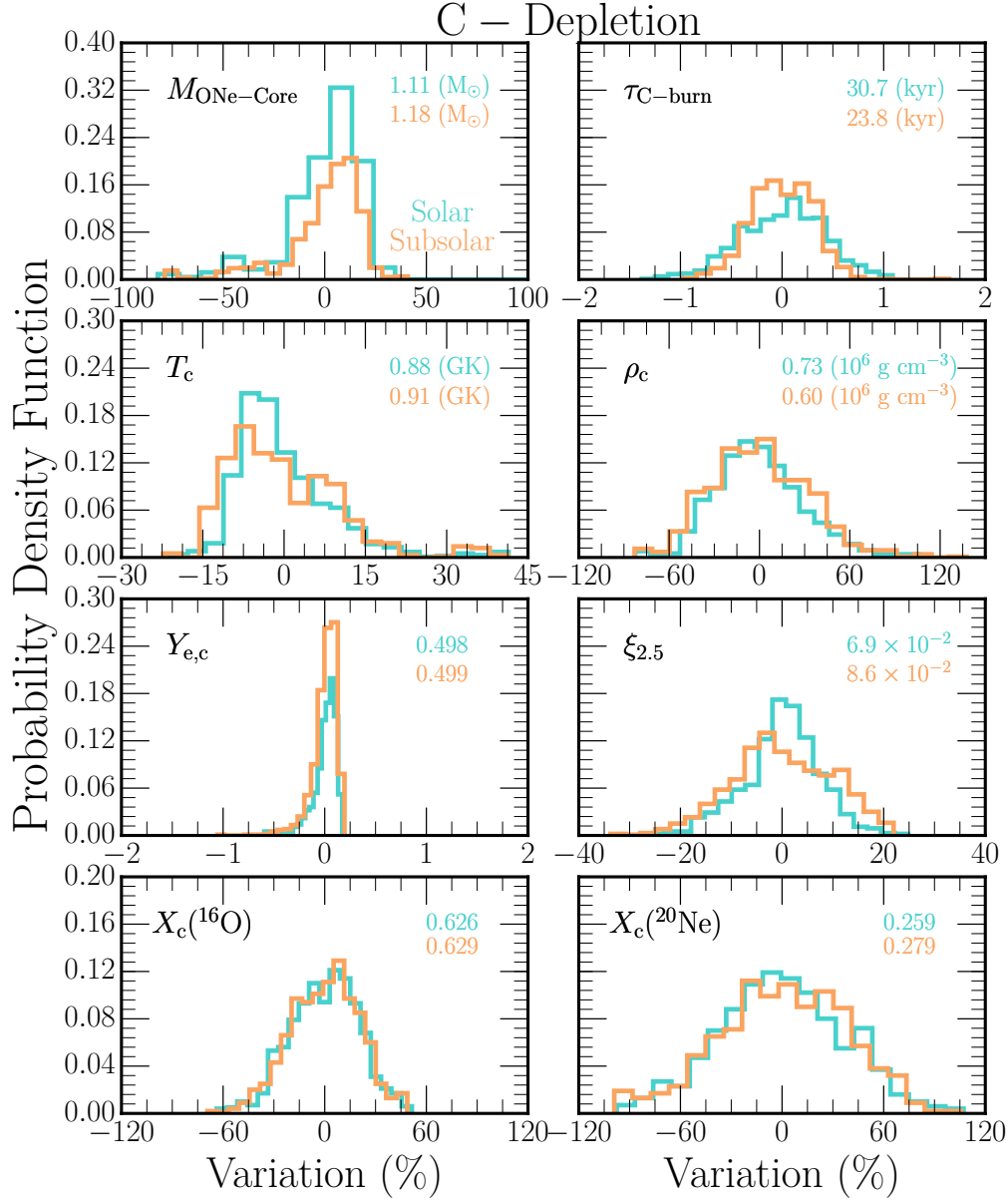
Figure 2.13: Same as in Figure 2.10 except we consider $M_{\text{ONe-Core}}$ - the mass of the ONe core, $\tau_{\text{C-burn}}$ - the elapsed time between He-depletion to C-depletion, T_{c} - the central temperature, ρ_{c} - the central density, $Y_{\text{e,c}}$ - the central electron fraction, $\xi_{2.5}$ - the compactness parameter, $X_{\text{c}}(^{16}\text{O})$ - the central oxygen-16 mass fraction, and $X_{\text{c}}(^{20}\text{Ne})$ - the central neon-20 mass fraction. All quantities are measured at C-depletion.

2.6.3.1 Probability Distribution Functions

Figure 2.13 shows the PDFs of eight properties of the $15\,M_\odot$ models at C-depletion: mass of the ONe core $M_{\text{ONe-Core}}$, the elapsed time between He-depletion and C-depletion $\tau_{\text{C-burn}}$, central
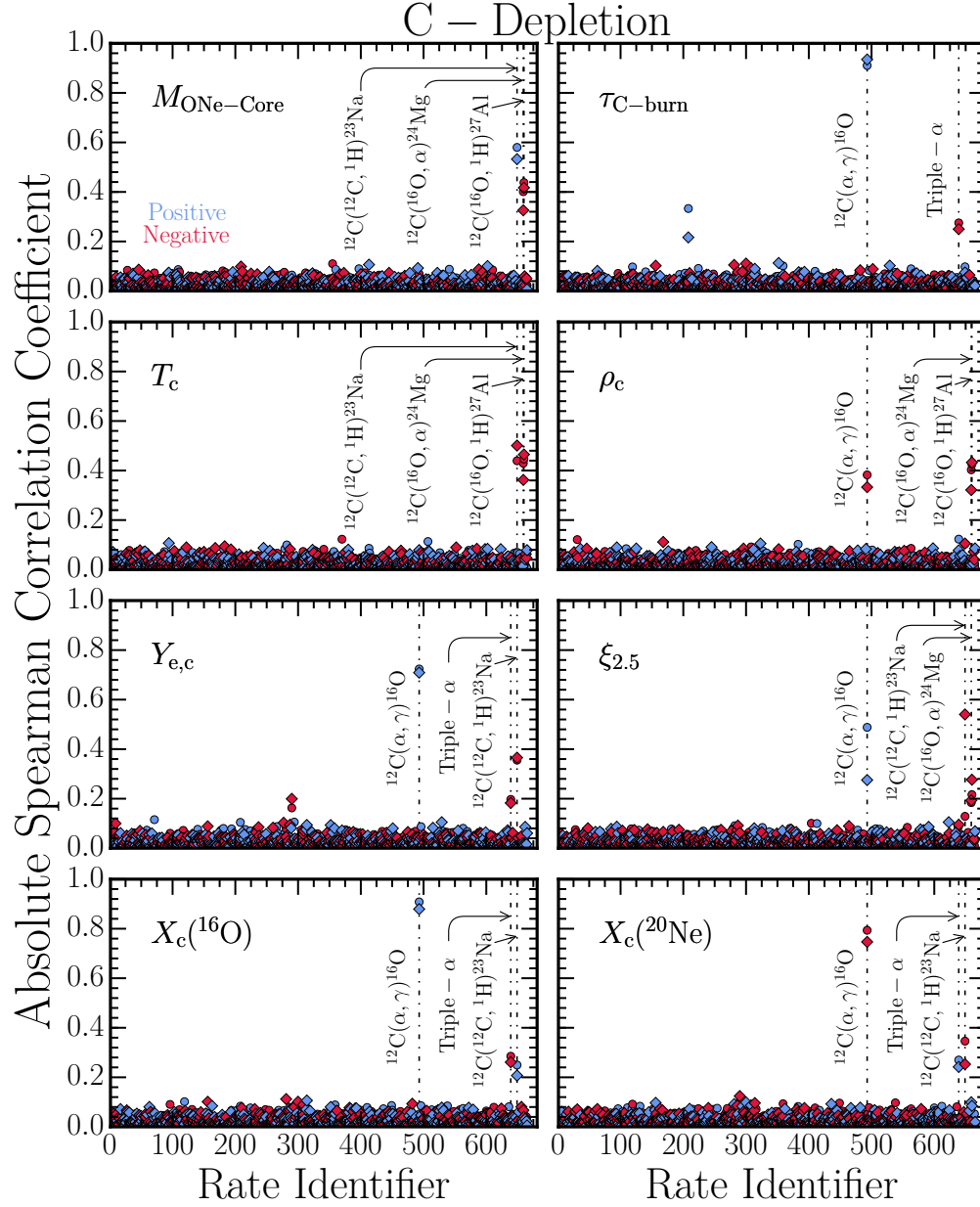
Figure 2.14: Same as in Figure 2.10 except we consider $M_{\text{ONe-Core}}$ - the mass of the ONe core, $\tau_{\text{C-burn}}$ - the elapsed time between He-depletion and C-depletion, T_{c} - the central temperature, ρ_{c} - the central density, $Y_{\text{e,c}}$ - the central electron fraction, $\xi_{2.5}$ - the compactness parameter, $X_{\text{c}}(^{16}\text{O})$ - the central oxygen-16 mass fraction, and $X_{\text{c}}(^{20}\text{Ne})$ - the central neon-20 mass fraction. All quantities are measured at C-depletion.

temperature T_{c}, central density ρ_{c}, central electron fraction $Y_{\text{e,c}}$, compactness parameter $\xi_{2.5}$, central ^{16}O mass fraction $X_{\text{c}}(^{16}\text{O})$, and central ^{20}Ne mass fraction $X_{\text{c}}(^{20}\text{Ne})$.

The $M_{\text{ONe-Core}}$ distribution has 95% CI variation limits of $\simeq +23\%$ and $\simeq -50\%$ for the solar and subsolar models. This is wider than the spread in the He core mass at H-depletion ($\simeq \pm 0.1\%$)

or the CO core mass at He-depletion ($\simeq \pm 3\%$). We defer explanation to Section 2.6.3.3 In addition, the solar model PDF has a larger peak amplitude compared to the subsolar model PDF.

In contrast, the 95% CI spread of the $\tau_{\text{C-burn}}$ distribution shows about the same narrow width of $\simeq \pm 1\%$ as τ_{TAMS} and $\tau_{\text{He-burn}}$. This is chiefly due to the CO core mass to be burned laying within a relative narrow range ($\simeq \pm 3\%$, see Figure 2.10). The solar model PDF has a zero variance of $\tau_{\text{C-burn}} \simeq 30.7$ kyr, while the subsolar model PDF has a zero variance of $\tau_{\text{C-burn}} \simeq 23.8$ kyr. This reflects the subsolar models undergoing hotter, less dense core C-burning (see Figure 2.4).

Carbon burning and the later stages of evolution in massive stars have large core luminosities whose energy is carried away predominantly by free-steaming neutrinos. These burning stages are thus characterized by short evolutionary time scales. When thermal neutrinos instead of photons dominate the energy loss budget, carbon and heavier fuels burn at a temperature chiefly set by the balanced power condition $\langle \epsilon_{\text{nuc}} \rangle \simeq \langle \epsilon_{\nu} \rangle$. For core C-burning this gives $T_c \simeq 0.9$ GK and, assuming a T^3/ρ scaling, $\rho_c \simeq 6 \times 10^6$ g cm^{-3}. This is commensurate with the zero variation values annotated in Figure 2.13. The T_c and ρ_c distributions show 95% CI widths of $\simeq \pm 15\%$ and $\simeq \pm 60\%$ for the solar and subsolar models, respectively. This is wider than the 95% CI spreads of the T_c and ρ_c distributions at H-depletion and He-depletion.

The $Y_{\text{e,c}}$ distributions show strong peaks at $Y_{\text{e,c}} \simeq 0.499$ and 95% CI spreads of $\lesssim 1\%$ for the solar and subsolar models. This is commensurate with significant neutronization not occurring during quiescent core C-burning, and shows $Y_{\text{e,c}}$ is not strongly affected by the uncertainties in the reaction rates.

C-depletion marks the first occurrence of significant variation in $\xi_{2.5}$. The solar and subsolar distributions show 95% CI widths of $\simeq \pm 16\%$. The mean value of $\xi_{2.5} \simeq 6.9 \times 10^{-2}$ for the solar models is smaller than the mean value of $\xi_{2.5} \simeq 8.6 \times 10^{-2}$ for the subsolar models. This is due to the smaller ρ_c and shallower density gradient in the subsolar models relative to the solar models.

The dominant isotopes at C-depletion are ^{16}O and ^{20}Ne. These two isotopes follows nearly Gaussian profiles with 95% CI spreads of $\simeq \pm 40\%$ and $\simeq \pm 70\%$ for $X_c(^{16}$O$)$ and $X_c(^{20}$Ne$)$, respectively. Despite this spread, the zero variation values of ^{16}O and ^{20}Ne for the solar and

subsolar models are within $\simeq 1\%$.

2.6.3.2 Spearman Correlation Coefficients

Figure 2.14 shows the absolute SROCs for the 665 sampled reaction rates for the eight quantities considered in Figure 2.13 for the solar and subsolar grid of models.

Competition between the $^{12}C + ^{12}C$ and $^{12}C + ^{16}O$ reaction rates largely determines the mass of the ONe core at C-depletion. The $^{12}C(^{12}C,p)^{23}Na$ rate have significant positive SROC values of $r_s = (+0.58, +0.56)$ for the solar and subsolar models, respectively. Protons produced by $^{12}C(^{12}C,p)^{23}Na$ are usually captured by $^{23}Na(p,\alpha)^{20}Ne$, which increases $M_{ONe\text{-}Core}$. Uncertainties in the $^{12}C(^{16}O,p)^{27}Al$ and $^{12}C(^{16}O,\alpha)^{27}Mg$ rates have significant negative SROC values, $r_s \simeq -0.40$, because the main products from these reactions ultimately produce ^{28}Si, which decreases $M_{ONe\text{-}Core}$ by effectively transferring ^{16}O to ^{28}Si (Woosley et al., 1971; Martínez-Rodríguez et al., 2017; Fang et al., 2017).

The $^{12}C(\alpha, \gamma)^{16}O$ rate impacts the time between He-depletion and C-depletion $\tau_{C\text{-}burn}$ with SROC values of $\simeq +0.91$ and $\simeq +0.94$ for the solar and subsolar models, respectively. This occurs because this rate sets the mass of the CO core, which has a relatively narrow 95% CI range of $\simeq \pm 2\%$ (see Figure 2.10). Smaller uncertainties in the triple-α rate (negative correlation) and the $^{14}N(p, \gamma)^{15}O$ rate (positive correlation) occur because these two reactions play a diminished role in setting the mass of the CO core.

The SROC analysis for T_c and ρ_c shows dependencies on the $^{12}C(\alpha, \gamma)^{16}O$, $^{12}C + ^{12}C$, and $^{12}C + ^{16}O$ rates for the solar and subsolar models. All these rates have negative SROCs of $r_s \simeq -0.4$. These magnitude and sign are partially due to thermal neutrino losses playing a key role in the evolution, and partially due to the thermostat mechanism, namely larger energy producing reaction rates yield cooler and less dense cores.

The quantities $Y_{e,c}$ and $\xi_{2.5}$ inherit a dependence on the $^{12}C(\alpha, \gamma)^{16}O$ rate from He-burning, with SROCs of $r_s \simeq (+0.7, +0.5)$, respectively. Uncertainties in the $^{12}C(^{12}C,p)^{23}Na$ and $^{12}C(^{16}O,p)^{27}Al$ rates also contribute with negative coefficients.

Likewise, $X_c(^{16}O)$ and $X_c(^{20}Ne)$ also inherit a strong dependence on the $^{12}C(\alpha, \gamma)^{16}O$ rate from He-burning, with SROCs of $r_s \simeq (+0.9, -0.8)$, respectively. The $X_c(^{16}O)$ has a positive correlation coefficient because during He-burning a larger $^{12}C(\alpha, \gamma)^{16}O$ rate produces more ^{16}O. The $X_c(^{20}Ne)$ has a negative SROC because a larger $^{12}C(\alpha, \gamma)^{16}O$ rate produces less ^{12}C, the principal fuel of C-burning, which produces less ^{20}Ne. Both isotopes also share a smaller dependency on the triple-α rate uncertainty, inherited from He-burning, and a small dependence on C-burning rates. These smaller dependencies are also anti-correlated – increases in rates that increase $X_c(^{16}O)$ also decrease $X_c(^{20}Ne)$, and vice versa.

2.6.3.3   Impact of the Measurement Point

The 95% CI width of the $M_{ONe\text{-}Core}$ PDF in Figure 2.13 is partly due to the measurement point. The $M_{ONe\text{-}Core}$ is still growing in mass due to the off-center convective C-burning episodes (See Figure 2.5). This contrasts with H and He where convective core burning accounted for complete mixing of the ash of the nuclear burning.

In more detail, carbon ignites centrally and convectively in these 15 $M_\odot$ models. The extent of the convective core burning reaches $\simeq 0.6\,M_\odot$. Convection retreats as carbon is depleted, and by $X_c(^{12}C) \simeq 10^{-2}$ the entire core is radiative. Subsequently, the first off-center convective C-burning episode occurs when $X_c(^{12}C) \simeq 10^{-4}$ and extends from $\simeq 0.6\,M_\odot$ to $1.2-2.0\,M_\odot$ depending on the amount of C fuel available from core He-burning. It is the variability of the location and extent of the off-center convective C-burning episodes, which occurs *before* the measurement point of $X_c(^{12}C) \lesssim 1 \times 10^{-6}$, that drives the 95% CI spread in the $M_{ONe\text{-}Core}$ PDF.

Figure 2.15 shows the impact of the measurement point on $M_{ONe\text{-}Core}$ as a function of $X_c(^{12}C)$ for six solar grid models. The dashed vertical line shows our measurement point for C-depletion, $X_c(^{12}C) \lesssim 1 \times 10^{-6}$. Given different compositions and thermodynamic trajectories inherited from core He-burning, some models are further along in transforming the CO core to a ONe core. Despite the 95% CI range in the $M_{ONe\text{-}Core}$ PDF, our SROC analysis yields qualitatively similar results. Moreover, two models - the green and gold lines, grow larger ONe cores due to the extent
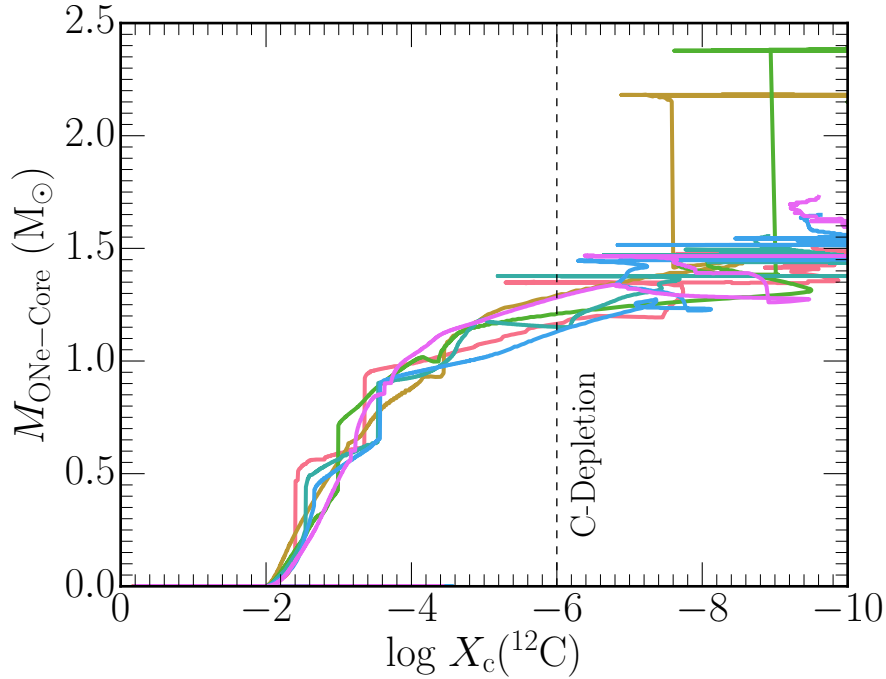
Figure 2.15: Mass of the ONe core as a function of the central ^{12}C mass fraction for six solar grid models. Our adopted measurement point for C-depletion, $X_c(^{12}\text{C}) \lesssim 1 \times 10^{-6}$, is shown by the dashed vertical line. Variation in the mass of the ONe core is driven by the size and extent of off-center convective C-burning episodes.

of convective zone of the final off-center C burning episode mixing the fuel and ash of C-burning outward to a larger mass coordinate than the remaining three models.

2.6.4 Neon Depletion

Core Ne-depletion is the next evolutionary stage considered. We measure the integrated impact of the rate uncertainties at the point when the central neon mass fraction $X_c(^{20}\text{Ne}) \lesssim 1 \times 10^{-3}$. This is a larger mass fraction than the 1×10^{-6} used for H, He and C-depletion. We use a larger depletion value because a growing convective core feeds unburned neon into the core. Ne does not deplete to 1×10^{-6} until well into core O-burning.

2.6.4.1 Probability Distribution Functions

Figure 2.16, shows the PDFs of eight properties of the stellar models at Ne-depletion. We consider the mass of the O core $M_{\text{O-Core}}$, elapsed time between C-depletion and Ne-depletion $\tau_{\text{Ne-burn}}$,

Figure 2.16:]
Same as in Figure 2.13 except we consider $M_{\text{O-Core}}$ - the mass of the O core, $\tau_{\text{Ne-burn}}$ - the elapsed time between C-depletion and Ne-depletion, T_c - the central temperature, ρ_c - the central density, $Y_{e,c}$ - the central electron fraction, $\xi_{2.5}$ - the compactness parameter, $X_c(^{16}\text{O})$ - the central oxygen-16 mass fraction, and $X_c(^{28}\text{Si})$ - the central silicon-28 mass fraction. All quantities are measured at Ne-depletion.

central temperature T_c, central density ρ_c, central electron fraction $Y_{e,c}$, compactness parameter $\xi_{2.5}$, central oxygen-16 mass fraction $X_c(^{16}\text{O})$, and central silicon-28 mass fraction and $X_c(^{28}\text{Si})$.

The $M_{\text{O-Core}}$ PDF shows a strong peak for the solar and subsolar models with zero variation
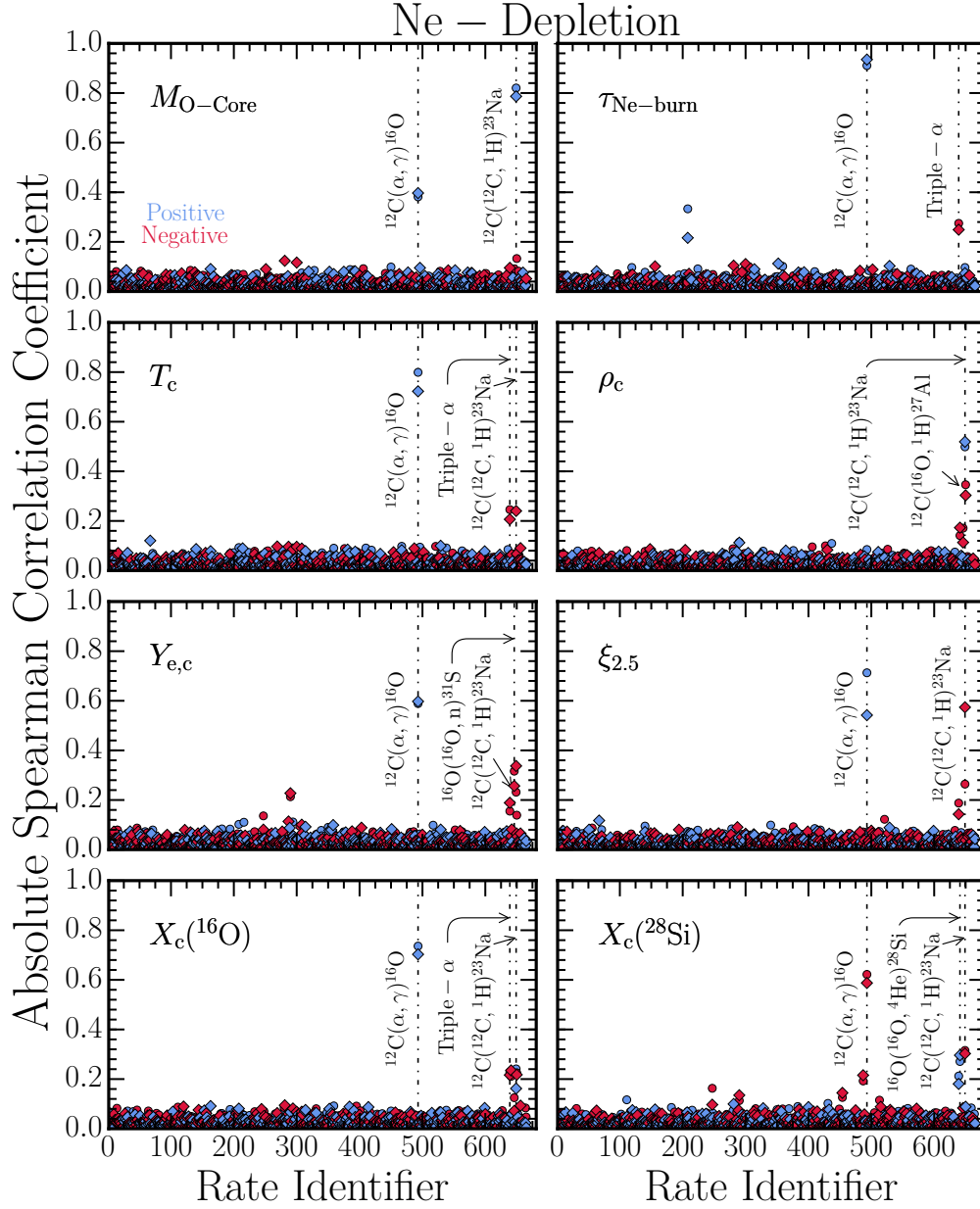
Figure 2.17: Same as in Figure 2.14. The quantities considered are $M_{\text{O-Core}}$ - the mass of the O core, $\tau_{\text{Ne-burn}}$ - the elapsed time between C-depletion and Ne-depletion, T_{c} - the central temperature, ρ_{c} - the central density, $Y_{\text{e,c}}$ - the central electron fraction, $\xi_{2.5}$ - the compactness parameter, $X_{\text{c}}(^{16}\text{O})$ - the central oxygen-16 mass fraction, and $X_{\text{c}}(^{28}\text{Si})$ - the central silicon-28 mass fraction. All quantities are measured at Ne-depletion.

values of $1.44\,M_\odot$ and $1.49\,M_\odot$, respectively. The 95% CI spread is $\simeq \pm 30\%$ for both sets of models. The peaks are offset from zero due to the long tail of positive variations. The $\tau_{\text{Ne-burn}}$ PDFs show 95% CIs of $\simeq \pm 1\%$, commensurate with the $\tau_{\text{C-burn}}$ in Figure 2.13. The 95% CI spread of the solar grid is slightly larger than the spread for the subsolar grid. Both PDFs are symmetric

about zero variations of 10.1 yr and 8.10 yr, respectively.

The T_c distribution has zero variation values of 1.60 GK and 1.63 GK for the solar and subsolar grids, respectively. Both PDFs are symmetric about their zero variation values, and have 95% CI widths of $\simeq \pm 6\%$. The ρ_c PDF has zero variation values of 5.12×10^6 g cm^{-3} and 4.42×10^6 g cm^{-3} for the solar and subsolar gridss, respectively. Both PDFs have 95% CI widths of $\simeq \pm 50\%$. The subsolar model PDF has a slight bimodality with equal peaks of $\simeq 18\%$. The T_c and ρ_c PDFs have 95% spreads that are smaller than the corresponding 95% CI widths for C-depletion.

The $Y_{e,c}$ PDFs for both metallicity grids strongly peak about their means, 0.498 and 0.499 respectively, with a 95% spread of $\lesssim 0.25\%$. This is about the same 95% CI spread as at C-depletion, reflecting that significant neutronization does not occur during Ne-burning. The $\xi_{2.5}$ PDF shows a 95% CI spread of $\simeq \pm 20\%$ without a strong central peak for both metallicity grids.

$X_c(^{16}O)$ follows a broad distribution about the mean with variations of $\simeq (+20\%,-30\%)$. In contrast, $X_c(^{28}Si)$, the other dominant isotope at Ne-depletion, follows a more centrally peaked distribution but with a larger width of $\simeq -120\%$ and a slight, long tail showing variations out to $\simeq +200\%$ of the mean.

2.6.4.2 Spearman Correlation Coefficients

Figure 2.17 shows the SROC correlations for the eight quantities considered in Figure 2.16. Markers and colors are the same as in Figure 2.14.

Ne-depletion inherits most of the reaction rate dependencies from He-depletion and C-depletion. This is consistent with Ne-burning being a photodisintegration rearrangement, whose net reaction is $2(^{20}Ne) \rightarrow {}^{16}O + {}^{24}Mg + 4.6$ Mev. The nucleosynthesis products also resemble those at C-depletion but lack ^{23}Na and has more of the heavier nuclei $^{26,27}Al$, $^{29,30}Si$, and ^{31}P.

The 95% CI spread of $M_{\text{O-Core}}$ is mainly driven by rate uncertainties in $^{12}C(^{12}C,p)^{23}Na$, with $r_s \simeq +0.8$ for both metallicity grids. The $^{12}C(\alpha,\gamma)^{16}O$ rate also affects the O core mass but to a lesser extent, with $r_s \simeq +0.4$. The 95% CI variation of $\tau_{\text{Ne-burn}}$ follows that of the spread of $\tau_{\text{C-burn}}$. It is affected primarily by uncertainties in the $^{12}C(\alpha,\gamma)^{16}O$ rate with smaller dependencies
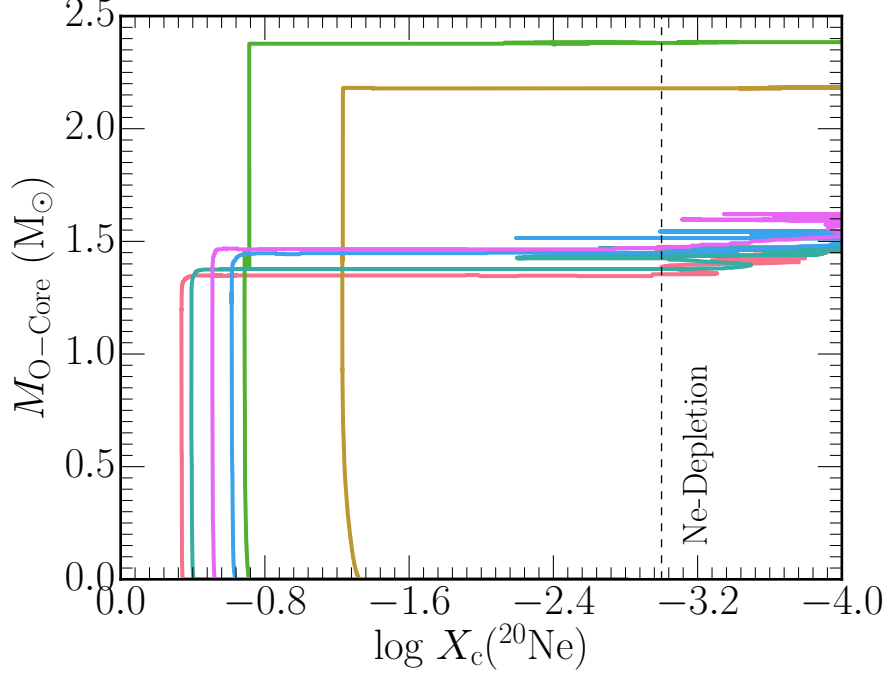
Figure 2.18: Mass of the O core as a function of the central ^{20}Ne mass fraction for the same six solar grid models from Figure 2.15. Our adopted measurement point for Ne-depletion, $X_c(^{20}\text{Ne}) \lesssim 1 \times 10^{-3}$, is shown by the dashed vertical line. Variation in the mass of the O core is driven by the extent of the final off-center C flash prior to Ne-depletion.

on rate uncertainties in ^{14}N$(p, \gamma)^{15}$O (positive SROC) and triple-α (negative SROC). In general, the SROC values are larger for the solar grid.

The T_c PDF depends mostly on the uncertainties in the ^{12}C$(\alpha, \gamma)^{16}$O rate for both solar and subsolar grids. The positive SROC implies that a larger ^{12}C$(\alpha, \gamma)^{16}$O rate yields a hotter stellar core. This is the first occurrence of an inversion of the thermostat mechanism. A small dependency is also found for triple-α and the ^{12}C$(^{12}$C$,p)^{23}$Na rates.

The central density has an SROC value of $r_s \simeq +0.5$ for the ^{12}C$(^{12}$C$,p)^{23}$Na rate. However, ρ_c is also affected by uncertainties in the ^{16}O$(^{16}$O$,p)^{31}$P rate with $r_s \simeq -0.3$. This indicates O-burning is beginning to take place at Ne-depletion. There is also a weaker dependence on the ^{16}O$(^{16}$O$,^4$He$)^{28}$Si rate with a negative SROC.

Uncertainties in the ^{12}C$(\alpha, \gamma)^{16}$O rate drive the variations in $Y_{e,c}$ and $\xi_{2.5}$ with SROC values of $r_s \simeq +0.6$. Smaller SROCs are also found for $Y_{e,c}$ and the 95% CI ^{27}Al$(\alpha, p)^{30}$Si, triple-α, ^{16}O$(^{16}$O$,p)^{31}$P, ^{16}O$(^{16}$O$,n)^{31}$S, and ^{12}C$(^{12}$C$,p)^{23}$Na rates. Similar to ρ_c, the compactness of the

stellar core is weakly affected by the inherited uncertainties from the $^{12}C(^{12}C,p)^{23}Na$ rate.

$X_c(^{16}O)$ inherits a dependence on the $^{12}C(\alpha,\gamma)^{16}O$ rate with $r_s \simeq +0.7$ for both metallicity grids. The $^{12}C + ^{12}C$ and $^{16}O + ^{16}O$ rates have smaller, competing affects on $X_c(^{16}O)$ with $|r_s| \simeq 0.25$. $X_c(^{28}Si)$ is slightly anti-correlated with $X_c(^{16}O)$, with the $^{12}C(\alpha,\gamma)^{16}O$ rate having the largest (negative) SROC. Smaller effects from the uncertainties in the heavy ion, carbon and oxygen channels also play a role in its variation.

2.6.4.3 Impact of the Measurement Point

Some of the quantities measured at Ne-depletion partly inherit their 95% CI spread from the spread at C-depletion. However, the spread of most quantities at Ne-depletion is larger than the 95% CI spreads at C-depletion because of the thermodynamic conditions imposed by the depletion of carbon.

Figure 2.15 shows the extent of the ONe core, measured at C-depletion is sensitive to the extent of the final off-center convective carbon episode. Figure 2.18 shows $M_{O\text{-Core}}$ as a function of the central ^{20}Ne mass fraction for the same six solar grid models as in Figure 2.15. The same two stellar models which yield larger ONe core masses in Figure 2.15, introduce larger 95% CI variations in the O core mass measured at Ne-depletion. The variation in the ONe core mass inherited from C-depletion can cause variations in the other measured quantities. We stress that our analysis measures the integrated impact of the reaction rate uncertainties on the evolution of the stellar model up to the measurement point.

2.6.5 Oxygen Depletion

The last evolutionary point we consider is core O-depletion, defined when $X_c(^{16}O) \lesssim 1 \times 10^{-3}$. We consider eight properties of the stellar model at this epoch: mass of the Si core $M_{Si\text{-Core}}$, time between Ne-depletion and O-depletion $\tau_{O\text{-burn}}$, central temperature T_c, central density ρ_c, central electron fraction $Y_{e,c}$, compactness parameter $\xi_{2.5}$, central silicon-28 mass fraction $X_c(^{28}Si)$, and central sulfur-32 mass fraction $X_c(^{32}S)$.
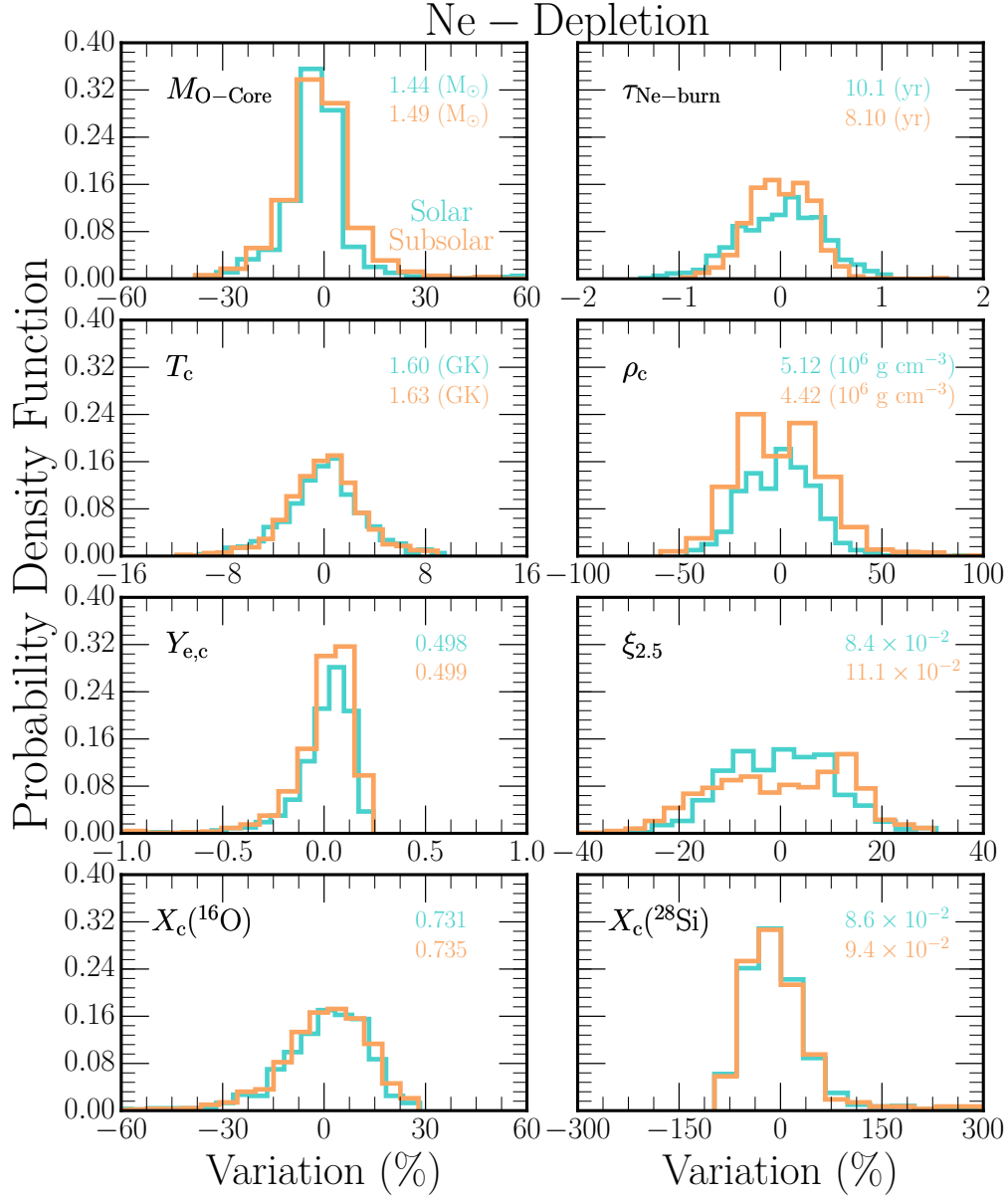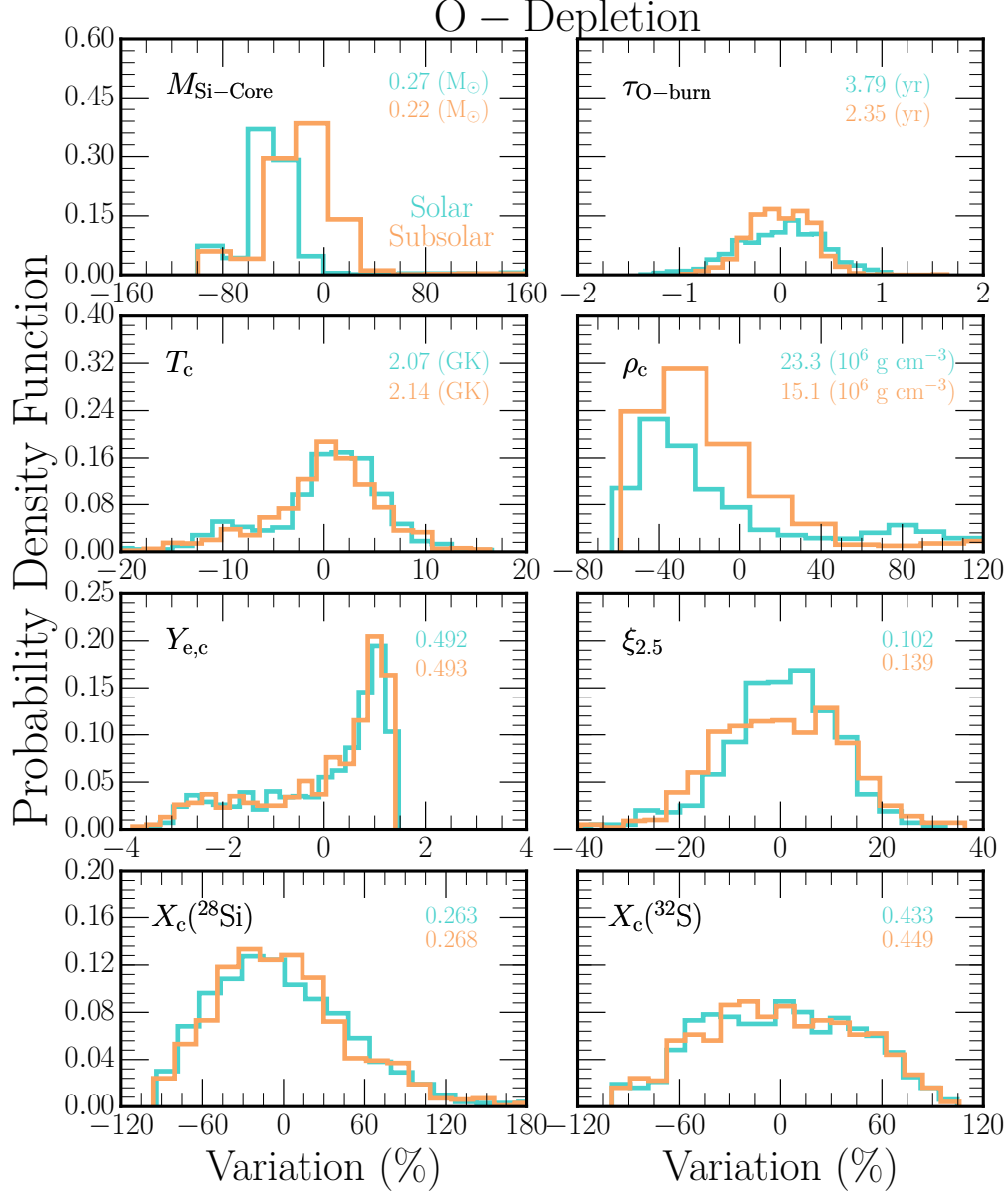
Figure 2.19: Same as in Figure 2.16 except we consider $M_{\text{Si-Core}}$ - the mass of the Si core, $\tau_{\text{O-burn}}$ - the elapsed time between Ne-depletion and O-depletion, T_{c} - the central temperature, ρ_{c} - the central density, $Y_{\text{e,c}}$ - the central electron fraction, $\xi_{2.5}$ - the compactness parameter, $X_{\text{c}}(^{28}\text{Si})$ - the central silicon-28 mass fraction, and $X_{\text{c}}(^{32}\text{S})$ - the central sulfur-32 mass fraction all measured at O-depletion.

2.6.5.1 Probability Distribution Functions

Figure 2.19 shows the variation of these quantities in the same format as for previous depletion epochs. The $M_{\text{Si-Core}}$ PDF for the solar models span $\simeq -120$ to $+400$. Only the range ± 120 is

62

shown in Figure 2.19. The full range, which is taken into account in the analysis, causes the peak to center at $\simeq -30\%$. Despite the wide range, the zero variation values of 0.27 $M_\odot$ for the solar grid and 0.22 $M_\odot$ for the subsolar grid are similar. The 95% CI spreads are ≈ 4 times larger for O-depletion than for Ne-depletion for both the solar and subsolar grids.

The solar and subsolar $\tau_{\text{O-burn}}$ PDFs have zero variation values of 3.79 yr and 2.35 yr, respectively. The 95% CI spreads of $\simeq \pm 1\%$ are consistent with the 95% CI lifetimes of previous epochs. The subsolar model PDF has a slightly larger peak amplitude and smaller range.

The solar and subsolar T_c PDFs have a 95% CI width of $\simeq \pm 10\%$. The negative variation tail causes a $\simeq -20\%$ shift away from the zero variation values of 2.07 GK for the solar models and 2.14 GK for the subsolar models. The ρ_c PDFs have 95% CI spreads of $\simeq \pm 60\%$ with tails out to $\simeq +160\%$ for both metallicities. These tails cause the peak in the PDF to shift away from the arithmetic means of 23.3×10^6 g cm^{-3} for the solar models and 15.1×10^6 g cm^{-3} for the subsolar models. Commensurate with Figure 2.4, the solar models remain cooler and denser than the subsolar models at O-depletion.

At the elevated T_c and ρ_c that occurs during O-depletion, the reactions $^{16}\text{O}(^{16}\text{O},n)^{31}\text{S}$, $^{33}\text{S}(e^-,\nu)^{33}\text{P}$, $^{37}\text{Ar}(e^-,\nu)^{33}\text{Cl}$, and $^{35}\text{Cl}(e^-,\nu)^{35}\text{S}$ decrease $Y_{\text{e,c}}$. This is reflected in the $Y_{\text{e,c}}$ PDF having zero variation values of 0.492 and 0.493 for the solar and subsolar grids, respectively. Peaks in the $Y_{\text{e,c}}$ PDF are shifted from these zero variation because both the solar and subsolar grids have tails of negative variations extending to $\simeq -2\%$.

The $\xi_{2.5}$ PDFs show 95% CI spreads of $\simeq \pm 20\%$ for the solar and subsolar grids. The arithmetic means of $\xi_{2.5} \simeq 0.102$ for the solar grid and $\xi_{2.5} \simeq 0.139$ for the subsolar grid are larger than the arithmetic means at Ne-depletion, but the difference in $\xi_{2.5}$ between the two metallicities are similar. The $X_\text{c}(^{28}\text{Si})$ PDF is log-normal with a peak at $\simeq$ -45% with extrema extending to variations of $\simeq -120\%$ and $\simeq +180\%$. The $X_\text{c}(^{32}\text{S})$ PDF is broad with tails extending to $\simeq \pm 80\%$.

The 95% CI widths of the PDFs for $M_{\text{Si-Core}}$ is driven by the fact that the Si-core is still forming at the measurement point of $X_\text{c}(^{16}\text{O}) \lesssim 1 \times 10^{-3}$. Additional dynamic range is introduced by some models forming heavier isotopes of Si and S, and MESA only considering ^{28}Si in the definition of the

Si-core mass boundary. For example, the central composition at O-depletion for one of the models in Figure 2.15 and 2.18 is $X_c(^{28}Si) \simeq 4.6 \times 10^{-2}$, $X_c(^{30}Si) \simeq 3.5 \times 10^{-1}$, $X_c(^{32}S) \simeq 4.6 \times 10^{-2}$, and $X_c(^{34}S) \simeq 4.4 \times 10^{-1}$. This model reports a very small $M_{Si\text{-}Core}$ because Si is primarily in the neutron rich ^{30}Si. This also accounts for the negative tail in the $Y_{e,c}$ PDF and the dynamic range in ρ_c.

2.6.5.2 Spearman Correlation Coefficients

Figure 2.20 shows the SROC coefficients for the solar and subsolar grid against the eight quantities in Figure 2.19. The format is the same as in previous figures.

The $M_{Si\text{-}Core}$ has a negative correlation of $r_s \simeq -0.25$ with the $^{16}O(^{16}O,\alpha)^{28}Si$ rate and a smaller dependence on the $^{12}C(\alpha,\gamma)^{16}O$ rate. Reaction rates whose uncertainty most impacts $\tau_{O\text{-}burn}$ are inherited from previous stages, namely $^{12}C(\alpha,\gamma)^{16}O$, $^{14}N(p,\gamma)^{15}O$, and triple-α.

T_c has a negative correlation with the $^{16}O(^{16}O,n)^{31}S$ rate for the solar and subsolar grid. ρ_c inherits its dependence on the $^{12}C(\alpha,\gamma)^{16}O$ rate with $r_s \simeq -0.45$. The other $^{16}O + ^{16}O$ exit channels have smaller effects on T_c and ρ_c. The $^{16}O(^{16}O,n)^{31}S$ rate dominate the SROCs for $Y_{e,c}$ with $r_s \simeq -0.6$ for both grids. $\xi_{2.5}$ inherits dependencies on the $^{12}C(\alpha,\gamma)^{16}O$ and $^{12}C(^{12}C,p)^{23}Na$ rates. The mass fractions $X_c(^{28}Si)$ and $X_c(^{32}S)$ are chiefly the result of the competition between the $^{16}O(^{16}O,\alpha)^{28}Si$ and $^{28}Si(\alpha,\gamma)^{32}S$ rates.

Table 2.1 summarizes the properties of the PDFs and the SROC analysis at O-depletion, along with the results for previous depletion points of the major fuels.
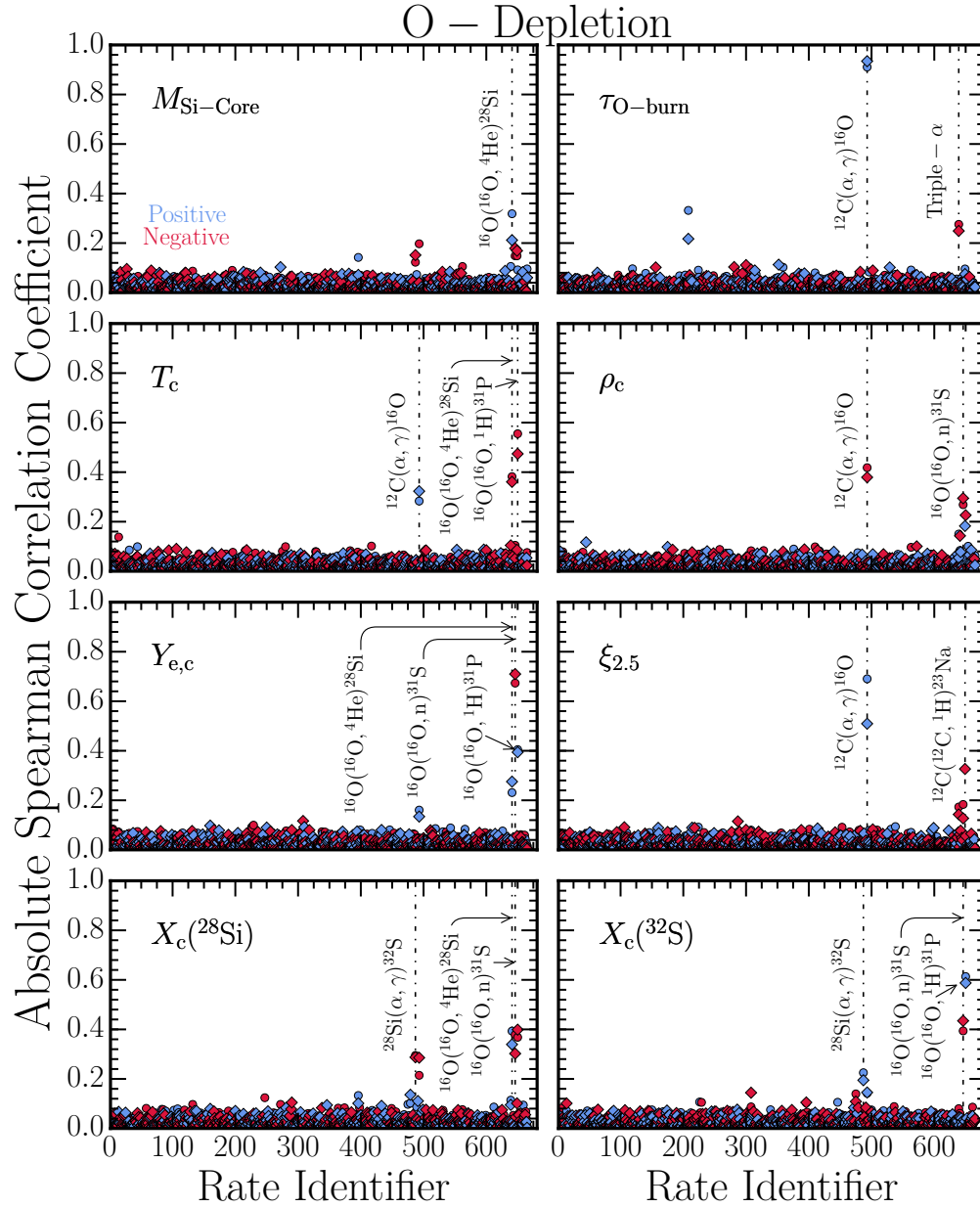
Figure 2.20: Same as in Figure 2.17. The quantities considered are $M_{\text{Si-Core}}$ - the mass of the Si core, $\tau_{\text{O-burn}}$ - the elapsed time between Ne-depletion and O-depletion, T_{c} - the central temperature, ρ_{c} - the central density, $Y_{\text{e,c}}$ - the central electron fraction, $\xi_{2.5}$ - the compactness parameter, $X_{\text{c}}(^{28}\text{Si})$ - the central silicon-28 mass fraction, and $X_{\text{c}}(^{32}\text{S})$ - the central sulfur-32 mass fraction. All quantities are measured at O-depletion.

Properties of 15 M$_\odot$ Solar and Subsolar Monte Carlo Stellar Models

Property	Solar			Subsolar			95% CI Limits of Variation (%)
	Values	Key Reaction	r_s	Values	Key Reaction	r_s	
				H-Depletion			
$M_{\text{He-Core}}(\text{M}_\odot)$	$2.802^{2.806}_{2.799}$	$^{14}\text{N}(p,\gamma)^{15}\text{O}$	+0.35	$2.86^{2.863}_{2.857}$	$\cdots$	+0.33	(+0.13, -0.12) (+0.12,-0.12)
τ_{TAMS} (Myr)	$11.27^{11.29}_{11.249}$	$^{14}\text{N}(p,\gamma)^{15}\text{O}$	+1.0	$11.769^{11.78}_{11.759}$	$\cdots$	+1.0	(+0.18,-0.19) (+0.09,-0.09)
T_c (10^8 K)	$0.628^{0.635}_{0.621}$	$^{14}\text{N}(p,\gamma)^{15}\text{O}$	-0.99	$0.807^{0.816}_{0.799}$	$\cdots$	-0.99	(+1.19,-1.12) (+1.07,-1.11)
ρ_c (g cm^{-3})	$42.402^{43.917}_{40.978}$	$^{14}\text{N}(p,\gamma)^{15}\text{O}$	-0.97	$88.198^{91.241}_{85.122}$	$\cdots$	-0.98	(+3.57,-3.36) (+3.45,-3.49)
$\xi_{2.5}$	$0.007^{0.007}_{0.007}$	$^{14}\text{N}(p,\gamma)^{15}\text{O}$	-0.99	$0.008^{0.009}_{0.008}$	$\cdots$	-0.99	(+1.19,-1.14) (+1.09,-1.13)
$X_c(^{14}\text{N}) \times 10^3$	$9.234^{9.317}_{9.128}$	$^{15}\text{N}(p,\gamma)^{16}\text{O}$	-0.56	$0.194^{0.195}_{0.192}$	$^{14}\text{N}(p,\gamma)^{15}\text{O}$	-0.66	(+0.89,-1.15) (+0.83,-1.08)
				He-Depletion			
$M_{\text{CO-Core}}$ (M$_\odot$)	$2.414^{2.522}_{2.347}$	$^{12}\text{C}(\alpha,\gamma)^{16}\text{O}$	+0.79	$2.952^{3.062}_{2.909}$	$\cdots$	+0.84	(+1.94,-3.10) (+1.53,-2.44)
$\tau_{\text{He-burn}}$ (Myr)	$1.594^{1.696}_{1.479}$	$^{12}\text{C}(\alpha,\gamma)^{16}\text{O}$	+0.92	$1.315^{1.393}_{1.234}$	$\cdots$	+0.94	(+0.81,-0.90) (+0.58,-0.63)
T_c (10^8 K)	$3.126^{3.185}_{3.092}$	Triple-α	-0.80	$3.207^{3.26}_{3.171}$	$\cdots$	-0.77	(+1.89,-1.07) (+1.67,-1.11)
ρ_c (10^3 g cm^{-3})	$5.535^{5.756}_{5.364}$	Triple-α	-0.69	$5.053^{5.265}_{4.892}$	$\cdots$	-0.67	(+3.99,-3.08) (+4.19,-3.20)
$X_c(^{22}\text{Ne}) \times 10^2$	$1.081^{1.217}_{0.887}$	$^{22}\text{Ne}(\alpha,\gamma)^{26}\text{Mg}$	-0.70	$0.021^{0.024}_{0.017}$	$\cdots$	-0.64	(+12.6,-17.9) (+15.5,-21.5)
$\xi_{2.5}$	$0.031^{0.031}_{0.03}$	Triple-α	-0.83	$0.031^{0.032}_{0.031}$	$\cdots$	-0.74	(+1.56,-0.97) (+1.41,-1.06)
$X_c(^{12}\text{C})$	$0.260^{0.467}_{0.077}$	$^{12}\text{C}(\alpha,\gamma)^{16}\text{O}$	-0.95	$0.265^{0.459}_{0.082}$	$\cdots$	-0.95	(+79.9,-70.2) (+73.1,-69.1)
$X_c(^{16}\text{O})$	$0.716^{0.896}_{0.512}$	$^{12}\text{C}(\alpha,\gamma)^{16}\text{O}$	+0.95	$0.731^{0.910}_{0.538}$	$\cdots$	+0.95	(+25.1,-28.5) (+24.5,-26.3)

		C-Depletion					
$M_{\text{ONe-Core}}$ (M$_\odot$)	$1.110^{1.365}_{0.550}$	$^{12}\text{C}(^{12}\text{C},p)^{23}\text{Na}$	+0.58	$1.175^{1.444}_{0.575}$	...	+0.53	(+22.9,-50.5) (+22.9,-51.1)
$\tau_{\text{C-burn}}$ (kyr)	$30.74^{41.87}_{26.51}$	$^{12}\text{C}(\alpha,\gamma)^{16}\text{O}$	+0.91	$23.75^{32.95}_{21.00}$	...	+0.94	(+0.78,-0.86) (+0.56,-0.62)
T_c (GK)	$1.158^{1.412}_{1.025}$	$^{12}\text{C}(^{16}\text{O},p)^{27}\text{Al}$	-0.45	$1.196^{1.598}_{1.034}$	$^{12}\text{C}(^{12}\text{C},p)^{23}\text{Na}$	-0.50	(+21.9,-11.5) (+33.6,-13.6)
ρ_c (10^6 g cm^{-3})	$5.317^{8.815}_{2.711}$	$^{12}\text{C}(^{16}\text{O},p)^{27}\text{Al}$	-0.43	$4.371^{7.285}_{1.978}$	...	-0.43	(+65.8,-49.0) (+66.7,-54.8)
$Y_{e,c}$	$0.498^{0.499}_{0.497}$	$^{12}\text{C}(\alpha,\gamma)^{16}\text{O}$	+0.72	$0.498^{0.500}_{0.497}$	...	+0.71	(+0.15,-0.35) (+0.15,-0.37)
$\xi_{2.5}$	$0.083^{0.095}_{0.069}$	$^{12}\text{C}(\alpha,\gamma)^{16}\text{O}$	+0.49	$0.109^{0.129}_{0.088}$	$^{12}\text{C}(^{12}\text{C},p)^{23}\text{Na}$	-0.54	(+14.28,-16.6) (+17.9,-19.4)
$X_c(^{16}\text{O})$	$0.622^{0.861}_{0.373}$	$^{12}\text{C}(\alpha,\gamma)^{16}\text{O}$	+0.91	$0.625^{0.869}_{0.369}$	...	+0.88	(+38.4,-40.0) (+38.9,-41.0)
$X_c(^{20}\text{Ne})$	$0.266^{0.459}_{0.072}$	$^{12}\text{C}(\alpha,\gamma)^{16}\text{O}$	-0.79	$0.280^{0.474}_{0.043}$	...	-0.75	(+72.4,-73.0) (+69.1,-84.5)
		Ne-Depletion					
$M_{\text{O-Core}}$ (M$_\odot$)	$1.439^{2.368}_{1.113}$	$^{12}\text{C}(^{12}\text{C},p)^{23}\text{Na}$	+0.82	$1.493^{1.965}_{1.157}$	...	+0.79	(+64.5,-22.7) (+31.6,-22.5)
$\tau_{\text{Ne-burn}}$ (yr)	$10.114^{44.452}_{0.493}$	$^{12}\text{C}(\alpha,\gamma)^{16}\text{O}$	+0.91	$8.103^{37.39}_{0.143}$	...	+0.94	(+0.78,-0.86) (+0.56,-0.62)
T_c (GK)	$1.603^{1.702}_{1.501}$	$^{12}\text{C}(\alpha,\gamma)^{16}\text{O}$	+0.80	$1.626^{1.727}_{1.520}$	...	+0.72	(+6.15,-6.40) (+6.21,-6.52)
ρ_c (10^6 g cm^{-3})	$5.119^{6.986}_{3.485}$	$^{12}\text{C}(^{12}\text{C},p)^{23}\text{Na}$	+0.50	$4.422^{6.322}_{2.770}$	...	+0.52	(+36.5,-31.9) (+43.0,-37.4)
$Y_{e,c}$	$0.498^{0.499}_{0.496}$	$^{12}\text{C}(\alpha,\gamma)^{16}\text{O}$	+0.59	$0.499^{0.500}_{0.497}$	...	+0.60	(+0.19,-0.41) (+0.19,-0.41)
$\xi_{2.5}$	$0.084^{0.101}_{0.068}$	$^{12}\text{C}(\alpha,\gamma)^{16}\text{O}$	+0.71	$0.111^{0.136}_{0.084}$	$^{12}\text{C}(^{12}\text{C},p)^{23}\text{Na}$	-0.57	(+20.2,-19.3) (+22.5,-24.4)
$X_c(^{16}\text{O})$	$0.731^{0.888}_{0.503}$	$^{12}\text{C}(\alpha,\gamma)^{16}\text{O}$	+0.74	$0.735^{0.893}_{0.501}$	...	+0.70	(+21.4,-31.2) (+21.4,-31.8)
$X_c(^{28}\text{Si})$	$0.086^{0.240}_{0.021}$	$^{12}\text{C}(\alpha,\gamma)^{16}\text{O}$	-0.62	$0.094^{0.296}_{0.018}$	...	-0.59	(+179,-75.2) (+216,-81.1)

		O-Depletion					
$M_{\text{Si-Core}}$ (M$_\odot$)	$0.270^{0.979}_{0.012}$	^{16}O(^{16}O,α)^{28}Si	+0.32	$0.219^{0.965}_{0.013}$	$\ldots$	+0.21	(+262,-95.7) (+341,-94.2)
$\tau_{\text{O-burn}}$ (yr)	$3.786^{7.574}_{1.554}$	^{12}C(α,γ)^{16}O	+0.91	$2.348^{5.546}_{0.857}$	$\ldots$	+0.93	(+0.76,-0.88) (+0.52,-0.61)
T_{c} (GK)	$2.073^{2.278}_{1.793}$	^{16}O(^{16}O,p)^{31}P	-0.56	$2.141^{2.350}_{1.860}$	$\ldots$	-0.47	(+9.92,-13.5) (+9.77,-13.2)
ρ_{c} (10^6 g cm^{-3})	$23.34^{54.06}_{10.32}$	^{12}C(α,γ)^{16}O	-0.42	$15.10^{43.06}_{7.140}$	$\ldots$	-0.38	(+132,-55.8) (+185,-52.7)
$Y_{\text{e,c}}$	$0.492^{0.498}_{0.479}$	^{16}O(^{16}O,n)^{31}S	-0.67	$0.493^{0.499}_{0.479}$	$\ldots$	-0.71	(+1.18,-2.74) (+1.18,-2.88)
$\xi_{2.5}$	$0.102^{0.122}_{0.075}$	^{12}C(α,γ)^{16}O	+0.69	$0.139^{0.174}_{0.106}$	$\ldots$	+0.51	(+19.9,-27.0) (+24.98,-23.6)
X_{c}(^{28}Si)	$0.263^{0.526}_{0.106}$	^{16}O(^{16}O,α)^{28}Si	+0.39	$0.268^{0.544}_{0.111}$	^{16}O(^{16}O,p)^{31}P	-0.40	(+99.7,-59.8) (+103,-58.6)
X_{c}(^{32}S)	$0.433^{0.736}_{0.058}$	^{16}O(^{16}O,p)^{31}P	+0.61	$0.449^{0.778}_{0.067}$	$\ldots$	+0.59	(+70.1,-86.7) (+73.1,-85.1)

Table 2.1: Properties of the 15 $M_\odot$ solar and subsolar stellar models at five different epochs. The values given are arithmetic means, with upper and lower limits from the 95% CI. Also listed are the min. or max. SROC coefficient values and the corresponding key nuclear reaction. The last column are the limits of the 95% CI for the variations for the solar (left) and subsolar (right) stellar models. Ellipses indicate the variation of a given quantity for the subsolar models is dominated by the same key reaction as the solar models.
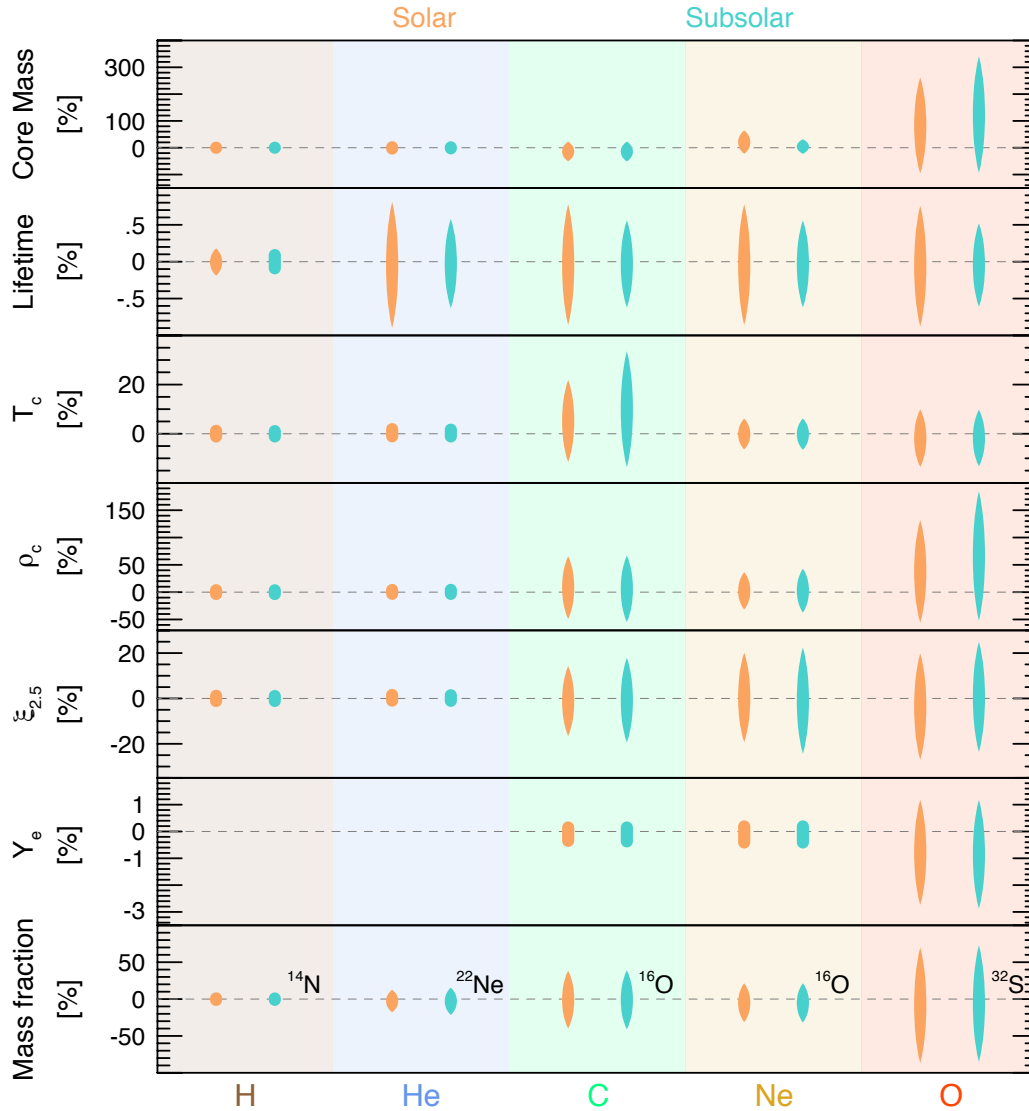
Figure 2.21: Percent variations of the core mass, lifetime, central temperature, central density, compactness parameter, electron fraction, and a chosen "interesting" mass fraction (top to bottom) at H-, He-, C-, Ne-, and O-depletion (left to right). The vertical length of each tapered uncertainty band is the 95% CI for variations about the mean arithmetic value, listed in the last column of Table 2.1, and the horizontal width of each tapered uncertainty band schematically represents the underlying PDF. Solar metallicity models are shown by the orange bands and subsolar metallicity models by the green bands. The first occurrence of significant variation in the compactness parameter $\xi_{2.5}$ occurs at C-depletion. For the mass fractions, we choose to show $X_c(^{14}N)$ at H-depletion as it holds the star's initial CNO abundances, $X_c(^{22}Ne)$ at He-depletion as it holds the neutronization of the core, $X_c(^{16}O)$ at C- and Ne-depletion as it is dominant nucleosynthesis product of massive stars, and $X_c(^{32}S)$ at O-depletion as it is a key component of the ashes of O-burning.

69

2.7 Discussion

Figure 2.21 shows the 95% CI variations listed in Table 2.1 for seven properties across five evolutionary epochs for the solar and subsolar grids. Across these properties, the magnitude of the 95% CI spreads generally grow with each successive stage of evolution. The variations grow for two reasons. One, each evolutionary stage inherits variations from the previous evolutionary stage because we measure the integrated impact of the uncertainties in the reaction rates. Two, each stage imprints its own contributions to the variations due to the uncertainties in the specific reaction rates that impact that stage. Finally, there is a trend for the 95% CI variations of the subsolar models to be smaller than the variations of the solar models, particularly for measurements at H-, He- and C-depletion.

We next discuss the reaction rates identified in Table 2.1 which have the largest impact on the variations of the core mass, burning lifetime, composition, and structural properties.

2.7.1 Key Reaction Rates

At H-depletion, Table 2.1 shows the uncertainties from the ^{14}N$(p, \gamma)^{15}$O reaction rate cause 95% CI variations of $\approx \pm 0.1\%$ in $M_{\text{He-Core}}$, $\approx \pm 0.2\%$ in τ_{TAMS}, $\approx \pm 1\%$ in T_{c}, $\approx \pm 3\%$ in ρ_{c}, $\approx \pm 1\%$ in $\xi_{2.5}$, and $\approx \pm 1\%$ in $X_{\text{c}}(^{14}$N$)$ for both solar and subsolar models. The ^{14}N$(p, \gamma)^{15}$O reaction rate is the slowest step in the CNO cycle and thus determines the rate at which H is depleted in the core (e.g., Iliadis, 2007). STARLIB currently adopts the reaction rate of Imbriani et al. (2005).

The lowest positive-energy resonance of ^{14}N$(p, \gamma)^{15}$O is located at a center-of-mass energy of 259 keV, too high in energy to strongly influence quiescent stellar burning (e.g., LUNA Collaboration et al., 2006b). However, the strength of this resonance is often used as a cross-section normalization for lower-energy measurements. Daigle et al. (2016) report measurements of the energy, strength, and γ-ray branching ratios for the 259 keV resonance. Their recommended strength of $\omega\gamma = 12.6$ MeV is in agreement with the previous value but more precise, and offers a more reliable normalization. Using this result, they suggest the *S*-factor data of Imbriani et al. (2005) should be

reduced by 2.3%. For this reduction of the S-factor, in our stellar models at H-depletion the largest variation is $\approx +0.2\%$ with respect to the mean for ρ_c. Other properties have variations $\lesssim 0.1\%$.

STARLIB currently adopts the triple-α reaction rate of Angulo (1999). Uncertainties in this reaction rate dominate the 95% CI variations of $\approx \pm 1.5\%$ in T_c, $\approx \pm 3.5\%$ in ρ_c, and $\approx \pm 3.5\%$ in $\xi_{2.5}$, during core He-burning. Nguyen et al. (2012) combine Faddeev hyperspherical harmonics and the R-matrix method to suggest the triple-α reaction rate is significantly enhanced at temperatures below 0.06 GK. For an increased reaction rate in this temperature range, our analysis suggest T_c and ρ_c will decrease by $\approx 2\%$ in our MESA models.

STARLIB currently adopts the Kunz et al. (2002) reaction rate for ^{12}C$(\alpha, \gamma)^{16}$O. Experimental uncertainties in this reaction rate dominate the 95% CI variations of $\approx 2.5\%$ in $M_{\text{CO-Core}}$, $\approx \pm 1\%$ in $\tau_{\text{He-burn}}$, $\approx +80/-70\%$ in $X_c(^{12}$C$)$, and $\approx +25/-27\%$ in $X_c(^{16}$O$)$ during core He-burning. Core C-, Ne-, and even O-burning inherit some of these dependencies. deBoer et al. (2017) use the R-matrix method to derive a new ^{12}C$(\alpha, \gamma)^{16}$O rate. The uncertainties in the deBoer et al. (2017) rate are smaller than the uncertainties in the Kunz et al. (2002) rate near temperatures of $0.05 \lesssim T \lesssim 1$ GK and slightly larger near $T \simeq 1 - 3$ GK. deBoer et al. (2017) show their rate can lead to changes of $\simeq \pm 1.5\%$ for $M_{\text{CO-Core}}$ in their 15 $M_\odot$ solar metallicity MESA models. This is slightly smaller than our 95% CI spread.

STARLIB adopts the ^{12}C $+^{12}$C, ^{12}C $+^{16}$O, and ^{16}O $+^{16}$O rates and branching ratios of Caughlan & Fowler (1988). Uncertainties in these reaction rates and branching ration dominate the 95% CI variations of $\approx +23/-50\%$ in $M_{\text{ONe-Core}}$ at C-depletion and $\approx +40/-35\%$ in ρ_c at Ne-depletion.

The ^{12}C $+^{12}$C is one of the most studied heavy ion reactions. Despite several decades of dedicated experimental efforts, the low-energy reaction rate still carries considerable uncertainties due to pronounced resonance structures that are thought to be associated with molecular configurations of carbon in the ^{24}Mg excited state (e.g., Mişicu & Esbensen, 2007) However, it has been argued that low-energy cross section of fusion reactions declines faster with decreasing energy than projected by common potential models (Jiang et al., 2007a; Gasques et al., 2007; Carnelli et al., 2014).

The impact of changes in the ^{12}C $+^{12}$C in 1D Geneva stellar evolution (GENEC) models are

investigated in Bennett et al. (2012) and Pignatari et al. (2013). They find that an increase in the $^{12}\text{C}+^{12}\text{C}$ reaction rate causes core C-burning ignition at lower temperature. This reduces the thermal neutrino losses, which in turn increases the core C-burning lifetime. They also find an increased $^{12}\text{C}+^{12}\text{C}$ rate increases the upper initial mass limit for when a star undergoes convective C-burning rather than radiative C-burning (Lamb et al., 1976; Woosley & Weaver, 1986; Petermann et al., 2017). The subsequent evolution of these more massive stars may yield a bimodal distribution of compact objects (Timmes et al., 1996; Zhang et al., 2008; Petermann et al., 2017).

Fang et al. (2017) use a high-intensity oxygen beam impinging upon an ultrapure graphite target to make new measurements of the total cross section and branching ratios for the $^{12}\text{C}+^{16}\text{O}$ reaction. They find a new broad resonance-like structure and a decreasing trend in the S-factor data towards lower energies, in contrast to previous measurements. For massive stars, they conclude the impact of the new rate $^{12}\text{C}+^{16}\text{O}$ rate might be small for core and shell burning (also see Jiang et al., 2007b), although the impact might be enhanced by multidimensional turbulence (Cristini et al., 2017) or rotation (Chatzopoulos et al., 2016a) of the pre-supernova star during the last phases of its stellar life.

Of the key nuclear reaction rates identified in this study, those with the largest uncertainty over the temperature ranges consider here are heavy ion $^{12}\text{C}+^{12}\text{C}$, $^{12}\text{C}+^{16}\text{O}$, and $^{16}\text{O}+^{16}\text{O}$ reactions. Due to the larger Coulomb barrier for the $^{12}\text{C}+^{16}\text{O}$ reaction it is expected to be less efficient during carbon burning. Our results suggest that variation in this rate, especially the p exit channel, can lead to non-negligible variations in core temperature and density during carbon burning. Our results suggest that for a decrease in the uncertainty in these heavy ion reactions rates over stellar temperatures, along with the $^{12}\text{C}(\alpha,\gamma)^{16}\text{O}$ reaction, we can expect a *decrease* in variation of stellar model properties of below the level of variations induced by uncertainties due to stellar winds, convective boundary mixing, and mass/network resolution.

2.7.2 Assessing The Overall Impact

Paper F16 applies the Monte Carlo framework to stellar models that form CO white dwarfs. They evolve 3 $M_\odot$ solar metallicity models from the pre-MS to the first thermal pulse. They sample 26 out of 405 nuclear reactions and consider one evolutionary epoch − the first thermal pulse, a time shortly after core He-depletion. Comparing our Figure 2.11 with their Figure 11, we find similar results despite the different masses. The $^{12}C(\alpha, \gamma)^{16}O$ dominates the mass of the CO core, The ^{12}C, and ^{16}O mass fractions at He-depletion (their first thermal pulse) have similar sign and magnitude SROC coefficients. In agreement with their CO white dwarf models, variations in the central temperature are driven by uncertainties in the triple-α reaction rate. They report that the central density is primarily correlated with uncertainties in the $^{12}C(\alpha, \gamma)^{16}O$ rate, while we find the variations in the central density are chiefly correlated with uncertainties in the triple-α rate. This difference is due to the masses considered. The hotter, less dense, cores of our 15 $M_\odot$ models favor the triple-α rate as the primarily source of the central density variations, whereas the cooler, more dense 3 $M_\odot$ models favor $^{12}C(\alpha, \gamma)^{16}O$.

Farmer et al. (2016) explore uncertainties in the structure of massive star stellar models with respect to mass resolution, mass loss, and the number of isotopes in the nuclear reaction network. Farmer et al. (2016) and this paper both report results for 15 $M_\odot$, $\dot{M} \neq 0$, 127 isotope, solar metallicity, `MESA` r7624 models. The primary difference between this paper and Farmer et al. (2016) is the use of STARLIB reaction rates.

Our results at H-depletion can be compared with their results at He-ignition. For example, Table 2.1 shows our mean He core mass is $M_{\text{He-Core}} = 2.80\,M_\odot$ while their median He core mass is $\text{He}_{core} = 2.77\,M_\odot$, a difference of $< 1\%$. Our 95% CI for $M_{\text{He-Core}}$ is within 1% of their He_{core} upper and lower limits. As another example, our mean H burning lifetime is $\tau_{\text{TAMS}} = 11.27\,\text{Myr}$ and their median H burning lifetime is $\tau_{\text{H}} = 10.99\,\text{Myr}$, a difference of $\simeq 3\%$. In addition, our 95% CI for τ_{TAMS} is $\simeq 2\%$ larger than their upper and lower bounds for τ_{H}.

Our He-depletion results can also be compared to their results at C-ignition. We find a mean $M_{\text{C-Core}} = 2.41\,M_\odot$ while their median $\text{C}_{core} = 2.44\,M_\odot$, a difference of $< 1\%$. Our 95% CI spread

due to uncertainties in the nuclear reaction rates is $\simeq (+1.9\%, -3.1\%)$ while their upper and lower bounds suggest variations of $\simeq (+3.7\%, -0.4\%)$ due to changes in mass and network resolution. In addition, our mean $\tau_{He\text{-}burn} = 1.594$ Myr and their median $\tau_{He} = 1.74$ Myr, a difference of $\simeq 8\%$. Our 95% CI for $\tau_{He\text{-}burn}$ is $\simeq (+1.9\%, -3.1\%)$ while their upper and lower bounds are $\simeq (+1.2\%, -12.1\%)$.

Comparing our Ne-depletion results with their O-ignition results, we find a mean $M_{O\text{-}Core} = 1.44\,M_{\odot}$ while their median $O_{core} = 1.40\,M_{\odot}$, a difference of $\lesssim 1\%$. Our 95% CI spread due to uncertainties in the nuclear reaction rates is $\simeq (+65\%, -23\%)$ while their upper and lower bounds suggest variations of $\simeq (+0.1\%, -5.6\%)$ due to changes in mass and network resolution. In addition, our mean $\tau_{C\text{-}burn} = 30.74$ kyr and their median $\tau_C = 85.55$ yr differs by approximately three orders of magnitude. This large difference is due to the exact measurement points. In this work, we assumed the time to be the difference between the age of the star at C-depletion and He-depletion. This does not necessarily correspond to the exact burning lifetime for C as the star undergoes reconfiguration after He-depletion for a few thousand years before conditions for C-burning are met. In Farmer et al. (2016) they measure the time to transition to the next major fuel source. Our 95%CI for $\tau_{C\text{-}burn}$ is $\simeq (+1.9\%, -3.1\%)$ while their upper and lower bounds are $\simeq (+1.2\%, -12.1\%)$.

Variations in properties of stellar evolution models can be found to be caused by other sources of uncertainty beyond those discussed above. Renzo et al. (2017) considered uncertainties in the mass loss prescriptions and efficiencies used in solar-metallicity, non-rotating, single stars. They find that changes in these parameters can lead to a spread of $\Delta M_{CO} \approx 0.28\,M_{\odot}$ in CO core masses measured at O-depletion, though defined differently in their work as the moment when $X_c(^{16}O) \lesssim 0.04$. This spread represents a variation of about $\pm 5\%$ variation about the arithmetic mean. The treatment of mixing at the convective boundaries can also have a significant effect on the evolution of massive stellar models. Davis et al. (2017) show that for their $25\,M_{\odot}$ model at Ne-ignition, they find a variation of $+5\%$ in the ONe core mass due to changes in the efficiency of convective boundary mixing at metal burning interfaces.

Farmer et al. (2016) find that mass resolution has a larger impact on the variations than the

number of isotopes up to and including C burning, while the number of isotopes plays a more significant role in determining the span of the variations for Ne-, O-, and Si-burning. Comparisons of the core masses and burning lifetimes suggests that at H- and He-depletion, the variations induced by uncertainties in nuclear reaction rates are of comparable magnitude to the variations induced by the modeling choices of mass resolution and network resolution. At Ne-depletion the integrated impact of the uncertainties in the reaction rates appear to be larger than the variations caused by mass and network resolution.

The scale of variations due to different mass loss prescriptions and efficiencies were found to be of comparable scale to those due to reaction rate uncertainties at early epochs such as H- and He-depletion for the stellar properties considered. At early epochs, convective boundary mixing is likely to cause significant variations in core masses and lifetimes that are of larger scale than those due to nuclear reaction rate uncertainties. However, uncertainties in convective boundary mixing are likely to be smaller than the integrated impact of rate uncertainties at advanced burning stages.

2.8   Summary

We investigated properties of pre-supernova massive stars with respect to the composite uncertainties in the thermonuclear reaction rates by coupling the reaction rate PDFs provided by the STARLIB reaction rate library with MESA stellar models. We evolved 1000 15 $M_\odot$ models with solar and subsolar initial compositions from the pre main-sequence to core oxygen depletion for a total of 2000 Monte Carlo stellar models. For each stellar model we sampled 665 forward thermonuclear reaction rates concurrently, and used them in an in-situ 127 isotope MESA reaction network. With this infrastructure we surveyed the core mass, burning lifetime, central temperature, central density, compactness parameter, and key abundances at H-, He-, C-, Ne-, and O-depletion.

At each stage, we measured the PDFs of the variations of each property and calculated SROC coefficients for each sampled reaction rate. This allowed identification of the reaction rates that have the largest impact on the variations of the properties surveyed. Table 2.1 summarizes the stellar properties, the reaction rates causing their variation, and the largest correlation coefficient

75

(positive or negative) for that reaction rate.

In general, variations induced by nuclear reaction rates grow with each passing phase of evolution. Relative to variations induced by mass resolution and the number of isotopes in the nuclear reaction network, we found that variations induced by uncertainties in nuclear reaction rates at core H- and He-depletion are of comparable magnitude to the variations induced by the modeling choices of mass resolution and network resolution. Beyond these evolutionary epochs, our models suggest that the reaction rate uncertainties can dominate the variation in properties of the stellar model significantly altering the evolution towards iron core-collapse.

<div align="center">

CHAPTER 3

ON THE DEVELOPMENT OF MULTIDIMENSIONAL PROGENITOR MODELS FOR CORE-COLLAPSE SUPERNOVAE

</div>

If you don't know where you are going, any road will get you there. - Lewis Carrol

This chapter is based on the published work of C. E. Fields and Sean M. Couch 2020 *ApJ* **901** 33.

3.1   Abstract

Multidimensional hydrodynamic simulations of shell convection in massive stars suggest the development of aspherical perturbations that may be amplified during iron core-collapse. These perturbations have a crucial and qualitative impact on the delayed neutrino-driven core-collapse supernova explosion mechanism by increasing the total stress behind the stalled shock. In this paper, we investigate the properties of a 15 $M_\odot$ model evolved in 1-,2-, and 3-dimensions (3D) for the final ∼424 seconds before gravitational instability and iron core-collapse using `MESA` and the `FLASH` simulation framework. We find that just before collapse, our initially perturbed fully 3D model reaches angle-averaged convective velocity magnitudes of $\approx$ 240-260 km s^{-1} in the Si- and O-shell regions with a Mach number ≈ 0.06. We find the bulk of the power in the O-shell resides at large scales, characterized by spherical harmonic orders (ℓ) of 2-4, while the Si-shell shows broad spectra on smaller scales of $\ell \approx 30 - 40$. Both convective regions show an increase in power at $\ell = 5$ near collapse. We show that the 1D `MESA` model agrees with the convective velocity profile and speeds of the Si-shell when compared to our highest resolution 3D model. However, in the O-shell region, we find that `MESA` predicts speeds approximately *four* times slower than all of our 3D models suggest. All eight of the multi-dimensional stellar models considered in this work are publicly available.

3.2 Introduction

Stars with an initial zero age main-sequence (ZAMS) mass of greater than approximately 8-10 $M_\odot$ may end their lives via core-collapse supernova (CCSN) explosions (Janka, 2012; Farmer et al., 2015; Woosley & Heger, 2015; Woosley et al., 2002). Core-collapse supernova explosions facilitate the evolution of chemical elements throughout galaxies (Timmes et al., 1995; Pignatari et al., 2016; Côté et al., 2017), produce stellar mass compact object systems (Özel et al., 2012; Sukhbold et al., 2016; Couch et al., 2019), and provide critical feedback to galaxy and star formation (Hopkins et al., 2011; Botticella et al., 2012; Su et al., 2018). Hydrodynamic simulations of CCSNe have helped inform our understanding of all of these aspects, beyond that which can be inferred directly from current observations.

CCSN simulations now include 3D hydrodynamics as well as more accurate treatments of key physical aspects of the problem. Many advances have been made to produce such simulations, such as the inclusion of two-moment neutrino transport schemes (e.g., Hanke et al., 2013; Lentz et al., 2015; O'Connor & Couch, 2018a; Vartanyan et al., 2019), a general relativistic treatment for gravity as opposed to a Newtonian approach (Roberts et al., 2016; Müller et al., 2017), and spatial resolutions that allow us to accurately capture the Reynolds stress (Radice et al., 2016; Nagakura et al., 2019), a key component in the dynamics of the shock. Despite these advances, the vast majority of these simulations rely on one dimensional (1D) initial conditions for the progenitor star. These progenitors are typically produced using stellar evolution codes where convection is treated using mixing length theory (MLT) (Cox & Giuli, 1968). MLT has been shown to accurately represent convection in 1D models when calibrated to radiation hydrodynamic simulations of surface convection in the Sun (Trampedach et al., 2014). Despite the utility of MLT in 1D stellar models, multidimensional effects in the late stages of nuclear burning in the life of a massive star can lead to initial conditions that differ significantly from what 1D stellar evolution models suggest (Arnett et al., 2009; Arnett & Meakin, 2011; Viallet et al., 2013).

Couch & Ott (2013) investigated the impact of asphericity in the progenitor star on the explosion

of a 15 $M_{\odot}$ stellar model that has been investigated in detail (Woosley & Heger, 2007). Motivated by results of multidimensional shell burning in massive stars (Meakin & Arnett, 2007; Arnett & Meakin, 2011), they implemented velocity perturbations within the Si-shell to assess the impact on the explosion dynamics. They found that the models with the velocity perturbations either exploded successfully or evolved closer to explosion where the models without the perturbations failed to successfully revive the stalled shock. The non-radial velocity perturbations resulted in stronger convection and turbulence in the gain layer. These motions play a significant role in contributing to the turbulent pressure and dissipation which can supplement the thermal pressure behind the shock and, thus, enable explosions at lower effective neutrino heating rates (Couch & Ott, 2015; Mabanta & Murphy, 2018). Couch & Ott (2013) compared models with and without perturbations and with either fiducial or slightly enhanced neutrino heating. Their 3D model *without* initial perturbations but slightly enhanced heating (2% larger than fiducial) followed a similar trajectory as the perturbed model (peak perturbation Mach number of $\mathcal{M}_{\text{pert}} = 0.2$) with no enhanced heating. However, neither of these models were able to revive the stalled shock and both resulted in a failed explosion. These results suggested that the multidimensional structure of the progenitor star can provide a favorable impact on the likelihood for explosion by increasing the total stress, both thermal and turbulent, behind the shock. Without perturbations, the progenitor star used by Couch & Ott (2013) required more neutrino heating (5% larger than fiducial) to achieve shock revival (Couch & O'Connor, 2014).

One of the first efforts to produce multidimensional CCSN progenitors began with the seminal work of Arnett (1994). They performed hydrodynamic O-shell burning simulations in a two-dimensional wedge using an approximate 12 species network. In this work, they found maximum flow speeds that approached $\approx 200 \, \text{km s}^{-1}$ which induced density perturbations and also observed mixing beyond stable boundaries. Much later, Meakin & Arnett (2007) presented the first results of O-shell burning in 3D. They evolved a 3D wedge encompassing the O-shell burning region using the `PROMPI` code for a total of about eight turnover timescales. In comparing the 3D model to a similar 2D model they found flow speeds in the 2D model were significantly larger and also found

that the interaction between the convectively stable layers with large convective plums can facilitate the generation of waves. The combined efforts of these previous works all suggested the need for further investigation into the role of the late time properties of CCSN progenitors near collapse.

Building upon previous work, Couch et al. (2015) (hereafter C15) presented the first three-dimensional (3D) simulation of iron core collapse in a $15 M_\odot$ star. They evolved the model in 3D assuming octant symmetry and an approximate 21 isotope network for a total of ≈ 160 s up to the point of gravitational instability and iron core collapse. Their simulation captured ~8 convective turnovers in the Si-burning shell region with speeds in the Si-shell region on the order of several hundred km s^{-1} and significant non-radial kinetic energy. They then followed the 3D progenitor model through core collapse and bounce to explosion using similar methods as in Couch & O'Connor (2014), i.e. parameterized deleptonization, multispecies neutrino leakage scheme, and Newtonian gravity. When comparing the explosion of the 3D progenitor model to the angle-average of the same model, they find that the turbulent kinetic energy spectrum ahead of the shock front (in the accretion flow) was more than an order-of-magnitude larger for the 3D case during accretion of the Si-shell, around post-bounce times of $t_{pb} = 125 \pm 25$ ms. The more turbulent accretion flow led to enhanced total turbulent kinetic energy in the gain region by up to almost a factor of two for the 3D initial conditions than the angle-averaged model, with most of the turbulent kinetic energy residing at scales of $\ell \approx 6 - 10$, where ℓ is the principle spherical harmonic order. These differences resulted in an overall more rapidly expanding shock radius and a diagnostic explosion energy approximately a factor of two larger than the 1D initial model. However, the model presented in that work suffered from approximations that may have affected the results. The main issues were the use of octant symmetry and the modification of the electron capture rates used in the simulation. The first of these approximations can lead to a suppression of perturbations of very large scales while the second can lead to larger convective speeds within the Si-shell region due to the rapid artificial contraction fo the iron core.

Müller et al. (2016b) aimed to address these issues by conducting a full 4π 3D simulation of O-shell burning in a $18 M_\odot$ progenitor star. Using the `Prometheus` hydrodynamics code they evolved

the model in 3D for ~294 s up to the point of iron core collapse. They alleviate the use of enhanced electron capture rates by imposing an inner boundary condition that follows the radial trajectory of the outer edge of the Si-shell according to the 1D initial model generated by the `Kepler` stellar evolution code. In their simulation, they capture approximately 9 turnover timescales in the O-shell finding Mach numbers that reach values of ~0.1 as well a large scale $l = 2$ mode that emerges near the point of collapse. Their results build on those of C15 with further evidence suggesting the need for full 4π simulations. Recently, (Yadav et al., 2019) presented a 4π 3D simulation of O-shell burning where a violent merging of the O/Si interface and Ne layer merged prior to gravitational collapse. This simulation of an 18.88 $M_\odot$ progenitor for 7 minutes captured the mixing that occurred after the merging and was found to lead to Mach numbers of ~0.13 near collapse. All of these efforts suggest that 3D progenitor structure increases the likelihood for explosion of massive stars by the delayed neutrino heating mechanism.

In this paper, we present 1D, 2D, and 3D hydrodynamical simulations of Si- and O- shell burning of a 15 $M_\odot$ progenitor star for the final ~424 seconds of its life up to the point of gravitational instability and iron core collapse. Using these models, we: 1) provide a detailed description of the convective regions in the Si- and O- burning shells, 2) estimate key stellar evolution parameters that may impact the explosion properties of CCSNe and compare them to their 1D counterparts, and 3) study how the properties of these models may depend on resolution, dimensionality/symmetry, and initial perturbations. In order to self-consistently simulate secular core contraction and ultimate collapse, we include the iron core and both Si- and O-shell regions in our simulation. To address the dependence of resolution, dimensionality, and symmetry on our results we consider 2D and 3D models at varying finest resolution and cylindrical versus octant symmetry, respectively. We improve on the work of C15 by alleviating the use of accelerated electron capture rates, evolving two 3D simulations that cover the full solid angle (4π steradian) rather than octant symmetry, and significantly increase the timescale of the simulation. Lastly, to assess the impact of initial conditions, our two 4π 3D models differ only in the initialization of the velocity field. Using these models, we characterize the qualitative properties of the flow amongst different parameter

choices while also comparing to the predicted properties of the 1D input model for our simulations. We present a detailed analysis of the convective properties of the 4π 3D models and discuss the implications for the 3D state of CCSN progenitors at collapse. This paper is organized as follows. In Section 5.3 we discuss our computational methods and input physics, in Section 5.4 we present the results of our 2- and 3D hydrodynamical `FLASH` simulations, Section 5.5 summarizes our results and compares them to previous efforts.

3.3 Methods and Computational Setup

Our methods follow closely those used in C15 in that we evolve a 1D spherically symmetric stellar evolution model using `MESA` and, at a point near iron core collapse, map the model into the `FLASH` simulation framework and continue the evolution in multi-D to collapse. In the following subsections, we will describe these steps in detail.

3.3.1   1D `MESA` Stellar Evolution Model

We evolve a 15 $M_\odot$ solar metallicity stellar model using the open-source stellar evolution toolkit, Modules for Experiments in Stellar Astrophysics (`MESA`) (Paxton et al., 2011, 2013, 2015, 2018, 2019). The model is evolved from the pre-main sequence to a time approximately 424 seconds before iron core collapse, defined by `MESA` as the time when any location of the iron core reaches an infall velocity of greater than 1000 km s^{-1}. We use temporal and spatial parameters similar to those used in Farmer et al. (2016) and Fields et al. (2018). These parameters result in timesteps on the order of $\bar{\delta t} \approx 41$ kyr during the main sequence, $\bar{\delta t} \approx 24$ yr during core carbon burning, and $\bar{\delta t} \approx$ 19 sec when the model is stopped. At the point when the model is stopped, the model has 3611 cells with an enforced maximum $\bar{\delta m} \approx 0.01$ $M_\odot$. The `MESA` model uses an α-chain network that follows 21 isotopes from ^{1}H to ^{56}Cr. This network is chosen for its computational efficiency and to match the network currently implemented in `FLASH` and used in (Couch et al., 2015). This approximate network aims to capture important aspects of pre-supernova evolution of massive star models which include reactions between heavy ions and iron-group photodisintegration and similar approaches
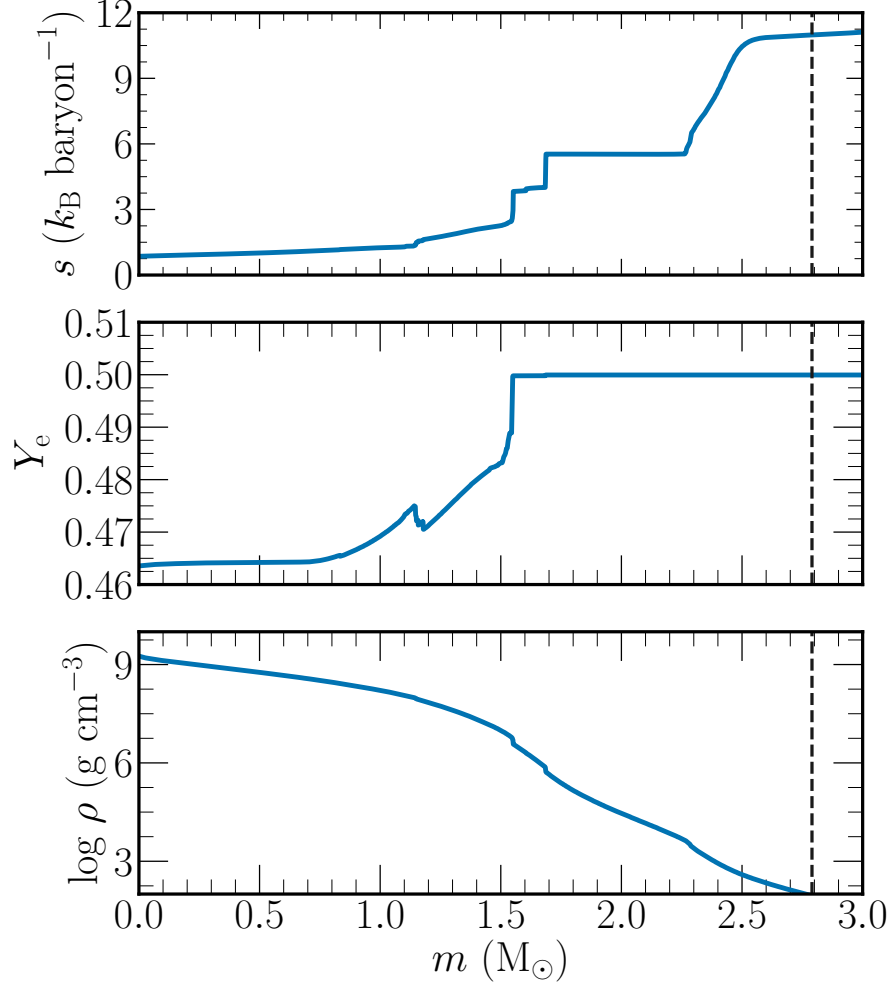
Figure 3.1: Specific entropy, electron fraction, and mass density profiles as function of stellar mass for the 1D `MESA` model at the time of mapping into `FLASH`. The dashed black vertical line denotes the edge of the domain used in the `FLASH` simulations.

have been used in many previous studies (Heger et al., 2000; Heger & Woosley, 2010). We include mass loss using the 'Dutch' wind scheme with an efficiency value of 0.8. Mixing processes due to convective overshoot, thermohaline, and semi-convection are considered with values from Fields et al. (2018). We do not include rotation and magnetic fields in this model.

In Figure 3.1 we show the specific entropy, electron fraction, and mass density profiles as a function of mass coordinate from the `MESA` model at the point which it is mapped into `FLASH`. The dashed black line denotes the edge of the domain considered in the `FLASH` simulations. Overall, the model used in this work has a similar structure to the progenitor used in C15 except for the case of the lower central electron fraction in the core. This difference is partially due to the different

network used in C15, a basic 8 isotope network that was automatically extended during evolution compared to our static 21 isotope network used in the MESA model for this work. The input MESA model in C15 also had a slightly smaller initial iron core mass, 1.3 $M_\odot$, than the model considered here.

Figure 3.2 shows the mass fraction profiles for some of the most abundant isotopes for the input MESA model. The label 'Iron' denotes the sum of mass fractions of ^{52,54,56}Fe isotopes. At the point of mapping the stellar model has an iron core mass of approximately 1.44 $M_\odot$. The Si-shell region is located at a specific mass coordinate of $m \approx 1.53 - 1.68$ $M_\odot$ while the O-shell region extends from the edge of the Si-shell out to mass coordinate of $m \approx 2.26$ $M_\odot$. Figure 3.3 shows the time evolution of the Brunt-Väisälä frequency (left) and convective velocity speeds (right) as a function of mass coordinate as predicted by MESA for the 1D model evolved from the point at which it is mapped into FLASH until core collapse. The 1D model predicts convective speeds in the O-shell regions with a peak of approximately 100 km s^{-1} up to the point of collapse. In the Si-shell region, only the inner most region is convectively active with speeds on the order of those in the O-shell. At a time of $t \approx 200$ s, the innermost Si-shell burning convective region ceases and convective proceeds instead at a further mass coordinate of $m \approx 1.60 - 1.68$ $M_\odot$ with speeds increasing to values greater than in the O-shell near collapse at ≈ 160 km s^{-1}.

3.3.2   2- and 3D FLASH Stellar Evolution Model

3.3.2.1   Overview

We perform a total of eight multidimensional stellar evolution models at various resolutions and symmetries. All models are evolved using the FLASH simulation framework (Fryxell et al., 2000; Dubey et al., 2009). Similar to Couch et al. (2015), we utilize the "Helmholtz" EoS (Timmes & Swesty, 2000) and the same 21 isotope network but with an improvement to the weak reaction rate used for electron capture onto ^{56}Ni. The original network used tabulated rates from Mazurek et al. (1974) while the updated rates were adopted from Langanke & Martínez-Pinedo (2000). The new rates are enhanced by close to a factor of 5-10 alleviating any need to artificially enhance the total
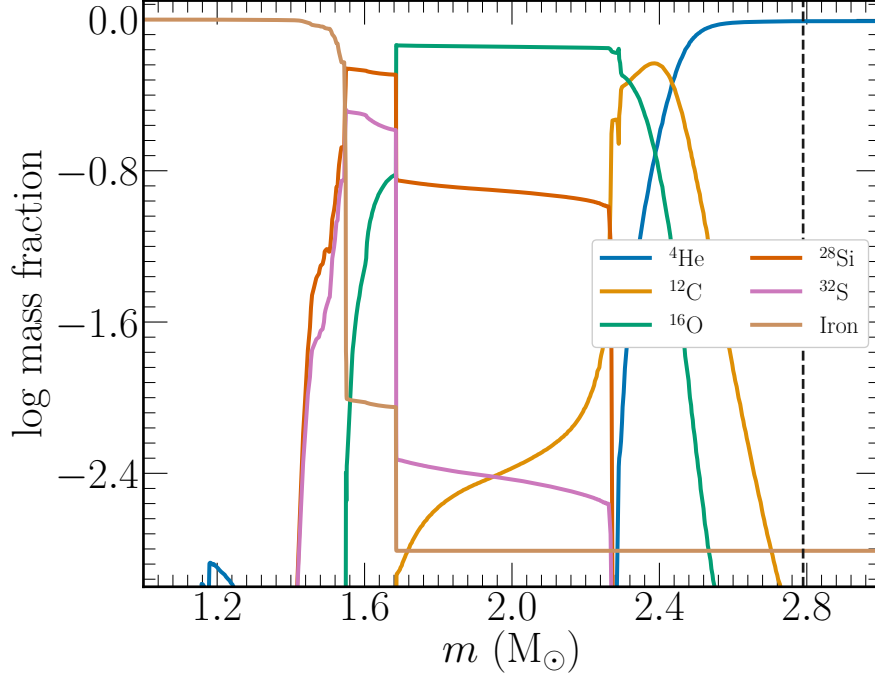
Figure 3.2: Mass fractions of the most abundant isotopes as a function of stellar mass for the 1D `MESA` model at time of mapping into `FLASH` . The label 'Iron' denotes the sum of mass fractions of ^{52,54,56}Fe isotopes. The dashed black vertical line denotes the edge of the domain in `FLASH` .
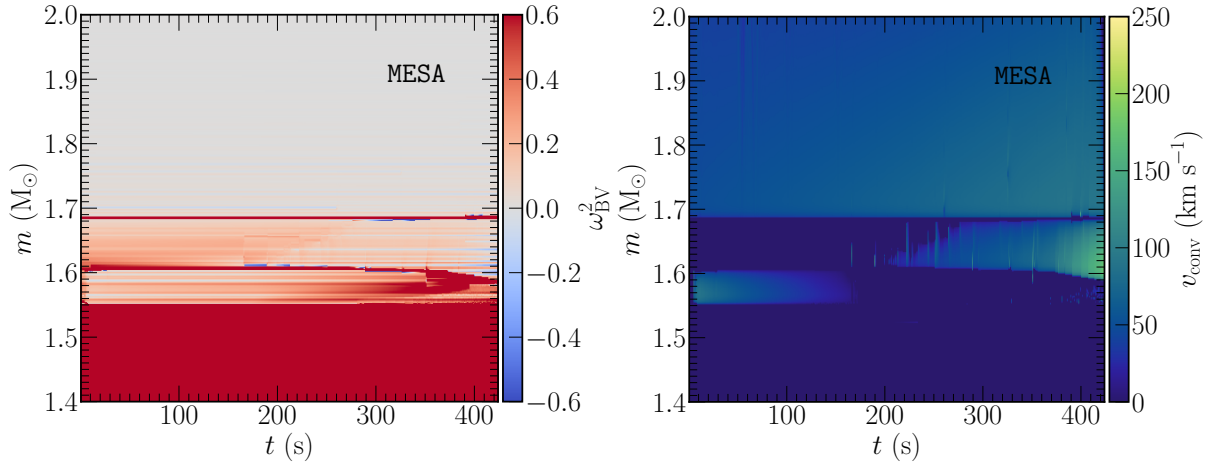
Figure 3.3: Time evolution of the 1D profile data for the `MESA` model. The (left) subplot shows the Brunt-Väisälä frequency while the (right) shows the convective velocity speeds according to MLT. The red regions denote regions that are stable against convection while gray and blue regions show regions that are unstable to convection according to `MESA`.

electron capture rates in the models presented in this work and are also in agreement with the table values used in `MESA`.

3.3.2.2 Hydrodynamics, Gravity, and Domain

The equations of compressible hydrodynamics are solved using `FLASH`'s directionally unsplit piece-wise parabolic method (PPM) (Lee & Deane, 2009) and HLLC Riemann solvers (Toro, 1999) with a Courant factor of 0.8. Self-gravity is solved assuming a spherically symmetric (monopole) gravitational potential approximation (Couch et al., 2013). Our computational domain extends to 10^{10} cm from the origin in each dimension for both the 2D and 3D models. Four 2D models are evolved with varying levels of finest grid spacing resolution of 8,16, 24, and 32 km. The 2D models use cylindrical geometry with symmetry about the azimuthal direction. Four 3D models are evolved: two assuming octant symmetry with two different values of finest grid resolution, 16 and 32 km, and two full 4π 3D models at 32 km finest grid resolution, one with an initialized velocity field and one without. All 3D models use Cartesian coordinates. The models are labeled according to their dimensionality and finest grid spacing, and in the case of 3D according to the use of octant symmetry or not. For example, the 3D 32 km octant model is labelled `3DOct32km` for ease of model identification throughout the remainder of this paper. The initially perturbed 4π 3D model is labeled `3D32kmPert`.

The velocity field initialization for the perturbed model follows the methods used in Müller & Janka (2015) and extended to 3D in O'Connor & Couch (2018b). The method introduces solenoidal velocity perturbations to the v_r and v_θ components using spherical harmonics and sinusoidal radial dependence. We use the convective velocity profile of the 1D `MESA` model at the time of mapping to inform our choices of parameters to initialize the velocity field. We take the innermost convective Si-shell region to be from $r_{1,\min} \approx 2220$ km to $r_{1,\max} \approx 2740$ km, and choose spherical harmonic coefficients to be $\ell = 5, m = 1$ with a single radial sinusoid ($n = 1$). The second convective Si-shell region, at $r_{2,\min} \approx 2740$ km to $r_{2,\min} \approx 3760$ km, uses the same spherical harmonic and radial numbers as the first; $n = 1, \ell = 5, m = 1$. Lastly, the O-shell region, taken to be $r_{3,\min} \approx 3770$ km to $r_{3,\max} \approx 26,620$ km, assumes an initially larger scale flow with quantum numbers of $n = 1, \ell = 5, m = 3$.

All velocity amplitude scaling factors (C) for the initial perturbations were chosen to match

approximately 1% (in the Si-shell regions) and 5% (in the O-shell region) of the convective velocity speed as predicted by the MESA model at time of mapping. The resulting perturbations led to an angle-averaged Mach number of $\mathcal{M} \approx 2 \times 10^{-3}$ and $\mathcal{M} \approx 1.3 \times 10^{-2}$ in the Si-shell and O-shell regions, respectively. For comparison, the scaling factors used in (O'Connor & Couch, 2018b) to replicate pre-collapse perturbations were on the order of $O \sim 10^3$ larger than values used here. In terms of the total initial kinetic energy the perturbed model begins with a value of $E_{\text{kin.}} \approx 5.8 \times 10^{45}$ erg, approximately 4% of the peak total kinetic energy observed at later times.

All models utilize adaptive mesh refinement (AMR) with up to eight levels of refinement. To give an example of the grid structure for our models we consider the refinement boundaries for the 2D8km and 2D32km models. In both of these models, the entire Si-shell region has a grid resolution of 32 km with effective angular resolution of $\approx 0.9°$ to $0.5°$ at the base (≈ 2000 km) and edge of the shell (≈ 3500 km), respectively. The resolution within the Si-shell region for these model corresponds to an average of $\approx 5\%$ of the local pressure scale height, H_{p}. The grid resolution in the 2D models are representative of the respective 3D models as well. The two finer resolution levels of the 2D8km model are situated within the iron core with the second highest level of refinement at the base of the Si-shell region and down to a radius of 1000 km. In this region, the 2D8km and 2D32km grid resolutions provide a value of $\approx 6\%$ and $\approx 12\%$ of H_{p}, respectively. The O-shell region in these models is at 64 km resolution out to a radius of ≈ 6000 km then decreases to 128 km from there to 10,000 km. Within these two regions the effective angular resolution ranges from $0.73°$ to $0.61°$ and corresponds to an average of $\approx 0.04H_{\text{p}}$ and $\approx 0.05H_{\text{p}}$, respectively. In the 2D32km, the finest resolution level goes out to a radius of 3500 km, the approximate edge of the Si-shell, giving the model similar resolution in this and the O-shell to that of the 2D8km without the two finer resolution levels within the iron core. The location of refinement levels used is determined as a function of radius and chosen based on logarithmic changes in specific density, pressure, and velocity. The refinement levels are static throughout the simulation and chosen based on the input model.

For the 3D octant symmetry planes and the 2D axis plane we use reflecting boundary conditions

while the outer boundaries utilize a boundary condition that applies power-law extrapolations of the velocity and density fields to approximate the roughly hydrostatic outer envelope of the stellar interior. The 4π 3D models use the same custom boundary condition at all domain edges. To help reduce any artificial transients that occur from mapping from a Lagrangian to an Eulerian code with different grid resolution, we use the approach of Zingale et al. (2002). This approach takes the initial 1D `MESA` model and maps it to a uniform grid with resolution four times finer than that used in our `FLASH` grid. The density in the remapped model is then slightly modified while the pressure is held fixed to force the model into hydrostatic equilibrium (HSE), such that it satisfies

$$\nabla P = \rho g \,, \tag{3.1}$$

in the absence of initial velocities. The procedure is then closed by calling the equation of state (EOS) for the new profile.

3.3.2.3   Nuclear Burning

During the growth of the iron core, thermal support is removed from the core due to photo-disintegration of iron nuclei that cause the gas to cool. The subsequent contraction of the stellar core causes an increase in the rate of electron captures onto protons therefore decreasing the pressure support contribution from electron degeneracy. This further reduction of pressure support in the core accelerates nuclear burning in the silicon burning shell leading to faster growth of the iron core. In the moments prior to iron core collapse the core moves towards nuclear statistical equilibrium while the neutrino cooling and photo-disintegration rates begin to dominate and lead to a negative specific nuclear energy generation rate, $\epsilon_{\rm nuc}$, in the inner core. Within this cooled material, the electron capture rates increase significantly and give rise to a positive specific $\epsilon_{\rm nuc}$ and cause the temperature to rise again. Within this region a numerical instability can occur for calculations which employ operator split burning and hydrodynamics (Timmes et al., 2000). In order to avoid this instability from occurring in the models considered here, we place a limiter on the maximum timestep such that any change in the internal energy across all zones in the domain is limited to a maximum of a 1% per timestep.

Figure 3.4: Slices of the magnitude of the velocity field for the `2D32km` (left) and `2D8km` model (right) at four different times. At $t = 200$ s, both models exhibit a "square" like imprint in the velocity field that is due to the stiff entropy barrier at the edge of the Si-shell region along with increased velocity speeds along the axis. These speeds are due to numerical artifacts common in 2D simulations assuming axisymmetry. The increased velocity along the axis causes outflows in the positive radial direction at the top and bottom of the Si-shell region. Beyond $t = 200$ s, both models become characterized by large scale cyclones in the O-shell region with convective activity in the Si-shell having three to five times slower flow speeds.

The large and opposite specific nuclear energy generation rates within the core can also lead to significant difficulties in solving the nuclear reaction network at a given timestep and lead to significant load imbalance of the computational workload per MPI rank. Zones within the core can take several hundred iterations to obtain a solution while outside of the iron core, a solution is found in a fraction of the time. In order to help circumvent these issues, we employ a moving "inner boundary condition" within the iron core, well below the region of interest for this paper.

For all simulations considered here, the profiles of ρ, Y_e, and P in the inner 1000 km of the models are evolved according to the profile from the MESA model at the corresponding time. A 2D table is constructed from the MESA profile data from the point of mapping to FLASH (≈ 424 s) until iron core collapse. Four point Lagrange linear interpolation is then performed in time and radius to ensure accurate values are mapped for the FLASH models, which take on the order of 100 timesteps for every MESA timestep. This mapping effectively provides a time-dependent inner boundary condition that ensures the model follows the central evolution of the MESA model while still allowing us to capture the pertinent multi-D hydrodynamic behavior with FLASH .

For all models, we simulate ≈ 424 s of evolution prior to collapse capturing Si- and O-shell burning up to gravitational instability and iron core collapse. The full 4π 3D models had an approximate total of 46M zones, took ≈ 0.6 M core hours on the laconia compute cluster at Michigan State University. All the multidimensional CCSN progenitor models considered in this work are available publicly.

3.4 Multi-Dimensional Evolution to Iron Core-Collapse

3.4.1 Results from 2D Simulations

We evolve a total of four 2D simulations at 8,16, 24, and 32 km finest grid spacing resolution. In the following subsection we consider the global properties of all of the 2D models, compare the lowest and highest resolution model, and consider in detail the convective properties of the highest resolution 2D model.

The structure of the flow at large scale within the shell burning regions can have a significant impact on the CCSN explosion mechanism. Perturbations within these region can be amplified during collapse of the iron core and aid in the development of turbulence during explosion (Lai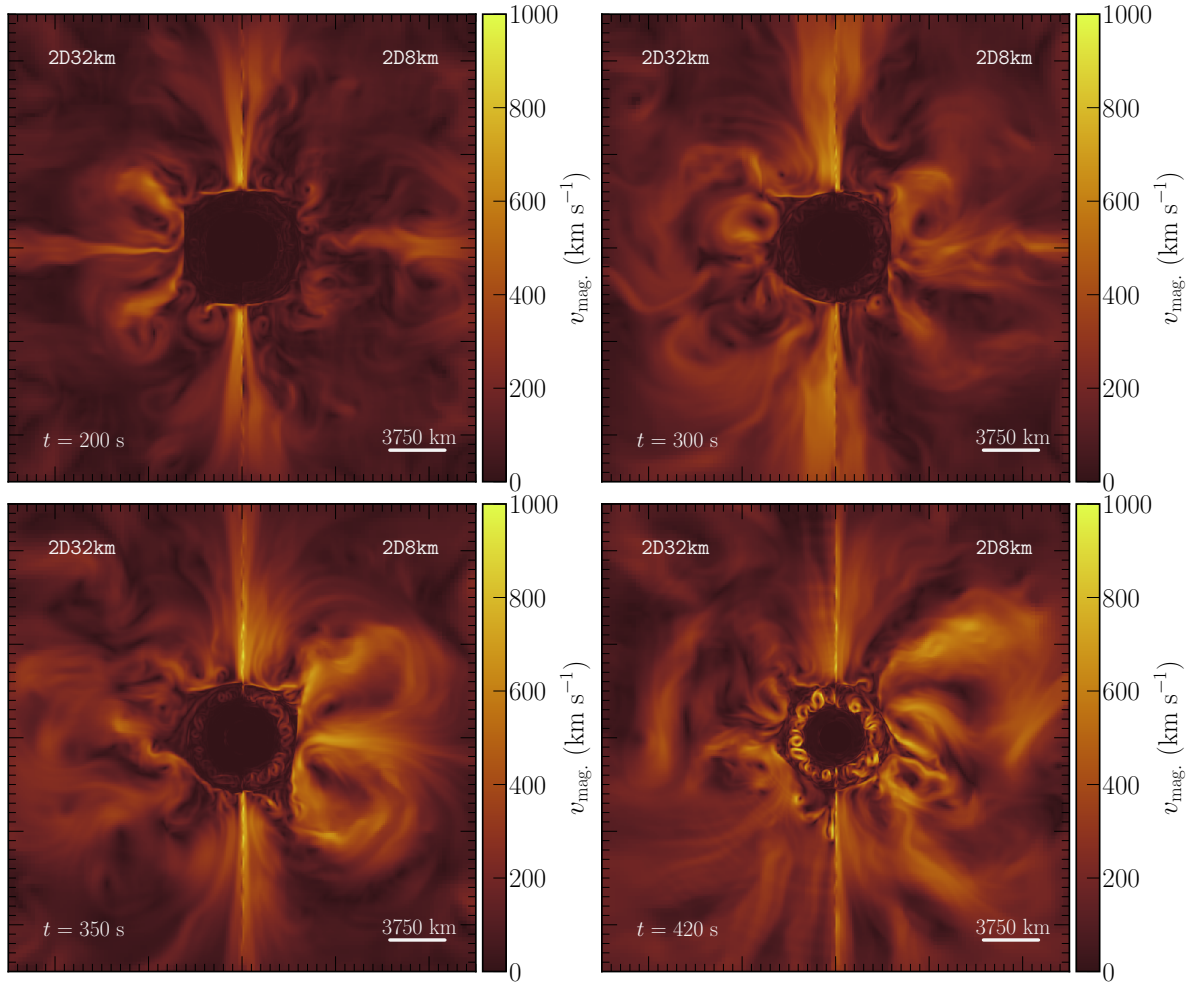 & Goldreich, 2000; Couch & Ott, 2013, 2015). In Figure 3.4 we show slices of the magnitude of the velocity field for the 2D32km (left) and 2D8km models (right) at four different times. At early times, we see convection developing in a similar matter for both the 8 km and 32 km models. Both models exhibit a "square" like imprint in the velocity field that is due to the stiff entropy barrier at
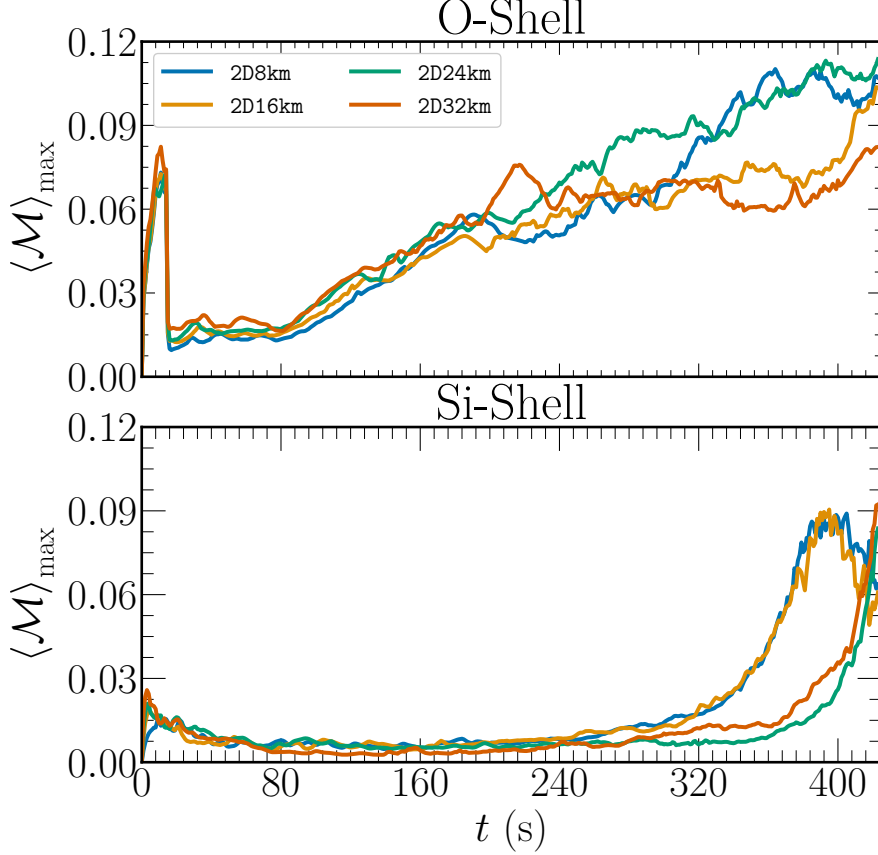
Figure 3.5: Time evolution of the maximum angle-averaged Mach number within the Si- and O-shell for all 2D models.

the edge of the Si-shell region interacting with the Cartesian-like 2D axisymmetric grid. $t = 200$ s both models characterized by large scale cyclones in the O-shell region At late times, beyond $t = 350$ s, the 8 km model appears to reach flow speeds in the Si-shell that are on the order of those observed in the O-shell. In the O-shell, the scale of the convection increases as cyclones on the order of ≈ 4000 km dominate the flow with the scale of convection within the Si-shell region being restricted by the width of the shell. Seconds prior to collapse, the 32 km model reaches Si-shell convective speeds that agree with the 8 km model.

To begin our assessment of the convective properties of the models, we compute the angle-averaged maximum Mach number, defined as,

$$\langle \mathcal{M} \rangle = \left\langle \frac{|\mathbf{v}|}{c_{\mathrm{s}}} \right\rangle , \tag{3.2}$$

where $|\mathbf{v}|$ is the local magnitude of the velocity field and c_{s} the local sound speed, and the averaging

91
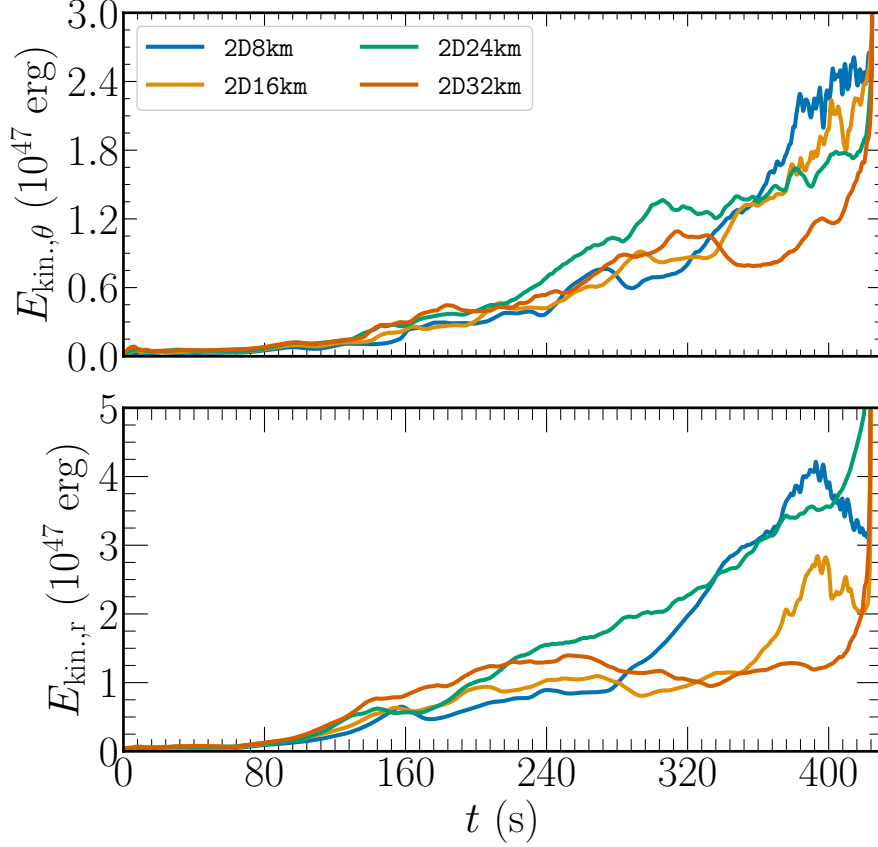
Figure 3.6: Time evolution of the radial and non-radial kinetic energy for the four 2D models.

is performed over solid angle. We also compute the Mach number within the Si-shell and within the O-shell to characterize their behavior independently. The shell region for silicon-28 is defined as the region where $X(^{28}\text{Si}) > 0.2$ and $X(^{16}\text{O}) < 0.2$ and for oxygen-16 $X(^{16}\text{O}) > 0.2$ and $X(^{28}\text{Si}) < 0.2$.

In Figure 3.5 we show the time evolution of the maximum angle-averaged Mach number for all 2D models. The maximum Mach number reported at the start of the simulation reflects the initial transient as it traverses the domain. Beyond $t \approx 15$ s, the transient has either traversed the shell region or been sufficiently damped that the Mach numbers reflect the convective properties of the shells and not the initial radial wave. The Si-shell appears to reach a quasi-steady state in the first ≈ 80 seconds, this is seen by all models reaching a characteristic Mach number within the shell. In the O-shell, the Mach number remains relatively flat although larger than the approximate mean in the Si-shell, this suggests little to no convective activity in the O-shell during this time. To
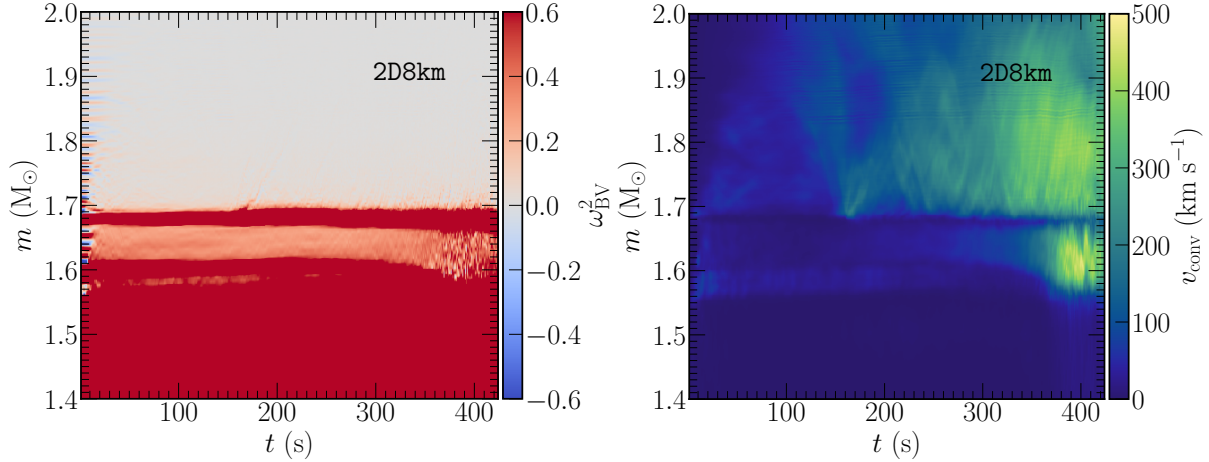
Figure 3.7: Same as in Figure 3.3 but for the `2D8km` `FLASH` simulation. The slightly negative values of ω^2_{BV} denoted by the gray/light blue regions represent regions unstable to convection.

make an estimate of the time at which these two regions would be expected to reach a quasi-steady convective state, we can estimate a convective turnover timescale for each region. The Si-shell spans a radius of approximately 800 km with convective speeds of $v_{\text{Si-shell}} \approx 80$ km s^{-1} at early times. Using this, we can estimate an approximate convective turnover time within the Si- shell of $\tau_{\text{Si}} \approx 2r_{\text{Si}}/v_{\text{Si}} \approx 20$ seconds. This value suggests that after the transient has traversed the Si-shell region, a total of approximately three turnover timescales elapse before the region reaches a quasi-steady state represented by an average Mach number oscillating on the approximate timescale of the turnover time. A similar estimate can be made to the O-shell where we determine a turnover time of $\tau_{\text{O}} \approx 100$ seconds. This value suggests that the lack of change in Mach number for the O-shell is due to the fact that the region has not yet reached a quasi-steady convective state.

By the end of the simulation, the models span a range of Mach numbers of $\approx 0.08 - 0.12$.

The late time behavior of the Si-shell region of the two highest resolution models can be attributed to an expansion of the width of the convective Si-shell region observed in the last slice of Figure 3.4 . the two highest resolution models, the convective velocity speeds reach enough to overcome the barrier between the convective and non-convective silicon shell regions causing them to merge. After this merging of these two regions, the entire region becomes fully convective. However, due to the expansion of the width of the Si-shell region after merging, the burning within
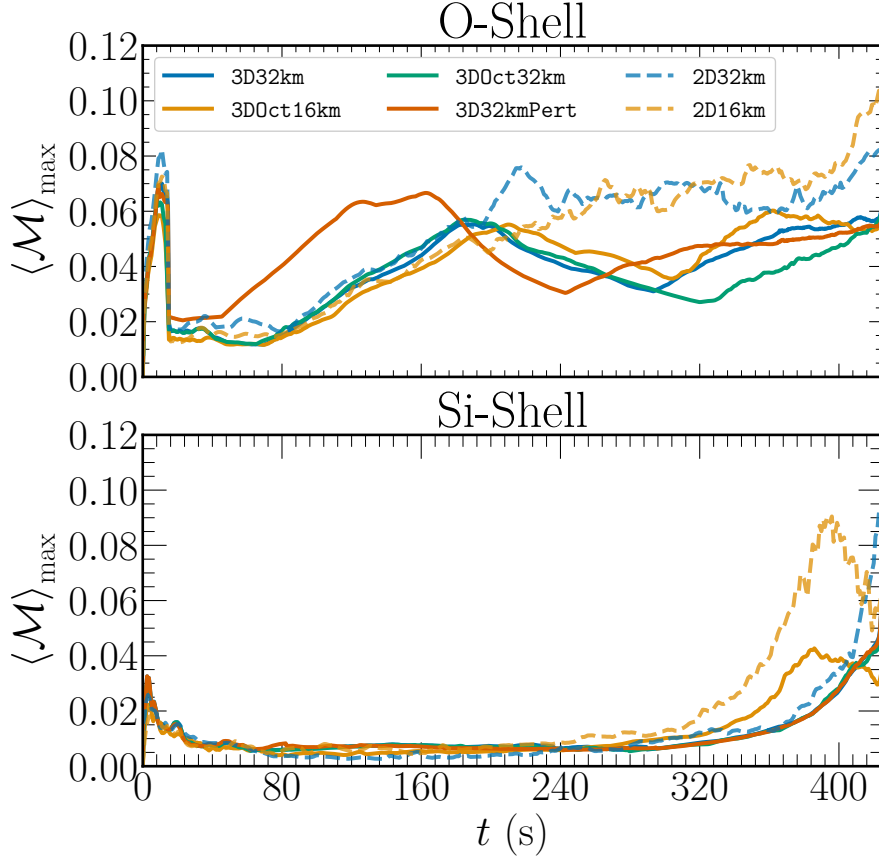
Figure 3.8: Same as in Figure 3.5 but for all the 3D models for the duration of the simulation.

this region occurs at lower density. Because the local sound speed goes as $c_s \propto \rho^{-1/2}$, a decrease in density leads to an increase in the sound speed therefore decreasing the local maximum Mach number. The two lower resolution models do not experience this merging of the two regions until moments before collapse when the flow speeds are large enough ≈ 150 km s^{-1} to merge.

In Figure 3.6 we show the time evolution of the total kinetic energy in the radial and non-radial components for the 2D FLASH models. When considering the non-radial kinetic energy components for the four models we see that the peak value of the energy at collapse increases with an increase in model resolution with the highest resolution model showing a peak value of $E_{\text{kin.},\theta} \approx 2.5 \times 10^{47}$ erg at collapse. The radial kinetic energy shows further evidence for the expansion of the Si-shell region in the two highest resolution models with the energies showing local maxima around $t \approx 390$ s followed by a steady decline for the duration of the simulation. This transition time is also reflected in the non-radial kinetic energy where one can notice a slight increase in the energy from
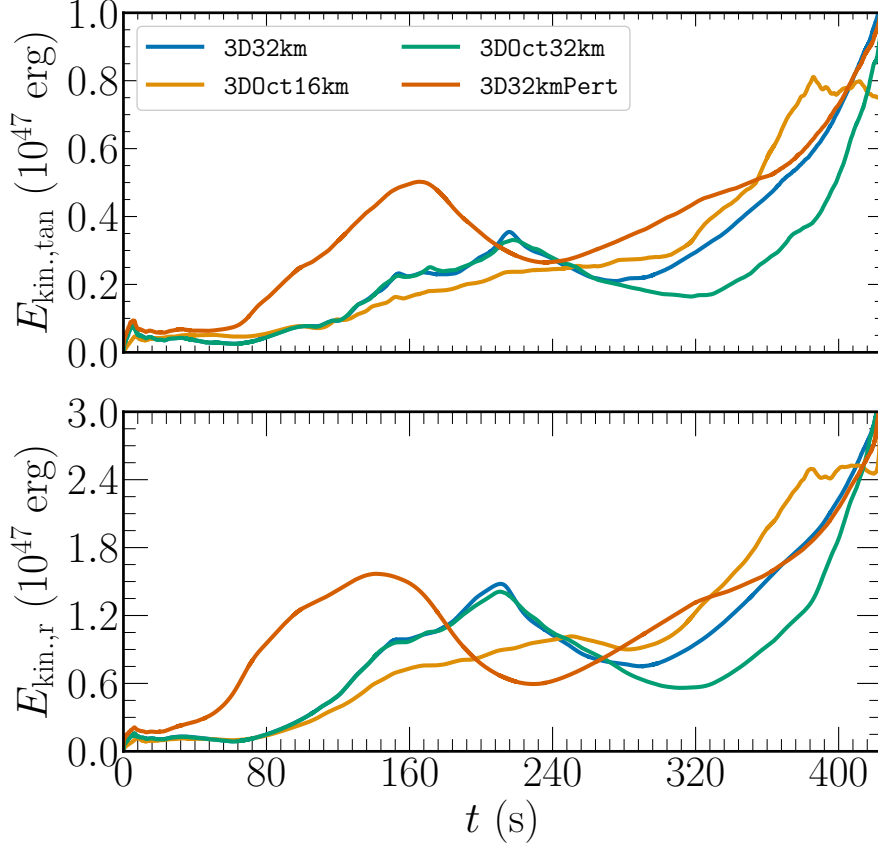
Figure 3.9: Same as in Figure 3.6 but for the four 3D models.

$t \approx 390$ s to collapse.

In Figure 3.7 (left) we show the time evolution of the Brunt-Väisälä frequency for the assuming the Ledoux criterion for convection which states that a region is stable against convection if

$$\nabla_{\text{rad.}} < \nabla_{\text{ad.}} - \frac{\chi_\mu}{\chi_T} \nabla_\mu . \tag{3.3}$$

Under this criterion, we can compute the Brunt-Väisälä frequency for the FLASH simulations as

$$\omega_{\text{BV}}^2 = g \left(\frac{1}{\rho} \frac{\partial \rho}{\partial r} - \frac{1}{\rho c_{\text{s}}^2} \frac{\partial P}{\partial r} \right) , \tag{3.4}$$

where g is the local gravitational acceleration, ρ the mass density, c_{s} the adiabatic sound speed, and P the pressure. This form of the Brunt-Väisälä frequency equation is equivalent to forms that explicitly include the entropy and electron fraction gradients (Müller et al., 2016b). For each timestep for which these 2D data are available, we compute angle average profiles as a function of

95

radius before using Equation 3.4 to compute the frequency. Using this convention a positive value implies a region stable against convection.

In Figure 3.7 we also show the time evolution of the convective velocity (right), here defined as $v_{\mathrm{conv}} = \sqrt{|\mathbf{v}|^2 - v_{\mathrm{rad.}}^2}$, as a function of time for the same model. The base of the O-shell region is shown at an approximate mass coordinate of 1.7 $M_\odot$. Within the O-shell, the convective velocity reach speeds of nearly 500 km s^{-1} as the model approaches iron core collapse. Prior to this, the model shows values on the order of 50-100 km s^{-1} in the Si-shell and 200-400 km s^{-1} in the O-shell. The expansion of the convective Si-shell region due to the merging is observed as well in the convective velocity, again around $t \approx 390$ s, the same time at which the velocity begins to reach values observed in the O-shell for this model. In comparing to Figure 3.3, the `FLASH` model predicts two initial inner and outer convectively active regions that eventually merge into one larger region near collapse. On the other hand, the `MESA` model predicts a transition of the location of the convective region followed by late time expansion of this region near collapse. Despite these somewhat different evolutionary pathways both models agree in their qualitative description of the location of the convective regions near collapse. The major difference between the two models are the magnitude of the convective velocities predicted by `MESA/MLT`.

3.4.2   Results from 3D Simulations

We perform a total of 3D stellar models: two models in octant symmetry at 16 and 32 km finest grid spacing and full 4π models at 32 km finest resolution . In this subsection, we will consider the global properties of all 3D models, describe the perturbed 4π 32 km in detail, and, lastly, consider the impact of octant symmetry and resolution.

In Figure 3.8 we show the time evolution of the maximum Mach number in the Si- and O-shell at each timestep for all 3D models. Contrary to the trend seen in Figure 3.5 for the O-shell one can observe a periodic nature in the Mach number values that follows our estimate for the convective turnover timescales from Section 3.4.1. Similar to the comparable 2D case (see Figure 3.6), the `3DOct16km` model appears to reach a peak Mach number in the Si-shell at around $t \approx 390$ s before a
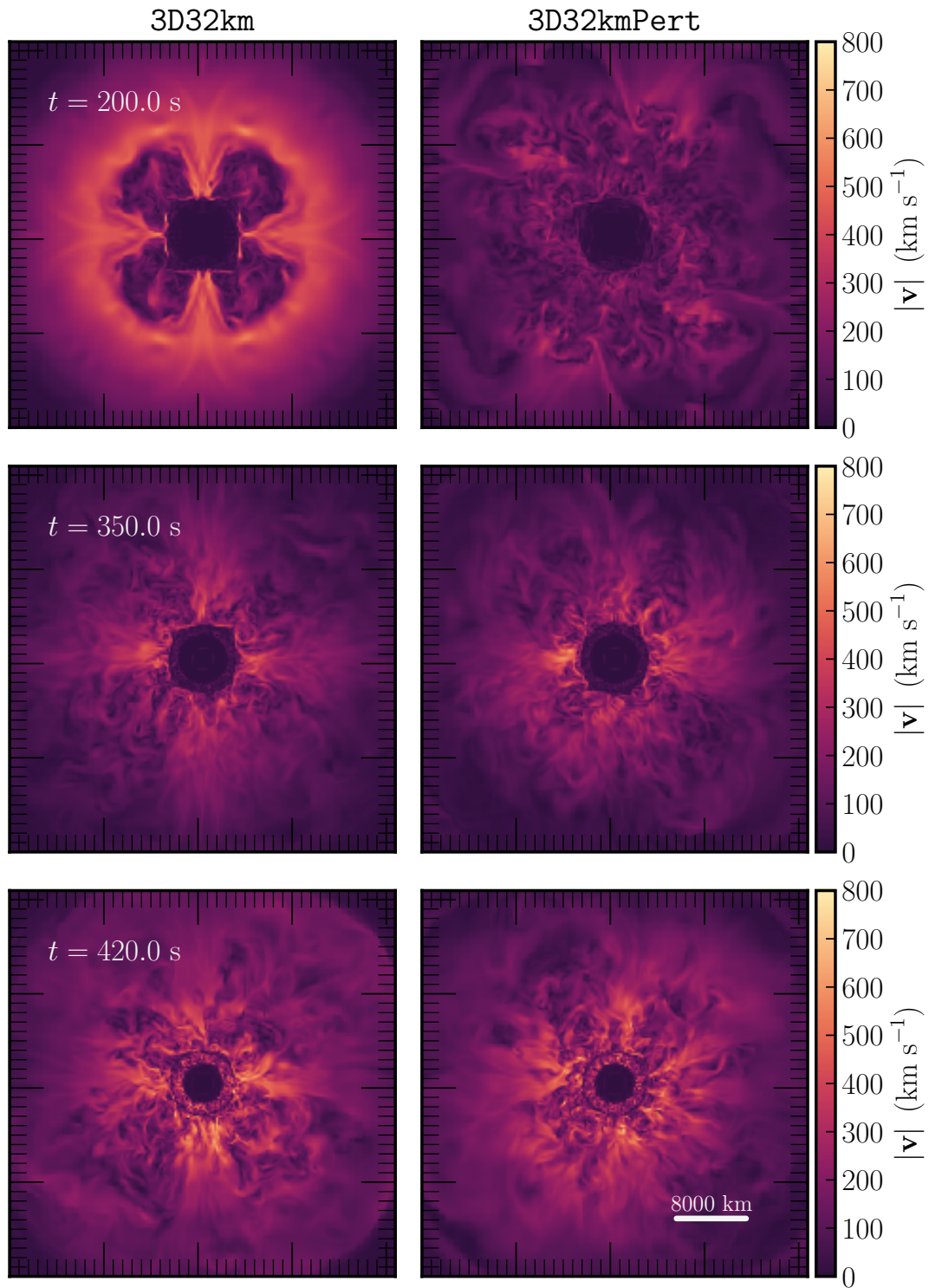
Figure 3.10: Slices of the the magnitude of the velocity field for the 3D32km (left) and 3D32kmPert (right) models at $t = 200$ s, 350 s, and 420 s in the $x - y$ plane.

steady decline as the model approaches collapse, this behavior is also attributed to expansion of the Si-shell after the merging of the convective and non-convective regions. This result suggests that the merger is independent of geometry and dimensionality but instead depends on the resolution of the inner core region.

Figure 3.9 shows the time evolution of the radial and non-radial kinetic energy for the 3D models. In general, the 32 km resolution models behave similarly with the 4π models having larger kinetic energy values than the octant model beyond $t \approx 280$ s. The 16 km octant model has larger kinetic energy values than both models at late times while also reaching a local peak value approximately 30 s before collapse. Prior to about 200 s, the bulk of the energy in the radial direction for the two unperturbed 32 km models is due to an the initial transient that traverses the domain at the start of the simulation and leaves the domain at $t \approx 60$ s. The 16 km model experiences a less significant initial transient and therefore undergoes less initial expansion/contraction as the model readjusts to a new equilibrium.

The evolution of the magnitude of the velocity field for models `3D32km` (left) and `3D32kmPert` (right) is compared in Figure 3.10.

In Figure 3.11 we show a 3D volume rendering of the magnitude of the velocity field for the `3D32kmPert` model at $t \approx 423$ s. The approximate location of the edge of the iron core (shown in teal) is taken to be an isocontour surface at a radius where $s \approx 4$ k_{KB} / baryon. At this time, the iron core has a radius of $r \approx 1982$ km. The light purple plumes show the fast moving convective motions in the O-shell region depicted by a Guassian transfer function with a peak at $|\mathbf{v}| \approx 300$. The slower moving, larger scale motions are shown using a similar transfer function with a peak at $|\mathbf{v}| \approx 100$ in light blue.

Similar to the analysis done for the `MESA` model and the 2D `FLASH` models, in Figure 3.12 we show the Brunt-Väisälä frequency (left) and convective velocity (right) as a function of time for the `3D32kmPert FLASH` model. Unlike the `2D8km`, this model does not experience the merging of the two Si regions until a few seconds prior to collapse leading to a similar fully convective Si-shell at the end of the simulation. Another notable feature of this model is the slight expansion and then
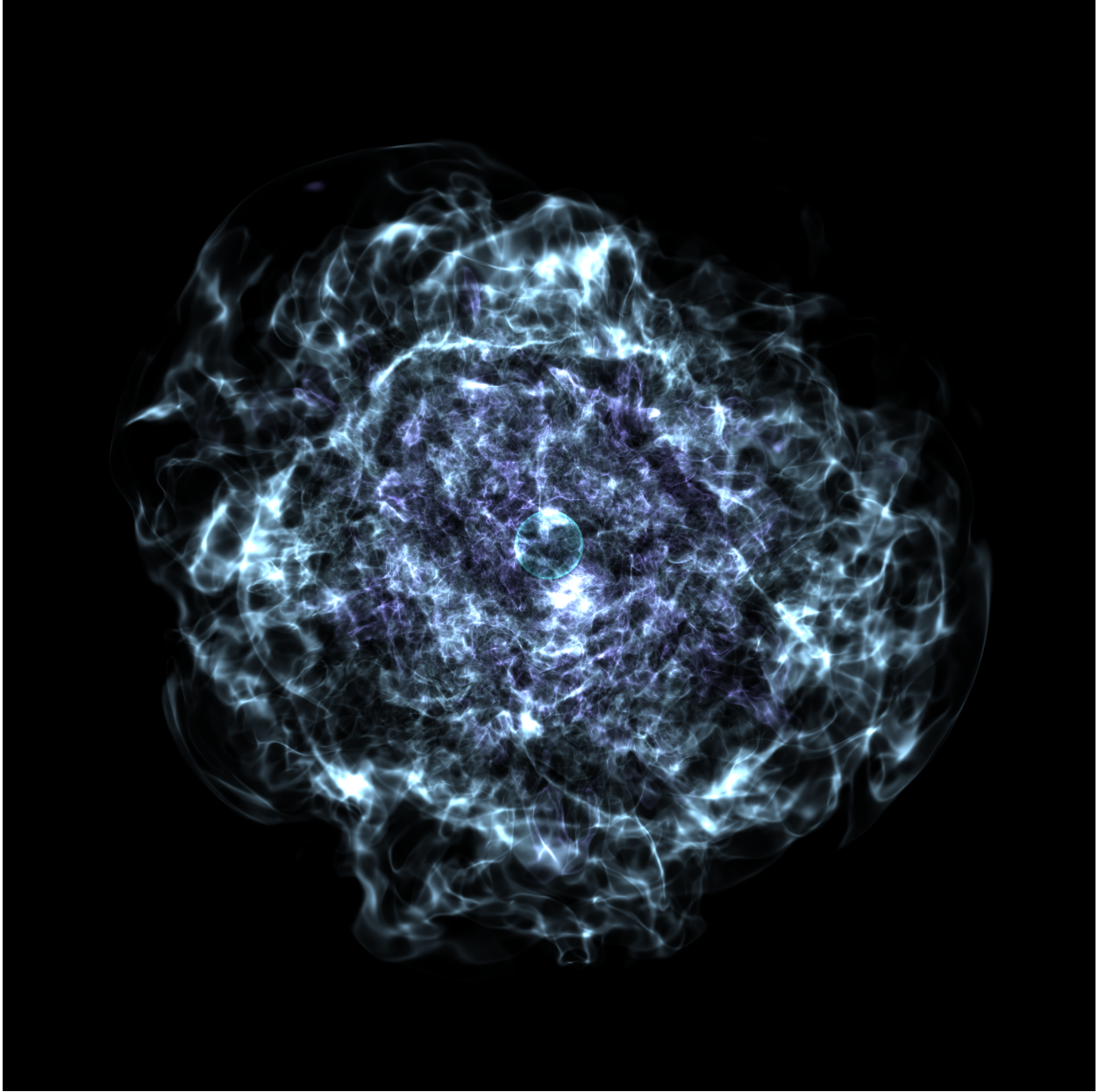
Figure 3.11: 3D volume rendering of the magnitude of the velocity field for the 4π `3D32kmPert` model at a time ≈ 2 seconds before iron core collapse. The teal contour denotes the edge of the iron core defined to be the radius at which $s \approx 4 \; k_{\mathrm{KB}}$ / baryon. At this time, the iron core spans a radius of $r \approx 1982$ km. The light purple plumes represent O-shell burning convection speeds following a Guassian with a peak at $|\mathbf{v}| \approx 300$ while the light blue plumes $|\mathbf{v}| \approx 100$ This image was made using `yt` and the color map library `cmocean`.

contraction of different regions of the model. For example, the base of the O-shell region begins

at a mass coordinate of $m \approx 1.68 \; M_\odot$ in all models but appears to expand outward to a coordinate

of $m \approx 1.72 \; M_\odot$ for the `3D32km` model at about $t \approx 200$ s. This expansion is not observed in the
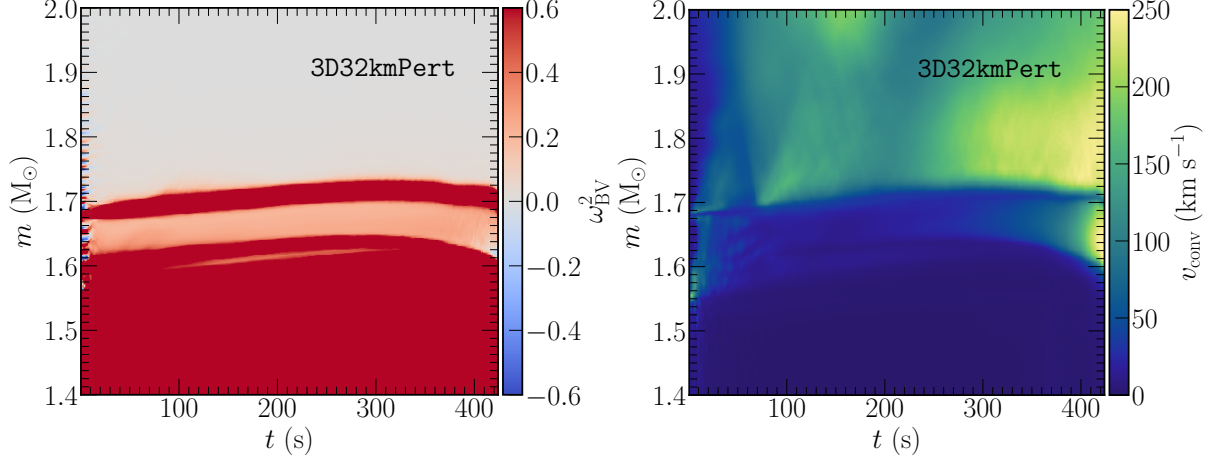
Figure 3.12: Same as in Figure 3.3 but for the `3D32kmPert FLASH` simulation.
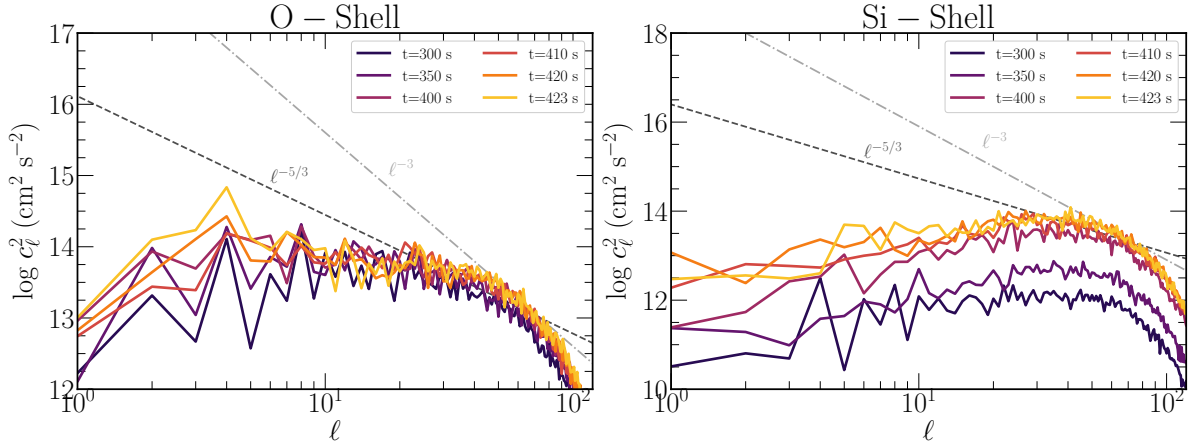
Figure 3.13: Power spectrum distribution of the spherical harmonic decomposition of the magnitude of the velocity in the O- and Si-shell regions at six different times for the `3D32kmPert` model.

`2D8km` model but is partially due to the initial transient at the beginning of the simulation, . The impact of this effect on our main results will be considered in Section 3.4.2.2.

3.4.2.1 Characterizing the convection in the `3d32kmPert` model

To characterize the scales of the convective eddies and the overall evolution of the strength of convection throughout the duration of the simulations we

$$c_\ell^2 = \sum_{m=-\ell}^{\ell} \left| \int Y_\ell^m(\theta, \phi) \, |\mathbf{v}|' \, (r_{\text{Shell}}, \theta, \phi) d\Omega \right|^2 , \qquad (3.5)$$
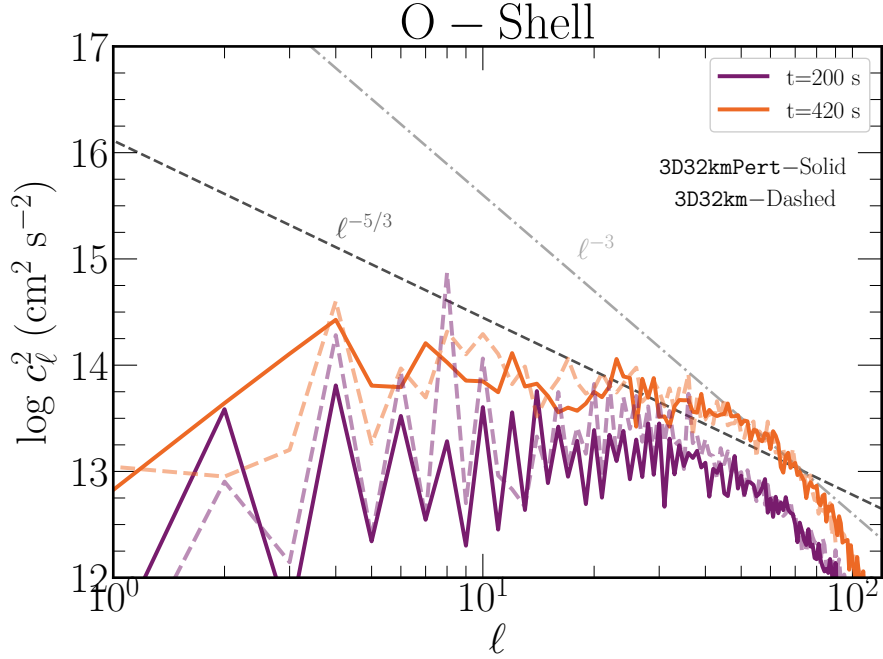
Figure 3.14: Same as in Figure 3.13 but only considering the O-shell region for the `3D32km` and `3D32kmPert` models at two different times.
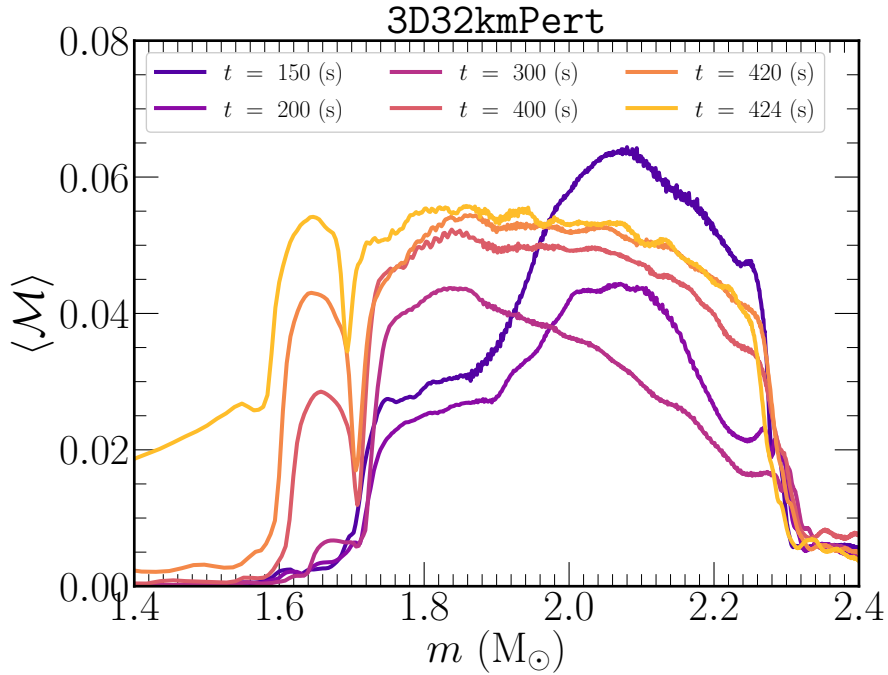
Figure 3.15: The profile of the angle averaged Mach number as a function of mass coordinate at six different times for the `3D32kmPert` stellar model. At $t = 424$ s the average Mach number reaches $\langle \mathcal{M} \rangle \approx 0.06$ in the Si-shell and at the base of the O-shell.
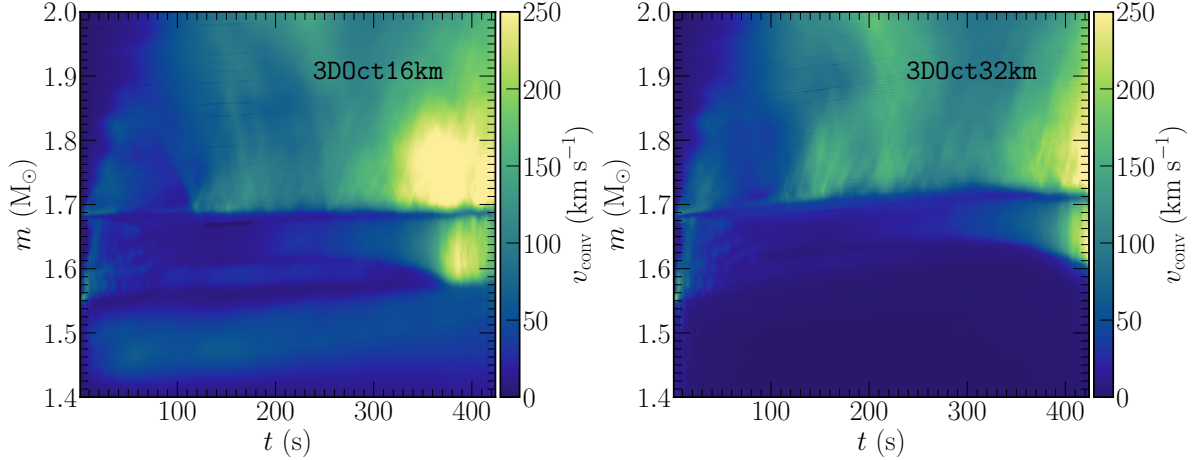
Figure 3.16: The evolution of the convection velocity profiles for the 16km and 32km 3D octant models.

In Figure 3.14, we compare the power spectrum for the perturbed and non-pertubed models at $t = 200$ s and $t = 420$ s. At $t = 200$ s, the unperturbed model (purple dashed line) shows an excess in power at $\ell = 4$ and $\ell = 8$, also reflected by the Cartesian aligned nature of the convection shown in the top panel of Figure 3.10. The perturbed model (solid purple line) does not show excess power in these modes but instead shows a range of power across modes including those at larger scales at $\ell \leq 4$. When considering $t = 420$ s, the spectrum of the O-shell region for the unperturbed model (dashed orange line) shows a slightly larger peak at $\ell = 4$ and a deficit of power by an order of magnitude for the $\ell = 2$ and $\ell = 3$ modes. Despite these differences, the spectra at this time are relatively similar, both having a peak at $\ell = 4$ and an intermediate range of scales just below what is expected for a Kolmogorov scaling of $\ell^{-5/3}$.

In Figure 3.15 we show the angle-averaged Mach number profile as a function of mass coordinate for the 3D32kmPert model at six times. The Si-shell region is situated at a mass coordinate of approximately 1.6 to 1.7 $M_\odot$. The evolution of the Mach number in this region is further representative of the power spectra shown in Figure 3.13. For the majority of the simulation, the Mach numbers in this region are on the order of $\langle \mathcal{M} \rangle \lesssim 0.01$. Only at times beyond $t \approx 300$ s do they increase significantly reaching values of $\langle \mathcal{M} \rangle \approx 0.06$ prior to collapse. In the O-shell region, at mass coordinates of $m \approx 1.7 - 2.3\ M_\odot$, the Mach numbers reach values of about $\langle \mathcal{M} \rangle \approx 0.06$ as
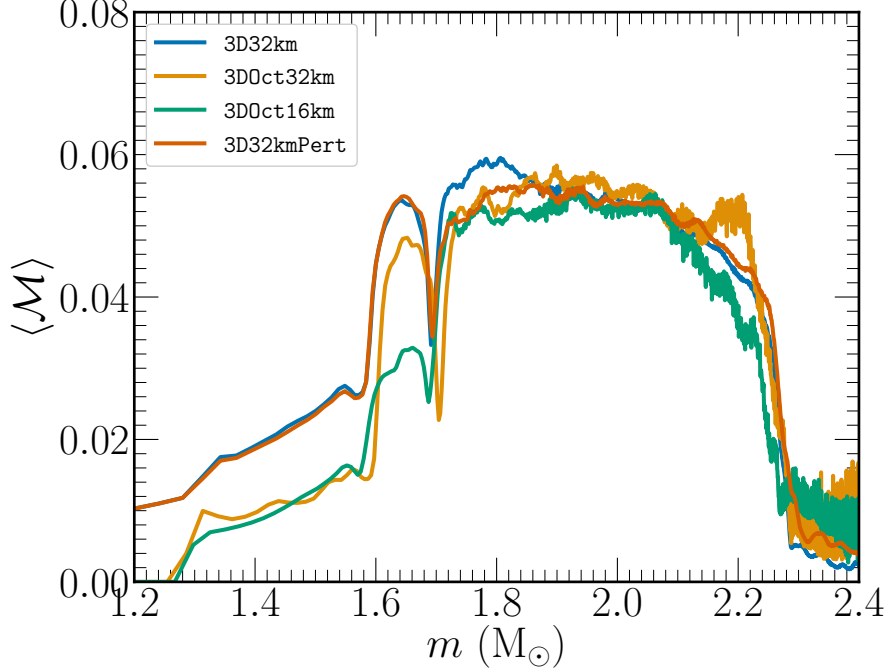
Figure 3.17: The Mach number profiles as a function of mass coordinate for the four 3D models .

early as $t \approx 150$. At late times, the O-shell region approaches Mach numbers of $\langle \mathcal{M} \rangle \approx 0.06$ near collapse.

3.4.2.2 Effect of Spatial Resolution and Octant Symmetry

To assess the impact of spatial resolution and octant symmetry we compare the results of the two 4π `3D32km` simulations with the two 3D octant models. In Figure 3.16 we show the time evolution of the convective velocity profiles for the `3DOct16km` and `3DOct32km` models. We can observe the same expansion of the O-shell region in the 32 km octant model as with the full 4π models. In contrast, the 16 km octant model does not appear to undergo this contraction and the base of the O-shell stays at a steady mass coordinate for the duration of the simulation. Moreover, the 16 km model reaches larger convective velocities in the Si- and O-shell regions at $t \approx 350$ s. This time corresponds to the same time at which we observe a peak in the Mach numbers in Figure 3.8 and is due to the merging of the convective and non-convective regions. These results suggest that due to the stability of the O-shell in the 16 km model, the model follows a slightly different evolution than that of the 32 km octant and 4π models characterized by larger convective velocity speeds that

103
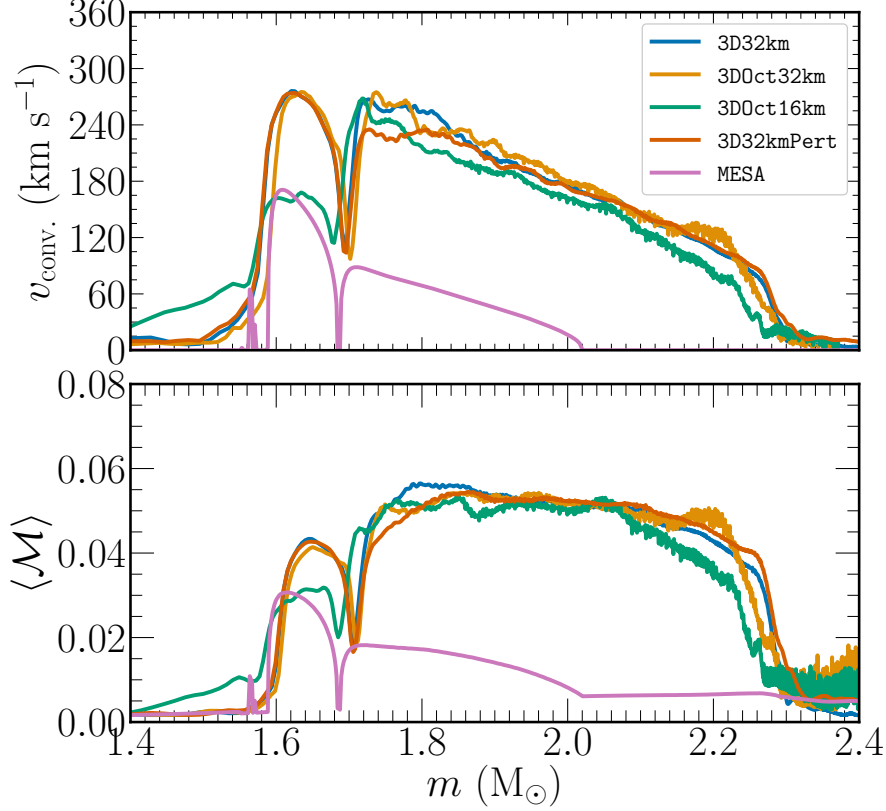
Figure 3.18: The convective velocity (top) and Mach number (bottom) for the 1D `MESA` model and angle-averaged profiles of the four 3D models at the $t \approx 420$ s.

facilitate merging of convective and non-convective regions in the Si-shell. Moreover, it suggests that these differences are attributed more to the finest grid spacing of the inner core region and less dependent on the symmetry imposed for the octant models. Despite the differences found in the evolution of the Si-shell region between these two models, the O-shell region appears less impacted by the difference in resolution and arrive at similar qualitative properties among the 3D models.

We can further determine the effect that resolution and symmetry has on our results by considering some keys aspects of our 3D stellar models at collapse that have significant implications for simulations of CCSNe. Couch & Ott (2013) considered the effect of ashpericities of imposed perturbations in the -shell regions characterized by the magnitude of the Mach number. They found large Mach number perturbations can result in enhanced strength of turbulent convection in the CCSN mechanism, aiding explosion. In Figure 3.17, we plot the profiles of the Mach number at the start of collapse, , for the 3D models. In general, we see that the estimates of the Mach number
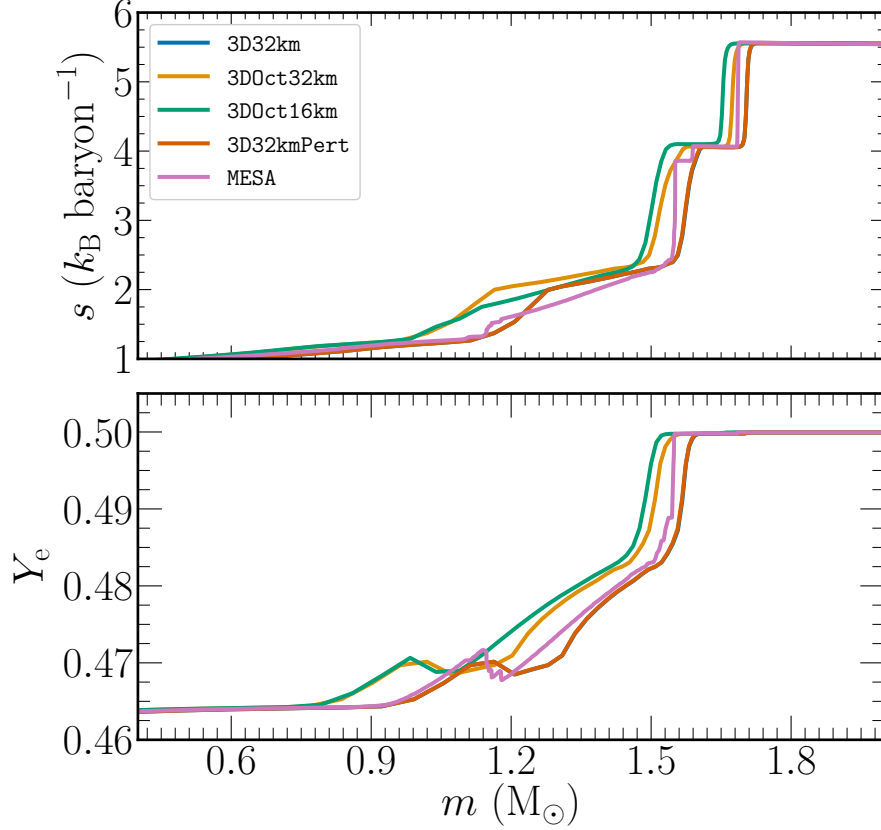
Figure 3.19: The specific entropy (top) and specific electron fraction (bottom) for the 1D `MESA` model and angle-averaged profiles of the four 3D models at the $t \approx 420$ s.

in the O-shell region between $\approx$1.7-2.3 $M_\odot$ across all models, the at the base of the O-shell in the 4π model, showing an $\approx 8\%$ larger value. The main difference is observed in the Si-shell region where the Mach number is approximately larger in the 32 km models, which agree with each other to $\approx 10\%$.

When comparing the 32 km octant and 4π models it is likely the case that the convective speeds are able to reach larger values as large scale flow is not suppressed at the symmetry planes. This is supported further by the larger non-radial kinetic energy in the 4π models as seen in Figure 3.9.

Another important diagnostic of the presupernova structure is the compactness parameter (O'Connor & Ott, 2011),

$$\xi_m = \left. \frac{m/M_\odot}{R(M_{\mathrm{bary}} = m)/1000 \text{ km}} \right|_{t=t_{\mathrm{cc}}}, \tag{3.6}$$

where a value of 2.5 $M_\odot$ is typically chosen for evaluation at the start of core collapse. The

value of this quantity in the progenitor star has been shown to be highly non-monotonic with ZAMS mass but gives some insight to the ensuing dynamics of the CCSN mechanism for a given progenitor (Sukhbold et al., 2018; Couch et al., 2019). We can compute this quantity for our three 3D models to determine how much variation exists due to the effects of resolution and symmetry. Using Equation (4.1) for the three 3D models at a time $t = 424$ s, moments before collapse. We find values of $\xi_{m=2.5M_\odot} = 0.0473$, 0.0474, 0.0331, and 0.0359, for the `3D32kmPert`, `3D32km`, `3DOct16km`, and `3DOct32km` models respectively. These values suggest that the imposed octant symmetry can under estimate the compactness of the stellar model at collapse by $\approx 25\%$ while the differences in grid resolution but assuming octant symmetry can result in a difference of less than $\approx 10\%$. The compactness value at approximately the equivalent time for the `MESA` model was $\xi_{m=2.5M_\odot} = 0.0492$ agreeing with the `3D32km` to within less than 4%. Our values are approximately a factor of two less than those found in Sukhbold et al. (2018) and a factor of four less than those in Sukhbold & Woosley (2014) .

3.4.3   Comparison between the 1- and 3D Simulations

In this subsection we compare the angle-averaged properties of the of the 1D `MESA` model and the 3D models at a time near iron core collapse. In Figure 3.18 we show the convective velocity (top) and Mach number (bottom) for these models at $t \approx 420$ s. Considering first the O-shell region, situated at a mass coordinate between $m \approx 1.7 - 2.3\ M_\odot$, the convective velocity speeds of the 3D models agree quite well in shape and magnitude. This is with exception to the `3DOct16km` model for which the velocities in this region are $\approx$ 5-10 km s^{-1} slower. In this region, the 1D `MESA` model matches the shape of the convective velocity profile somewhat well but predicts a region with considerable convective activity that is smaller in extent, ranging only from $m \approx 1.7 - 2.0$ $M_\odot$. Additionally, the magnitude of the speeds in this region according to MLT are significantly less, $\approx 4 - 5$ times less, than the values found in our 3D models. The Si-shell region is situated at a mass coordinate of $m \approx 1.55 - 1.7\ M_\odot$. The convective speeds in the 3D 32 km models agree well within this region while the `3DOct16km` model shows a lower speed of $v_{\text{conv.}} \approx 160$ km s^{-1}

owing to the merging of the convectively burning and non-convectively burning regions discussed in Section 3.4.2. The 1D MESA model agrees with 3DOct16km remarkably well in the shape and magnitude of the convective velocity speeds in this region with only slight differences at the outer edge of the Si-shell region being steeper in the 3D model. These trends follow a similar behavior when looking at the Mach number profiles. The MESA model agrees well in shape and magnitude with the 3DOct16km model but significantly underestimates the values in the O-shell region.

We consider the core properties in Figure 3.19 where we show the specific entropy (top) and electron fraction (bottom) for the same models considered in Figure 3.18. Note that owing to the "inner boundary condition" used for the core, the specific electron fraction for all the models up to a mass coordinate of $m \approx 0.8\ M_\odot$ should be the same value. All models follow a similar specific entropy profile with only minor differences in mass of the iron core, the mass coordinate where $s \approx 4\ k_B$ baryon^{-1}. Qualitatively, the specific entropy and electron fraction profiles for the 3D simulations are smoother than those of the MESA model.

3.5 Summary and Discussion

We have investigated the long term, multidimensional, hydrodynamical evolution of a 15 $M_\odot$ star for the final seven minutes of Si- and O- shell burning prior to and up to the point of iron core collapse. Using the FLASH simulation framework we evolved eight stellar models at varying resolution, dimensions, and symmetries to characterize the nature of the convective properties of the stellar models and their implications for CCSN explosions.

We find that in general the angle averaged properties of the multidimensional models with predictions made by MESA. The largest differences observed were found when comparing the convective velocities in the O-shell region to those in the MESA model. . Our 2D models showed a convectively active Si-shell region with peak velocities of approximately 500 km s^{-1} near collapse and Mach numbers of ≈ 0.1 near collapse. Within the O-shell region the 2D models show slightly slower convective speeds of ≈ 400 km s^{-1} and Mach numbers of 0.8-0.12 depending on the resolution of the simulation. The 3D models show velocities and Mach numbers lower than this in

all cases. The 4π 3D models had convective velocities of $\approx$ 240-260 km s^{-1} in the Si- and O- shell moments prior to collapse with Mach values of 0.06.

To characterize the behavior of the convection of the 4π 3D , we computed power spectra of the Si- and O-shell regions by at different times throughout the simulation.

However, despite the differences between these evolutionary paths in the Si-shell, the results of the O-shell region appear largely unaffected by resolution or geometry, resulting in quantitatively similar properties near collapse in all of the 3D models. When comparing the 3D models for different resolutions and symmetries we also found that the Mach number profiles in the O-shell region agreed across all models with only a slight difference shown in the 4π where larger Mach numbers ($\approx$ 8%) are found at the base of the O-shell. The Si-shell region Mach number profiles showed that the `3DOct16km` model has a smaller value of $\approx$ 0.03 while the `3DOct32km` reached a value approximately twice of that. This difference is again linked to the merging of the convective and non-convective regions in the 16 km models. Another important diagnostic linking the presupernova structure to the dynamics of the CCSN mechanism is the compactness parameter. When comparing values of this parameter,

In C15, they investigated the final three minutes of Si-shell burning in a $15M_\odot$ star evolved assuming octant symmetry and a reaction network that included enhanced electron capture rates. They found that convective speeds in the silicon shell reach values of 80-140 km s^{-1} near collapse. These values are approximately a factor of smaller than what we find in all of our 3D simulations and a factor of four smaller than the results suggested by our 2D models. A major cause of these differences can likely be attributed to the length of their simulation. In all our multidimensional models considered here the convective velocity speeds did not increase considerably until about five minutes into the simulation. Measuring the turbulent kinetic energy power spectrum for their model they found the bulk of the energy residing at small l values (large scales), at $l \approx 4$ due to the imposed octant symmetry. They also found significant power at an $l \approx 10$ value for the Si-shell region near collapse.

Müller et al. (2016b) investigated the last minutes of O-shell burning in a 18 $M_\odot$ star. They

evolved the model for $\approx$ five minutes using a contracting inner boundary condition situated at the base of the O-shell mapped to follow the mass trajectory from the initial `Kepler` model. In their simulation of O-shell burning they find transverse velocity speeds that reach values of $\approx$ 250 km s^{-1} approximately a minute prior to collapse. These values are slightly larger by about 50-100 km s^{-1} than the values we find in all of our 3D models at a similar epoch. At the onset of collapse, they observe peak Mach numbers in the O-shell of $\langle \mathcal{M} \rangle \approx 0.1$ where we find a value of ~0.06. They compute the power spectrum for the radial velocity component into spherical harmonics to characterize the scale of the convection. At the early times, $t = 90.9$ s they find a similar characteristic scale at $l \approx 4$ where the bulk of the power resides. As the simulation evolves the bulk of the power in their model shifts to larger scales at $l \approx 2 - 4$.

Recently, Yadav et al. (2019) presented a 4π 3D simulation of O-/Ne-shell burning using a similar method as presented in Müller et al. (2016b). The simulation was evolved for 420 s and captured the merging of a large scale O-Ne shell merger leading to significant deviations from the properties predicted by the 1D initial model. In this work, they found at $t \approx 250$ s, the barrier separating the O- and Ne-shells disappears due to an increase in entropy in the O-shell leading to the merging of the two convective regions. The merger leads to large scale density fluctuations characterized by $l \approx 1 - 2$ modes within the merged shell. After the merger they observe velocity fluctuations on the order of 800 km s^{-1} that increase to as large at 1600 km s^{-1} near collapse. At collapse they observe Mach numbers of ≈ 0.13 in the O/Ne mixed region. These values both suggest that the merger can lead to significantly larger deviations from spherical symmetry than as suggested by the model presented in this work and other simulations of quasi-steady state convection prior to core collapse. Despite the merging of the two unique convective regions in the Si-shell observed in most of our models, we do not observe merging of different burning shell regions in any of our models.

High resolution, long term, 4π 3D simulations of CCSN progenitors can provide accurate initial conditions for simulations of CCSNe. An accurate representation of the state of the progenitor prior to collapse can have a favorable impact on the delayed neutrino-driven explosion mechanism

and has important implications for the predictions of key observables from CCSN simulations. In addition to fully 3D convection motions, most massive stars are also rotating differentially in their cores. In the presence of weak seed magnetic fields, this rotation can facilitate a large scale dynamo that can have an impact on the progenitor evolution and the explosion mechanism. As such, a next step in increasing the physics fidelity of supernova progenitor models would be to consider the impact of a rotating and magnetic progenitor on the observed scale and magnitude of perturbations within the late time burning shell regions. The direct link between multidimensional rotating and magnetic CCSN progenitors and the CCSN mechanism is an important question and is the direction of future work.

<div align="center">CHAPTER 4</div>

THE LAST TEN MINUTES BEFORE IRON CORE-COLLAPSE IN A MASSIVE STAR

Double, double toil and trouble; Fire burn and cauldron bubble. - W. Shakespeare (Macbeth)

This chapter is based on the unpublished work of C. E. Fields *et al* 2021 *ApJ*, in prep.

4.1   Abstract

Pre-supernova perturbations, either artificially imposed or from a multidimensional progenitor model, have been shown to have a qualitative impact on the properties of core collapse supernova explosion simulations including the multi-messenger signals they produce. These perturbations can drive explosion by increasing turbulence in the post shock region and the non-radial turbulent kinetic energy in the gain region. Here, we report on a set of four 4π 3D hydrodynamic simulations of O- and Si-shell burning in massive star models using `MESA` and the `FLASH` simulation framework, evolving up to the final ten minutes prior to iron core collapse. We consider initial 1D `MESA` models of 14-, 20-, and 25 $M_\odot$ to survey a range of O/Si shell density and compositional configurations. We characterize the convective shells of our 3D models and compare them to the corresponding 1D `MESA` models. In general, we find that the convective velocity speeds predicted by `MESA` are *three* to *four* times smaller than the angle-average speeds of our 3D simulations near collapse. In three of our simulations, we observe significant power in the spherical harmonic decomposition of the radial velocity field at harmonic index of $\ell = 2$ near collapse. Our results suggest that large-scale modes are common in massive stars near collapse and should be considered a key component in pre-supernova perturbations for CCSN explosion models.

4.2 Introduction

Three-dimensional (3D) simulations of core-collapse supernova (CCSN) explosions have benefitted from imposing pre-supernova velocity perturbations that aim to replicate nuclear burning in Si- and O-shell convective regions. The inclusion of these perturbations were shown to lead to larger non-radial kinetic energy in the gain region providing turbulent pressure behind the stalled shock capable of driving explosion in a model that otherwise failed to explode without perturbations (Couch & Ott, 2013). In the work of O'Connor & Couch (2018a), they impose perturbations in the 3D CCSN explosion of a 20 $M_\odot$ model (Farmer et al., 2016). Their 3D perturbed CCSN models evolved closer towards shock runaway and explosion but they did not observe shock runaway in any of the eight 3D simulations performed. The pre-supernova perturbations in the Si-shell region lead to an increase in the gravitational wave (GW) amplitude at $t_{\mathrm{pb}} \approx 200$ ms over a frequency band of 200 - 1000 Hz. This result suggests that convective perturbations can also lead to qualitative differences in the multi-messenger signals produced in CCSN simulations.

Work by Couch et al. (2015) presented the results of a 3D CCSN progenitor model evolved for the final ≈ 155 s prior to and including iron core collapse. Using this 3D progenitor model they performed two CCSN explosion simulations using the 3D progenitor model and a 1D angle-average of the 3D model. They found that increased turbulent motions in the post shock region in the 3D progenitor explosion model can aid in successful explosion. This model also showed a slight increase in turbulent kinetic energy in the gain region, a similar result to the CCSN models with artificial perturbations in Couch & Ott (2013). More recently, Müller et al. (2017) used the 18 $M_\odot$ 4π 3D progenitor of Müller et al. (2016b) to perform three 3D CCSN explosion models. In their 3D explosion model using a 3D progenitor they found an increasing diagnostic explosion energy and baryonic mass of the PNS values closer agreement with those expected from observations (Pejcha & Thompson, 2015). The two additional CCSN explosion models in their study - one a reduced velocity field 3D progenitor and the other a 1D angle-average initial model were less energetic and the 1D progenitor model failed to explode. The results of this study suggest that 3D progenitors

can also aide in closing the gap between low explosion energy and PNS properties predicted by other works using 1D progenitors (Burrows et al., 2020).

Multidimensional CCSN progenitor models have been performed recently (Müller et al., 2016b; Yoshida et al., 2019; Fields & Couch, 2020; Yadav et al., 2019; Yoshida et al., 2021). Many of these simulations show convective properties that suggest favorable impact on the neutrino-driven CCSN explosion mechanism. In Yadav et al. (2019) they observe large-scale mixing due to merger of the O- and Ne-shells, a results which lead to large radial mach numbers in the merged shell regions. Despite this progress, it is expected that the convective properties in massive star will span a range of strength and flow dynamics over the initial mass range for CCSNe (Müller & Janka, 2015). Currently, only a handful of 3D simulations sample this mass range and provide predictions for the Si- and O-shell convective properties of 3D massive star models.

In this Paper, we build on previous efforts exploring 3D progenitor models in the moments prior to collapse. We perform a total of four 4π 3D hydrodynamic simulations of Si- and O-shell burning for up to the final ten minutes prior to and including gravitational instability and iron core-collapse. We evolve models of initial $M_{\mathrm{ZAMS}} = 14$-, 20, and 25 $M_{\odot}$ using the `FLASH` simulation framework and the 1D stellar evolution code, `MESA` (Fryxell et al., 2000; Paxton et al., 2011, 2013, 2015, 2018). This work is novel because: (1) - we present four 3D long-term hydrodynamic simulations of O/Si shell burning in multiple progenitors, (2) - we investigate the impact of initial perturbations in pre-supernova hydrodynamic simulations in two 3D simulations of a 20 $M_{\odot}$ model, and (3) we compare the convective properties to the predictions of Mixing Length Theory (`MLT`) in three different initial progenitor models.

This paper is organized as follows. In § 4.3 we describe our computational methods and initial 1D `MESA` progenitor models. In § 4.4 we present the results of our 3D simulations including characterizing their convective properties. Lastly, in § 4.5 we summarize our main findings and compare them to previous works.

4.3 Computational Methods and Initial Models

Our methods follow those of Fields & Couch (2020) (hereafter referred to as FC20). We draw an initial 1D progenitor for mapping into 3D to simulate the final minutes of Si- and O-shell burning towards iron core-collapse. Here, we mainly highlight the difference in our initial conditions and the initial progenitor set chosen for this study.

4.3.1 1D `MESA` Stellar Evolution Models

We employ the stellar evolution toolkit, Module for Stellar Astrophysics (`MESA`-revision 12115) (Paxton et al., 2011, 2013, 2015, 2018, 2019), for our spherically-symmetric 1D models. In total, we evolve three solar metallicity, zero-age main-sequence (ZAMS) mass progenitors: $14M_\odot$, $20M_\odot$, and $25M_\odot$. Each progenitor is evolved in `MESA` from the pre-MS to a time approximately *10 minutes* prior to iron core-collapse.

We use temporal/spatial parameters from previous studies shown to provide adequate converge in core quantities at the level of uncertainty due to network size and reaction rates (Farmer et al., 2016; Fields et al., 2018). Our 1D models use the same approximate network as used in FC20, an α-chain network that follows 21 isotopes from ^{1}H to ^{56}Cr (Timmes et al., 2000). Our `MESA` models are non-rotating and do not include magnetic fields. Mass loss is included using the '`Dutch`' wind scheme with an efficiency value of η_{Dutch} =0.8. Mixing processes and efficiency values are the same as used in FC20. All `MESA` inlist used to produce these models will be made publicly available.

4.3.2 3D `FLASH` Hydrodynamic Stellar Models

We simulate a total of four 4π 3D hydrodynamic models using the `FLASH` simulation framework (Fryxell et al., 2000; Dubey et al., 2009). Our models solve the equations of compressible hydrodynamics using the directionally unsplit piecewise parabolic method (PPM), third-order spatial accuracy, solver implemented in `FLASH` (Lee & Deane, 2009). We employ an HLLC Riemann solver (Toro, 1999) and use a Courant factor of 0.8. Self gravity is included assuming a monopole
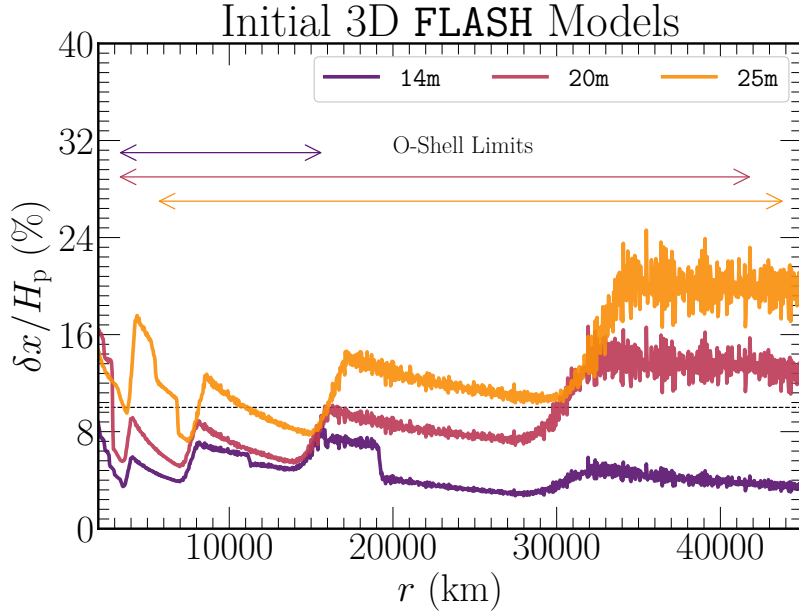
Figure 4.1: The angle-average cell resolution as a percentage of the relative pressure scale height for the three 3D models at $t = 0$. Also shown are the approximate O-shell radial limits. The dashed horizontal line corresponds to 10% of the pressure scale height.

($\ell = 0$) gravitational potential (Couch et al., 2013). Our domain extends to 100,000 km from the origin along an axis in Cartesian geometry. Each model uses adaptive mesh refinement (AMR) with up to eight levels of refinement.

The finest level of refinement for each model results in a grid spacing of ≈ 32.5 km. The approximate effective resolution for each model varies due to their different initial shell configurations. For the 14 $M_\odot$ model, the finest resolution level is situated at the center of the simulation and extends out to a radius of $r \approx 3500$ km. This region includes the entire iron core and Si-shell resulting in an average resolution of ≈ 8 % of the local pressure scale height, $H_\mathrm{p} = P/\rho G$. The resolution decreases beyond this radius by a factor of two out to $r \approx 7100$ km. In this region, our simulation has a resolution that equates to $\approx 7\% H_\mathrm{p}$. The resolution continues to decrease beyond this radius based based on logarithmic changes in specific density, pressure, and velocity. After initialization, the location of the refinement levels do not change throughout the simulation. The 20 $M_\odot$ model has a qualitatively similar grid with the finest resolution level containing the entire

iron and Si-shell region. In the 25 $M_\odot$, model, the finest refinement level extends out to $r \approx 4100$ km. Unlike the other models, in the 25 $M_\odot$ model, this only encompasses the iron core and a portion of the Si-shell region. Within this finest refinement level, the resulting resolution equates to an average of $\approx 5\% H_p$. Beyond this radius, the grid resolution is decreased by a factor of two but the simulation maintains an approximate effective resolution of $\approx 5\% H_p$ out to $r \approx 8100$ km. The remainder of the grid resolution is similar to the other two models. In Figure 4.1 we show the average cell reolution as a percentage of the pressure scale height according to the 3D models. Also shown are the approximate O-shell radial limits for each model.

Properties of the initial progenitor models at the time of mapping

Initial Mass	$\xi_{2.5}$	$r_{\text{low,Si}}$	$r_{\text{high,Si}}$	C_{Si}	$\mathcal{M}_{\text{rad.,Si}}$	$r_{\text{low,O}}$	$r_{\text{high,O}}$	C_{O}	$\mathcal{M}_{\text{rad.,O}}$	Simulation Time
$(M_\odot)$		(km)	(km)	(g s^{-1})		(km)	(km)	(g s^{-1})		(sec)
14m	0.016	2400	3000	1.2×10^{28}	3.0×10^{-3}	3130	15820	8×10^{27}	1.6×10^{-2}	530.71
20m	0.151	2366	2854	5×10^{27}	1.0×10^{-3}	3120	42000	7×10^{27}	5.0×10^{-3}	643.83
25m	0.519	3700	4150	6×10^{27}	8.0×10^{-4}	5500	44000	5.25×10^{27}	3.2×10^{-3}	606.95

Table 4.1: 3D FLASH simulation properties of the initial progenitor models at the time of mapping including the initial mass, compactness at a mass coordinate of $m = 2.5\ M_\odot$, O/Si-shell radial limits, the scaling factor used to produce a 1 or 5% convective velocity profile according to MESA, the resulting radial mach number due to the perturbations, and the total simulation time.

The 3D models are initialized with perturbations in the Si- and O-shell region that are informed by their 1D `MESA` counterpart at the time of mapping. We use the same notation as in FC20, also used in Müller & Janka (2015) and O'Connor & Couch (2018b). In Table 4.1 we show properties of our initial progenitor models at the time of mapping into `FLASH` including the compactness ($\xi_{2.5}$), shell radii, simulation time, perturbation scaling factor C, and the resulting radial mach number at the start of the simulation caused by the perturbations. The imposed perturbations are performed in the r and θ components of the velocity field with topology determined by spherical harmonic indices and a scaling factor informed by the convective velocity profile of the 1D `MESA` model.

For the 14 $M_\odot$ model we take the Si-shell region to be at a location of ≈ 2400 km to 3000 km within this region, a scaling factor C of 1.2×10^{28} g s^{-1}. The O-shell region is taken to be from ≈ 3130 km to 15820 km and we choose a value of C of 8.0×10^{27} g s^{-1}. The locations of the shell regions were determined by the composition profiles and corresponded to the radius at which the isotope was the most abundant and had a non-zero convective velocity according to `MESA`. For the Si-shell, the C value was chosen to represent the average value needed to produce 1% of the convective velocity predicted by `MESA`. In other words, we compute an approximate scaling factor such that the initial angle-average `FLASH` convective velocity profile is equal 1% of the mean convective speed in the 1D `MESA` model in this region. In the O-shell region the value of C was chosen in a similar way except corresponding to 5%. The Si-shell region used spherical harmonic and radial numbers of $n = 1, \ell = 9, m = 5$ while the O-shell region used $n = 1, \ell = 7, m = 5$ (initially larger scale perturbations). The resulting average radial mach number in the Si- and O-shell regions due to these perturbations were $\mathcal{M}_{\mathrm{rad.,Si}} \approx 3 \times 10^{-3}$ and $\mathcal{M}_{\mathrm{rad.,O}} \approx 1.6 \times 10^{-2}$, respectively.

Our 20 $M_\odot$ model was initialized in a similar fashion except the scaling factors chosen for both the Si- and O-shell regions corresponded to a value of 1% of the average value needed to reproduce the convective velocity speeds predicted by `MESA`. In this model, the Si-shell region is located $\approx$ 2366 km to 2854 km within this region, a scaling factor C of 5.0×10^{27} g s^{-1}. The O-shell region is located at ≈ 3120 km to 42000 km and we choose a value of C of 7.0×10^{27} g s^{-1}. For this

particular model, a non-convective predominantly silicon region exists between these two regions. This model uses the same perturbation shape parameters. In this model, the initial perturbations produce average radial mach numbers in the Si- and O-shell regions of $\mathcal{M}_{\mathrm{rad.,Si}} \approx 1 \times 10^{-3}$ and $\mathcal{M}_{\mathrm{rad.,O}} \approx 5 \times 10^{-3}$, respectively.

Lastly, the $25 M_\odot$ model has a Si-shell region from ≈ 3700 km to 4150 km where we apply a scaling factor of C of 6×10^{27} g s^{-1}. The O-shell region for this model extends from 5500 km to 44000 km where we use an average scale factor of C of 5.25×10^{27} g s^{-1}. Similar to the 20 $M_\odot$ model these scalings were chosen to reproduce approximately 1% of the convective velocity predicted by MESA at the time of mapping. This model uses the same spherical shape parameters as the $20 M_\odot$ model as well. In this model, the perturbations produce mach numbers in the SI- and O-shell regions of $\mathcal{M}_{\mathrm{rad.,Si}} \approx 8.0 \times 10^{-4}$ and $\mathcal{M}_{\mathrm{rad.,O}} \approx 3.2 \times 10^{-3}$, respectively.

Our FLASH simulations utilize the approximate 21 isotope network (approx21) with the same updated weak reaction rate used for electron capture onto ^{56}Ni from Langanke & Martínez-Pinedo (2000). The Helmholtz stellar equation of state (EoS) as implemented in FLASH is used in all of our 3D simulations (Timmes & Swesty, 2000). We do not artificially enhance the total electron capture rates in any simulations presented here. All of our 3D simulations utilize a similar methods as in FC20 where we produce a 2D table from the MESA profile data for the inner 1000 km from the point of mapping into FLASH until iron core-collapse. Lagrange linear interpolation is then performed in time and radius to obtain a solution FLASH models without the need for a call to the nuclear reaction network. This mapping provides a time-dependent inner boundary condition that ensures the model follows the central evolution of the MESA model but is still significantly below the regions of interest for our study of the multi-D hydrodynamic properties. To help reduce artificial transient during mapping, we use the methods of Zingale et al. (2002) in which we remap the 1D MESA models to a new uniform grid with four times higher resolution than the finest grid spacing. We then alter the density profile to enforce hydrostatic equilibrium (HSE) and close the system with a call to the equation of state.

Figure 4.2: Profiles of the specific entropy (top), electron fraction (middle), and density (bottom) for the three 1D `MESA` models at time of mapping into `FLASH`. Also shown is the 15 $M_\odot$ progenitor model from FC20 denoted by the black dashed line.

4.3.3 Progenitor Models

In this study, we aim to explore the range in hydrodynamic properties observed in pre-SN models in their evolution towards iron core-collapse. A metric commonly used to predict the outcome of a

Figure 4.3: Profiles of the convective velocity (top), oxygen-16 mass fraction (middle), and silicon-28 mass fraction (bottom) for the 1D MESA models at the same time as Figure 4.2.

pre-SN models is the compactness parameter,

$$\xi_m = \left. \frac{m/M_\odot}{R(M_{\mathrm{bary}} = m)/1000 \text{ km}} \right|_{t=t_{\mathrm{cc}}} .$$ (4.1)

This quantity has been used to determine the outcome: explosion vs. implosion, in a range of different progenitors (O'Connor & Ott, 2011; Sukhbold et al., 2016). In general, it has been shown that a lower compactness value favors explosion while a higher value $\xi_{2.5} > 0.45$ can result in

failed explosion and formation of stellar mass black hole. The compactness parameter has also been shown to correlate with the integrated total neutrino emission count in successfully exploding model (Warren et al., 2020). Models with larger $\xi_{2.5}$ were found to produce more to neutrinos owing to the more massive baryon proto-neutron star (PNS) mass associated to its larger value.

To sample the range of compactness seen in other studies we choose our initial 1D MESA to span a range of values of compactness: $\xi_{2.5} \approx 0.016$, 0.151, and 0.519, for the 14 $M_\odot$, 20 $M_\odot$, and 25 $M_\odot$ models respectively. For comparison, the 15 $M_\odot$ model of FC20 had a core compactness of $\xi_{2.5} \approx 0.014$. O'Connor & Ott (2011) predict that models with $\xi_{2.5} \geq 0.45$ such as our 25 $M_\odot$ would failed to explode (assuming a moderately stiff EoS such as LS220 (Lattimer & Swesty, 1991)) forming a BH within 0.5 s post bounce. It should be noted that the core compactness values quoted in Table 4.1 should be viewed as a lower limit as we measure this quantity at the time of mapping into FLASH and not at core-collapse as done in the works referenced above.
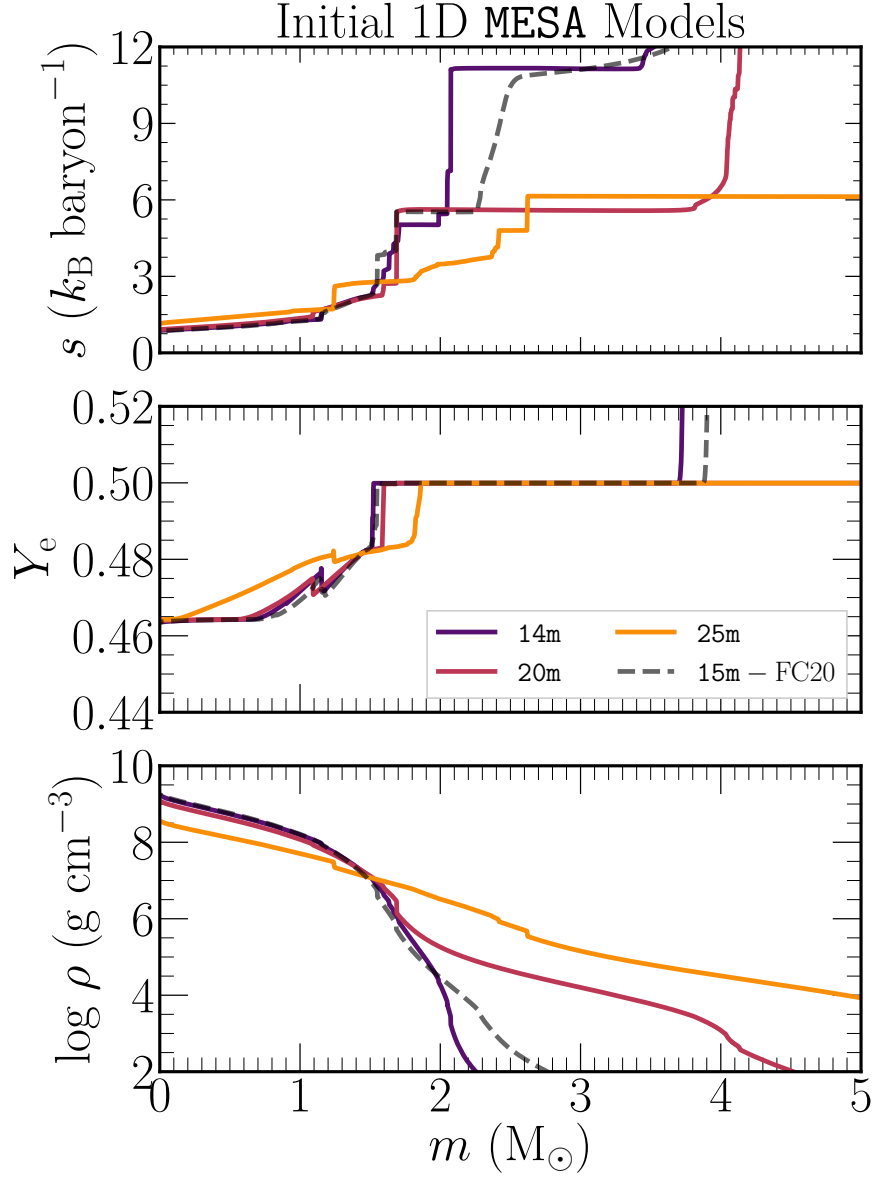
In Figure 4.2 we show the specific entropy (top), electron fraction (middle), and density (bottom) for the 1D MESA models at time of mapping into FLASH. For comparison, we also plot the 15$M_\odot$ progenitor from FC20. Most of the models show similarities in their profile properties. The 25$M_\odot$ represents the most shallow density profile likely contributing to its larger compactness value. The 14$M_\odot$ density is most similar to that of the 15$M_\odot$ model of FC20. The 20$M_\odot$ has a density profile whose shallowness is somewhat in between the 14$M_\odot$ and 25$M_\odot$ model. This is consistent with the trend seen for the values of compactness for these models.
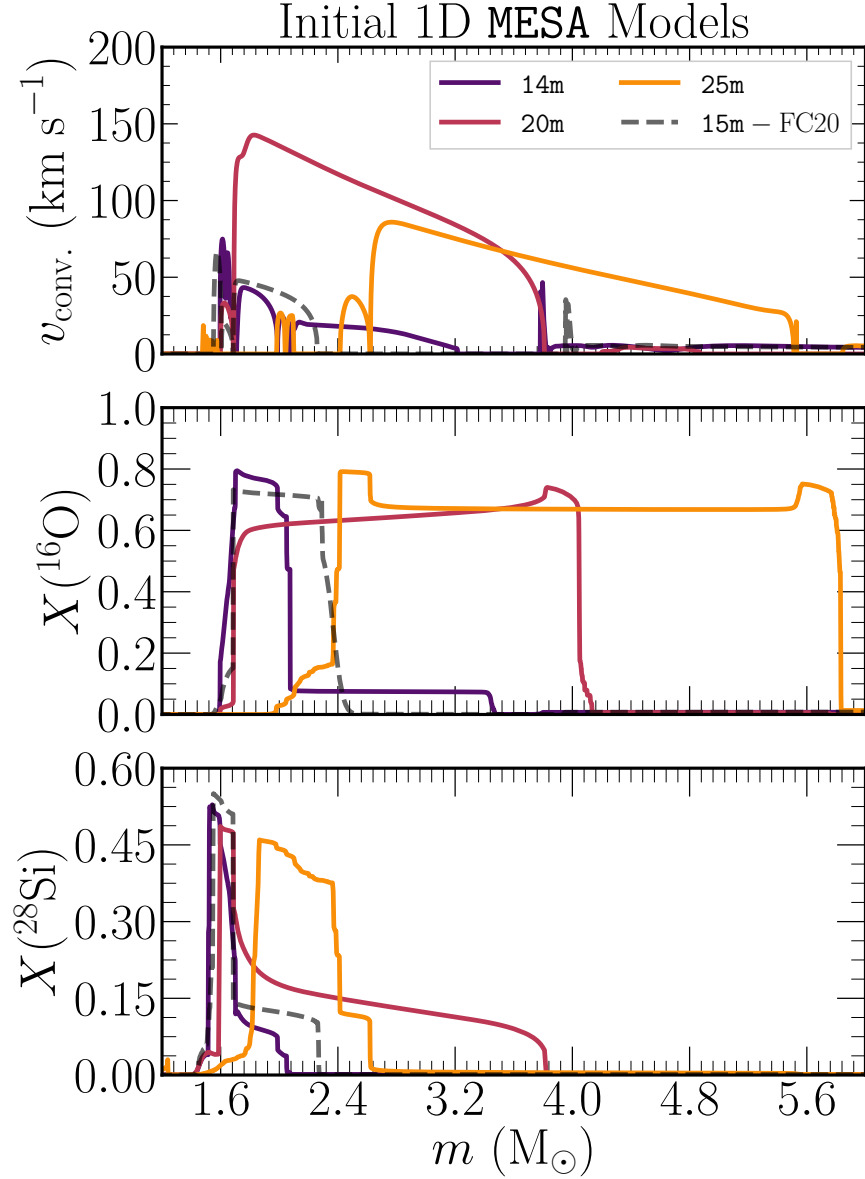
In Figure 4.3 we show the convective velocity (top), oxygen-16 mass fraction (middle), and silicon-28 mass fraction (bottom) for the 1D MESA models time of mapping into FLASH. The 14$M_\odot$ and 20$M_\odot$ models, similar to the 15$M_\odot$ model from FC20 have a rather narrow Si-shell region. However, in the 25$M_\odot$ model we see a Si-shell region that spans from $m \approx 1.9$-2.4$M_\odot$. The 14$M_\odot$ and 15$M_\odot$ model have a similar O-shell region width and location. The 20$M_\odot$ model has a much wider O-shell region that extends from $m \approx 1.4$-4.0 $M_\odot$. The 25$M_\odot$ model also has a larger O-shell extending from $m \approx 2.4$-5.7 $M_\odot$.

The convection speeds as predicted by MESA and mixing length theory (MLT) are largest in the
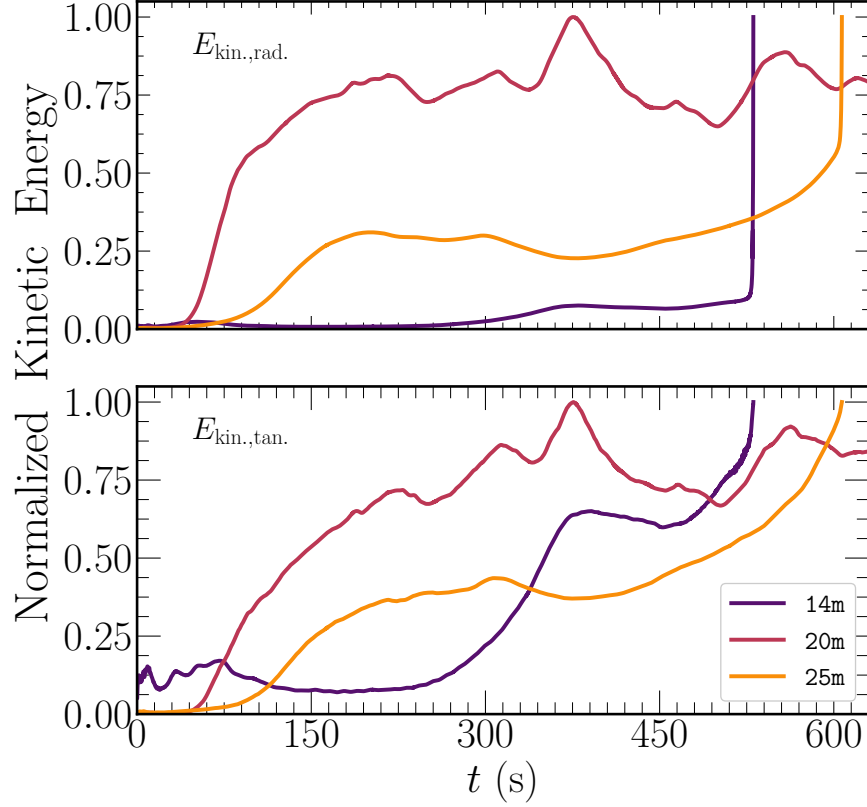
Figure 4.4: Time evolution of the radial and tangential $(\theta + \phi)$ kinetic energy throughout the simulation. For comparison between the different progenitor models, we normalize each simulation to the peak kinetic energy in the simulation.

O-shell region for the 20 $M_\odot$ model with $v_{\text{conv.}} \approx 120$ km s^{-1}. The 25 $M_\odot$ model shows the second largest speeds with $v_{\text{conv.}} \approx 70$ km s^{-1}. The 14 $M_\odot$ and 15 $M_\odot$ model show similar, slower speeds of $v_{\text{conv.}} \approx 40$ km s^{-1}. In all of the 1D models, the convection in the Si-shell region is either weak or non-existent, leading to speeds of $v_{\text{conv.}} \lesssim 50$ km s^{-1}.

4.4 3D Evolution To Iron Core-Collapse In Multiple Progenitors

We evolve a total of three 4π3D hydrodynamical massive star models for approximately the final 10 minutes up to and including gravitational instability and iron core-collapse. Each simulation is evolved up to the simulation time corresponding to iron core-collapse as determined by MESA. This time corresponds with to that at which the peak infall velocity within the iron core exceeds 1000 km s^{-1}. In the following section we summarize the general properties of our three models, analyze

Figure 4.5: Slice plot for the specific ^{28}Si mass fraction (left column), the radial velocity (middle column), and the radial mach number (right column) in the $x - y$ plane at a time approximately 5 seconds before iron core-collapse for all three 3D models.

the character of turbulence in the convective shells for each model, and compare the angle-averaged profiles of our 3D simulations to the 1D results from MESA.
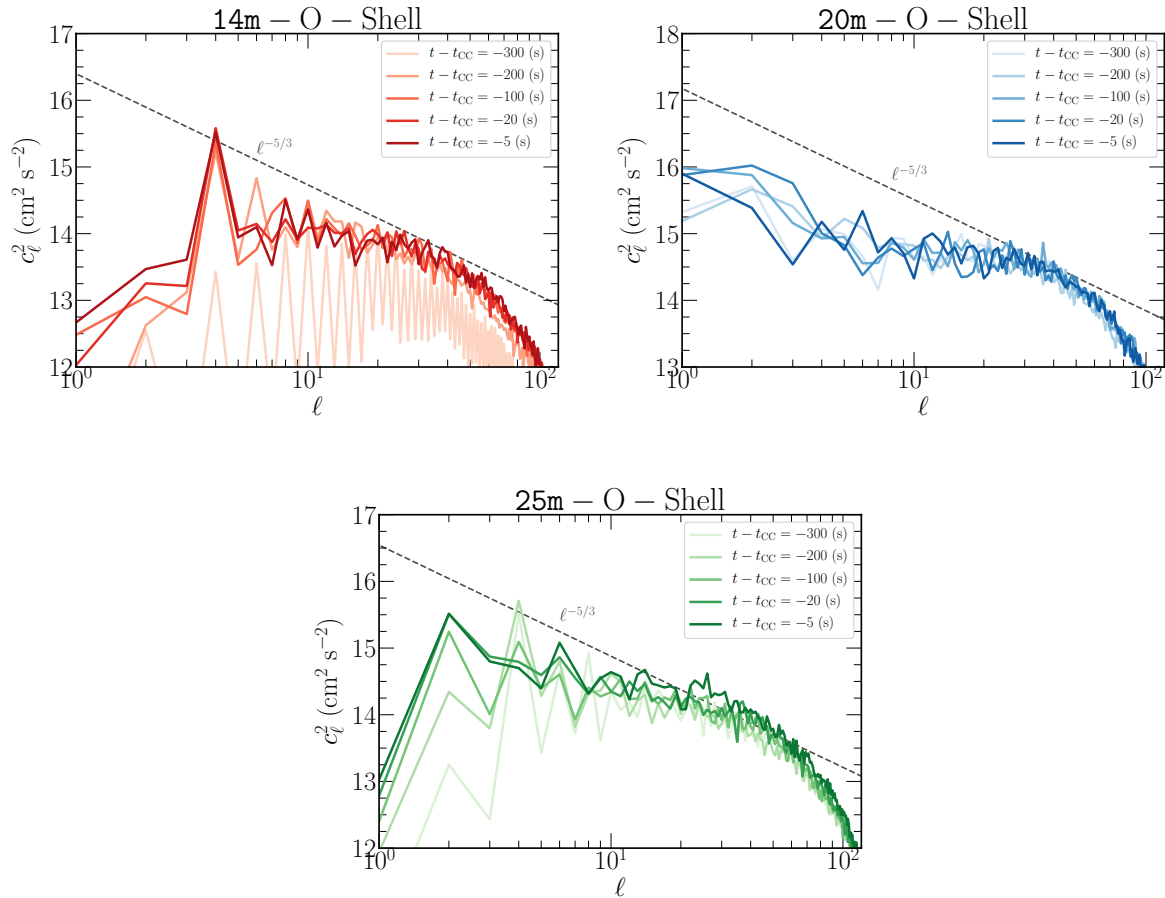
Figure 4.6: Power spectrum of the radial velocity decomposition in the convective O-shell region for the 3D models. Also shown is the expected Kolmogorov scaling of $\ell^{-5/3}$ for a turbulent flow in the inertial subrange.

4.4.1 Global Properties

In Figure 4.4 we show the time evolution of the radial and tangential components of the kinetic energy for the three 3D models. After an initial transient phase, the 14 $M_\odot$ model reaches a quasi-steady state represented by a near constant value of 20% of the peak total kinetic energy ($\approx 1 \times 10^{46}$ erg) until $t \approx 300$ s. Beyond this time, the convective velocity speeds in the O-shell region increase until a new local minima is found near $t \approx 375$ sec. At this point in the simulation, the convective velocity speeds are approximately 200 km s^{-1} throughout the shell with a corresponding total kinetic energy of $E_{kin.} \approx 1 \times 10^{47}$ erg. Assuming the initial radii for the O-shell configuration

we can compute an approximate convective turnover time of $\tau_{conv.,O} \approx 2r_O/v_{tan.,O} \approx 127$ s. The model undergoes a full convective turnover within this new state before core contraction continues to accelerate and increase the convective velocities further and pushing the model out of equilibrium towards collapse.

The 20-$M_\odot$ model follows a qualitatively different evolution. For the first ~160 s of simulation, the radial and tangential components of the kinetic energy show a continued increase until reaching a saturation point. At this time, the model maintains a total kinetic energy value of $E_{kin.} \approx 6\times10^{48}$ erg. Within the O-shell region during this time, we observe tangential velocity speeds of $v_{tan.} \approx 450$ km s^{-1}. Using the shell radius, we can similar convective turnover time $\tau_{conv.,O} \approx 172$ s. This suggests that our 20-$M_\odot$ model completed approximately three full convective turnovers in the O-shell region. In this simulation, the Si-shell region is thin and experiences only very weak convection. Therefore, our discussion will be limited to the O-shell for this model. We find large-scale mixing between the different shells in the 20 $M_\odot$ model.

Our 25 $M_\odot$ model follows an evolutionary path that is different yet from the other two models. The model reaches about 30% of the peak radial kinetic energy at a time of $t \approx 150$ s. The kinetic energy fluctuates only slightly once reaching this saturated value of total kinetic energy corresponding to a value of $E_{kin.} \approx 1 \times 10^{48}$ erg. We can estimate a convective turnover time for the O-shell utilizing the tangential velocity speeds of $v_{tan.} \approx 240$ km s^{-1} observed from $t \approx 150$ to 500 s. The speeds observed in the convective O-shell region lead to a turnover time of $\tau_{conv.,O} \approx 320$ s. The turnover time in the O-shell region suggests that our model completed one full turnovers from $t \approx 150$ to 500 s. At $t \approx 500$ s and beyond, the acceleration of the contracting iron core leads to a gradual increase of both of the components of the kinetic energy relative to their max values at collapse. In this model, we find a larger Si-shell region where convection becomes efficient and relevant to the dynamics of the model near collapse. At $t \approx 300$ s, the width of the Si-shell expands and the convective velocity speeds begin to increase. The speeds in this shell region saturate at a value of $v_{tan.} \approx 160$ km s^{-1} at $t \approx 400$ s, maintaining this value until core-collapse. Within the Si-shell region, we find a convective turnover time of $\tau_{conv.,Si} \approx 6$ s suggesting that from $t \approx 400$ s
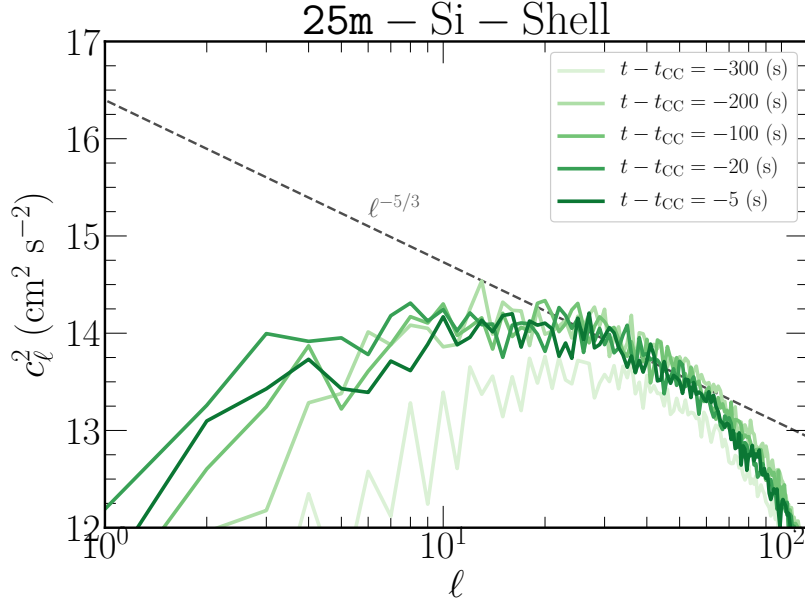
Figure 4.7: Same as in Figure 4.6 but for the 25 $M_\odot$ Si-shell region.

to core-collapse, our 25 $M_\odot$ captures 34 convective turnovers.

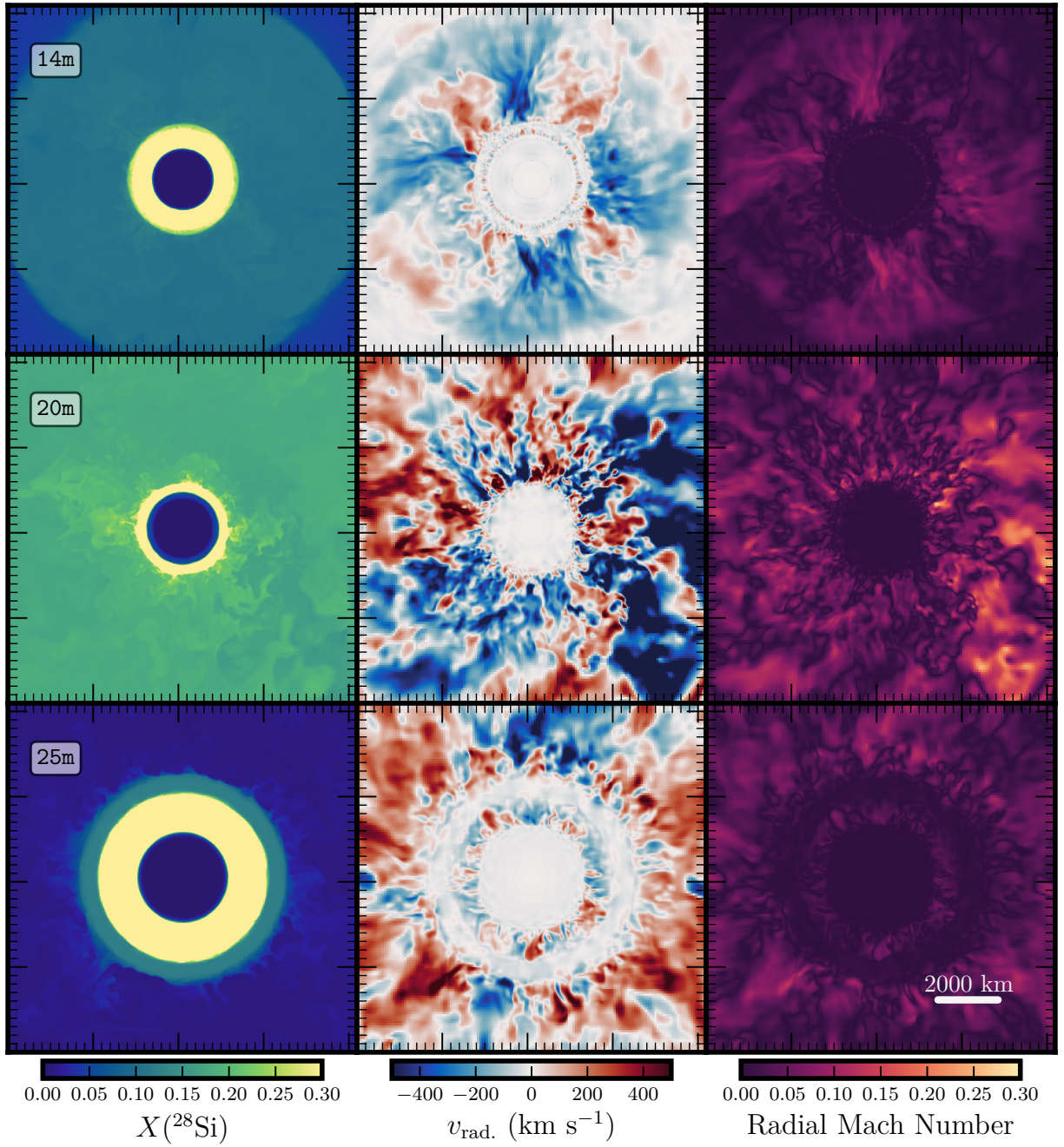In Figure 4.5 we show the a pseudocolor slice plot for the specific ^{28}Si mass fraction (left column), the radial velocity (middle column), and the radial mach number (right column) in the $x - y$ plane at a time approximately 5 seconds before iron core-collapse. The differences between the three simulations are shown here mainly in the relative size of the O-shell regions, convective flow properties, and mixing within the different shell regions.

4.4.2 Power Spectrum Of Convective Shells

To further quantify the convective properties in our three 3D models, we decompose the perturbed velocity field into spherical harmonics for the O-shell region (and also the Si-shell region for the 25 $M_\odot$ model). Similar to FC20, the total power for a given spherical harmonic order, ℓ, as

$$c_\ell^2 = \sum_{m=-\ell}^{\ell} \left| \int Y_\ell^m(\theta, \phi) v'_{\text{rad.}}(r_{\text{Shell}}, \theta, \phi) d\Omega \right|^2 , \qquad (4.2)$$

where $v'_{\text{rad.}} = v_{\text{rad.}} - \tilde{v}_{\text{rad.}}$, with $\tilde{v}_{\text{rad.}}$ corresponding to the mean background radial velocity speed at the chosen shell radius (Schaeffer, 2013). In the 14 $M_\odot$, 20 $M_\odot$, and 25 $M_\odot$ models the O-shell
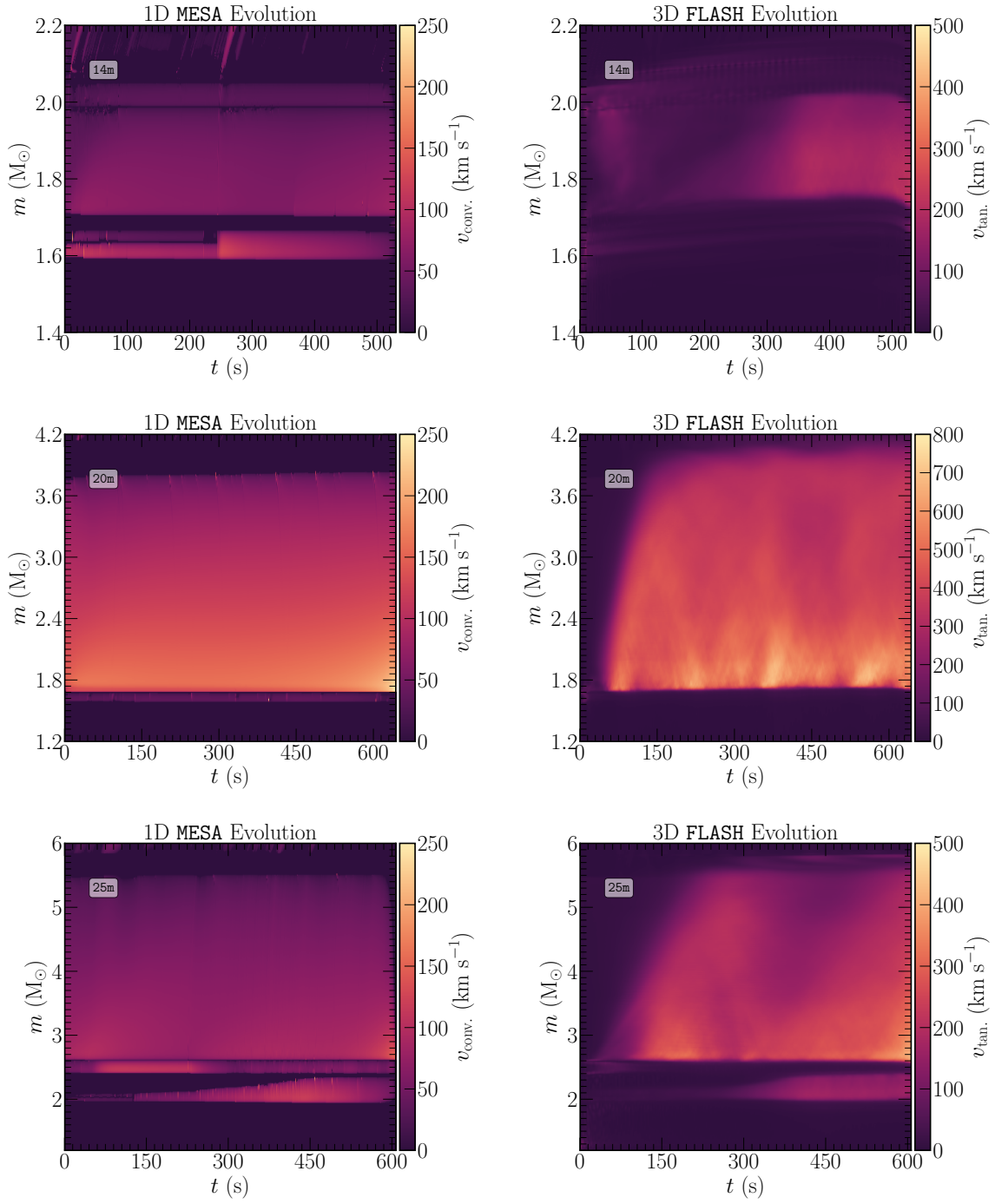
Figure 4.8: Pseudocolor heatmaps of the convective velocity profiles according to the 1D MESA models (left column) compared the angle-averaged profiles of the tangential velocity component for the three 3D FLASH simulations (right column). In all case, the scale for the 3D simulations is more than twice that of the MESA models.
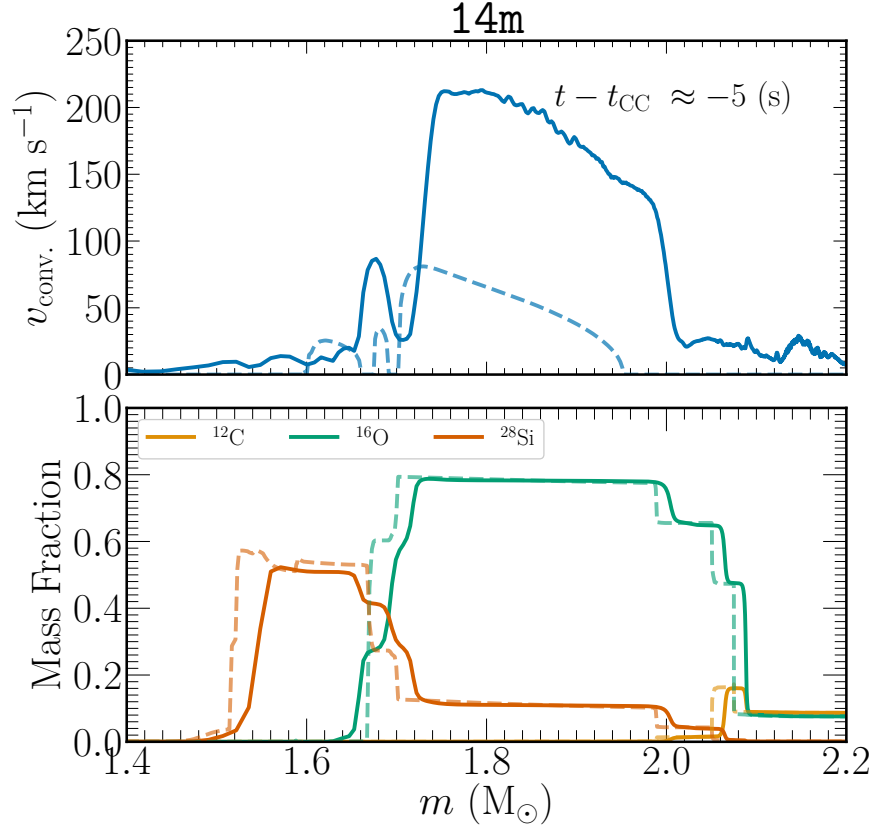
Figure 4.9: Angle-averaged tangential velocity (top, `FLASH`) and mass fraction profiles for ^{12}C, ^{16}O, and ^{28}Si compared to the 1D profiles from `MESA` at a time approximately 5 seconds prior to iron core-collapse. The dashed line in both plots corresponds to the `MESA` profile and the solid line corresponds to the 3D `FLASH` simulation.

regions are evaluated at r_O =5000 km, r_O =5000 km, and r_O =10 000 km, respectively. In the 25 $M_\odot$ model, the Si-shell region is evaulated at r_{Si} =3900 km.

In Figure 4.6 we show the resulting O-shell power spectra for all 3D models. The $14M_\odot$ model shows a relatively constant power spectrum during the last 100 s prior to collapse, the spectra is peaked at a spherical harmonic index of $\ell = 4$. Before this, at 300 seconds prior to collapse, convective is relatively underdeveloped and power is significantly less across scales. At $t - t_{CC} = -200$ s, the spectrum shows a peak at $\ell = 7$, the driving scale due to our initial perturbations. Energy is then transferred to larger scales at $\ell = 4$ and remains there for the duration of the simulations. As the simulation approaches collapse, we observe a slight increase in power at larger scales $\ell = 1, 2$. The excess in power at $\ell = 4$ is likely attributed to the Cartesian nature of
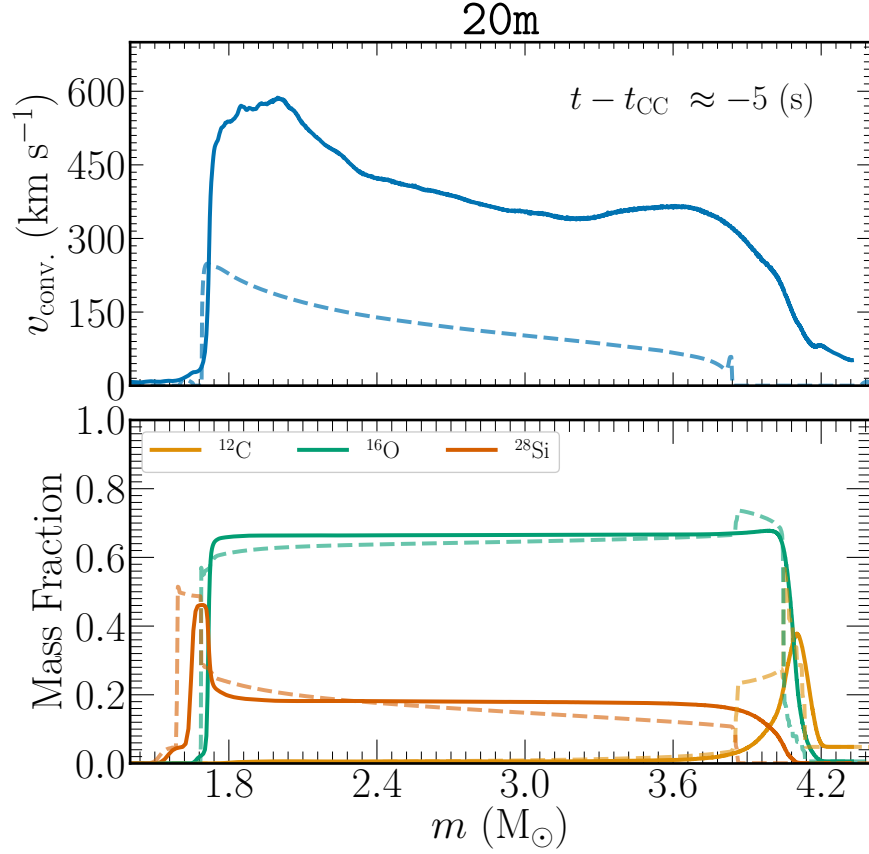
Figure 4.10: Same as in Figure 4.9 but for the corresponding 20 $M_\odot$ models.

our grid geometry and increased numerical viscosity near the grid axes.

The power spectrum for the $20M_\odot$ model (top right of Figure 4.6) shows a significantly different qualitative evolution towards collapse. At $t - t_{CC} = -200$ s, the power is distributed across many scales with a characteristic peak at $\ell = 2$ suggesting the flow is dominated by a large scale dipolar flow. A similar feature was observed in the $18M_\odot$ model of Müller et al. (2016b) in the final moments prior to collapse. At $t - t_{CC} = -100$ s, energy in this mode increases as well as in the $\ell = 1$ mode which becomes the dominate mode at this point. At later times closer to collapse, the peak at $\ell = 2$ increases with power in neighboring scales of $\ell = 1, 3$ increasing as well. In the final 5 seconds prior to collapse, energy in $\ell = 2, 3$ and transferred to intermediate scales of $\ell = 4 - 8$.

Our 25 $M_\odot$ simulation shows a qualitative evolution towards collapse in the convection shell that has traits of the 14 $M_\odot$ and 20 $M_\odot$ models. At early times, of at $t - t_{CC} = -300$ s and $t - t_{CC} = -200$ s an excess of power is again observed at an $\ell = 4$ mode suggesting grid aligned
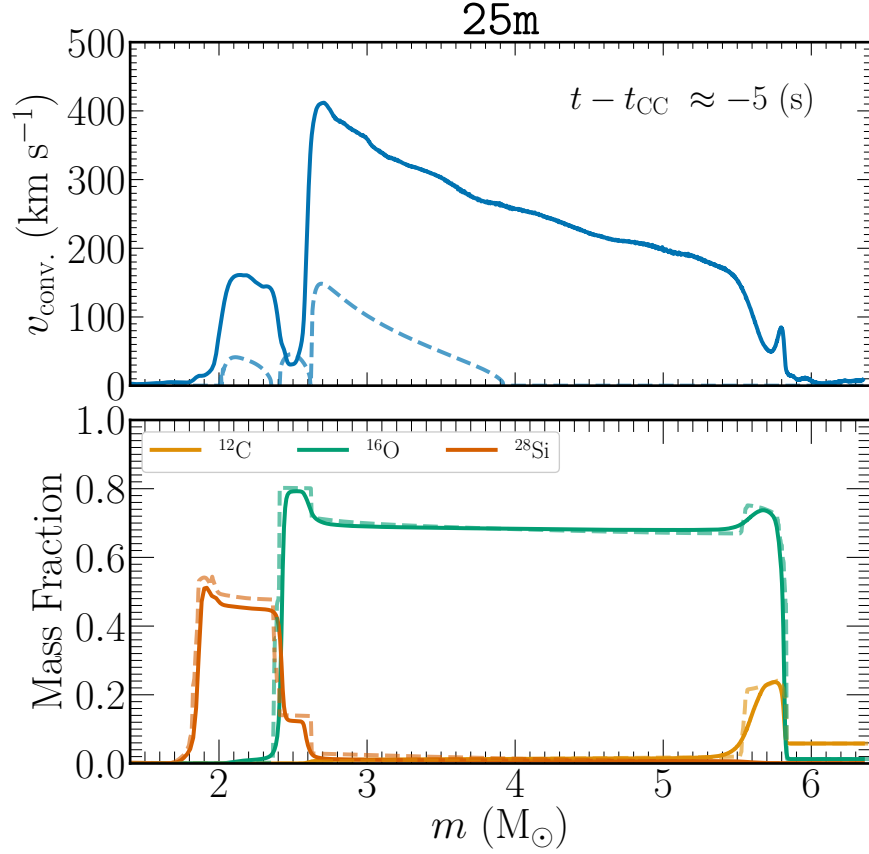
Figure 4.11: Same as in Figure 4.9 but for the corresponding 25 $M_\odot$ models.

artifacts contributing to the power spectrum of the radial velocity field. However, at times beyond this, the 25 $M_\odot$ model shows a reduction in power at this mode with a shift in the peak power contribution occurring at $\ell = 2$. The peak spherical harmonic mode remains $\ell = 2$ for the final 100 s of the simulation with a slight contribution at the driving scale ($\ell = 7$) observed in the final 5 seconds before core collapse.

In Figure 4.7 we show the power spectrum of the radial velocity field in the Si-shell region of the 25 $M_\odot$ model at five different times. Overall, the Si-shell region shows less power across scales. Convection begins to contribute to the power spectrum at times beyond 200 s prior to collapse. The spectrum at this point is characterized by a broad range of power at intermediate scales from $\approx \ell = 6 - 15$. At later times, we observe a slight increase in power at larger scales near $\ell = 2 - 4$. Five seconds prior to collapse, the dominant modes are found to be found near spherical harminc indices of $\ell = 10 - 20$.

4.4.3 Comparisons with 1D `MESA` models

An important aspect of our 3D will be their ability to inform 1D `MESA` models of CCSN progenitors. It was shown in FC20, that the 3D simulations found angle averaged convective speeds that were on the order of *four* times larger than predicted by `MESA`. Larger convetive velocity speeds in 3D CCSN progenitors than their 1D counterparts have implications that can lead to favorable conditions for explosion. Here, we compare angle average profiles from our full 4π 3D simulations to the 1D `MESA` counterparts.

In Figure 4.8 we show the time evolution of the angle-averaged tangential velocity component for each 3D model (right column) and the time evolution of the corresponding 1D `MESA` convective velocity profiles. The angle-average properties are weighted by the corresponding cell mass in each bin. For the profiles used to produce these heat maps we use $N = 2048$ bins and use linear interpolation to smooth the raw profiles. Qualitatively, most of the 3D models agree well with the `MESA` predictions. The largest differences are found for the 14 $M_\odot$ model where the convective region appears to expand and contract for the first few hundred seconds of the simulation at which point the tangential velocity speeds reach $v_\mathrm{tan.} \approx$ 200-300 km/s. The extent of the O-shell in the 20 $M_\odot$ model differs somewhat from the `MESA` model due to mixing at the convective boundary layer between the O- and C-shell regions. The 25 $M_\odot$ matches the `MESA` model qualitatvely well, where we see a slight expansion of the Si-shell region predicted by `MESA` also shown in the 3D model at $t \approx$ 350 s.

4.4.3.1 The 14 $M_\odot$ model

In Figure 4.9 we show the angle-average tangential velocity profile (top) and the specific mass fraction for three major isotopes: ^{12}C, ^{16}O, and ^{28}Si (bottom) for the 3D 14m model approximately five seconds prior to core-collapse. Also shown are the corresponding `MESA` profiles at the same time before core-collapse denoted by the dashed lines of the same color. For the 14$M_\odot$ model, we find that a few qualitative features worth mentioning between the 3D and 1D `MESA` models. FIrst, the 1D `MESA` model shows a peak convective velocity in the O-shell region of $v$conv. $\approx$ 50 km

s^{-1}. This value is approximately *four times* smaller than predicted by our 3D tangential velocity profiles where a peak value of velocity is found of $v$conv. ≈ 210 km s^{-1}. Beyond, this we observe that the 1D model is more compact with the shell locations closer to the iron core (lower specific mass coordinate). This difference is likely attributed to the slight expansion of the 3D model (See Figure 4.8, top right).

The expansion of the model can be explained in a similar manner to expansion observed in the $15 M_\odot$ model from FC20. The mass fraction profiles between the 1D and 3D models are qualitatively similar other than the 3D model being less compact (shells at larger mass coordinate) and the compositional gradients being smoothed at the boundary due to increased diffusion. One notable feature in the 3D model is the lack of a Si-rich region at the base of the Si-shell region. The 1D model shows a peak in ^{28}Si from $m \approx 1.50\text{-}1.54\ M_\odot$. However, in the 3D simulation, we observe instead one merged smoothed Si region. This merged region is able to reach higher tangential velocity speeds of $v$conv. ≈ 80 km s^{-1} in the 3D model.

4.4.3.2   The 20 $M_\odot$ model

Figure 4.10 shows the convective velocity and mass fraction profiles for the 3D and 1D `MESA` models at the same time as in Figure 4.9. One the first noticeably different property about the 20 $M_\odot$ model is that the convective velocity profiles are in better agreement between the 3D and 1D models. The location of the base of the O-shell is found at a specific mass coordinate of $m \approx 1.8 M_\odot$. The extent of the O-shell differs slightly between the two model, likely attributed to the mixing at the boundary between the O- and C-shell regions. Similar to the $14 M_\odot$ model, the convective velocity in the 1D model is less than observed in the 3D simulation. In this particular case, we find speeds three times larger in the 3D model than what is predicted by the 1D `MESA` model.

The mass fractions for both models follow similar behavior as the 14 $M_\odot$ models (but will less shell expansion / contraction) in that the profiles are smoothed out and sharp features from the 1D model are not present. One particular case is at the edge od the O-shell region where a slight increase of ^{12}C and ^{16}O from $m \approx 3.9\text{-}4.2\ M_\odot$ is not observed in the 3D simulation, suggested it

is mixed in or out of the O-shell region during the simulation.

4.4.3.3   The 25 $M_\odot$ model

Lastly, we show the convective and isotopic mass fractions for the $25M_\odot$ models in Figure 4.11 at $t - t_{CC} = -5$ s. In the $25M_\odot$ model, we see similar shell location agreement between the 3D and 1D MESA models suggesting less expansion / contraction compared to the $14M_\odot$ model and the $15M_\odot$ model of FC20. However, unlike the $20M_\odot$ model, and to some extent the $14M_\odot$ model, the the extent of the O-shell region disagrees significantly between the 3D and 1D models. The 3D $25M_\odot$ model suggests a convective O-shell region that extends from $m \approx$ 2.5-6.0 $M_\odot$ where and the MESA model has the convection speeds going to zero at $m \approx 4.0$ $M_\odot$. In the bottom panel, the ^{16}O mass fraction profiles agree remarkably aside from the smoothed composition gradients in the 3D profile. We find tangential velocity speeds in the O-shell region that peak at $v_{\rm conv.} \approx 400$ km s^{-1}, a factor of four times larger than predicted by the MESA model.

4.5   Summary and Discussion

We have presented 3D hydrodynamic simulations of O- and Si-shell burning in massive star models using MESA and the FLASH simulation framework. We follow up to the final ten minutes prior to core collapse to capture the development of the turbulent convective flow prior to collapse. In this study, we considered initial 1D progenitor models of 14-, 20-, and 25 $M_\odot$ to survey a range of O/Si shell density and compositional configurations.

In our 14 $M_\odot$ model, we observed relatively weak O-shell convection with the peak of the power spectrum near a spherical harmonic index of $\ell - 4$. Despite smaller convective velocity speeds observed in this model, we still find that angle-average convective velocity profile from our 3D model is approximately four times larger than the speeds predicted by MESA in the moments prior to collapse. The 20 $M_\odot$ showed the most energetic kinetic energy spectrum in the O-shell region with power residing at the largest scales of $\ell = 1 - 3$ near collapse. The convective velocity profile shows speeds *three* times larger than the 1D MESA model counterpart. This model also shows a

significant smoothing of the C profile at the edge of the O-shell convective region suggesting an increase in C ingested into the region in the 3D model. The results of our 25 $M_\odot$ showed qualitative properties similar to the 14- and 20 $M_\odot$ model. At early times, the power spectrum shows a peak near $\ell = 4$. However, at later times, energy is transferred towards larger scales with the bulk of energy at $\ell = 1 - 3$ near collapse. In this model, the convectively active Si-shell region can be characterized by power over a broad range of intermediate scales of $\ell = 10 - 20$ as the simulation approaches collapse.

The set of models presented in this work are a step forward in efforts to produce realistic 3D pre-supernova models that capture the properties of massive stars in their final moments prior to collapse. A crucial component not yet discussed in this paper is the effect of rotation and magnetism on the properties of the models presented here. Recent work by Müller & Varma (2020) suggests that pre-SN models with slow to moderately rotating cores near collapse could play a role in the delayed neutrino-driven mechanism of CCSNe. Efforts towards addressing the impact of magnetic fields in 3D simulations of O-shell burning were performed recently for a 18 $M_\odot$ model, although this model did not include the effect of rotation (Varma & Müller, 2021). A next step in our efforts will be to consider the impact of rotation and magnetism in realistic 3D progenitor models, a component that will be relevant to magnetically-driven and ordinary neutrino-driven CCSN explosions and the multi-messenger signals they produce.

CHAPTER 5

CORE-COLLAPSE SUPERNOVA EXPLOSIONS OF MULTIDIMENSIONAL PROGENITORS

Why should you leave the stars. And the sun and the moon. And the universe all alone? - Sun Ra

This chapter is based on the unpublished work of C. E. Fields *et al* 2021 *ApJ*, in prep.

5.1 Abstract

Multidimensional pre-supernova models have been shown to qualitatively impact the results of neutrino-radiation-hydrodynamic simulations of core-collapse supernova explosions. Recently, simulations of CCSNe have began to employ pre-supernova perturbations and very few have utilized 3D progenitors. Here, we report on a set of five CCSN explosion models utilizing 2D and 3D initial pre-supernova models. These models are evolved using the `FLASH` simulation framework, a two-moment scheme for neutrino transport, and effective general relativistic gravitational potential. When possible, we compare the multi-dimensional progenitor explosion model to a similar model using instead a 1D progenitor. We find explosion in four out of five of our explosion models and in our 3D simulation we observed evolution towards shock revival and explosion when the simulation is stopped. Comparing our 2D simulations, we observe an increase in broadband ($\approx 100 - 450$ Hz) gravitational wave emission due to perturbations in the Si-shell region as compared to the initially 1D explosion model. We compare two 1D explosion models and find that sharp gradients in the stellar structure when using a 1D `MESA` as compared to the 1D angle-average profile from a 3D progenitor model can lead to differences in explosion properties. Among these differences are a delayed (~ 50 ms) explosion time and smaller net neutrino heat rate in the non-`MESA` explosion. Our 3D simulation was evolved until a post bounce time of 490 ms. We expect this simulation to explode in the next 100 ms of simulation time.

5.2 Introduction

Simulations of neutrino-driven core-collapse supernova (CCSN) explosions have advanced our knowledge of the evolutionary fates of stars with an initial zero-age main sequence (ZAMS) of $M_{\mathrm{ZAMS}} > 9\ M_{\odot}$ (Woosley & Heger, 2015; Sukhbold et al., 2016, 2018). Multi-dimensional CCSN simulations have continuously innovated to include accurate and computationally feasible approximations to physical phenomena. Among these innovations include the coupling of multi-group multi-angle neutrino transport methods, high-order hydrodynamic solvers, and inclusion of the effects of a general relativistic potential (Roberts et al., 2016; O'Connor & Couch, 2018b,a; Vartanyan et al., 2019; Skinner et al., 2019). However, in most of these simulations, a 1D spherically-symmetric progenitor model is used as input for the explosion simulations. These models are typically evolved from collapse to a few of ms post bounce then mapped to higher-dimensionality. A potentially issue in this process is that the explosion model can have little to no information about the non-radial convective history of the pre-supernova model and / or the convective speeds can be underdetermined, a feature than can have qualitative impact on the properties of the explosion (Couch & Ott, 2013) .

Motivated by this consideration, recent works have explored the consequences of artificially imposed progenitor perturbations in the Si- and O-shell regions to replicate the 3D structure of a massive star near collapse. Work by Couch & Ott (2013) showed that perturbations in the aspherical velocity field motivated by multi-dimensional stellar convection models can lead to revival of the stalled shock in a 3D explosion model that otherwise fails. Building on this work Couch et al. (2015) evolved a 15 $M_{\odot}$ 3D progenitor for the final three minutes prior to and including gravitational collapse. They then used this model as their initial progenitor to perform a CCSN explosion simulation compared to the 1D initial model counterpart. Their work showed a similar result - multi-dimensional progenitor models can lead to qualitative differences in the explosion properties, some cases leading to explosion in a model that would not explode from a 1D progenitor.

Recently, work by Müller et al. (2017) performed 3D CCSN simulations utlizing a 3D pre-

supernova model evolved for the final five minutes up to and including iron core-collapse in an 18 $M_\odot$ star (Müller et al., 2016b). In their 3D CCSN simulations, they found that the 1D initial progenitor failed to explode after 0.6 s compared to the initial 3D progenitor model which explode at 0.4 s post bounce. The 3D explosion model utilizing the 3D progenitor showed an increase in non-radial kinetic energy and within the gain region compared to the 1D initial counterpart. The combination of these effect allowed the 3D models to surpass a critical ratio of the advective and heating timescales and eventually lead to explosion. The implication of this work showed that 3D progenitors can help facilitate explosion and lead to qualitative differences in explosion properties.

Work by Fields & Couch (2020) built on the earlier work of Couch et al. (2015) and Müller et al. (2016b) by simulating 2- and 3D simulations of Si- and O-shell burning in a 15 $M_\odot$ progenitor model for the final seven minutes prior to core-collapse. They compared results between resolution, dimensionality, and initial perturbations. In all of their simulations. they found slightly weak mach numbers in the Si and O convective shell regions, $\mathcal{M} \approx 0.06$ near collapse compared to 0.10 in Müller et al. (2016b). The consequence of the perturbations observed in their work will have an impact of the explosion properties and potentially the multi-messenger signals produced when exploded. These models serve as the basis of this paper.

We draw from the progenitors of Fields & Couch (2020) to perform 1-, 2-, and 3D CCSN simulations using multidimensional progenitor models. When possible we compare to the 1D initial progenitor counterpart to isolate the impact of progenitor perturbations. This project is novel because: (1) we investigate the impact of pre-supernova perturbations of CCSN explosion models in 2D and 3D, (2) - we perform a 3D CCSN explosion model of a 3D progenitor model evolved for the final seven minutes prior to collapse, and (3) - we explore the impact of perturbations of the neutrino and gravitational wave emission properties. This paper is organized as follows. In § 5.3 we present our computational method and initial progenitor models, in § 5.4 we present the results of our CCSN explosion simulations and discuss the impact of pre-supernova perturbations, and in § 5.5 we summarize our results and compare them to previous efforts.

Properties of the CCSN explosion models

Model Label	Progenitor Model	t_{bounce}	$t_{\text{exp.}}$
		(ms)	(ms)
1D-MESA	MESA	127	455
1D-3DAvg	Angle-Average 3D32km	182	505
2D-2DAvg	Angle-Average 2D32km	131	282
2D-2D32km	2D32km	130	293
3D-3D32km	3D32km	133	. . .

Table 5.1: List of all CCSN explosion models performed in this work. Each model is labeled according to the dimensionality of the explosion performed in `FLASH` and input progenitor model used. For example `2D-2DAvg` corresponds to a 2D `FLASH` explosion model that used a 1D angle-average profile computed from the `2D32km` model of Fields & Couch (2020). Also shown are the bounce and explosion times (if observed, defined as the time at which the average shock radius exceeds 400 km).

5.3 Computational Methods and Initial Models

We evolve a total five CCSN explosion simulations using the `FLASH` simulation framework (Fryxell et al., 2000). Our simulations utilize publicly available multi-dimensional progenitor models of a 15 $M_\odot$ star (Fields & Couch, 2020). The progenitor model was evolved in 2D and 3D for the final seven minutes up to and including gravitational instability and iron core-collapse. In their 4π3D non-perturbed model they observe mach numbers on the order of ≈ 0.06 in the convective O-shell region. Our 4π3D CCSN explosion utlizes this model following the model in 3D through collapse, bounce and explosion. In Table 5.1 we summarize the explosion models performed in this work and the input progenitor for each model. We perform two 1D, spherically symmetric CCSN explosion models utilizing the `ST1R` hydrodynamics module in `FLASH` (Couch et al., 2020). The only difference between these models is that one uses the 1D pre-supernova model predicted
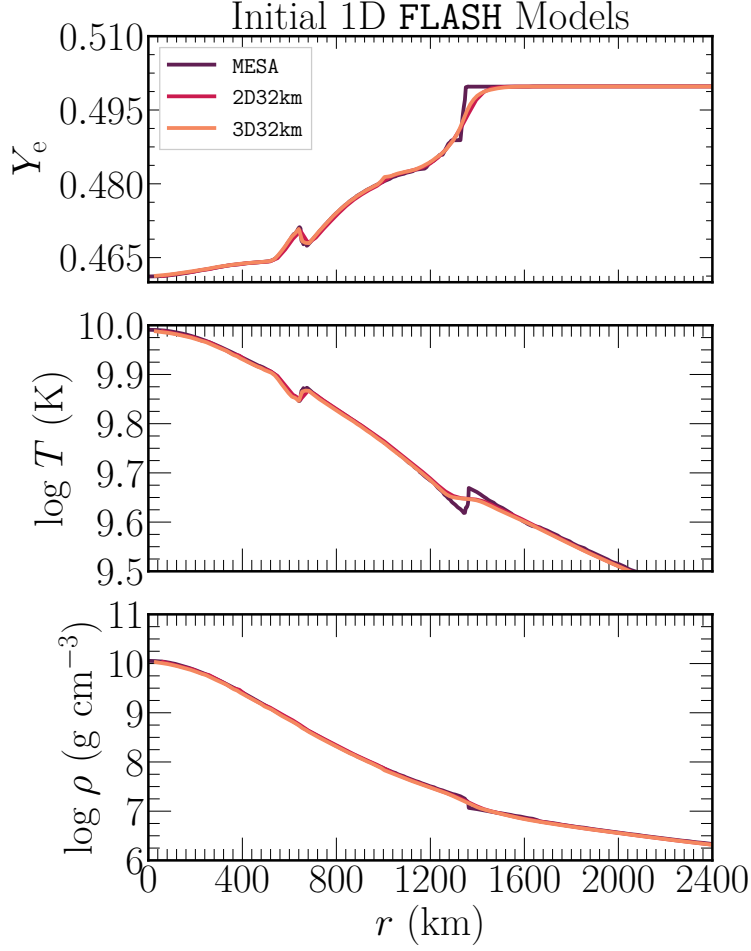
Figure 5.1: Profiles of the specific electron fraction, temperature and density of the three 1D initial progenitor models. The label corresponds to the three profiles used in the `1D-MESA`, `2D-2DAvg`, and `1D-3DAvg` explosion models respectively.

from `MESA` (`1D-MESA` in Table 5.1) and the other uses an angle-average of the 4π3D non-perturbed model (`3D32km`) from Fields & Couch (2020). Our 1D simulations $\alpha_{\mathrm{MLT}} = 1.25$, the value found to best match the velocity structure of the 3D comparison explosion model. Similarly, we evolve two 2D CCSN explosion simulations using different progenitors. Model `2D-2D32km` follows the 2D progenitor model (`2D32km`) from Fields & Couch (2020) in 2D through collapse, bounce, and the onset of explosion. The other 2D model uses an angle-average of this 2D progenitor model as input, this corresponds to model label `2D-2DAvg`. In Figure 5.1 we show the 1D profiles used in this work.

Our methods follow closely those of O'Connor & Couch (2018a). All of our simulations
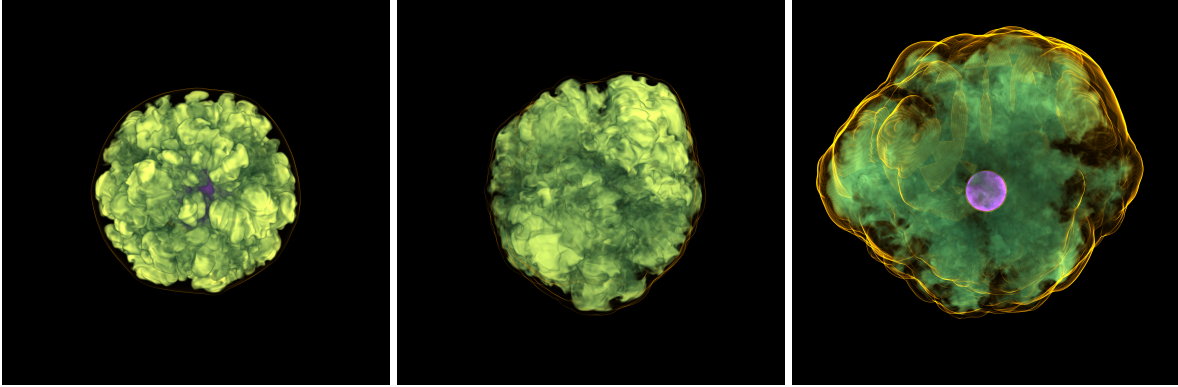
Figure 5.2: Volume rendering of the specific entropy of the `3D-3D32km` explosion model at three different times: $t_{\mathrm{pb}} \approx 75$, 232, and 491 ms from left to right, respectively. The edge of the shock is outlined in orange and the PNS is shown in pink.

employ multi-dimensional neutrino transport previously discussed in O'Connor & Couch (2018b). The `M1` scheme for neutrino-radiation-hydrodynamics evolves the zeroth and first moment of the neutrino distribution function. The scheme is then closed with an analytical approximation for the second moment of the distribution function (Shibata et al., 2011). We include three species of neutrinos, ν_{e}, $\bar{\nu}_{\mathrm{e}}$, and ν_{x}, electron, anti-electron, and heavy type neutrinos. We follow 12 energy groups binned logarithmically from 0 to 300 MeV with neutrino rate and opacity tables produced using `NuLib` (O'Connor, 2015). We use the SFHo nuclear equation of state (EOS) (Steiner et al., 2013).

We utilize the directionally unsplit hydrodynamics solver, a fifth-order weighted essentially non-oscillatory (WENO) spatial reconstruction scheme, and a hybrid HLLC Riemann solver. Gravity is treated using an o ptimized multipole solver (Couch et al., 2013) which includes general relativistic corrections to the monopole term (Marek et al., 2006). In 1D our domain extends to 15,000 km, in 2D this corresponds to the maximal extent in the ρ-direction while in the axial directions our domain extends this length from the origin. Our 3D simulation is 30,000 km on a side and utilizes a Cartesian coordinate system with adaptive mesh refinement (AMR) and up to 10 levels of refinement. None of our simulations include rotation and we do not include any initial perturbations other than those from the initial progenitor models.

141

5.4 Core-Collapse Supernova Explosions of Multidimensional Progenitors

We show a volume rendering of our 3D CCSN explosion model in Figure 5.2 at three different times post bounce. Our 3D was evolved to ≈ 0.5 s post bounce and at the end of the simulation is at the onset of shock runaway and explosion. The explosion is characterized by asymmetric expansion due to the initial progenitor perturbations in the pre-supernova model. We expect this simulation to continue to explode and that the average shock radius will increase experience shock runaway in the next ≈ 100 ms of simulation time.

In Figure 5.3 we show the time evolution of the angle-average shock radius for all five CCSN explosion simulations. All models except the 3D model explode before the end of the simulation. The Si-shell region is accreted rapidly at a time corresponding to $t_{\mathrm{bounce}} \approx 80$ ms. The accretion of the Si-shell leads to an increase in the shock radius in most models. The O-shell convective region accretes up to a later time of $t_{\mathrm{bounce}} \approx 400$ ms. When accreted, the O-shell enables shock runaway in the 1D simulations and a revival of the declining and stagnant average shock radius in the 3D model.

In Figure 5.4 we plot the antesonic ratio (top panel) of Pejcha & Thompson (2012) for explosion. This criteria is derived from determining a critical sound speed in an isothermal accretion flow above which the steady-state solution fails. Above this critical ratio ($\langle c_{\mathrm{s}}^2 \rangle / \langle v_{\mathrm{esc.}}^2 \rangle \approx 0.19$) shock runaway is expected and explosion proceed. We find that our 2D and 3D simulations cross this critical ratio at $t_{\mathrm{pb}} \approx 150$ ms. This leads to shock runaway in the 2D models while the 3D simulation shows shock recession despite being above the ratio. The 1D models do not cross the threshold until $t_{\mathrm{pb}} > 400$ ms, this time also coincides with the time in which the shock radius begins to runaway and explosion sets in.

In the bottom panel of Figure 5.4 we show another diagnostic metric often used to determine the explodability of a model, the ratio of the advective and heating timescales (Thompson et al., 2005; Raives et al., 2018). The advective timescale defined as

$$\tau_{\mathrm{adv.}} = \frac{M_{\mathrm{gain}}}{\dot{M}} \, , \tag{5.1}$$
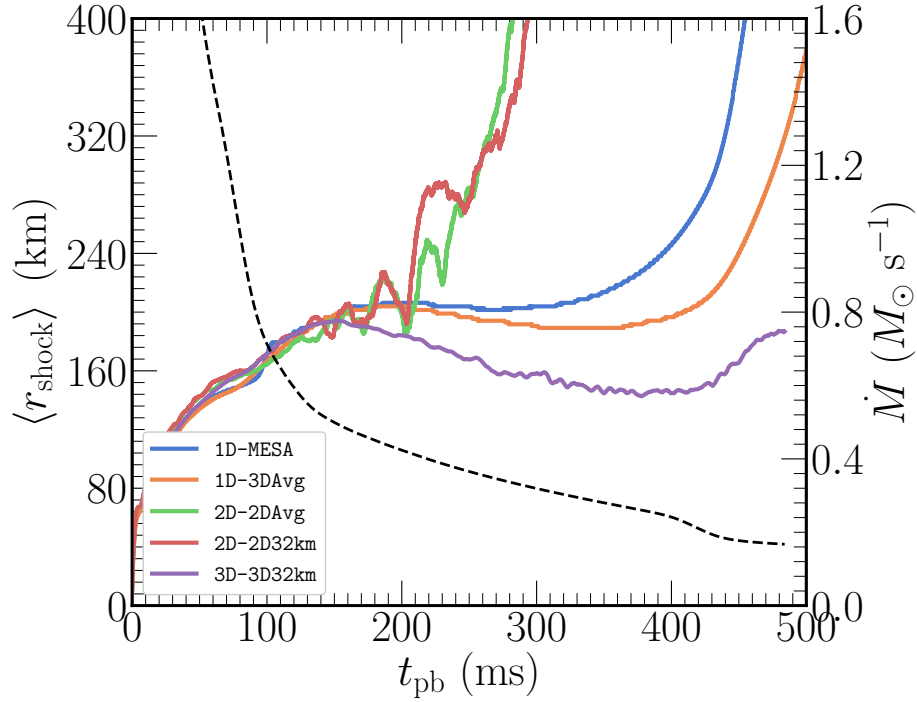
Figure 5.3: Evolution of the average shock radius for all five CCSN explosion models. All shock radii reach a radius of 400 km before the end of the simulation except the 3D simulation. All shown is the mass accretion rate for the 3D simulation as a function of time.

where M_{gain} is the mass in the gain region and $\dot{M}$ is the mass accretion rate. The heating timescale is defined as

$$\tau_{heat} = \frac{|E_{gain}|}{Q_{net}}, \tag{5.2}$$

where Q_{net} is the net neutrino heating rate and $|E_{gain}|$ is the total energy in the gain region. Previous works have studied stability at the onset of explosion in spherically symmetric models to suggest that solutions become unstable when the ratio exceeds unity (Fernández, 2012). All of our simulations cross this condition early in the simulation. The 1D models pass this threshold at $t_{pb} \lesssim 10$ ms while the multi-dimensional models cross at c. Despite all of the models crossing this value of unity, shock runaway in the exploding models is only observed when the antesonic condition shown in the top panel is satisfied.
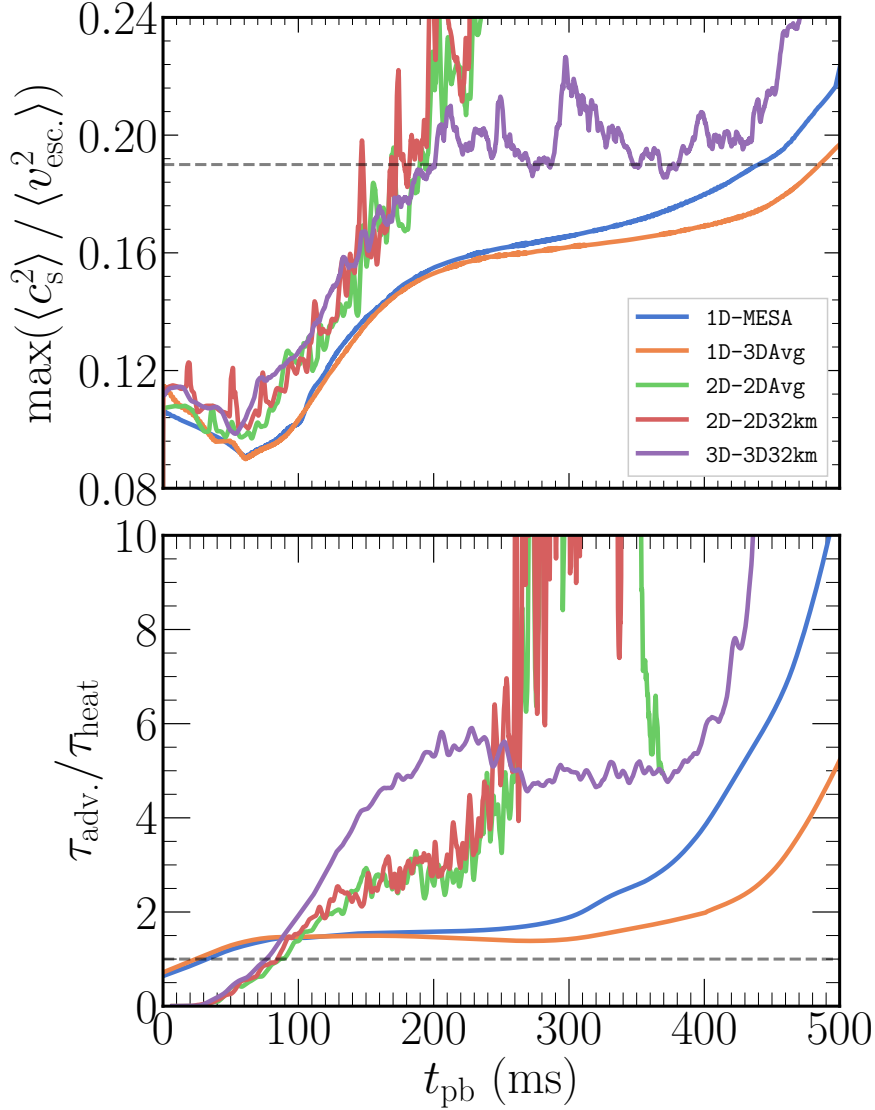
Figure 5.4: The antesonic condition, ratio of $\left\langle c_{\mathrm{s}}^2 \right\rangle / \left\langle v_{\mathrm{esc.}}^2 \right\rangle$ (top) and the ratio of the advective and heating timescales for all five CCSN explosion simulations. In the top panel the explosion threshold for an isothermal accretion flow (≈ 0.19) is denoted by a dashed horizontal line. In the bottom panel, a value of unit is denoted by a dashed horizontal line.

In Figure 5.5 we show the net neutrino heating rate (top) and the mass in the gain region for the five CCSN simulations. The 1D simulations show the lowest values for both of these quantities, the `1D-3DAvg` model shows a less steep decline in the net neutrino heating rate likely due to a smoothed compositional gradient as the Si-shell is accreted onto the PNS. While the O-shell is being accreted in the 1D simulations. the `1D-MESA` model shows a slightly large value of ≈ 0.5 B s^{-1}. The 2D and 3D models follow relatively similar trends with the 2D models showing larger
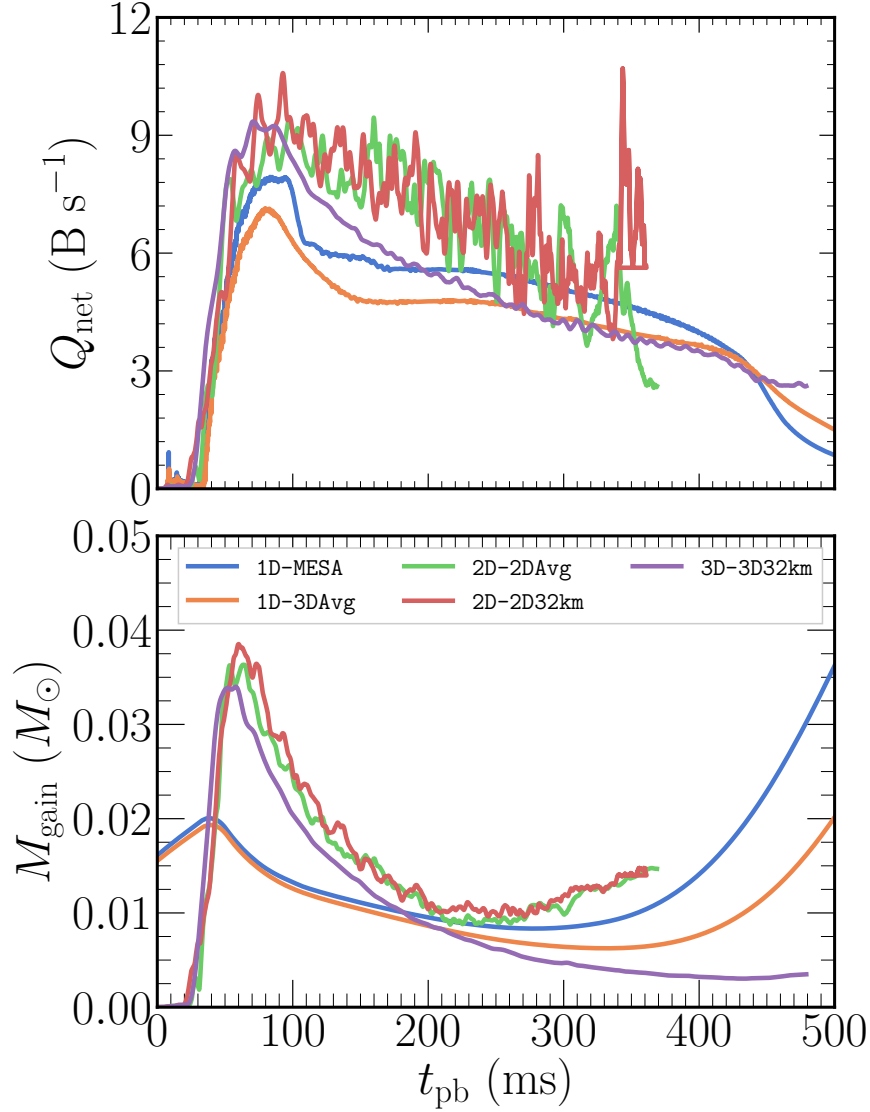
Figure 5.5: Same as in Figure 5.4 but for the net neutrino heating rate (top) and the mass contained within the gain region (bottom).

heating rates and mass in the gain region. This behavior is expected for 2D simulations due to the amplification of convective mass along the axis in 2D cylindrical coordinates (Couch & O'Connor, 2014). Between the two 2D simulations we find that the 2D-2D32km shows more mass in the gain region indirectly leading to an increase in the effective heating rate than the 2D model that used a 1D progenitor. The 3D model continues to decline in this quantities beyond the time which the 1D and 2D simulations show explosion but maintains a larger net heating rate than the 1D models until $t_{pb} \lesssim 200$ ms.
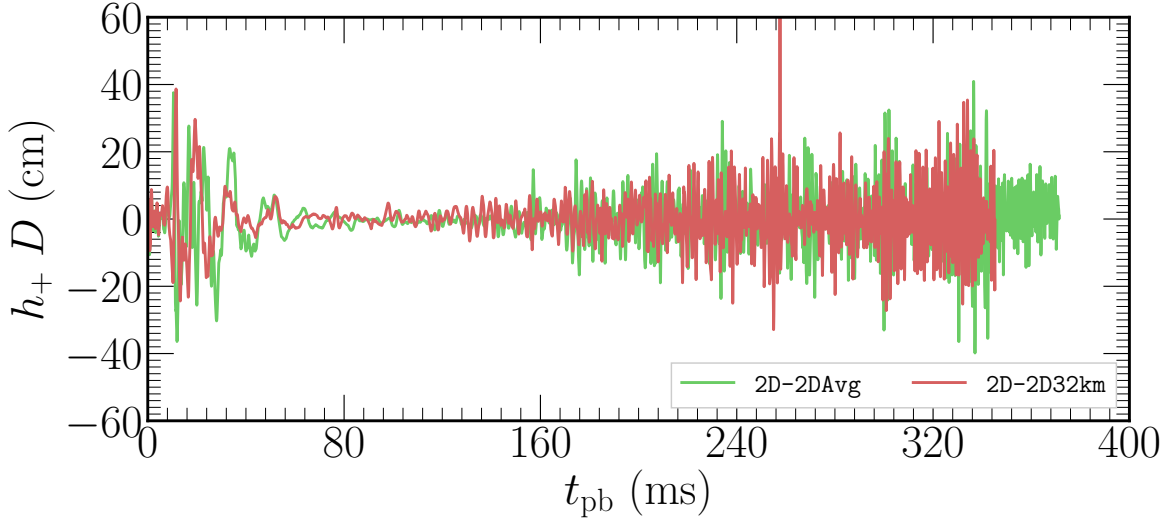
Figure 5.6: Gravitational wave strain for the two 2D simulations. The distance is taken to be $D = 10$ kpc.

5.4.1 Gravitational Wave Emission

We compute the approximate gravitational wave (GW) strain using the formalism of Blanchet et al. (1990). The plus polarization of the strain can be approximated as

$$h_+ \approx \frac{2G}{c^4 D} \frac{d^2 I_{zz}}{dt^2}, \tag{5.3}$$

where D is the distance to the source, c the speed of light, G the gravitational constant, and I_{zz} is the non-vanishing component of the mass quadrupole tensor. In Figure 5.6 we show the time evolution of the GW strain for the two 2D simulations assuming a nearby source of $D = 10$ kpc.

Both simulations show prompt convection in the PNS with a burst of GW that lasts for approximately 50 ms post bounce. Beyond this time, the GW emission is relatively weak until convection is again efficient enough to excite GW emission near the surface of the PNS. As the PNS cools, the fundamental frequency of the excited modes steadily increases represented by the gradual increase in emission at the simulation evolves towards shock runaway. Qualitatively, the simulations evolve similarly throughout the explosion. The 2D-2D32km model shows slightly less sharp beats in the
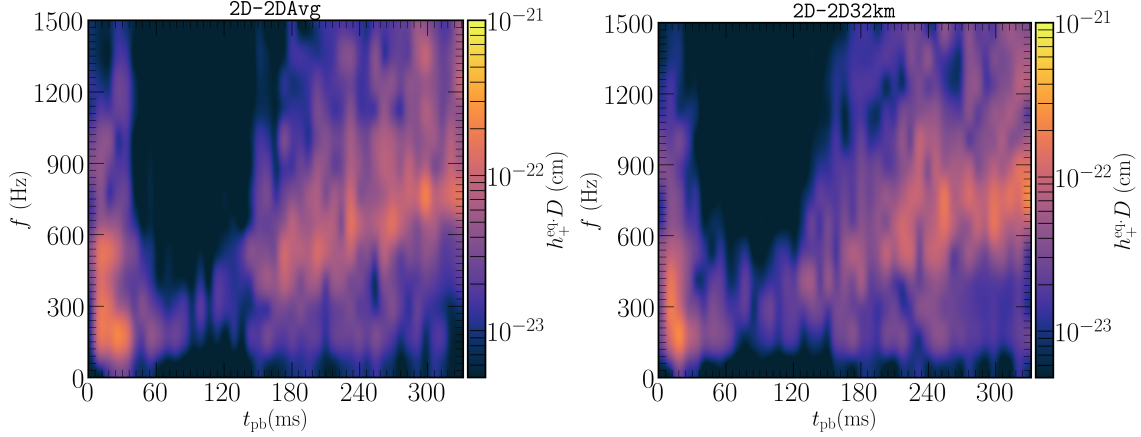
Figure 5.7: GW spectrum of the two 2D simulations in Fourier space.

periodic increases in the strain due to sloshing about the axis seen in both models.

Progenitor perturbations have been show to affect the gravitational wave emission properties. O'Connor & Couch (2018a) show a pronounced increase in the temporal evolution of the strain when the Si-shell is accreted onto the PNS. In Figure 5.6 we do not observe such an increase in GW strain due to the Si-shell region in the perturbed model. The difference is likely due to the magnitude of perturbations used in their model. The impose an effective mach number in the Si-shell region of ≈ 0.3, a factor of four times larger than observed in the 2D32km progenitor model of Fields & Couch (2020). The perturbations in the O-shell imposed in their model was also a factor of four times larger than observed in the 2D32km model.

In Figure 5.7 we show the computed GW spectrum in Fourier space for the two 2D simulations. When considering the difference in the spectra, we can observe a slight increase in power in frequencies of $f \approx 150$ - 600 Hz at a post bounce time of $t_{\rm pb} \approx 60$-100 ms, the approximate time at which the Si-shell is accreted onto the PNS. This region of frequency space is slightly smaller than the region than found in O'Connor & Couch (2018a) (see their Figure 14) where their peak emission caused by the Si-shell is found near $f \approx 600$ Hz.

5.5 Summary and Discussion

We have presented the results of 1-, 2-, and 3D CCSN simulations from multi-dimensional progenitor models. When possible, we have evolved the accompanying explosion model using

a spherically averaged 1D progenitor model to determine the impact of multi-dimensional pre-supernova models on properties of CCSN explosions. We found explosions in all of our simulations except the 3D model that is steadily evolving towards shock runaway and explosion at the time the simulation is stopped.

Our 1D simulations show shock runaway at relatively late post bounce times of $t_{\mathrm{pb}} > 400$ ms compared to the 2D simulations which explode near $t_{\mathrm{pb}} \approx 290$ ms. We showed that the 1D simulations were found to experience less net neutrino heating and mass in the gain region, likely attributing to the delayed explosion times. We find that the 1D explosion model utilizing a 1D progenitor model directly from `MESA` (`1D-MESA`) shows slightly enhanced net heating and mass in the gain region leading to a difference of ≈ 50 ms in explosion time. This difference can likely be attributed to the smoothing of density and entropy gradients in the `MESA` (`1D-3DAvg.`) model which used a 1D progenitor model derived from an angle-average of the non-perturbed 3D progenitor of Fields & Couch (2020).

Differences in the 2D models were small but non-negligible. Both simulations followed a qualitatively similar evolution with the `2D-2D32km` (the 2D model using a 2D progenitor) showed slightly enhanced net heating and mass in the gain region. Enhanced mass contained in the gain region was shown to indirectly affect the net neutrino heating in the 3D CCSN explosion of a 3D 18 $M_\odot$ progenitor model (Müller et al., 2017). We also showed that more subtle affects of the progenitor perturbations can be observed in the GW emission properties. Despite a smaller mach number in the Si-shell region for our 2D progenitor model (four times smaller than imposed in O'Connor & Couch (2018a)), we observe enhanced broadband GW emission compared to the CCSN model using a 1D progenitor.

Our 3D simulation did not reached the antesonic condition for explosion criteria at a post bounce time of $t_{\mathrm{pb}} \approx 190$ ms and the ratio of advective and heating timescales shortly after accretion of the Si-shell ($t_{\mathrm{pb}} \approx 90$ ms). At the time the simulation was stopped, the average shock had reached approximately 200 km s^{-1} and showed a positive gradient. It is expected our 3D simulation will explosion in the next ≈ 100 ms of simulation time.

CHAPTER 6

`MESA-WEB`: AN ONLINE INTERFACE TO THE `MESA` STELLAR EVOLUTION CODE

The beautiful thing about learning is nobody can take it away from you. - Riley B. King

This chapter is based on the unpublished work of C. E. Fields and F. X. Timmes 2021, in prep.

6.1   Abstract

We present `MESA-Web`, an online interface to the `MESA` stellar evolution code. `MESA-Web` allows users to evolve stellar models without the need to download / install `MESA`. Since being released in 2015, `MESA-Web` has evolved over 9200 models to over 2200 unique users and currently performs ~ 4.4 jobs per day. In its current form, `MESA-Web` can be used as an educational tool in the classroom or for scientific investigation of different nuclear astrophysics problems. We report on some of the capabilities of `MESA-Web` introduced since its release such as user-supplied nuclear reaction rates, custom stopping conditions, and expanded input parameters. We conclude by discussing the future goals of `MESA-Web` including its expansion to more computational resource within the next year.

6.2   Introduction

Stellar evolution codes can be complicated to use, so we present `MESA-Web`, a web-based interface to the stellar evolution code, Modules for Experiments in Stellar Astrophysics. `MESA` is an open-source stellar evolution toolkit based on the EZ stellar evolution code (Eggleton, 1971; Paxton, 2004). Since its inception in 2010 `MESA` has been a valuable tool in the field of astronomy and astrophysics with an active network on contributors building on its capabilities. The `MESA-Web` online interface is to allow educators to utilize `MESA` in the classroom without additional barriers that students may face in downloading / installing `MESA`. `MESA-Web` can be used to calculate stellar models over a range of physical parameters.

149

The original goal of `MESA-Web` was to provide an alternative to the online stellar evolution calculation tool, `EZ-Web`, created by Rich Townsend [1]. However, since its inception, the capabilities of `MESA-Web` make it not only a tool for use in astronomy education but also as a resource for scientific investigation for those unfamiliar with `MESA`. These two aspects of `MESA-Web`'s use will be the primary focus of future development. This paper is organized as follows. In § 6.3 we discuss the current capabilities of `MESA-Web`, in § 6.4 we highlight areas of use for `MESA-Web`, and lastly in § 6.5 we summarize and discuss future development goals.

6.3 Capabilities

The `MESA-Web` interface uses `MESA`-revision 11701 and is continually updated to reflect a modern version of the stellar evoltuion toolkit. The online tool uses a four core server hosted by the Ira A. Fulton School of Engineering at Arizona State University. `MESA-Web` improves on the accessibility of the stellar evolution toolkit by removing storage/software prerequisites that can often present challenges when trying to utilize `MESA` in the classroom. Users are able to specific a variety of input physics for single star models to perform stellar evolution calculations for a walltime time of up to four hours. The simulation output data are then compressed and stored on the `MESA-Web` server for 24 hours allowing the user to download via a link sent to their email address.

6.3.1 Output

As a part of the output data, users will receive an mp4 file of a plot of profile and history quantities of their stellar model. The movie is a time series of grid plots created using `MESA`'s `pgstar` plotting routines to showcase general structure and surface properties of the calculation before investigating the raw data in detail. An example snapshot for a non-rotating $1 M_\odot$ stellar model is shown in Figure 6.1. Also included in the directory of their calculation are numbered `profileX.data` where `X` corresponds to a specific profile number. The profiles are produced at a user specified interval and the `profiles.index` file is provided as a key to their correspondence. The profile

---

[1] www.astro.wisc.edu/ townsend/static.php?ref=ez-web
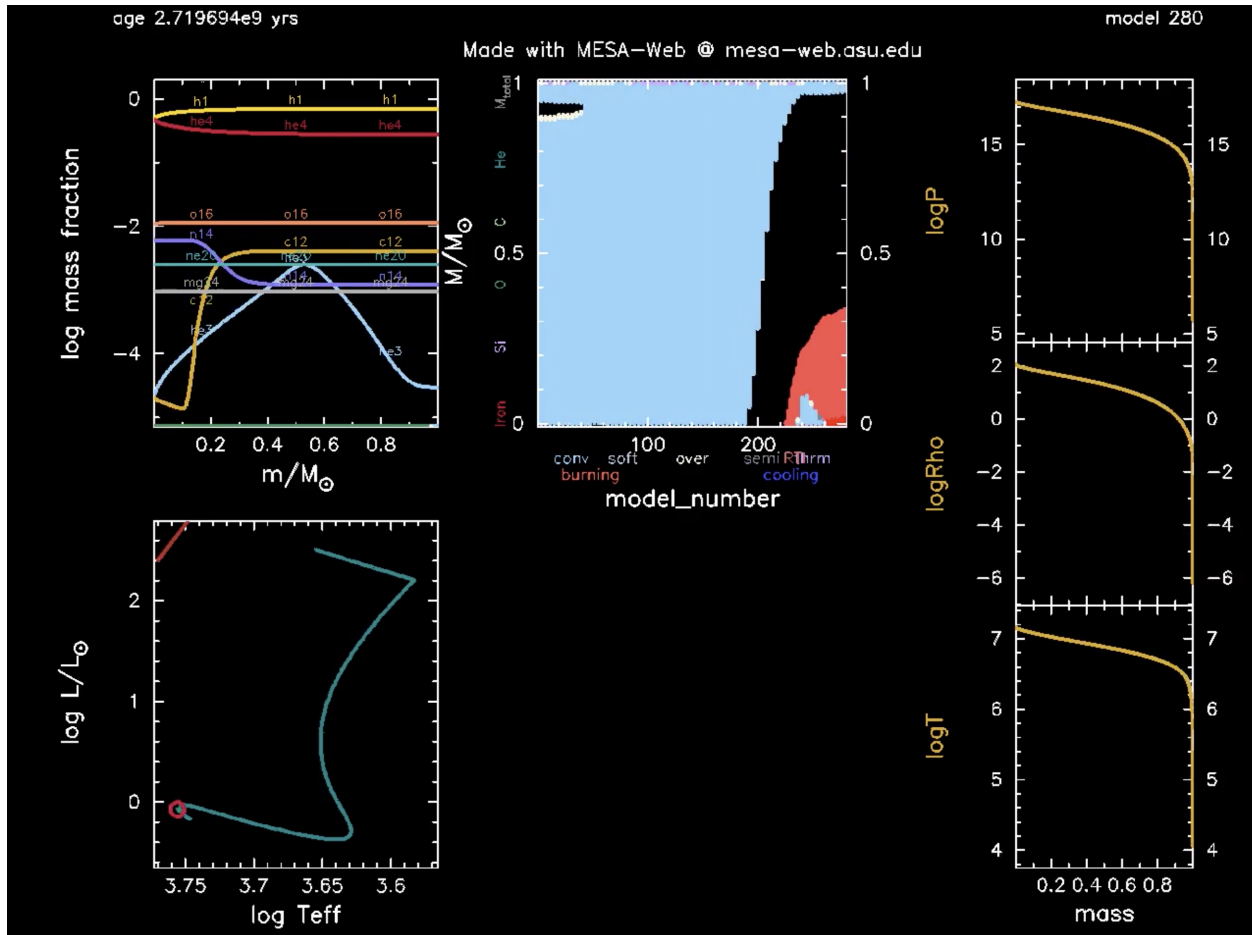
Figure 6.1: Snapshot showing grid plot of profile and history data for `MESA-Web` calculation of a 1 $M_{\odot}$ non-rotating stellar model. At this model number, the star is on the main-sequence.

data contain stellar structure information for 56 quantities as a function of mass coordinate. These data are useful for investigation which require information about cell-specific properties.

The completed stellar evolution calculation also includes a `history.data` file with data for total or location specific information about the model. For example, this file would include the surface luminosity for the stellar model as a function of timestep. This information can often also be obtained from the profile data but in some cases `MESA` pre-computes these quantities for ease of access instead. The history file contains information about 57 different variables recorded at every timestep taken by the stellar model.
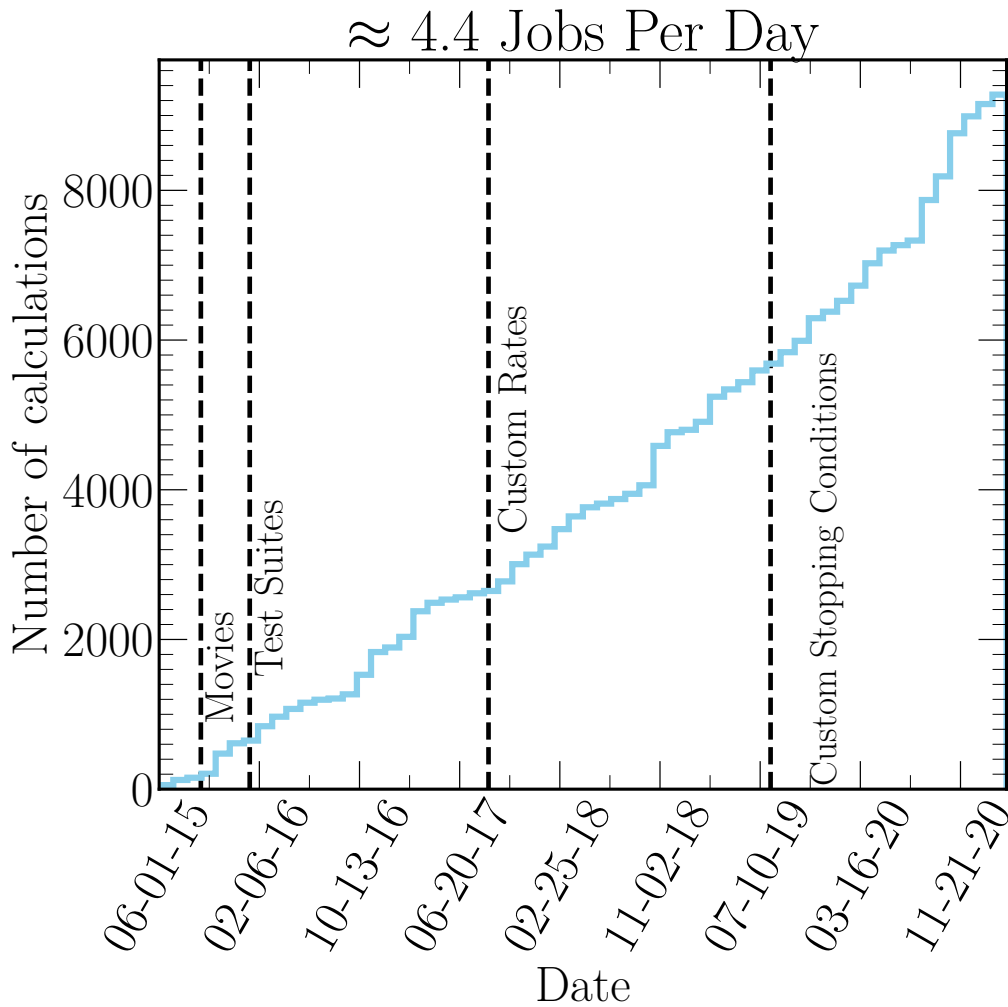
Figure 6.2: Cumulative number of `MESA-Web` calculations since its release. The horizontal dashed lines show the date that new capabilities were introduced.

6.4   `MESA-Web` and its role in astronomy

Since its inception in 2015, `MESA-Web` has evolved over 9200 models to over 2200 unique users and currently averages about 4.4 jobs per day (see Figure 6.2). The mp4 file included with the output was introduced early after the introduction of `MESA-Web`. Following that, we introduced example directories of the Test Suites that come included with the standard `MESA` distribution. The idea behind these examples was to provide the data and visualization of the Test Suite examples

152

as a resource for those that do not have an installation of `MESA`. Because of the complex nature of some of the Test Suites (multiple inlists, high computational demand, and different `pgstar` setups) pre-computing the examples proved to be the most efficient means of producing these data.

In the summer of 2017, we introduced the ability for a user to choose a specific nuclear reaction from a list of eight key nuclear reactions and to provide their own reaction rate. The introduction of this capability expanded `MESA-Web`'s impact beyond that of a tool in the classroom to a viable means of scientific investigation for the nuclear astrophysics community without significant prior experience with `MESA`. Following this, the focus of the future of `MESA-Web` shifted to continue to build on its capability in these two areas: astronomy education and in its accessibility to the stellar and nuclear astrophysics community-at-large. Of the last major improved capabilities to `MESA-Web` are custom stopping conditions. Users are now able to specify a limit to different stellar quantities as condition for which the model will complete. This new capability provides users an increase in throughput especially if investigating a particular evolutionary epoch.

`MESA-Web` has been used as a tool across the world in undergraduate and graduate astronomy courses. The importance of computational literacy in physics has been investigated previously (Odden, 2019). It was found that open-ended computatational projects such as those in many graduate stellar astrophysics courses can have a positive impact of student learning. The use of computation in astronomy specifically has also been a topic for advocacy amongst the AAS task force initiatives (Zingale et al., 2016). The University of Chicago, Stony Brook University, the University of California, Santa Cruz, University of Pittsburgh, Texas A&M University Commerce are among the institutions that have most utilized `MESA-Web` in the classroom since its release. We continue to improve, extend, and innovate the capabilities. We maintain communication with educators across the globe about new ways to build on `MESA-Web` to meet their needs in the classroom.

6.5 Summary

We have presented `MESA-Web`, an online interface to the `MESA` stellar evolution code. `MESA-Web` allows users to evolve stellar models using the `MESA` code for up to four hours online for free without the need to download or install the code itself. In its current form, the tool serves a valuable computational resource in classrooms across the world as well as a scientific tool for investigations relevant to nuclear astrophysics. The future of `MESA-Web` includes porting it to a large server that will allow for more jobs to be performed for longer walltimes. This expansion will take place over the summer of 2021. In addition, we look forward to including physics capabilities currently already supported by the full release of `MESA`. Among these capabilities are massive star explosion, binary star evolution, and light curves.

CHAPTER 7

SUMMARY

In this Thesis, we have investigated uncertainties in computational models of massive stars and core-collapse supernova explosions to explore the implications they have on our understanding of transient stellar phenomena. In Chapter 2 we focused on uncertainties due to nuclear reaction rates in massive star stellar evolution models. We presented the results of 2,000 stellar models of a 15 $M_\odot$ star at solar and subsolar metallicities. Each stellar model within this grid used a different random set of rates within their temperature-dependent uncertainties provided by the nuclear reaction rate library, STARLIB. At five evolutionary ephocs, we identified key nuclear reaction rates and computed the Spearman Rank-Order Correlation Coefficient to determine the sign and magnitude of the impact of the uncertainty for each of the 665 sampled reaction rates in our network following 127 isotopes. It was found that for each passing evolutionary epoch up to the depletion of Helium, the magnitude of the variation in stellar properties due to the rates was on the order of those for spatial, temporal and network resolution. However, beyond these evolutionary epochs, the uncertainty in the nuclear reactions can begin to dominate the sources of variation in the stellar model owing to the inherited characteristics from previous epochs.

In Chapter 3, we presented the results of 2D and 3D hydrodynamical simulations of the final seven minutes before iron core-collapse of a 15 $M_\odot$ star. In this work, we characterized the magnitude and characteristic scales of the convective Si- and O-shell regions. In our 4π 3D simulations, we reported angle-averaged velocity speeds of approximately 250 km / s in the O-shell near collapse. The resulting mach number in this region was found to reach 0.06 with the bulk of power residing at large scales, spherical harmonic indices of $\ell = 2 - 4$. Lastly, we compared the profiles of the convective velocity of our multidimensional models to that of the 1D predictions made by MLT and MESA. We found that in our 3D simulations, the speeds approximately *four* times larger than predicted in 1D, a result which has significant implications for CCSN explosion models.

Chapter 4 built on the work of the previous chapter by considering 3D hydrodynamic simulations

in three different progenitor models. In this work, we evolved models of M_{ZAMS} = 14-, 20-, and 25 $M_\odot$ for the final 10 minutes before iron core-collapse to assess the range of observed convective velocity speeds and scales. We found that in our 14 $M_\odot$ model the O-shell region was able to reach tangential velocity speeds of $\approx$ 200 km / s, a factor of four times larger than predicted by MESA. This model held a peak in the power spectrum distribution at ℓ = 4 up to the point of collapse. This suggests that the velocity field was not able to develop well beyond the initial perturbations imposed and that were a result of grid artifacts due to the Cartesian geometry. The 20 $M_\odot$ model is significantly more energetic with tangential O-shell velocity speeds of approximately 600 km / s, about three times larger than predicted by MESA. This model shows significant power at large scales, with a peak at ℓ = 2. Our 25 $M_\odot$ model showed properties in between the qualitative properties of the two previous models. This model showed Si- and O-shell convection speeds of approximately 150 km / s and 400 km / s, respectively. The peak harmonic indices are similar to the 20 $M_\odot$ model with ℓ = 2 in the O-shell region, and ℓ = 10 in the Si-shell near collapse. Overall, the 3D simulations presented in this work all report favorable conditions for explodability and the potential to alter multi-messenger signals during explosion.

In Chapter 5 we presented preliminary results of multidimensional core-collapse supernova explosion simulations using multidimensional progenitor models. In this work, we compared 2D explosions performed using the 2D progenitor model to the angle-averaged models from MESA. We also performed 1D and 3D explosion simulations utilizing the angle-average 3D progenitor model from Chapter 3. All models except the 3D simulation experience shock runaway at a post-bounce time less then approximately 400 ms. The 3D simulation has been evolved to 0.5 s post-bounce and an increase in the average shock radius is observed but the model has yet to experience shock runaway. Comparing our 2D simulations, we observe an increase in broadband ($\approx$ 100 − 450 Hz) gravitational wave emission due to perturbations in the Si-shell region as compared to the initially 2D explosion model using a 1D progenitor. The models presented in this work provide a basis for GW strain templates for non- or very slow-rotating 3D progenitors.

Lastly, in Chapter 6 we have discussed the development of the MESA-Web online web interface

to the stellar evolution code `MESA`. This online tool has been a part of my work during my graduate studies and has been utilized by many classrooms across the world. Since its inception, it has evolved over 8,000 unique stellar models to over 2000 users. In its current form, `MESA-Web` has the capability to be used as a tool for scientific investigation or as a computational supplement to astronomy courses. The future of this tool will be expanded to a larger set of computational resources and to include more of `MESA`'s advanced scientific capabilities such binary star simulations, explosion models, and more.

BIBLIOGRAPHY

BIBLIOGRAPHY

Abbott, B. P., Abbott, R., Abbott, T. D., et al. 2016a, Physical Review Letters, 116, 241103

—. 2016b, Physical Review Letters, 116, 061102

—. 2017, Physical Review Letters, 118, 221101

Alastuey, A., & Jancovici, B. 1978, The Astrophysical Journal, 226, 1034

Almgren, A. S., Beckner, V. E., Bell, J. B., et al. 2010, The Astrophysical Journal, 715, 1221

and J Aasi, Abbott, B. P., Abbott, R., et al. 2015, Classical and Quantum Gravity, 32, 074001

Andrassy, R., Herwig, F., Woodward, P., & Ritter, C. 2020, Monthly Notices of the Royal Astronomical Society, 491, 972

Andresen, H., Müller, E., Janka, H. T., et al. 2019, Monthly Notices of the Royal Astronomical Society, 486, 2238

Angulo, C. 1999, in American Institute of Physics Conference Series, Vol. 495, American Institute of Physics Conference Series, 365–366

Arnett, D. 1994, The Astrophysical Journal, 427, 932

Arnett, D., Meakin, C., & Young, P. A. 2009, The Astrophysical Journal, 690, 1715

Arnett, W. D., & Meakin, C. 2011, The Astrophysical Journal, 733, 78

Asplund, M., Grevesse, N., Sauval, A. J., & Scott, P. 2009, Annual Reviews of Astronomy and Astrophysics, 47, 481

Barkat, Z., Rakavy, G., & Sack, N. 1967, Physical Review Letters, 18, 379

Baron, E., & Cooperstein, J. 1990, The Astrophysical Journal, 353, 597

Bennett, M. E., Hirschi, R., Pignatari, M., et al. 2012, Monthly Notices of the Royal Astronomical Society, 420, 3047

Bethe, H. A., & Wilson, J. R. 1985, The Astrophysical Journal, 295, 14

Blanchet, L., Damour, T., & Schaefer, G. 1990, Monthly Notices of the Royal Astronomical Society, 242, 289

Botticella, M. T., Smartt, S. J., Kennicutt, R. C., et al. 2012, Astronomy & Astrophysics, 537, A132

Bromm, V., Kudritzki, R. P., & Loeb, A. 2001, The Astrophysical Journal, 552, 464

Brown, J. M., Garaud, P., & Stellmach, S. 2013, The Astrophysical Journal, 768, 34

Burrows, A., Radice, D., Vartanyan, D., et al. 2020, Monthly Notices of the Royal Astronomical Society, 491, 2715

Caffau, E., Ludwig, H.-G., Bonifacio, P., et al. 2010, Astronomy & Astrophysics, 514, A92

Carnelli, P. F. F., Almaraz-Calderon, S., Rehm, K. E., et al. 2014, Physical Review Letters, 112, 192701

Caughlan, G. R., & Fowler, W. A. 1988, Atomic Data and Nuclear Data Tables, 40, 283

Chan, C., Müller, B., & Heger, A. 2020, Monthly Notices of the Royal Astronomical Society, 495, 3751

Chatzopoulos, E., Couch, S. M., Arnett, W. D., & Timmes, F. X. 2016a, The Astrophysical Journal, 822, 61

Chatzopoulos, E., & Wheeler, J. C. 2012, The Astrophysical Journal, 748, 42

Chatzopoulos, E., Wheeler, J. C., & Couch, S. M. 2013, The Astrophysical Journal, 776, 129

Chatzopoulos, E., Wheeler, J. C., Vinko, J., et al. 2016b, The Astrophysical Journal, 828, 94

Chen, K.-J., Woosley, S. E., & Sukhbold, T. 2016, The Astrophysical Journal, 832, 73

Clausen, D., Piro, A. L., & Ott, C. D. 2015, The Astrophysical Journal, 799, 190

Côté, B., O'Shea, B. W., Ritter, C., Herwig, F., & Venn, K. A. 2017, The Astrophysical Journal, 835, 128

Couch, S. M., Chatzopoulos, E., Arnett, W. D., & Timmes, F. X. 2015, The Astrophysical Journal Letters, 808, L21

Couch, S. M., Graziani, C., & Flocke, N. 2013, The Astrophysical Journal, 778, 181

Couch, S. M., & O'Connor, E. P. 2014, The Astrophysical Journal, 785, 123

Couch, S. M., & Ott, C. D. 2013, The Astrophysical Journal Letters, 778, L7

—. 2015, The Astrophysical Journal, 799, 5

Couch, S. M., Warren, M. L., & O'Connor, E. P. 2019, arXiv e-prints, arXiv:1902.01340

—. 2020, The Astrophysical Journal, 890, 127

Cox, J. P., & Giuli, R. T. 1968, Principles of Stellar Structure (New York: Gordon & Breach)

Cristini, A., Meakin, C., Hirschi, R., et al. 2017, Monthly Notices of the Royal Astronomical Society, 471, 279

Cyburt, R. H., Amthor, A. M., Heger, A., et al. 2016, The Astrophysical Journal, 830, 55

Cyburt, R. H., Amthor, A. M., Ferguson, R., et al. 2010, The Astrophysical Journal Supplement, 189, 240

Daigle, S., Kelly, K. J., Champagne, A. E., et al. 2016, Physical Review C, 94, 025803

Davis, A., Jones, S., & Herwig, F. 2017, ArXiv e-prints, arXiv:1712.00114

Davis, A., Jones, S., & Herwig, F. 2018, Monthly Notices of the Royal Astronomical Society, 484, 3921

deBoer, R. J., Görres, J., Wiescher, M., et al. 2017, Reviews of Modern Physics, 89, 035007

Deinzer, W., & Salpeter, E. E. 1965, The Astrophysical Journal, 142, 813

Dessart, L., Hillier, D. J., Livne, E., et al. 2011, Monthly Notices of the Royal Astronomical Society, 414, 2985

Dubey, A., Antypas, K., Ganapathy, M. K., et al. 2009, Parallel Computing, 35, 512

Eftekhari, T., Berger, E., Margalit, B., et al. 2019, The Astrophysical Journal Letters, 876, L10

Eggleton, P. P. 1971, Monthly Notices of the Royal Astronomical Society, 151, 351

Eldridge, J. J., & Tout, C. A. 2005, in Astronomical Society of the Pacific Conference Series, Vol. 342, 1604-2004: Supernovae as Cosmological Lighthouses, ed. M. Turatto, S. Benetti, L. Zampieri, & W. Shea, 126

Evans, M., Hastings, N., & Peacock, B. 2000, Statistical Distributions, 3rd edn. (New York, NY: Wiley)

Fang, X., Tan, W. P., Beard, M., et al. 2017, Phys. Rev. C, 96, 045804

Farmer, R., Fields, C. E., Petermann, I., et al. 2016, The Astrophysical Journal Supplement, 227, 22

Farmer, R., Fields, C. E., & Timmes, F. X. 2015, The Astrophysical Journal, 807, 184

Faulkner, J. 1967, The Astrophysical Journal, 147, 617

Fernández, R. 2012, The Astrophysical Journal, 749, 142

Fields, C. E., & Couch, S. M. 2020, The Astrophysical Journal, 901, 33

Fields, C. E., Farmer, R., Petermann, I., Iliadis, C., & Timmes, F. X. 2016, The Astrophysical Journal, 823, 46

Fields, C. E., Timmes, F. X., Farmer, R., et al. 2018, The Astrophysical Journal Supplement, 234, 19

Filippenko, A. V. 1997, Annual Reviews of Astronomy and Astrophysics, 35, 309

Fowler, W. A., & Hoyle, F. 1964, The Astrophysical Journal Supplement, 9, 201

Fraley, G. S. 1968, Astrophysics and Space Science, 2, 96

Frebel, A., Simon, J. D., Geha, M., & Willman, B. 2010, The Astrophysical Journal, 708, 560

Fryer, C. L., & Kalogera, V. 2001, The Astrophysical Journal, 554, 548

Fryer, C. L., Woosley, S. E., & Heger, A. 2001, The Astrophysical Journal, 550, 372

Fryxell, B., Olson, K., Ricker, P., et al. 2000, The Astrophysical Journal Supplement, 131, 273

Fuller, G. M., Fowler, W. A., & Newman, M. J. 1985, The Astrophysical Journal, 293, 1

Garaud, P., Medrano, M., Brown, J. M., Mankovich, C., & Moore, K. 2015, The Astrophysical Journal, 808, 89

Gasques, L. R., Brown, E. F., Chieffi, A., et al. 2007, Physical Review C, 76, 035802

Glebbeek, E., Gaburov, E., de Mink, S. E., Pols, O. R., & Portegies Zwart, S. F. 2009, Astronomy & Astrophysics, 497, 255

Gómez Iñesta, Á., Iliadis, C., & Coc, A. 2017, ArXiv e-prints, arXiv:1710.01647

Goriely, S., Hilaire, S., & Koning, A. J. 2008, Astronomy & Astrophysics, 487, 767

Gossan, S. E., Sutton, P., Stuver, A., et al. 2016, Physical Review D, 93, 042002

Grevesse, N., & Sauval, A. J. 1998, Space Science Reviews, 85, 161

Hanke, F., Marek, A., Müller, B., & Janka, H.-T. 2012, The Astrophysical Journal, 755, 138

Hanke, F., Müller, B., Wongwathanarat, A., Marek, A., & Janka, H.-T. 2013, The Astrophysical Journal, 770, 66

Hansen, C. J., Kawaler, S. D., & Trimble, V. 2004, Stellar interiors : physical principles, structure, and evolution (New York: Springer-Verlag)

Harris, J. A., Hix, W. R., Chertkow, M. A., et al. 2017, The Astrophysical Journal, 843, 2

Heger, A., Fryer, C. L., Woosley, S. E., Langer, N., & Hartmann, D. H. 2003, The Astrophysical Journal, 591, 288

Heger, A., Langer, N., & Woosley, S. E. 2000, The Astrophysical Journal, 528, 368

Heger, A., & Woosley, S. E. 2010, The Astrophysical Journal, 724, 341

Herwig, F., Austin, S. M., & Lattanzio, J. C. 2006, Physical Review C, 73, 025802

Hopkins, P. F., Quataert, E., & Murray, N. 2011, Monthly Notices of the Royal Astronomical Society, 417, 950

Hoyle, F., & Lyttleton, R. A. 1942, Monthly Notices of the Royal Astronomical Society, 102, 177

Iben, I. 1967, Annual Review of Astronomy and Astrophysics, 5, 571

Iben, Jr., I. 1966, The Astrophysical Journal, 143, 516

—. 1991, The Astrophysical Journal Supplement, 76, 55

Iliadis, C. 2007, Nuclear Physics of Stars (Wiley-VCH Verlag)

Iliadis, C., Anderson, K. S., Coc, A., Timmes, F. X., & Starrfield, S. 2016, The Astrophysical Journal, 831, 107

Iliadis, C., Longland, R., Champagne, A. E., & Coc, A. 2010, Nuclear Physics A, 841, 251

Iliadis, C., Longland, R., Coc, A., Timmes, F. X., & Champagne, A. E. 2015, Journal of Physics G Nuclear Physics, 42, 034007

Imbriani, G., Costantini, H., Formicola, A., et al. 2004, Astronomy & Astrophysics, 420, 625

—. 2005, European Physical Journal A, 25, 455

Itoh, N., Hayashi, H., Nishikawa, A., & Kohyama, Y. 1996a, The Astrophysical Journal Supplement, 102, 411

—. 1996b, The Astrophysical Journal Supplement, 102, 411

Itoh, N., Totsuji, H., Ichimaru, S., & Dewitt, H. E. 1979, The Astrophysical Journal, 234, 1079

Janka, H.-T. 2012, Annual Review of Nuclear and Particle Science, 62, 407

Janka, H.-T., Melson, T., & Summa, A. 2016, ArXiv e-prints, arXiv:1602.05576

Janka, H. T., & Mueller, E. 1996, Astronomy & Astrophysics, 306, 167

Jerkstrand, A., Timmes, F. X., Magkotsios, G., et al. 2015, The Astrophysical Journal, 807, 110

Jiang, C. L., Back, B. B., Janssens, R. V. F., & Rehm, K. E. 2007a, Physical Review C, 75, 057604

Jiang, C. L., Rehm, K. E., Back, B. B., & Janssens, R. V. F. 2007b, Physical Review C, 75, 015803

Jones, S., Andrassy, R., Sandalski, S., et al. 2017, Monthly Notices of the Royal Astronomical Society, 465, 2991

Karakas, A. I., & Lattanzio, J. C. 2014, ArXiv e-prints, arXiv:1405.0062

Kasen, D., Woosley, S. E., & Heger, A. 2011, The Astrophysical Journal, 734, 102

Kobayashi, C., Karakas, A. I., & Lugaro, M. 2020, The Astrophysical Journal, 900, 179

Kruckow, M. U., Tauris, T. M., Langer, N., et al. 2016, Astronomy & Astrophysics, 596, A58

Kunz, R., Fey, M., Jaeger, M., et al. 2002, The Astrophysical Journal, 567, 643

Lai, D., & Goldreich, P. 2000, The Astrophysical Journal, 535, 402

Lamb, S. A., Iben, Jr., I., & Howard, W. M. 1976, The Astrophysical Journal, 207, 209

Lane, D. 2013, Online Statistics Education: A Multimedia Course of Study

Langanke, K., & Martínez-Pinedo, G. 2000, Nuclear Physics A, 673, 481

Langer, N., Fricke, K. J., & Sugimoto, D. 1983, Astronomy & Astrophysics, 126, 207

Lattimer, J. M., & Swesty, D. F. 1991, **??**jnlNuPhA, 535, 331

Lee, D. 2013, Journal of Computational Physics, 243, 269

Lee, D., & Deane, A. E. 2009, Journal of Computational Physics, 228, 952

Leloudas, G., Fraser, M., Stone, N. C., et al. 2016, Nature Astronomy, 1, 0002

Lentz, E. J., Bruenn, S. W., Hix, W. R., et al. 2015, The Astrophysical Journal Letters, 807, L31

Limongi, M. 2017, ArXiv e-prints, arXiv:1706.01913

Lodders, K., Palme, H., & Gail, H.-P. 2009, Landolt Börnstein, arXiv:0901.1149

Longland, R. 2012, Astronomy & Astrophysics, 548, A30

Longland, R., Iliadis, C., Champagne, A. E., et al. 2010, Nuclear Physics A, 841, 1

LUNA Collaboration, Lemut, A., Bemmerer, D., et al. 2006a, Physics Letters B, 634, 483

—. 2006b, Physics Letters B, 634, 483

Lunnan, R., Yan, L., Perley, D. A., et al. 2020, The Astrophysical Journal, 901, 61

Mabanta, Q. A., & Murphy, J. W. 2018, The Astrophysical Journal, 856, 22

Magkotsios, G., Timmes, F. X., Hungerford, A. L., et al. 2010, The Astrophysical Journal Supplement, 191, 66

Marek, A., Dimmelmeier, H., Janka, H. T., Müller, E., & Buras, R. 2006, Astronomy & Astrophysics, 445, 273

Martínez-Rodríguez, H., Badenes, C., Yamaguchi, H., et al. 2017, The Astrophysical Journal, 843, 35

Mazurek, T. J., Truran, J. W., & Cameron, A. G. W. 1974, Astrophysics and Space Science, 27, 261

Meakin, C. A., & Arnett, D. 2007, The Astrophysical Journal, 665, 690

Mişicu, Ş., & Esbensen, H. 2007, Physical Review C, 75, 034606

Müller, B., Heger, A., Liptai, D., & Cameron, J. B. 2016a, Monthly Notices of the Royal Astronomical Society, 460, 742

Müller, B., & Janka, H. T. 2015, Monthly Notices of the Royal Astronomical Society, 448, 2141

Müller, B., Melson, T., Heger, A., & Janka, H.-T. 2017, Monthly Notices of the Royal Astronomical Society, 472, 491

Müller, B., & Varma, V. 2020, Monthly Notices of the Royal Astronomical Society, 498, L109

Müller, B., Viallet, M., Heger, A., & Janka, H.-T. 2016b, ArXiv e-prints, arXiv:1605.01393

Myers, J. L., & Well, A. D. 1995, Research Design & Statistical Analysis, 1st edn. (Routledge)

Nagakura, H., Burrows, A., Radice, D., & Vartanyan, D. 2019, arXiv e-prints, arXiv:1905.03786

Nguyen, N. B., Nunes, F. M., Thompson, I. J., & Brown, E. F. 2012, Physical Review Letters, 109, 141101

Nieuwenhuijzen, H., & de Jager, C. 1990, Astronomy & Astrophysics, 231, 134

Nishimura, N., Hirschi, R., Rauscher, T., Murphy, A. S. J., & Cescutti, G. 2017, Monthly Notices of the Royal Astronomical Society, 469, 1752

Nomoto, K. 1984, The Astrophysical Journal, 277, 791

Nomoto, K., Kobayashi, C., & Tominaga, N. 2013, Annual Reviews of Astronomy and Astrophysics, 51, 457

Nordhaus, J., Burrows, A., Almgren, A., & Bell, J. 2010, The Astrophysical Journal, 720, 694

Nugis, T., & Lamers, H. J. G. L. M. 2000, Astronomy & Astrophysics, 360, 227

Ober, W. W., El Eid, M. F., & Fricke, K. J. 1983, Astronomy & Astrophysics, 119, 61

O'Connor, E. 2015, The Astrophysical Journal Supplement, 219, 24

O'Connor, E., & Ott, C. D. 2011, The Astrophysical Journal, 730, 70

O'Connor, E. P., & Couch, S. M. 2018a, The Astrophysical Journal, 865, 81

—. 2018b, The Astrophysical Journal, 854, 63

Oda, T., Hino, M., Muto, K., Takahara, M., & Sato, K. 1994, Atomic Data and Nuclear Data Tables, 56, 231

Odden, T. O. B. 2019, Physical Review Physics Education Research, 15, doi:10.1103/PhysRevPhysEducRes.15.020152

Ofek, E. O., Sullivan, M., Shaviv, N. J., et al. 2014, The Astrophysical Journal, 789, 104

Özel, F., Psaltis, D., Narayan, R., & Santos Villarreal, A. 2012, The Astrophysical Journal, 757, 55

Pagel, B. E. J., & Portinari, L. 1998, Monthly Notices of the Royal Astronomical Society, 298, 747

Pajkos, M. A., Couch, S. M., Pan, K.-C., & O'Connor, E. P. 2019, Astrophysical Journal, 878, 13

Pan, K.-C., Liebendörfer, M., Couch, S., & Thielemann, F.-K. 2020, arXiv e-prints, arXiv:2010.02453

Paxton, B. 2004, Publications of the Astronomical Society of the Pacific, 116, 699

Paxton, B., Bildsten, L., Dotter, A., et al. 2011, The Astrophysical Journal Supplement, 192, 3

Paxton, B., Cantiello, M., Arras, P., et al. 2013, The Astrophysical Journal Supplement, 208, 4

Paxton, B., Marchant, P., Schwab, J., et al. 2015, The Astrophysical Journal Supplement, 220, 15

Paxton, B., Schwab, J., Bauer, E. B., et al. 2018, The Astrophysical Journal Supplement, 234, 34

Paxton, B., Smolec, R., Gautschy, A., et al. 2019, arXiv e-prints, arXiv:1903.01426

Pejcha, O., & Thompson, T. A. 2012, The Astrophysical Journal, 746, 106

—. 2015, The Astrophysical Journal, 801, 90

Petermann, I., Timmes, F. X., Fields, C. E., & Farmer, R. J. 2017, In preparation

Pignatari, M., Hirschi, R., Wiescher, M., et al. 2013, The Astrophysical Journal, 762, 31

Pignatari, M., Herwig, F., Hirschi, R., et al. 2016, The Astrophysical Journal Supplement, 225, 24

Portinari, L., Casagrande, L., & Flynn, C. 2010, Monthly Notices of the Royal Astronomical Society, 406, 1570

Radice, D., Morozova, V., Burrows, A., Vartanyan, D., & Nagakura, H. 2019, The Astrophysical Journal, 876, L9

Radice, D., Ott, C. D., Abdikamalov, E., et al. 2016, The Astrophysical Journal, 820, 76

Raives, M. J., Couch, S. M., Greco, J. P., Pejcha, O., & Thompson, T. A. 2018, Monthly Notices of the Royal Astronomical Society, 481, 3293

Rakavy, G., & Shaviv, G. 1967, The Astrophysical Journal, 148, 803

Rakavy, G., Shaviv, G., & Zinamon, Z. 1967, The Astrophysical Journal, 150, 131

Rauscher, T., Heger, A., Hoffman, R. D., & Woosley, S. E. 2002, The Astrophysical Journal, 576, 323

Rauscher, T., Nishimura, N., Hirschi, R., et al. 2016, Monthly Notices of the Royal Astronomical Society, 463, 4153

Reilly, E., Maund, J. R., Baade, D., et al. 2016, Monthly Notices of the Royal Astronomical Society, 457, 288

Renzo, M., Ott, C. D., Shore, S. N., & de Mink, S. E. 2017, Astronomy & Astrophysics, 603, A118

Richers, S., Ott, C. D., Abdikamalov, E., O'Connor, E., & Sullivan, C. 2017, Physical Review D, 95, 063019

Roberts, L. F., Ott, C. D., Haas, R., et al. 2016, The Astrophysical Journal, 831, 98

Sallaska, A. L., Iliadis, C., Champange, A. E., et al. 2013, The Astrophysical Journal Supplement, 207, 18

Salpeter, E. E. 1955, The Astrophysical Journal, 121, 161

Scalo, J. M. 1986, Fundam. Cosm. Phys., 11, 1

Schaeffer, N. 2013, Geochemistry, Geophysics, Geosystems, 14, 751

Schönberg, M., & Chandrasekhar, S. 1942, The Astrophysical Journal, 96, 161

Shibata, M., Kiuchi, K., Sekiguchi, Y., & Suwa, Y. 2011, Progress of Theoretical Physics, 125, 1255

Skinner, M. A., Dolence, J. C., Burrows, A., Radice, D., & Vartanyan, D. 2019, The Astrophysical Journal Supplement Series, 241, 7

Smartt, S. J. 2009, Annual Review of Astronomy and Astrophysics, 47, 63

Smartt, S. J. 2009, Annual Reviews of Astronomy and Astrophysics, 47, 63

—. 2015, Publications of the Astron. Soc. of Australia, 32, 16

Smartt, S. J., Eldridge, J. J., Crockett, R. M., & Maund, J. R. 2009, Monthly Notices of the Royal Astronomical Society, 395, 1409

Smith, N. 2014, Annual Review of Astronomy and Astrophysics, 52, 487

Smith, N., Andrews, J. E., Van Dyk, S. D., et al. 2016, Monthly Notices of the Royal Astronomical Society, 458, 950

Spruit, H. C. 2013, Astronomy & Astrophysics, 552, A76

Stancliffe, R. J., Chieffi, A., Lattanzio, J. C., & Church, R. P. 2009, Publications of the Astronomical Society of Australia, 26, 203

Steiner, A. W., Hempel, M., & Fischer, T. 2013, The Astrophysical Journal, 774, 17

Su, K.-Y., Hopkins, P. F., Hayward, C. C., et al. 2018, Monthly Notices of the Royal Astronomical Society, 480, 1666

Sukhbold, T., Ertl, T., Woosley, S. E., Brown, J. M., & Janka, H.-T. 2016, The Astrophysical Journal, 821, 38

Sukhbold, T., Woosley, S., & Heger, A. 2017, ArXiv e-prints, arXiv:1710.03243

Sukhbold, T., & Woosley, S. E. 2014, The Astrophysical Journal, 783, 10

—. 2016, The Astrophysical Journal Letters, 820, L38

Sukhbold, T., Woosley, S. E., & Heger, A. 2018, The Astrophysical Journal, 860, 93

the StarKiller Microphysics Development Team, Bishop, A., Fields, C. E., et al. 2019, starkiller-astro/Microphysics: 19.04, doi:10.5281/zenodo.2620545

Thompson, T. A., Quataert, E., & Burrows, A. 2005, The Astrophysical Journal, 620, 861

Timmes, F. X., Hoffman, R. D., & Woosley, S. E. 2000, The Astrophysical Journal Supplement, 129, 377

Timmes, F. X., & Swesty, F. D. 2000, The Astrophysical Journal Supplement, 126, 501

Timmes, F. X., Woosley, S. E., & Weaver, T. A. 1995, The Astrophysical Journal Supplement, 98, 617

—. 1996, The Astrophysical Journal, 457, 834

Tognelli, E., Moroni, P. G. P., & Degl'Innocenti, S. 2011, Astronomy & Astrophysics, 533, A109

Toro, E. F. 1999, Riemann Solvers and Numerical Methods for Fluid Dynamics (Springer, Berlin, Heidelberg)

Trampedach, R., Stein, R. F., Christensen-Dalsgaard, J., Nordlund, Å., & Asplund, M. 2014, Monthly Notices of the Royal Astronomical Society, 445, 4366

Traxler, A., Garaud, P., & Stellmach, S. 2011, The Astrophysical Journal, 728, L29

Ugliano, M., Janka, H.-T., Marek, A., & Arcones, A. 2012, The Astrophysical Journal, 757, 69

Vagnozzi, S., Freese, K., & Zurbuchen, T. H. 2017, The Astrophysical Journal, 839, 55

Van Dyk, S. D., Peng, C. Y., King, J. Y., et al. 2000, Publications of the Astronomical Society of the Pacific, 112, 1532

Varma, V., & Müller, B. 2021, arXiv e-prints, arXiv:2101.00213

Vartanyan, D., Burrows, A., Radice, D., Skinner, M. A., & Dolence, J. 2019, Monthly Notices of the Royal Astronomical Society, 482, 351

Viallet, M., Meakin, C., Arnett, D., & Mocák, M. 2013, The Astrophysical Journal, 769, 1

Vink, J. S., de Koter, A., & Lamers, H. J. G. L. M. 2001, Astronomy & Astrophysics, 369, 574

Wanajo, S., Janka, H.-T., & Müller, B. 2011, The Astrophysical Journal Letters, 726, L15

Wang, L., & Wheeler, J. C. 2008, Annual Reviews of Astronomy and Astrophysics, 46, 433

Warren, M. L., Couch, S. M., O'Connor, E. P., & Morozova, V. 2020, The Astrophysical Journal, 898, 139

Weiss, A., Serenelli, A., Kitsikis, A., Schlattl, H., & Christensen-Dalsgaard, J. 2005, Astronomy & Astrophysics, 441, 1129

West, C., & Heger, A. 2013, The Astrophysical Journal, 774, 75

West, C., Heger, A., & Austin, S. M. 2013, The Astrophysical Journal, 769, 2

Woosley, S. E. 2016, The Astrophysical Journal Letters, 824, L10

—. 2017, The Astrophysical Journal, 836, 244

Woosley, S. E., Arnett, W. D., & Clayton, D. D. 1971, Physical Review Letters, 27, 700

Woosley, S. E., & Heger, A. 2007, Physics Reports, 442, 269

—. 2015, The Astrophysical Journal, 810, 34

Woosley, S. E., Heger, A., & Weaver, T. A. 2002, Rev. Mod. Phys., 74, 1015

Woosley, S. E., & Weaver, T. A. 1986, Annual Reviews of Astronomy and Astrophysics, 24, 205

Xu, Y., Takahashi, K., Goriely, S., et al. 2013, Nuclear Physics A, 918, 61

Yadav, N., Müller, B., Janka, H. T., Melson, T., & Heger, A. 2019, arXiv e-prints, arXiv:1905.04378

Yoshida, T., Takiwaki, T., Kotake, K., et al. 2019, The Astrophysical Journal, 881, 16

Yoshida, T., Takiwaki, T., Kotake, K., et al. 2021, The Astrophysical Journal, 908, 44

Zaussinger, F., & Spruit, H. C. 2013, Astronomy & Astrophysics, 554, A119

Zhang, W., Woosley, S. E., & Heger, A. 2008, The Astrophysical Journal, 679, 639

Zingale, M., Timmes, F. X., Fisher, R., & O'Shea, B. W. 2016, arXiv e-prints, arXiv:1606.02242

Zingale, M., Dursi, L. J., ZuHone, J., et al. 2002, The Astrophysical Journal Supplement, 143, 539